

PRECIPITATION OF RADIATION BELT  
ELECTRONS BY LIGHTNING-GENERATED  
MAGNETOSPHERICALLY REFLECTING  
WHISTLER WAVES

A DISSERTATION  
SUBMITTED TO THE DEPARTMENT OF ELECTRICAL ENGINEERING  
AND THE COMMITTEE ON GRADUATE STUDIES  
OF STANFORD UNIVERSITY  
IN PARTIAL FULFILLMENT OF THE REQUIREMENTS  
FOR THE DEGREE OF  
DOCTOR OF PHILOSOPHY

Jacob Bortnik  
January 2005

© Copyright by Jacob Bortnik 2005  
All Rights Reserved

I certify that I have read this dissertation and that, in my opinion, it is fully adequate in scope and quality as a dissertation for the degree of Doctor of Philosophy.

---

Umran S. Inan  
(Principal Adviser)

I certify that I have read this dissertation and that, in my opinion, it is fully adequate in scope and quality as a dissertation for the degree of Doctor of Philosophy.

---

Timothy F. Bell

I certify that I have read this dissertation and that, in my opinion, it is fully adequate in scope and quality as a dissertation for the degree of Doctor of Philosophy.

---

Antony C. Fraser-Smith

Approved for the University Committee on Graduate Studies.

# Abstract

This dissertation presents a study of several aspects of the resonant interaction between energetic radiation-belt electrons and lightning generated, magnetospherically-reflecting (MR) whistler mode waves in the inner magnetosphere.

We initially develop a first-order model to estimate the  $L$ -shell dependence of the precipitation flux of energetic electrons driven by MR whistlers injected at  $25^\circ$ ,  $35^\circ$ , and  $45^\circ$  geomagnetic latitude, assuming first a horizontally stratified ionosphere and then an ionosphere containing realistic horizontal density gradients as given by the International Reference Ionosphere (IRI) model. Results indicate that in the region  $1.4 < L < 1.62$ , a narrow (in  $L$ -shell extent) peak in the precipitation signature can result due to the focusing of the whistler wave packet on the first magnetospheric traverse. A wide bulge is formed in the region  $L > 1.8$  due to subsequent “hops” of the whistler wave energy, and the tendency of the whistler to move slowly outward in  $L$  with each hop. By examining the flux of electrons with energy  $> 150$  keV, we obtain excellent agreement with measurements of flux enhancements observed in the drift loss-cone, aboard the SAMPEX satellite.

We then turn our attention to the detailed calculation of the frequency-time ( $f-t$ ) characteristics and power of an MR whistler generated by a single cloud-ground discharge at a given latitude, as it would appear on a satellite at any point in the magnetosphere. By developing an extensive ray tracing and interpolation technique, we simulate a whistler observed aboard the OGO 1 satellite to find excellent agreement between theory and measurement. We then simulate the  $f-t$  spectra that would be produced by lightning injection latitudes of  $25^\circ$ ,  $35^\circ$ ,  $45^\circ$  and  $55^\circ$  geomagnetic latitude, and observed on the geomagnetic equator at  $L = 2, 2.5, 3, 3.5$ , and  $4$ . We vary the cold

plasma density distribution through which the whistler wave propagates, and obtain MR whistler signatures that clearly reflect the properties of the medium traversed by the wave.

Using the formulation described above, we compute the  $f-t$  spectra of an MR whistler at  $1^\circ$  latitude bins along a given field line, thus estimating the wave structure as a function of frequency and time. By treating the pitch-angle scattering in each latitude bin as being incoherent with respect to that produced in any other latitude bin, we calculate the precipitated flux of energetic electrons as a function of time, at every latitude bin on the field-line, including gyro-harmonic resonance interactions of order  $+5$  to  $-5$ , as well as the zero order or Landau resonance. We use a realistic AE8 flux distribution for the trapped flux composing the radiation belts, with a sinusoidal pitch-angle distribution tending to zero at the loss-cone. Results indicate that MR whistler-induced precipitation episodes can last for tens of seconds and moves to higher  $L$ -shells (and hence latitudes) on both short (0.1 sec) and long (10 sec) timescales, covering a geographic region measuring hundreds of kilometers.

We conclude that the flux of precipitating, energetic, radiation belt electrons driven by lightning generated magnetospherically reflecting whistler waves is consistently detectable in the drift loss cone, and produces unique signatures which can be detected using either satellite-borne instruments or ground-based techniques.

# Acknowledgements

With so many amazing people in my life, one of the greatest difficulties in writing my acknowledgements is knowing where to start!

First and foremost, I would like to express my deep gratitude to my contagiously enthusiastic principal advisor, Prof. Umran S. Inan. He has been a source of strength and inspiration to me, and has continually astounded me with his keen scientific insight, depth and breadth of knowledge, unsurpassed dedication to his work and family, and genuine humility. However, what impressed me the most about Umran, was that he believed in me and took me seriously right from the beginning, well before he had any reason to do so.

I would like to thank my second advisor, Prof. Timothy F. Bell, for countless hours of patient discussion on all aspects of the theory shown in this thesis. He is by far the most gifted theorist I know, and I aspire to emulate him one day.

My appreciation goes out to Prof. Tony Fraser-Smith for his help and support, and agreeing to be my third reader (despite his best efforts to retire). I also thank the various faculty and emeriti with whom I have interacted over the years, namely Professors R. N. Bracewell, D. L. Carpenter, R. A. Helliwell, and M. Walt. They have been uniformly generous in sharing with me their lives of scholarship and learning, and I am humbled by their respective achievements. I also acknowledge Shaolan Min and Helen Niu for all their help with the myriad of administrative tasks which they quietly and faithfully perform in the background.

Being part of the VLF group for the past six years can be likened only to belonging to a large family. I cannot think of a finer group of individuals with whom I would have liked to have shared my Ph.D. experiences more.

I thank my good friends Dana Porrat and Neal Bangerter for fun times getting through classes, the Cromem Chefs for zany dinner-time conversations (and not half-bad meals!), the infamous Stanford-Club Squash team (plus super-coach Jon Perry) who keeps me youthful (or at least youthful-looking), and last but not least all the folks at IV who have cared for me and covered me with their prayers before I even knew to ask.

I am eternally grateful to my parents, Judith and Vladimir Bortnik for the love, support, and encouragement they have abundantly poured over me throughout my entire life. They have instilled in me a love of learning, and I long to honour them with this work.

Finally, I acknowledge my beautiful wife, Kirsty Bortnik, who has been the light of my life, my best friend and faithful partner. Words cannot express how much she means to me, but even this, I suspect, she knows.

Jacob Bortnik

*Stanford, California*

*May 25, 2004*

This research was sponsored by the National Aeronautics and Space Administration (NASA) under grant NAG5-11821-0002, by the Air Force Office of Scientific Research (AFOSR) under grant F49620-03-1-0338, and also by NASA through sub-contract via the University of Iowa under grant 4000083338-4 for the POLAR mission and under grant 4000061641 for the CLUSTER mission.

# Dedication

To borrow a line from one of the coolest songs, of one of the best South African bands<sup>1</sup>:

I'm just so glad,  
That what I can't You can,  
And where I end,  
That's where You begin.

Thank You for waiting<sup>2</sup>. Let me be a joy to You always<sup>3</sup>.

---

<sup>1</sup>“So Glad”, *The Answer to the Question*, Tree63, Inpop Records, March 2004

<sup>2</sup>Luke 15:11–32

<sup>3</sup>“Joy”, *Tree63*, Inpop records, Tree63, October 2000



# Preface

Whether the following is an attestation to my diligence and strife for perfection, or simply stubborn (yes, I was warned) lack of foresight, I would like to hereby claim the dubious honor of being the very first member of the VLF group to have prepared my entire dissertation (bugs and all) in both Microsoft Word 2002, and Latex 2e (WinEdt V5.4, MikTeX 2.3).

As an additional reward (besides the obvious reward of calloused fingertips and degenerating eyesight) I was the recipient of a free lunch (courtesy of Umran) and hereby vow to treat my successor (who can challenge, or better my feat) to the same esteemed booty.

# Contents

|  |             |
|--|-------------|
| <b>Abstract</b>  | <b>iv</b>   |
| <b>Acknowledgements</b>                                | <b>vi</b>   |
| <b>Dedication</b>                                      | <b>viii</b> |
| <b>Preface</b>   | <b>ix</b>   |
| <b>1 Introduction</b>                                  | <b>1</b>    |
| 1.1 Purpose . . . . .                                  | 1           |
| 1.2 Scientific background . . . . .                    | 2           |
| 1.2.1 What is an MR whistler? . . . . .                | 2           |
| 1.2.2 The magnetosphere and plasmasphere . . . . .     | 5           |
| 1.2.3 The radiation belts . . . . .                    | 7           |
| 1.3 Review of past work . . . . .                      | 9           |
| 1.4 Thesis organization . . . . .                      | 14          |
| 1.5 Scientific contributions . . . . .                 | 15          |
| <b>2 Theoretical background</b>                        | <b>17</b>   |
| 2.1 Lightning induced electron precipitation . . . . . | 17          |
| 2.2 Lightning illumination model . . . . .             | 19          |
| 2.3 Ray tracing methodology . . . . .                  | 20          |
| 2.3.1 Ray tracing formulation . . . . .                | 21          |
| 2.3.2 Refractive index . . . . .                       | 23          |

|          |   |           |
|----------|---|-----------|
| 2.3.3    | Description of the medium . . . . .   | 29        |
| 2.3.4    | The Stanford VLF ray tracing code . . . . .                                   | 33        |
| 2.4      | Oblique wave-particle interaction . . . . .                                   | 35        |
| 2.4.1    | Adiabatic motion . . . . .  | 36        |
| 2.4.2    | Wave-particle interaction . . . . .   | 39        |
| 2.5      | Landau damping . . . . .  | 44        |
| <b>3</b> | <b><i>L</i>-Dependence of MR precipitation</b>                                | <b>49</b> |
| 3.1      | Introduction . . . . .  | 49        |
| 3.2      | Description of the model . . . . .  | 51        |
| 3.2.1    | Construction of the wave property distribution . . . . .                      | 52        |
| 3.2.2    | Calculation of the wave-induced precipitation . . . . .                       | 54        |
| 3.3      | Results for 25° lightning source latitude . . . . .                           | 55        |
| 3.3.1    | Focusing of ray ensemble . . . . .  | 55        |
| 3.3.2    | Horizontal density gradients . . . . .  | 57        |
| 3.3.3    | Pitch angle scattering and interpolation . . . . .                            | 60        |
| 3.3.4    | Comparison with SAMPEX data . . . . .   | 61        |
| 3.4      | Effect of injection parameters on the precipitation signature . . . . .       | 61        |
| 3.4.1    | IRI Model at 190° longitude . . . . .   | 62        |
| 3.4.2    | Injection with vertical wave normals . . . . .                                | 63        |
| 3.4.3    | Lightning source latitudes of 35° and 45° . . . . .                           | 64        |
| 3.4.4    | Formation of multiple narrow peaks . . . . .                                  | 64        |
| 3.5      | Discussion and model limitations . . . . .                                    | 67        |
| <b>4</b> | <b>Frequency-time spectra of MR whistlers</b>                                 | <b>70</b> |
| 4.1      | Introduction . . . . .  | 70        |
| 4.2      | Description of the model . . . . .  | 71        |
| 4.2.1    | Wave power density at the point of injection of rays . . . . .                | 72        |
| 4.2.2    | Deposition of MR wave energy at frequency-specific <i>L</i> -shells . . . . . | 73        |
| 4.2.3    | Lifetime of MR whistler waves . . . . .                                       | 75        |
| 4.2.4    | Detection of whistler waves at an observation point . . . . .                 | 79        |
| 4.2.5    | Interpolation between sample rays . . . . .                                   | 81        |

|          |   |            |
|----------|---|------------|
| 4.2.6    | Construction of the frequency-time spectrogram . . . . .  | 84         |
| 4.2.7    | Plasmaspheric medium . . . . .                            | 85         |
| 4.2.8    | Model validation . . . . .                                | 86         |
| 4.3      | Smooth plasmasphere . . . . .                             | 88         |
| 4.3.1    | General observations . . . . .                            | 88         |
| 4.3.2    | Wave damping and spatial dispersion . . . . .             | 90         |
| 4.3.3    | Peculiar frequency-time features . . . . .                | 91         |
| 4.4      | Non-smooth plasmaspheres . . . . .                        | 92         |
| 4.4.1    | Randomizing ionosphere . . . . .                          | 93         |
| 4.4.2    | Plasmasphere permeated by ducts . . . . .                 | 95         |
| 4.4.3    | Plasmasphere permeated by one-sided ledges . . . . .      | 98         |
| 4.5      | Summary and discussion . . . . .                          | 99         |
| <b>5</b> | <b>MR Whistler precipitation signatures</b>               | <b>102</b> |
| 5.1      | The wave-particle interaction model . . . . .             | 102        |
| 5.1.1    | Wave characteristics along a single field line . . . . .  | 103        |
| 5.1.2    | Calculation of the change in pitch-angle . . . . .        | 104        |
| 5.1.3    | Determination of the precipitated flux . . . . .          | 119        |
| 5.1.4    | Modeling of the trapped particle distribution . . . . .   | 122        |
| 5.2      | Simulation results . . . . .                              | 125        |
| 5.2.1    | Differential number flux . . . . .                        | 126        |
| 5.2.2    | Energy flux . . . . .                                     | 131        |
| 5.2.3    | Global view of precipitated energy flux . . . . .         | 138        |
| 5.2.4    | Precipitation hotspot in geographic coordinates . . . . . | 146        |
| 5.2.5    | Longitude integrated fluxes . . . . .                     | 158        |
| 5.3      | Summary and discussion . . . . .                          | 162        |
| <b>6</b> | <b>Summary and conclusions</b>                            | <b>165</b> |
| 6.1      | Summary . . . . .   | 165        |
| 6.2      | Discussion . . . . .                                      | 167        |
| 6.3      | Suggestions for future work . . . . .                     | 172        |

|          |  |            |
|----------|--|------------|
| <b>A</b> | <b>Derivations</b>   | <b>176</b> |
| A.1      | Calculation of the precipitation flux of Section 3.2.2 . . . . . | 176        |
| A.2      | Analytical evaluation of (2.26) . . . . .                        | 179        |
|          | <b>Bibliography</b>  | <b>185</b> |

# List of Tables

|     |   |     |
|-----|---|-----|
| 5.1 | Total precipitated energy and electron number . . . . . | 160 |
|-----|---|-----|

# List of Figures

|      |  |    |
|------|--|----|
| 1.1  | Example of an MR whistler . . . . .                                      | 2  |
| 1.2  | Propagation in Earth-ionosphere waveguide . . . . .                      | 3  |
| 1.3  | Formation of the MR whistler . . . . .                                   | 5  |
| 1.4  | The magnetosphere . . . . .  | 6  |
| 1.5  | Graphical depiction of the radiation belts . . . . .                     | 8  |
| 2.1  | Wave-particle interaction process . . . . .                              | 18 |
| 2.2  | Snell's law interpretation of ray path . . . . .                         | 22 |
| 2.3  | Refractive index with ray direction . . . . .                            | 27 |
| 2.4  | Refractive index including ions at 3 frequencies . . . . .               | 28 |
| 2.5  | Plasmaspheric electron number density . . . . .                          | 32 |
| 2.6  | Illustration of ray tracing and wave turnaround . . . . .                | 34 |
| 2.7  | Adiabatic motion of particles in the geomagnetic field . . . . .         | 36 |
| 2.8  | Dependence of mirror height on equatorial pitch angle . . . . .          | 38 |
| 2.9  | Wave-particle interaction geometry . . . . .                             | 41 |
| 2.10 | Landau damping cartoon . . . . .   | 47 |
| 3.1  | Precipitation signature observed on the SAMPEX satellite . . . . .       | 50 |
| 3.2  | Propagation of an MR whistler . . . . .                                  | 53 |
| 3.3  | Two outermost rays of an illumination region . . . . .                   | 57 |
| 3.4  | Equatorial focusing of an illumination region's outermost rays . . . . . | 58 |
| 3.5  | Wave normal refraction in the ionosphere . . . . .                       | 59 |
| 3.6  | Ionospheric electron number density profiles . . . . .                   | 60 |
| 3.7  | Precipitation signatures for $\lambda_s = 25^\circ$ . . . . .            | 62 |

|      |  |     |
|------|--|-----|
| 3.8  | Precipitation signatures under various conditions . . . . .                        | 65  |
| 4.1  | Comparison of 0.5 kHz and 5 kHz ray characteristics . . . . .                      | 74  |
| 4.2  | Settling frequencies $f_s$ as a function of $L$ -shell . . . . .                   | 75  |
| 4.3  | MR whistler lifetimes . . . . .  | 77  |
| 4.4  | Illustration of interpolation scheme . . . . .                                     | 82  |
| 4.5  | MR whistler observation and simulation . . . . .                                   | 87  |
| 4.6  | $f-t$ Spectrogram obtained in a smooth plasmasphere . . . . .                      | 89  |
| 4.7  | Ray path reflections from the plasmopause . . . . .                                | 92  |
| 4.8  | Spectra obtained assuming a randomizing ionosphere . . . . .                       | 94  |
| 4.9  | $f-t$ Spectra obtained assuming one and two-sided ducts . . . . .                  | 97  |
| 4.10 | Equatorial electron density profiles . . . . .                                     | 98  |
| 5.1  | Flux calculation technique illustrated . . . . .                                   | 106 |
| 5.2  | Computation procedure flowchart . . . . .  | 107 |
| 5.3  | $\Delta\alpha_{rms}$ vs velocity for a single $f-t$ cell . . . . .                 | 109 |
| 5.4  | Comparison of $\Delta\alpha_{itrms}$ using analytical versus full method . . . . . | 111 |
| 5.5  | Latitude discretization error study . . . . .                                      | 114 |
| 5.6  | Equatorial pitch angle of resonant test particle . . . . .                         | 115 |
| 5.7  | Pitch-angle deflection as a function of $E$ and $t$ . . . . .                      | 118 |
| 5.8  | Illustration of pitch angle scattering . . . . .                                   | 121 |
| 5.9  | Energetic electron flux for AE8 and analytical distributions . . . . .             | 124 |
| 5.10 | Equatorial energetic electron flux . . . . .                                       | 126 |
| 5.11 | Differential number flux signatures at $L=2.3$ and $L=3$ . . . . .                 | 128 |
| 5.12 | Resonant energies vs. latitude at $L=3$ . . . . .                                  | 129 |
| 5.13 | Integrated energy flux at $L=2.3$ and $L=3$ . . . . .                              | 133 |
| 5.14 | A 2 kHz ray showing polarization and associated quantities . . . . .               | 134 |
| 5.15 | Resonance condition satisfying various resonance modes . . . . .                   | 135 |
| 5.16 | Global precipitated flux for $\lambda_s=25^\circ$ . . . . .                        | 140 |
| 5.17 | Global precipitated flux for $\lambda_s=35^\circ$ . . . . .                        | 141 |
| 5.18 | Global precipitated flux for $\lambda_s=45^\circ$ . . . . .                        | 143 |
| 5.19 | Global precipitated flux for $\lambda_s=55^\circ$ . . . . .                        | 144 |



|      |   |     |
|------|---|-----|
| 5.20 | Longitude extrapolation technique . . . . .                 | 148 |
| 5.21 | Precipitation hotspot illustration . . . . .                | 151 |
| 5.22 | Time sequence of MR whistler driven precipitation . . . . . | 152 |
| 5.23 | Integrated flux versus $L$ -shell . . . . .                 | 159 |

# Chapter 1

## Introduction

### 1.1 Purpose

The purpose of this dissertation is to quantitatively examine the impact of terrestrial lightning discharges on the Earth’s electron radiation belts (or Van Allen belts), through the cyclotron resonant pitch-angle scattering of energetic electrons by magnetospherically reflected (MR) whistler waves, and the resultant precipitation of the electrons onto the ionosphere. The primary tool that we use is numerical modeling to determine whistler ray paths and to estimate the wave-induced pitch-angle scattering resulting from the resonant wave-particle interactions in the magnetosphere, with inputs based on satellite measurements (e.g., particle distributions, wave dynamic spectra) and ground-based observations (e.g., lightning spectra, ionospheric collisional damping). The specific areas we focus our attention on are: (i) determination of the broad spatial distribution of precipitation due to a single MR whistler wave packet and the primary factors affecting this distribution; (ii) development of a technique to effectively model the observed frequency-time ( $f-t$ ) spectra of MR whistler waves, which helps us to determine the factors affecting these spectra, and (iii) computation of the expected temporal signature of the differential number flux of precipitating energetic electrons at the northern and southern ‘feet’ of a given field line where an MR whistler wave scatters electrons into the loss-cone.

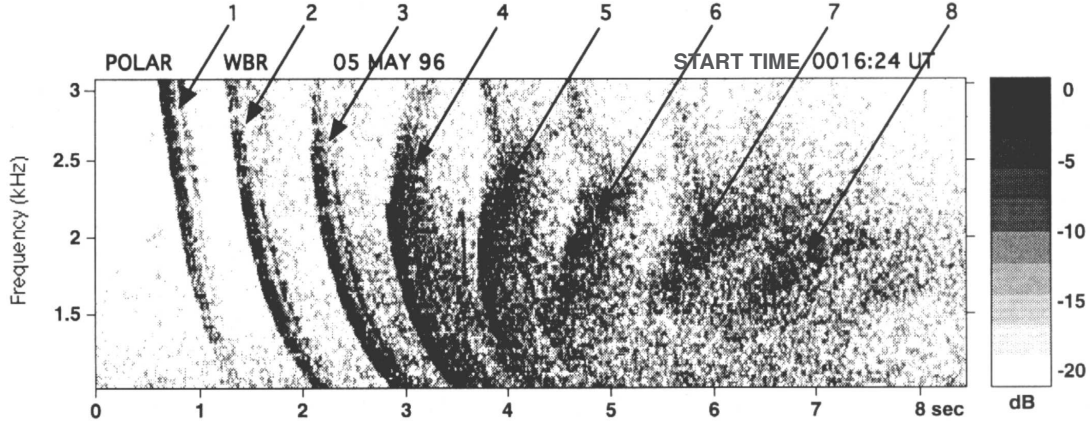


Figure 1.1: MR whistler observed aboard the POLAR satellite in the 8 sec interval starting at 0016:24 UT on May 5th 1996, showing 8 distinct components.

## 1.2 Scientific background

The general phenomenon of lightning-induced electron precipitation (LEP) is an important manifestation of the coupling of the dynamics of the radiation belts (an important component of what is now known as Space Weather), to those of lightning and thunderstorms (i.e., terrestrial weather). The particular topic of interest in this dissertation, namely electron precipitation driven by MR whistlers, is one component of the LEP process that has not been quantitatively studied up to now. In the following, we review some of the major elements involved in the LEP process, discuss the placement of this topic in the broader context of sun-Earth relations, and review past work upon which this dissertation is built.

### 1.2.1 What is an MR whistler?

Magnetospherically reflected whistler waves were first observed aboard the OGO 1 satellite [Smith and Angerami, 1968]. Fortunately, the technique of numerical ray tracing had matured just in time through the efforts of Hines [1957] and Kimura [1966] to allow Smith and Angerami [1968] to accurately interpret the multiple wave components in their observations as magnetospheric reflections of the obliquely propagating, lightning-generated whistler wave packet.

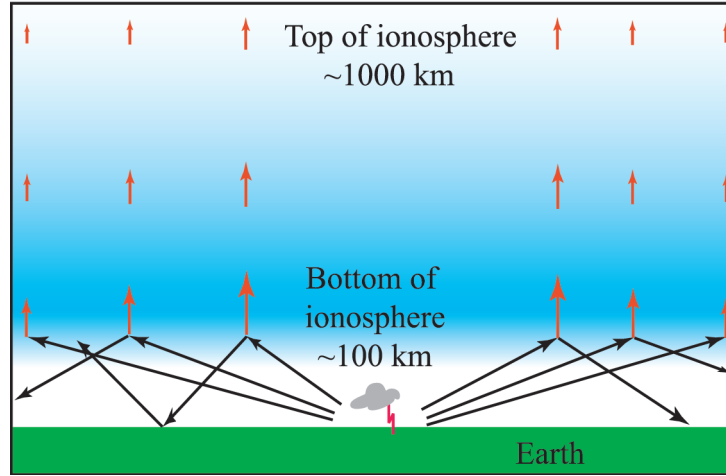


Figure 1.2: Illustration of a lightning discharge radiating ELF and VLF waves that propagate away from the source in the Earth-ionosphere waveguide and leak into the magnetosphere.

Figure 1.1 shows an example of a typical MR whistler observed with the plasma wave instrument (PWI) aboard the POLAR satellite. As shown, the frequency-time spectrum usually consists of several traces or components that are temporally spaced in a pattern determined largely by the location of the satellite (c.f. Section 4.3). The first trace shows relatively little dispersion indicating that the propagation path length between the lightning source and satellite was short compared to the propagation path length of subsequent components. The series of traces gradually develops “nose” frequencies, or frequencies of minimum time delay, and both the upper and lower cutoff frequencies of the traces tend towards a central value with time [Edgar, 1972]; for example, in Figures 1.1 and 1.3 this central value is  $\sim 2$  kHz.

The sequence of events leading up to the formation of a magnetospherically reflected whistler is as follows: first, a terrestrial cloud-to-ground lightning discharge occurs and radiates a broad spectrum of electromagnetic (EM) waves, including waves in the extra low frequency (ELF) and very low frequency (VLF) bands, i.e., 300 Hz to 30 kHz. These ELF/VLF waves propagate away from the lightning source in the Earth-ionosphere waveguide, reflecting many times between the surface of the Earth and the ionosphere.

Since the ionosphere is not perfectly conducting and because of the fact that the presence of the Earth’s magnetic field allows the propagation of wave modes well below the plasma frequency [*Helliwell*, 1965, p.31], a fraction of the wave energy leaks through and propagates to the top of the ionosphere, and further up to the magnetosphere as illustrated in Figure 1.2. During this transionospheric traverse, the wave power is diminished due to collisional damping between electrons and neutral particles [*Helliwell*, 1965, p.71].

Once the ELF/VLF waves reach the top of the ionosphere (taken in our work to be at 1000 km altitude), we assume that geometric optics theory holds (since the medium is slowly varying over spatial scales comparable to a wavelength) and employ the technique of numerical ray tracing to determine the ray paths of the whistler waves. The use of ray tracing is necessary to numerically determine the time evolution of the wave packet because, in general, nonducted propagation in the anisotropic and inhomogeneous magnetospheric medium cannot be analyzed using closed form expressions.

The formation of multiple  $f-t$  traces (labeled 1–8 in Figure 1.1) is illustrated in Figure 1.3, where we show that each trace forms as a result of the different ray paths followed by the MR whistler components. Due to the efficient spreading of the wave energy in the Earth-ionosphere waveguide, the whistler waves are injected into the magnetosphere over a broad range of latitudes surrounding the source, and waves from every portion of this latitude range may travel from their injection point to the satellite location along different paths.

For instance the first trace (labeled “1” in Figure 1.1 and 1.3a) comes about due to whistler waves propagating directly from their injection point to the satellite (purple ray path). The whistler waves injected at latitudes between those of the purple path and blue path in Figure 1.3 miss the satellite entirely, but the waves injected in the vicinity of the blue ray path are observed on the satellite after reflection (the nature of this type of reflection will be described in Section 2.3), forming the second trace. Similarly, waves injected between the blue and red paths are not observed, but those injected in the vicinity of the red path are recorded after a second reflection occurring in the northern hemisphere, thus constituting the third trace. We have only shown

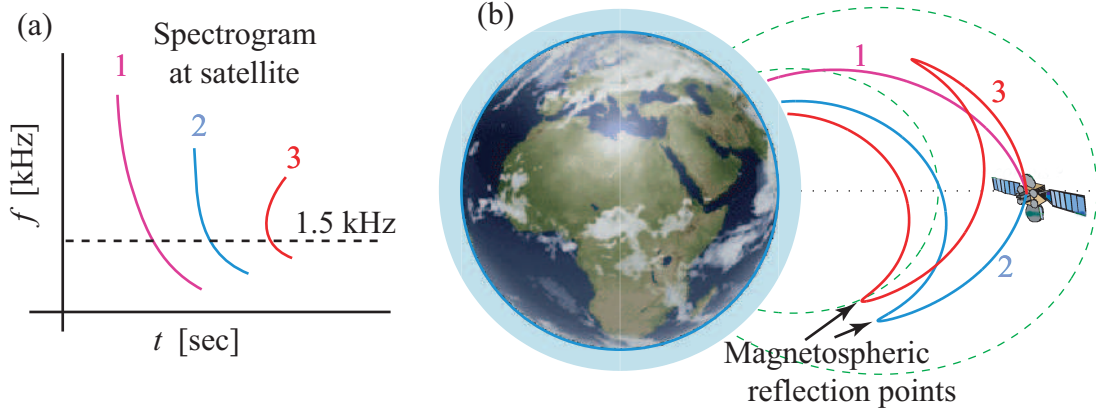


Figure 1.3: Formation of three distinct MR whistler traces resulting from the three different ray paths taken by portions of the MR whistler from lightning source to satellite. Only ray paths for 1.5 kHz are shown; ray paths for other frequencies are similar but not identical.

3 rays of a single frequency component, namely 1.5 kHz, as indicated by the dashed line in the left panel of Figure 1.3. Other frequency components behave similarly but their injection latitudes are slightly displaced from that of the 1.5 kHz component in order to intercept the satellite (due to their frequency-dependent ray paths).

In the context of MR whistlers the plasmasphere thus acts as a resonant cavity, storing the wave energy as it multiply reflects and traverses the magnetic equator multiple times [Inan *et al.*, 2003]. This stored whistler wave energy can, in turn, perturb the trajectories of trapped energetic electrons via cyclotron resonance interactions, causing them to precipitate and effectively be removed from the radiation-belts.

We now briefly introduce the magnetosphere and the plasmasphere before providing a brief background on the radiation belts and placing our work on MR whistlers in the context of past research.

### 1.2.2 The magnetosphere and plasmasphere

The magnetosphere is defined as that region of space where the behavior of the plasma is controlled primarily by the geomagnetic field, and is schematically illustrated in Figure 1.4. In the absence of the interplanetary plasma, the Earth's dipole field would

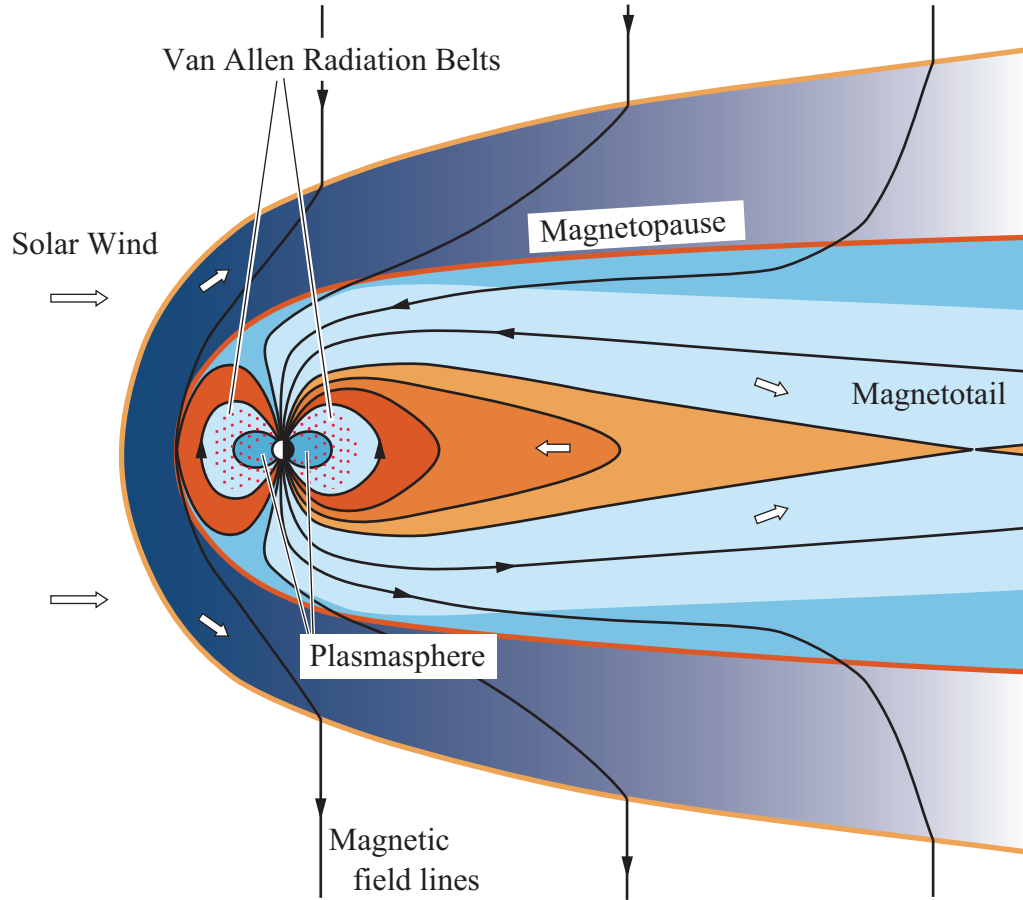


Figure 1.4: Schematic illustration of the magnetosphere showing the areas of greatest interest in this work, namely the (Van Allen) radiation belts, and plasmasphere (Figure modified from *Hill and Dessler* [1991] courtesy of T.W. Hill).

extend symmetrically in all directions, but in reality the solar wind exerts pressure on the dipole field, compressing it on the sun side (thus creating the boundary known as the magnetopause) at  $\sim 10R_E$  ( $1R_E \simeq 6370$  km) and extending it into a long tail on the night side that blends gradually into the background interplanetary field at  $> 60R_E$  [Tascione, 1994, p.57]. This distortion of the geomagnetic field is illustrated in Figure 1.4 where the black arrows indicate the direction of the magnetic field lines.

The constant stream of solar wind particles flowing past the Earth can interact with the geomagnetic field lines and create strong convection patterns in the tail that push the incoming plasma in the sunward direction [Dungey, 1961] as indicated by the

white arrows. Since the plasma near the Earth is “frozen in” to the geomagnetic field [Kivelson and Russel, 1995, p.314], a natural boundary (called the plasmopause) is established, separating the corotating plasma of the Earth from the convecting plasma [Carpenter, 1963]. The bulk of the plasma contained within the plasmopause (i.e., in the plasmasphere) is composed primarily of ‘cold’ electrons and protons with typical energies  $< 1$  eV, and is relatively dense with concentrations of  $\sim 10^2$  to  $10^4$  el/cm<sup>3</sup> at the inner edge of the plasmopause. The plasmasphere is the region that supports MR whistler propagation most efficiently, and is shown in blue color in Figure 1.4. This inner magnetospheric region which hosts the inner radiation belt and inner edge of the outer radiation belt is the only region of the vast magnetosphere that is considered in this work.

### 1.2.3 The radiation belts

Interpenetrating the cold plasma of the plasmasphere is an energetic (hot) population of particles constituting the radiation belts (red-dotted region in Figure 1.4). This hot particle population consists mostly of electrons and protons with energies  $> 100$  keV, that experience long-term trapping in the geomagnetic field. Such trapping requires stable magnetic fields, and near the magnetopause the magnetic field fluctuations induced by solar-wind variability prevent long-term trapping. On the low altitude side, frequent collisions between trapped particles and the dense upper atmospheric gases result in the removal of radiation belt particles. Thus, the region of prime interest in radiation belt studies is the volume of stable magnetic field above  $\sim 200$  km, and below  $\sim 7 R_E$  at the equator [Walt, 1994, p.4].

Trapped radiation-belt particles undergo three types of periodic motion (as shown in 2.7): the first is a rapid gyration about the static magnetic field line, the second is a mirroring motion between the northern and southern hemispheres, and the last is the relatively slow rotation about the Earth. These periodic motions occur on timescales of  $\sim 10^{-3}$ ,  $\sim 1$ , and  $\sim 10^3$  sec, respectively. The physics of these periodic motions is discussed in Section 2.4.1 and in Walt [1996, p.36], but for purposes of introduction it is sufficient to say that a large population of trapped electrons form structures as



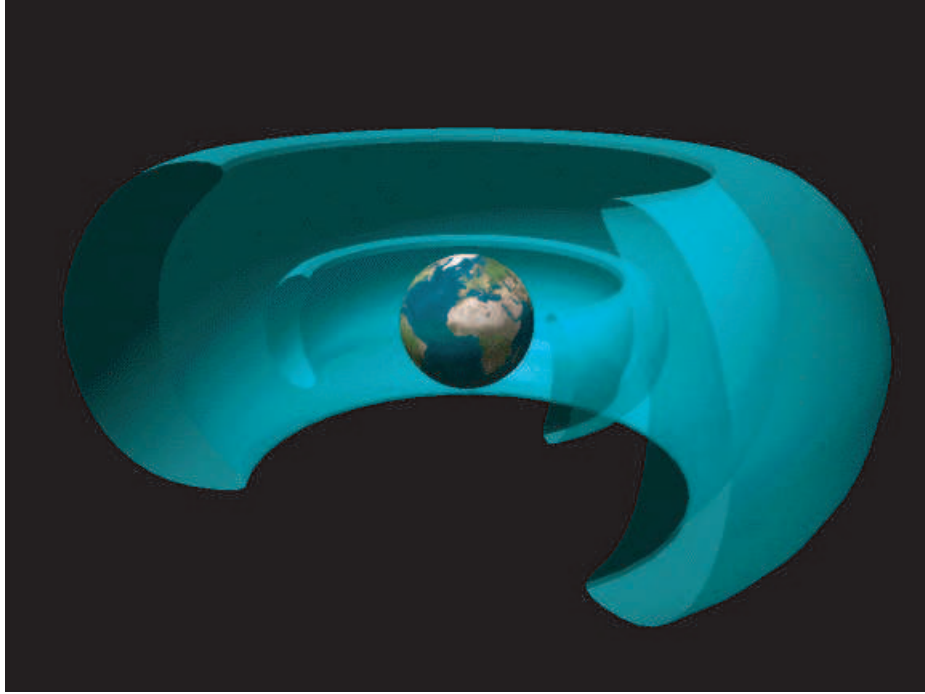


Figure 1.5: A graphical depiction of the Earth’s radiation belts, showing the inner and outer radiation belts to scale.

shown in Figure 1.5 which depicts an inner belt, an outer belt, and an intermediate region with depleted energetic fluxes known as the ‘slot-region’.

In the absence of perturbing forces, the trapped energetic particles of the radiation-belts would remain in their stable orbits indefinitely. However, it has been shown that such is not the case (see, for instance, [Li *et al.*, 1998]) with energetic particle fluxes undergoing large temporal variations. Although the radiation belts have been studied intensely since their discovery in 1958, their principal sources and loss mechanisms remain unclear [Walt, 1996, p.1]. The source of radiation belt particles is believed to be largely the solar wind, although there is some continuing debate about how the solar wind particles are accelerated from tens of keV to hundreds of keV or MeV energies and how they are able to migrate across magnetic shells in order to populate the inner magnetosphere [Walt, 1996, p.1; Horne, 2002].

The loss of radiation belt particles is likely due to interactions with whistler mode waves, as first suggested by Dungey [1963] (in connection with lightning generated

whistlers), but the origin of some of these waves is uncertain as well as the relative contributions of each wave type [Horne, 2002]. Possible types of ELF/VLF whistler-mode waves observed in the inner magnetosphere are plasmaspheric hiss, lightning generated whistler waves (ducted and nonducted), VLF transmitter signals, as well as power line harmonic radiation (PLR). The present work deals with a certain type of ELF/VLF whistler-mode wave, the lightning-generated magnetospherically reflecting whistler wave, and examines in detail the interaction of this particular wave with the energetic radiation belt electrons.

### 1.3 Review of past work

The study of whistler wave and energetic particle interactions in the magnetosphere has a long history and any comprehensive review would certainly not fit into a single subsection, or even a chapter of a manuscript of this length. We have thus chosen to focus on only a handful of studies that are very closely related to the present work, with the understanding that the majority of studies necessarily remains unmentioned.

As mentioned above, *Dungey* [1963] was the first to suggest that whistler waves originating in lightning discharges could be responsible for the loss of radiation belt particles through resonant wave-particle interactions, leading to a steady diffusion into the loss-cone. This concept was examined by *Roberts* [1966] who used the only data on wave frequencies and intensities (derived from ground measurements of ducted whistlers) available at that time in his model of pitch-angle scattering, and concluded that scattering by lightning-generated whistlers was insufficient to account for observed lifetimes. The wave-particle interaction mechanism was extended by *Kennel and Petschek* [1966], who considered incoherent whistler mode waves generated by the energetic electrons (the so-called plasmaspheric hiss) and included in their model the amplification of the whistler wave due to the anisotropy of the particle population, thus establishing an approximate upper limit on both available fluxes and wave intensities. While this work generated much interest initially, later measurements have shown that some of the necessary conditions for the mechanism are not generally present [Walt, 1996, p.5].

Subsequent modeling efforts have followed one of two main approaches: the diffusion (or “Fokker-Planck”) approach, and the test particle (or “Liouville”) approach. The former approach is a direct extension of the original *Kennel and Petschek* [1966] methodology, which assumes that a broad band of incoherent waves perturbs adiabatically-trapped electrons, causing a violation of the first adiabatic invariant and resulting in pitch angle diffusion and precipitation. This approach was originally applied to plasmaspheric hiss and subsequently extended to include oblique wave-particle interactions in studying the equilibrium structure of the radiation belts [Roberts, 1969; Lyons *et al.*, 1971; Lyons *et al.*, 1972; Lyons and Thorne, 1973].

A more recent study performed by *Abel and Thorne* [1998*a;b*] (henceforth *AT*) examined the relative contributions to the loss of radiation-belt electrons of coulomb interactions and three different wave types: plasmaspheric hiss (occupying the frequency band  $f = 1 \pm 0.5$  kHz), whistler wave originating in lightning discharges (including MR whistlers) ( $f = 4.5 \pm 2$  kHz), and VLF transmitters ( $f = 17.1$  kHz  $\pm 50$  Hz and 22.3 kHz  $\pm 50$  Hz). Although *AT* generally concluded that whistlers from lightning discharges were dominant in controlling 100 to 300 keV electron lifetimes in the range  $L \simeq 2 - 3$ , their choice of input parameters makes it unclear as to whether the potential role of the MR whistler component was properly accounted for. For instance, the frequency band occupied by MR whistlers decreases with increasing  $L$ -shell (see Section 4.2.2 and [Ristic'-Djurovic' *et al.*, 1998; Thorne and Horne, 1994]) with a corresponding increase in the resonant energies of interacting electrons, effectively decoupling the precipitated energy of electrons from any specific  $L$ -shell (in contrast to the conclusions reported by *AT*). The wave normal angle of all wave types was set by *AT* at  $\theta \sim 45^\circ \pm 22.5^\circ$  throughout the magnetosphere, also inconsistent with MR whistler behavior in which the wave normal angle tends to become very oblique ( $\theta \simeq 90^\circ$ ) as it propagates. While the diffusion-based analysis used by *AT* is useful in estimating the long-term equilibrium structure of the radiation belts, we believe that the MR whistler behavior (for example the variation of wave normal angle along the ray path) is more complicated than that represented by the simple parameterization of *AT*, a factor which may have led to somewhat inaccurate conclusions. The fact that the whistler is modeled as an incoherent band of waves is also misleading, since

whistlers are in fact coherent, and the series of scatterings experienced by the particles are thus not random. Further, diffusion analysis as applied under steady-state conditions provides no indication of the transient behavior (temporal signatures) of the precipitated flux of electrons, which could potentially be verified by satellite- or ground-based measurements.

The second broad approach involves integration of the equations of motion for individual test particles as they traverse the whistler wave packet, and inference of the behavior of the entire distribution function based on this sample, paying particular attention to the fraction of particles scattered into the loss cone. *Inan et al.* [1978] introduced this technique in modeling a monochromatic, ducted whistler-mode wave interacting with energetic electrons in a realistic magnetosphere. Subsequently, the model was extended to include the effects of finite-duration [*Inan et al.*, 1982; *Inan et al.*, 1985b], and variable frequency pulses [*Chang and Inan*, 1983b; *Chang and Inan*, 1985a; *Chang and Inan*, 1985b]. This model facilitated the first direct comparisons of theoretically predicted temporal and energy signatures of electron precipitation bursts with satellite observations of both VLF transmitter-induced [*Inan et al.*, 1985b] and lightning induced electron bursts in the loss-cone [*Inan et al.*, 1989].

Consideration of the interaction of particles with obliquely propagating whistler-mode waves led to the derivation of the gyro-averaged equations of motion, first for the longitudinal resonance [*Inan and Tkalcevic*, 1982], and then for a general (including cyclotron) resonance interaction [*Bell*, 1984]. Using the equations of *Ibid*, *Jasna et al.*, [1992], *Jasna* [1993], and *Ristic'-Djurovic' et al.* [1998] modeled the interaction of oblique and MR whistlers with radiation belt electrons. Although this work was the first of its kind which addressed MR whistler-induced scattering, it was limited in that only monochromatic waves were examined. Furthermore, the wave-induced pitch-angle scattering was calculated using only one pass of the wave across the magnetic equator, at the  $L$ -shell at which the ray path would eventually settle (i.e., ignoring the ray paths leading to the  $L$ -shell of interest), and using the results of the one-pass interaction, diffusion coefficients were computed and the lifetimes of energetic resonant electrons were estimated. Finally, only the first counterstreaming gyroresonance interaction was considered, the dynamics of the event were ignored and

only a time-integrated precipitation signature was obtained. Despite these limitations, the *Jasna et al.* [1992] and *Ristic-Djurovic* [1998] work is important because it showed that MR whistlers of reasonable intensity could cause significant and measurable precipitation fluxes that in turn would affect the lifetimes of radiation belt electrons.

The subsequent contributions of *Lauben* [1999], and *Lauben et al.* [2001] (henceforth *Lauben*) are the most recent in the field and are also most closely related to the present work. The present study is partially based upon the work of *Lauben*, in that the lightning discharge frequency spectrum, propagation in the Earth ionosphere waveguide, and transionospheric collisional damping are similarly modeled. Further, *Lauben* [1999] also used ray tracing to specify the whistler power density along a certain  $L$ -shell as a function of frequency and time. However, the *Lauben* [1999] work was limited in that only the first traverse of the magnetic equator (a so-called ‘hop’) of the oblique whistler was considered, and further, only frequency components below the ‘nose’ frequency were included. Wave-induced pitch angle scattering was computed only for the first counterstreaming gyroresonance mode, the effects of Landau damping on the wave were not included, and the trapped energetic electron distribution function was assumed to be constant throughout the magnetosphere. Finally, *Lauben* followed previous work [*Inan et al.*, 1978; *Inan et al.*, 1982; *Chang et al.*, 1983; *Chang and Inan*, 1983a; *Chang and Inan*, 1985a; *Chang and Inan*, 1985b; *Inan et al.*, 1985a; *Inan et al.*, 1985b; *Jasna et al.*, 1992; *Jasna*, 1993; *Ristic'-Djurovic' et al.*, 1998] and considered only fresh populations of electrons entering the wave packet distributed uniformly in pitch-angle above the loss cone, with no pre-existing flux inside the loss cone. In the present work, many of these assumptions are shown to be overly restrictive. More specifically, the inclusion of higher order resonance modes was suggested to be essential for oblique waves [*Albert*, 1994], and so we have considered resonance modes of order  $-5$  to  $5$  consistent with *AT*. During the course of interaction with an MR whistler typically enduring for up to ten seconds, the loss-cone distribution cannot remain sharp since the same population necessarily interacts with the same MR whistler many times. Accordingly, we use a softer ‘sinusoidal’ distribution which tends to zero at the loss-cone. Landau damping is included and a new formulation for calculating the wave power of the MR whistler is introduced, which also allows us

to retain frequency components above the ‘nose’ frequency.

The work of *Lauben* was recently confirmed experimentally by *Johnson et al.* [1999], who measured the temporal signatures and spatial extent of lightning-induced electron precipitation bursts over a range of  $L$ -shells via the associated perturbations in subionospheric VLF signals. The observations of differential onset time delays on different VLF paths confirmed many aspects of the model predictions including the affected ionospheric patch size, poleward latitudinal motion, and displacement from the causative lightning stroke. The observed LEP bursts were thus shown to be induced by nonducted whistlers in the course of their first ‘hop’ of propagation and equatorial crossing, before any magnetospheric reflection occurs. This observation also led to the realization that some of the past observations of subionospheric VLF signatures of LEP events [e.g., *Inan et al.*, 1990; *Yip et al.*, 1991], previously interpreted as being caused by ducted waves, are probably also produced by nonducted whistlers [*Lauben et al.*, 1999; *Johnson et al.*, 1999]. The ionospheric perturbation event described by *Clilverd et al.* [2002] and observed near the Antarctic Peninsula, apparently in correlation with lightning in the northern hemisphere but not associated with a ground observed whistler, may be yet another example of the observation of an oblique whistler precipitation event.

As mentioned above, our ray tracing model includes the calculation of the Landau damping experienced by each ray along its trajectory. A related study was performed by *Thorne and Horne* [1994], who have used suprathermal electron fluxes observed on OGO 3 [*Schild and Frank*, 1970] in calculating Landau damping of MR whistler rays, showing very rapid attenuation of the signal. In this work, we have used recent measurements made aboard the POLAR satellite [*Bell et al.*, 2002] (that are more representative of inner magnetospheric suprathermal flux levels) to demonstrate that MR whistlers can persist for several seconds (sometimes even tens of seconds) before being significantly damped, and are thus a potentially more important contributor to radiation belt loss processes.

Our work on modeling satellite-observed MR whistler signatures bears a marked resemblance to such studies as *Edgar* [1972; 1976] and *Shklyar and Jiricek* [2000]. In particular, the former author has used  $f-t$  signatures of MR whistlers to infer

plasmaspheric electron number densities and structures using ray tracing. Our work can be viewed as an extension of this past study, but performed for a much broader frequency range, and employing a new ray tracing and interpolation methodology which includes the effects of Landau damping and can thus provide information about the effect of density structures upon  $f-t$  characteristics as well as wave power.

Measurements of the larger scale poleward displacement of the disturbed ionospheric region, occurring over slower timescales (many seconds) have recently been realized by *Inan et al.* [2002; 2004] using the subionospheric VLF method. These measurements exhibit onset delays (with respect to the causative lightning discharge) and durations (representing the continuing precipitation) that are consistent with our predictions for MR whistler driven precipitation, and constitute the first observations in the bounce loss-cone of precipitation induced by MR whistlers.

Other work which deserves mention is the observation by *Blake et al.* [2001] of enhanced energetic electron fluxes in the drift loss cone coincident with lightning discharges, and believed to represent the accumulated sum of precipitation due to many MR whistlers [*Bortnik et al.*, 2002a]. Much of the analysis of Chapter 3 is based upon these drift loss-cone observations.

As a final note on related past work, MR whistler waves injected *in-situ* from a satellite have recently been predicted [*Inan et al.*, 2003] to reduce energetic electron lifetimes using only a moderate amount of injected wave-power, employing the same wave-particle interaction mechanism described in this dissertation.

## 1.4 Thesis organization

The present work is organized into 6 chapters:

Chapter 1 (the current chapter) introduces the concept of the MR whistler, places this wave type into the context of magnetospheric and radiation belt research, and reviews previous related research.

In Chapter 2 we lay the theoretical foundations for the models used in the remaining chapters. These include the ray tracing methodology, modeling oblique wave-particle interactions, and the inclusion of Landau damping.

In Chapter 3 a crude model to estimate the  $L$ -dependence of precipitation driven by MR whistlers is presented, where we also investigate the effect that lightning source location and horizontal ionospheric density gradients have on the  $L$ -dependent precipitation signatures.

In Chapter 4 we present an extensive ray tracing and interpolation methodology that we have developed to enable us to simulate the observation of an MR whistler at any point in the magnetosphere, due to a lightning discharge at any location on the surface of the Earth.

Using the technique of Chapter 4, we present in Chapter 5 a novel method of calculating the detailed differential energy flux of precipitating electrons as a function of time, at the northern and southern ‘feet’ of any given  $L$ -shell. Using this method we simulate the precipitating flux in the inner magnetosphere by evaluating the region  $L = 1.3 - 5.5$  in  $0.1L$  increments, due to lightning discharges at  $\lambda_s = 25^\circ$  and  $35^\circ$ .

Chapter 6 summarizes the results presented in Chapters 2 to 5, compares these results with those of related research, and concludes with a discussion of future extensions to this work including suggestions for experimental validation.

## 1.5 Scientific contributions

Several contributions were made in the course of this work which are summarized below:

1. Interpretation of SAMPEX satellite observations of  $L$ -dependent signatures of energetic electrons precipitated into the drift loss cone as being caused by lightning-generated, magnetospherically reflecting whistler waves [*Bortnik et al.*, 2002a]
2. Identification of a lightning-injected magnetospherically reflected whistler-wave energy maximum in the magnetospheric region depleted of energetic electrons (i.e., the slot-region) [*Bortnik et al.*, 2003a].
3. Development of a new method to determine the temporal and spectral signatures of whistler waves at any point in the magnetosphere, thus accounting for



group dispersion effects as well as wave damping [*Bortnik et al.*, 2003*b*].

4. Development and application of a novel method to determine the temporal and spatial signatures of energetic electrons precipitated into the atmosphere as a result of cyclotron resonant scattering driven by magnetospherically reflecting whistlers [*Bortnik et al.*, 2002*b*].

# Chapter 2

## Theoretical background

Throughout the work presented in this dissertation, we use a common set of analytical techniques and models, which we review in this chapter. We begin with an overview of the process of radiation-belt electron precipitation due to MR whistlers, and then discuss in greater detail the VLF illumination of the ionosphere by a single cloud-to-ground lightning stroke, the ray tracing of whistler mode waves in the magnetosphere, and finally the interaction of such waves with energetic electrons.

### 2.1 Lightning induced electron precipitation

The sequence of events leading to energetic electron precipitation from the radiation belts due to a lightning generated whistler can be roughly divided into four broad steps, illustrated in Figure 2.1:

1. At  $t=0$ , a lightning discharge radiates electromagnetic energy which propagates away from the source within the Earth-ionosphere waveguide. Since the ionosphere in the presence of a magnetic field allows the propagation of waves well below the plasma frequency, a portion of the VLF wave energy is transmitted through the ionosphere and into the magnetosphere, illuminating a certain magnetospheric region around the location of the lightning discharge.
2. The upward going wave energy propagates in the ionospheric plasma in the whistler mode, traveling along ray trajectories (shown in red) away from the Earth,

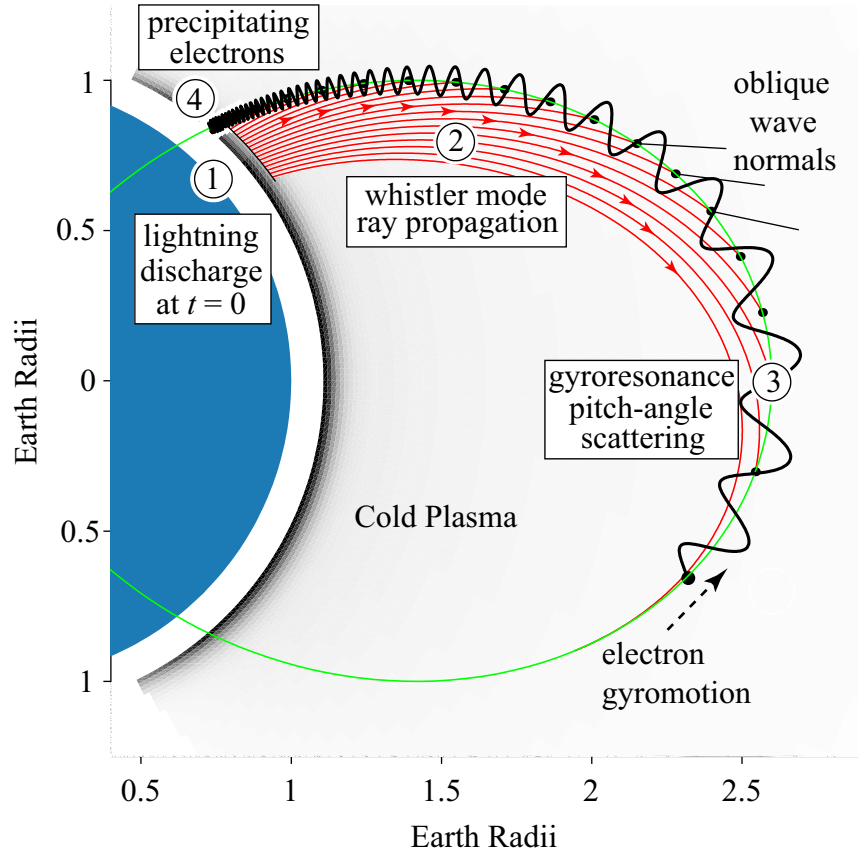


Figure 2.1: Illustration of the wave-particle interaction process: 1. Lightning discharge occurs at  $t=0$ ; 2. Propagation of whistler in the magnetosphere; 3. Energetic electrons enter the wave field, experience resonant scattering, and 4. Electrons precipitate into the dense upper atmosphere (adopted from *Lauben* [1999] courtesy of D.S. Lauben).

being guided by the gradients in the Earth's magnetic field strength, direction, and electron number density. In this context, the magnetospheric plasma acts as an inhomogeneous and anisotropic refractor.

3. Trapped energetic electrons near the edge of the loss cone interact with the whistler wave field and can resonate with the wave (under certain conditions), resulting in a change of particle momentum and pitch-angle, as well as growth or attenuation of the wave.

4. If the pitch-angle of the resonant energetic electron is sufficiently decreased, its

lowered mirror height lies in the dense upper atmosphere, resulting in the removal of the particle from the radiation belts, or its precipitation onto the lower ionosphere.

Since the lightning discharge injects whistlers over a range of latitudes around the source, and due to the multiple magnetospheric reflections (MR's) experienced by each ray, the range of  $L$ -shells illuminated by a single lightning stroke is typically large, spanning the entire plasmasphere ( $L \lesssim 5$ ). The ionospheric regions affected by precipitating electrons occur both northward and southward of the lightning stroke location, and typically the precipitating electrons move poleward on short ( $\sim 0.1$  sec) [Johnson *et al.*, 1999; Lauben, 1999; Lauben *et al.*, 2001] and long ( $\sim 10$  sec) timescales (see Chapter 5). We now discuss each of the four steps outlined above in greater detail, with particular emphasis on the specific tools and techniques employed in this dissertation.

## 2.2 Lightning illumination model

We follow the methodology developed by Lauben *et al.* [2001] and later used by Bortnik *et al.* [2002a,b] in calculating the power spectral density of lightning-generated whistler-mode waves exiting the top of the ionosphere at 1000 km altitude.

Using the expression given by Uman [1984, p.127] for the electric field  $E$  at a distance  $R$  from the base of a vertical cloud-to-ground lightning discharge, and a return current modeled as a double exponential [Jones, 1970; Cummer and Inan, 1997; Lauben *et al.*, 2001], the far-field, radiated power spectral density is given by:

$$S(\omega) = \frac{1}{Z_0} \left( \frac{\mu_0 h_e I_0}{2\pi} \right)^2 \left( \frac{\sin \kappa}{R} \right)^2 \frac{\omega^2 (a - b)^2}{(\omega^2 + a^2)(\omega^2 + b^2)} \quad (2.1)$$

where  $S(\omega)$  is in  $\text{W}\cdot\text{m}^{-2}\text{Hz}^{-1}$ ,  $\omega$  is the radial frequency of the electromagnetic wave in rad/sec,  $Z_0$  and  $\mu_0$  are the intrinsic impedance ( $\sim 377 \Omega$ ) and permeability of free space ( $\sim 8.854 \times 10^{-12} \text{ F/m}$ ) respectively,  $\kappa$  and  $R$  are respectively the angle of the observer with respect to the local zenith and the distance of the observer from the lightning source,  $h_e$  is the height of the cloud above ground (set to 5 km),  $I_0$  is the magnitude of the downward moving current (set to  $-10.53 \text{ kA}$ ), and  $a, b$  are model

parameters set to  $5 \times 10^3$  and  $10^5$  respectively. This choice of parameters was used in order to facilitate comparison with previous work [Lauben *et al.*, 2001] which uses the same values, and because it results in typical values such as an electric field amplitude of 10 V/m at 100 km, and  $\sim 8.5$  kA peak return current. Although (2.1) is derived for free space, it is adopted here on the basis that the attenuation of VLF wave energy in the Earth-ionosphere waveguide has been shown to have a  $R^{-2}$  dependence similar to that in free space [Crory, 1961; Inan *et al.*, 1984] for distances within  $\sim 1000$  km of the source.

Using (2.1), the wave power density along the bottomside ionosphere (assumed to be at 100 km altitude) is computed for the region surrounding the source. It should be mentioned that (2.1) predicts a radiation-pattern null directly above the lightning source, which in practice is likely washed out due to inhomogeneities in the ionosphere as evidenced by the lack of such a null in satellite observations of wave power distributions above fixed sources, such as VLF transmitters which utilize electrically short vertical monopole antennas [Inan *et al.*, 1984]. Noting that the artificial imposition of such a null would unnecessarily distort the magnetospheric wave power distribution in our numerical modeling, we take the source to be slightly displaced in longitude ( $0.9^\circ$ ) from the meridian of interest thereby avoiding the radiation pattern null.

The computed wave power density at 100 km altitude is translated to  $\sim 1000$  km altitude by properly attenuating it with a factor taken from *Helliwell* [1965, Fig. 3-35] representing the absorption of wave power in the collisional lower ionosphere. This procedure enables us to determine an array  $S(f, \lambda, \lambda_s)$ , the entries of which are dependent on the wave frequency  $f$  and latitude  $\lambda$  and represent power density at 1000 km due to a lightning discharge at a source latitude  $\lambda_s$ .

## 2.3 Ray tracing methodology

Our aim now is to use the wave power density calculated in Section 2.2 and to compute its propagation in, and distribution within the plasmasphere. Unlike the case of propagation in a medium which is homogeneous/isotropic for which the wave normal

lies in the direction of propagation of wave energy, the magnetosphere is an inhomogeneous/anisotropic magnetoplasma, and the wave energy, in general, propagates in a direction different than the wave normal angle, referred to as the ray direction. To determine the entire trajectory of the wave energy (i.e., the ray path), we use the technique of numerical ray tracing, and discuss below its formulation together with the determination of important associated quantities such as the refractive index, and quantitative description of the magnetospheric medium within which the ray propagates.

### 2.3.1 Ray tracing formulation

To accurately compute the ray trajectory, we require a set of first order differential equations, which is ‘closed’, i.e., comprising  $n$  equations of the form:

$$\frac{dy_i}{dx} = f_i(y_1, y_2, y_3, \dots, y_n) \quad (2.2)$$

where  $x$  is the independent variable and each derivative is expressed as a function of all the  $y_i$ ’s. Such a set of equations can be integrated numerically using standard methods, and was first derived by *Haselgrove* [1954]. These equations, taken from *Kimura* [1966] are repeated for convenience below:

$$\frac{dr}{dt} = \frac{1}{\mu^2} \left( \rho_r - \mu \frac{\partial \mu}{\partial \rho_r} \right), \quad (2.3a)$$

$$\frac{d\varphi}{dt} = \frac{1}{r\mu^2} \left( \rho_\varphi - \mu \frac{\partial \mu}{\partial \rho_\varphi} \right), \quad (2.3b)$$

$$\frac{d\phi}{dt} = \frac{1}{r\mu^2 \sin \varphi} \left( \rho_\phi - \mu \frac{\partial \mu}{\partial \rho_\phi} \right), \quad (2.3c)$$

$$\frac{d\rho_r}{dt} = \frac{1}{\mu} \frac{\partial \mu}{\partial r} + \rho_\varphi \frac{d\varphi}{dt} + \rho_\phi \frac{d\phi}{dt} \sin \varphi, \quad (2.3d)$$

$$\frac{d\rho_\varphi}{dt} = \frac{1}{r} \left( \frac{1}{\mu} \frac{\partial \mu}{\partial \varphi} - \rho_\varphi \frac{dr}{dt} + r\rho_\phi \frac{d\phi}{dt} \cos \varphi \right), \quad (2.3e)$$

$$\frac{d\rho_\phi}{dt} = \frac{1}{r \sin \varphi} \left( \frac{1}{\mu} \frac{\partial \mu}{\partial \phi} - \rho_\phi \frac{dr}{dt} \sin \varphi - r\rho_\varphi \frac{d\varphi}{dt} \cos \varphi \right), \quad (2.3f)$$

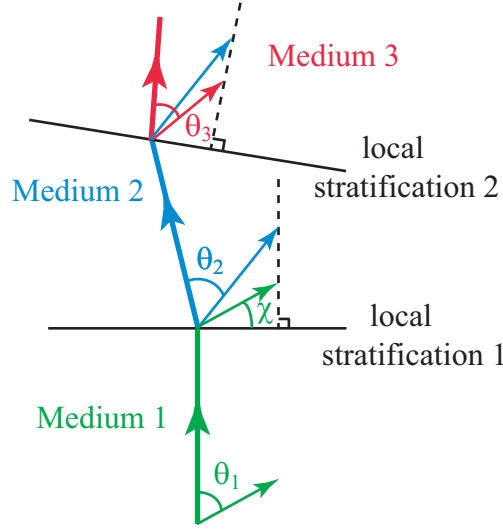


Figure 2.2: Snell's law interpretation of the ray tracing equations, showing a portion of an inhomogeneous medium divided into three slabs with Snell's law satisfied at each boundary.

where  $r$ ,  $\varphi$ , and  $\phi$  are the geocentric distance, colatitude (i.e., zenith angle or  $90^\circ$ –latitude) and longitude;  $\mu$  is the real part of the complex phase refractive index,  $\rho_r, \rho_\varphi, \rho_\phi$  are the components of the refractive index vector (a vector of length  $\mu$  oriented parallel to the wave normal vector),  $t$  is the variable of integration and  $f$  is the wave frequency. The choice of symbol 't' for the independent variable is somewhat misleading in that it is measured in units of distance, not time, and represents the time of phase travel along the ray path scaled by the velocity of light, i.e.,  $t = (\text{phase time}) \times (\text{speed of light})$ . Since we are interested in the rate of energy travel along the ray, we add the following equation to (2.3) to compute the group delay time,  $T$ :

$$\frac{dT}{dt} = \frac{1}{c} \left( 1 + \frac{f}{\mu} \frac{\partial \mu}{\partial f} \right) \quad (2.4)$$

The ray tracing equations, i.e., the set (2.3) and (2.4), determine the variation of the ray position and wave normal vector as a function of time, given a proper set of initial values for these quantities and a model description of the magnetospheric magnetoplasma. Although somewhat complex in their derivation, the ray tracing equations take on a relatively simple, geometrical interpretation when examined in

the two-dimensional case (i.e., neglecting all longitudinal variations). Consider a ray, as shown in Figure 2.2 propagating in Medium 1, with a certain wave normal angle,  $\theta_1$  (measured relative to the ray direction in this example). If the inhomogeneous medium varies slowly on spatial scales of a wavelength, then the medium can be divided into a series of uniform slabs (Media 1, 2, and 3), separated by local stratifications, i.e., loci of points on which the phase refractive index remains constant. The process of ray tracing then involves alternate propagation of wave energy along straight lines in the uniform slabs, followed by sharp changes in direction at local stratifications, where the condition that we need to satisfy is Snell's law, i.e.,  $\mu_i \cos \chi_i = \mu_{i+1} \cos \chi_{i+1}$ , or  $d(\mu \cos \chi)/ds = 0$  as written in differential form. The direction of propagation of the ray beyond the stratification (i.e., in the  $(i + 1)^{\text{th}}$  Medium) is determined by the new wave normal angle, being normal to the refractive index surface at that point as discussed in Section 2.3.2.

It is evident from the ray tracing equations that the properties of the propagation medium enter only through the refractive index  $\mu$  and its components  $\rho_r$ ,  $\rho_\varphi$ , and  $\rho_\phi$ . Thus, the determination of the refractive index is central to our ray tracing formulation, and is discussed next.

### 2.3.2 Refractive index

We follow the notation and approach as laid out in several textbooks [e.g., *Stix*, 1992, p.7; *Bittencourt*, 1995, p.414] to derive the expressions for the refractive index in a cold, collisionless, unbounded, magnetoplasma. Using the Langevin equation of motion [*Ibid*] together with Maxwell's equations, we linearize and search for harmonic plane wave solutions of the form  $e^{j(\mathbf{k} \cdot \mathbf{r} - \omega t)}$  to find:

$$m_s \frac{D\mathbf{u}}{Dt} = q_s (\mathbf{E} + \mathbf{u} \times \mathbf{B}) \rightarrow -j\omega m_s \mathbf{u} = q_s (\mathbf{E} + \mathbf{u} \times \mathbf{B}_0) \quad (2.5)$$

$$\nabla \times \mathbf{E} = -\frac{\partial \mathbf{B}}{\partial t} \rightarrow \mathbf{k} \times \mathbf{E} = \omega \mathbf{B}_1 \quad (2.6)$$

$$\nabla \times \mathbf{B} = \mu_0 \left( \mathbf{J} + \varepsilon_0 \frac{\partial \mathbf{E}}{\partial t} \right) \rightarrow j\mathbf{k} \times \mathbf{B}_1 = \mu_0 (q_s n_0 \mathbf{u} - j\omega \varepsilon_0 \mathbf{E}) \quad (2.7)$$



where  $D/Dt$  signifies the total or ‘convective’ derivative,  $m_s$  and  $q_s$  are the particle mass and charge for a particle of species ‘s’, and  $\varepsilon_0$  and  $\mu_0$  are the permittivity and permeability of free space respectively. The magnetic field vector and particle number density are divided into two parts,

$$\begin{aligned}\mathbf{B}(\mathbf{r}, t) &= \mathbf{B}_0 + \mathbf{B}_1(\mathbf{r}, t) \\ n(\mathbf{r}, t) &= n_0 + n_1(\mathbf{r}, t)\end{aligned}$$

where  $\mathbf{B}_0$  is the constant and uniform ambient magnetic field, and  $n_0$  is the undisturbed particle number density in the absence of the wave. The quantities  $\mathbf{E}$ ,  $\mathbf{B}_1$ ,  $\mathbf{u}$ , and  $n_1$  are all first order perturbation quantities, and respectively denote the wave electric and magnetic fields, the plasma fluid velocity, and the particle number density perturbation. The set of three vector equations (2.5) – (2.7) contains three vector unknowns, and thus forms a closed set. In the simplest case of a cold plasma with an assumed stationary ion background, the ‘particle’ mass and charge would be those of an electron, but in the general case (2.5) would be repeated for every particle species under consideration, and the current term  $\mathbf{J}$  in (2.7) would be a summation over all particle species. If more species are included the number of equations increases together with the number of unknowns (i.e., additional fluid velocities for every particle species), but the set of vector equations remains closed. To solve the set without loss of generality, we rotate our coordinate system such that the  $\hat{\mathbf{z}}$  direction is locally aligned with  $\mathbf{B}_0$ ,  $\mathbf{k}$  is entirely contained in the  $x-z$  plane making an angle  $\theta$  with the magnetic field, and introduce the *Stix* [1992, p.7] notation:  $S = (R + L)/2$ ,  $D = (R - L)/2$  where:

$$P \equiv 1 - \sum_s \frac{\omega_{ps}^2}{\omega^2}; \quad R \equiv 1 - \sum_s \frac{\omega_{ps}^2}{\omega(\omega + \omega_{\text{Hs}})}; \quad L \equiv 1 - \sum_s \frac{\omega_{ps}^2}{\omega(\omega - \omega_{\text{Hs}})}, \quad (2.8)$$

and  $\omega_{ps} = N_s q_s^2 / \varepsilon_0 m_s$ ,  $\omega_{\text{Hs}} = q_s B_0 / m_s$  are the plasma and cyclotron (or gyro-) frequencies respectively, and  $\omega_{\text{Hs}}$  changes sign with  $q_s$  and also with  $B_0$ . Noting that the refractive index  $\mu = kc/\omega$ , we solve the set (2.5)–(2.7) to yield:

$$\begin{pmatrix} (S - \mu^2 \sin^2 \theta) & -jD & \mu^2 \sin \theta \cos \theta \\ jD & (S - \mu^2) & 0 \\ \mu^2 \sin \theta \cos \theta & 0 & (P - \mu^2 \sin^2 \theta) \end{pmatrix} \begin{pmatrix} E_x \\ E_y \\ E_z \end{pmatrix} = 0 \quad (2.9)$$

Equation (2.9) enables us to examine wave polarization and phase relationships. Setting the determinant of (2.9) to zero and rearranging produces the dispersion relation  $A\mu^4 - B\mu^2 + C = 0$ , where:

$$\begin{aligned} A &= S \sin^2 \theta + P \cos^2 \theta, \\ B &= RL \sin^2 \theta + SP (1 + \cos^2 \theta), \\ C &= PRL \end{aligned} \quad (2.10)$$

Solving explicitly for  $\mu^2$  gives:

$$\mu^2 = \begin{cases} \frac{B - \sqrt{B^2 - 4AC}}{2A} & B > 0 \\ \frac{2C}{B + \sqrt{B^2 - 4AC}} & B < 0 \end{cases} \quad (2.11)$$

The two forms of writing  $\mu^2$  in (2.11) are equivalent but written in this fashion to emphasize computational accuracy [Kimura, 1966]. Where only electrons are included with an assumed stationary neutralizing ion background, the expression (2.11) can be written more explicitly as the well-known Appleton-Hartree equation [Appleton, 1927; 1932]:

$$\mu^2 = \frac{k^2 c^2}{\omega^2} = 1 - \frac{\frac{\omega_{pe}^2}{\omega^2}}{1 - \frac{\omega_{He}^2 \sin^2 \theta}{2(\omega^2 - \omega_{pe}^2)} \pm \left[ \left( \frac{\omega_{He}^2 \sin^2 \theta}{2(\omega^2 - \omega_{pe}^2)} \right)^2 + \frac{\omega_{He}^2}{\omega^2} \cos^2 \theta \right]^{1/2}} \quad (2.12)$$

There are several important points to note about (2.11) or (2.12). The first is that the propagation medium enters the calculation of refractive index, and hence affects the ray path [as given by (2.3)] only through the local values of magnetic field intensity, and particle number density (electrons, and several species of ions). These

parameters are reflected respectively in the gyrofrequency  $\omega_{\text{Hs}}$ , and the plasma frequency  $\omega_{ps}$  (both for the  $s^{\text{th}}$  particle species), and are then normalized by the wave radial frequency  $\omega$ , in such a way that the *Stix* parameters become dimensionless. Consequently, it is the ratios  $\omega_{\text{Hs}}/\omega$  and  $\omega_{ps}/\omega$  that ultimately determine the magnitude and behavior of the refractive index, implying that the problem is completely scalable so long as the appropriate ratios are preserved. In our case, we deal exclusively with whistler-mode signals, occurring in the region of the dispersion relation where  $\omega_{pe} > \omega_{\text{He}} > \omega > \omega_{pi}$ , where  $\omega_{pe}, \omega_{pi}$  are respectively the electron and proton plasma frequencies.

The second point to note is that the denominator of the second term on the RHS of (2.12) can take on the value of zero under specific conditions, causing  $\mu$  to become infinite. This specific case corresponds to a resonance condition where the phase velocity of the wave tends to zero, and is discussed further below.

The final point to note about (2.12) is that at a given location in the magnetosphere,  $\omega_{\text{Hs}}$ ,  $\omega_{ps}$ , and  $\omega$  are fixed, the only remaining variable being the wave normal angle  $\theta$ . Figure 2.3 shows a polar plot of the refractive index drawn as a function of wave normal angle, commonly referred to as the refractive index surface, since the contour shown is, in fact, a surface of revolution about  $\mathbf{B}_0$ .

This representation of the refractive index proves particularly useful in analyzing whistler mode ray propagation and magnetospheric reflections, due to the property that the direction of wave energy travel (ray direction) for any wave normal angle  $\theta$  is given as the direction normal to the surface at the tip of the  $\mu(\theta)$  vector [*Helliwell*, 1965, p.34; *Poeverlein*, 1948] as indicated by the red arrow in the above figure. Thus, the ray direction is dependent on the behavior of the wave normal angle, as is the entire ray path and hence the resulting distribution of the whistler wave energy in the magnetosphere. Shown in blue in Figure 2.3 is the resonance cone angle  $\theta_{\text{res}}$ , for which the refractive index becomes infinite, so that no whistler mode wave propagation is possible for  $\theta > \theta_{\text{res}}$ . This point is critically important in our work, since for magnetospheric reflection to occur, the refractive index surface must be finite at  $90^\circ$  (i.e., it must be a ‘closed’ surface), as discussed next. Finally, noted in green color in Figure 2.3 is the ‘Gendrin’ angle  $\theta_{\text{G}}$  [*Gendrin*, 1961] defined as the non-zero

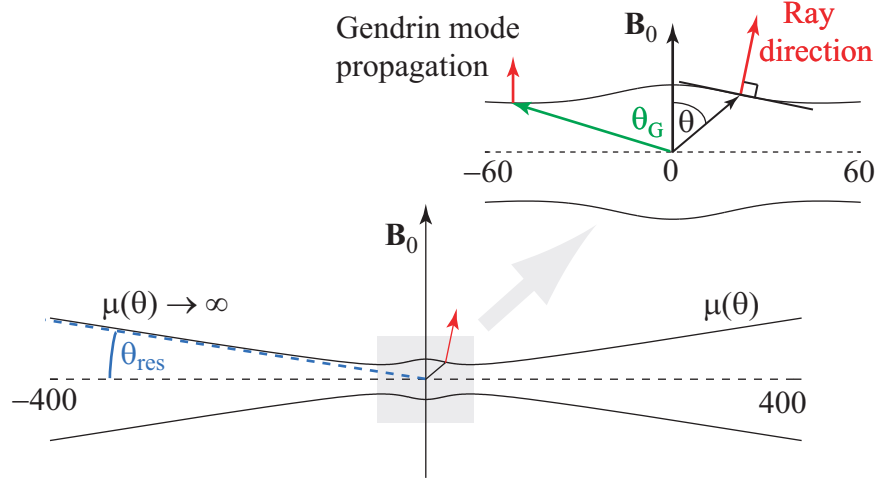


Figure 2.3: Refractive index surface indicating the resonance cone angle  $\theta_{\text{res}}$ . Expanded section shows the refractive index at an angle  $\theta$  with associated ray direction, as well as the Gendrin angle  $\theta_G$ .

wave normal angle at which the ray propagates along  $\mathbf{B}_0$ . This particular mode of propagation becomes important when a given propagating ray reaches a specific frequency-dependent  $L$ -shell at which the wave energy tends to settle (see Section 4.2.2).

It was mentioned above that the inclusion of ions into the vector set (2.5)–(2.7) is straightforward, and results in additional terms in the Stix parameters  $P$ ,  $R$ , and  $L$ , and that the refractive index surface needs to ‘close’, or become finite for all values of  $\theta$  in order for a magnetospheric reflection of the whistler ray to occur. In fact, as was first suggested by *Hines* [1957], and later demonstrated by *Kimura* [1966], inclusion of the ion terms is essential to the closing of the refractive index surface.

Figure 2.4 shows three refractive index surfaces calculated with plasma and cyclotron frequencies consistent with  $L \simeq 2.4$  on the magnetic equatorial plane, for (a) a 4 kHz wave, (b) a 1 kHz wave, and (c) a 100 Hz wave. The red curves show the refractive index surface calculated with the inclusion of ions and electrons, whereas the blue curves are computed by only accounting for the motion of electrons in a background of motionless neutralizing ions.

The progression of the refractive index surface from curve (a) to (c) shows the

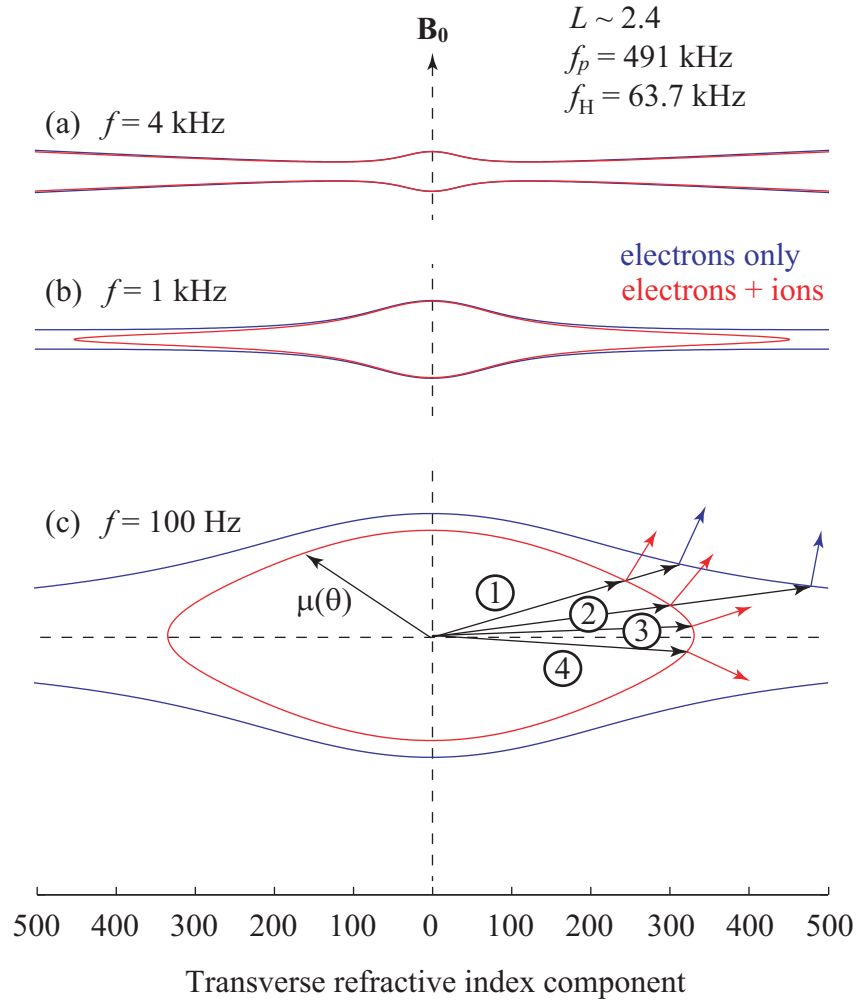


Figure 2.4: Refractive index surface calculated using parameter values at the geomagnetic equator at  $L \simeq 2.4$  for (a) 2 kHz, (b) 500 Hz, and (c) 50 Hz, showing the difference between including electrons only (blue) and electrons and ions (red). All curves are drawn to the scale shown below (abscissa and ordinate scales are identical, with only abscissa shown).

dramatic difference resulting from the inclusion of the ions. At 4 kHz, the two curves are almost identical, and both exhibit a resonance cone, but lowering the frequency to 1 kHz shows that the red curve has closed at  $90^\circ$ , whereas the blue curve has not. Lowering the frequency further to 100 Hz shows that the transverse component of the red refractive index curve has decreased significantly, whilst the blue one still exhibits a resonance cone. In fact, the blue surface is not closed at any frequency and thus does not support magnetospheric reflection (as described below in Section 2.3.4).

Curve (c) is labeled with a sequence of numbers 1–4, demonstrating the rotation of the wave normal past  $90^\circ$  during a magnetospheric reflection. Beginning with (1) on the red curve, the wave normal is oblique and the ray propagates toward the top-right. In (2) and (3), the wave normal and ray direction tend to  $90^\circ$ , and in (4) the wave normal has rotated past  $90^\circ$  and the ray has effectively changed direction from parallel to antiparallel propagation relative to  $\mathbf{B}_0$ . This sequence is contrasted with a similar wave normal rotation on the blue curve, where it is evident that the ray direction becomes progressively more parallel to the static magnetic field as the wave normal tends to the resonance cone, and is unable to rotate further. Thus, a magnetospheric reflection does not occur and the ray simply propagates roughly along the magnetic field line with an increasing wave normal angle (and increasing resultant Landau damping; see Section 2.5) towards the opposite hemisphere where any remaining wave energy would be absorbed via collisions in the lower ionosphere.

### 2.3.3 Description of the medium

For the purposes of ray tracing, the medium through which the rays propagate is described in terms of the magnetic field intensity and direction, as well as the distribution and composition of the cold plasma. We review each of these in turn.

#### Ambient magnetic field

Following previous authors [*Kimura*, 1966; *Inan et al.*, 1978; *Chang and Inan*, 1985b; *Jasna et al.*, 1992; *Lauben*, 1999; *Lauben et al.*, 1999; *Lauben et al.*, 2001; *Lauben et al.*, 2002], we assume a centered dipole model for the Earth’s magnetic field. This model

is represented by the lowest order term in Gauss's multipole expansion, and after taking the gradient of the magnetic potential field [Walt, 1994, p.27] the components of  $\mathbf{B}$  can be written as:

$$B_r = -2B_0 \left( \frac{R_E}{r} \right)^3 \sin \lambda, \quad B_\lambda = B_0 \left( \frac{R_E}{r} \right)^3 \cos \lambda \quad (2.13)$$

Having intensity

$$B = \sqrt{B_r^2 + B_\lambda^2} = B_0 \left( \frac{R_E}{r} \right)^3 \sqrt{1 + 3 \sin^2 \lambda} \quad (2.14)$$

where  $r$  and  $\lambda$  are the geocentric radial distance and latitude respectively,  $R_E$  is the Earth's radius ( $\sim 6370$  km), and  $B_0$  is the mean value of the field on the equator at the Earth's surface  $\sim 3.12 \times 10^{-5}$  T. The geomagnetic field described in this way is a good approximation to the real field, since our region of interest ( $L \simeq 2-5$ ) is far enough away from the Earth's surface for the rapidly decaying higher order terms to become insignificant, and yet sufficiently close to remain unaltered by solar wind deformation, and other external current systems (e.g., the ring current, magnetopause current) [Walt, 1994, p.29-33]. This model has the added advantage of simplifying the analysis of the motion of charged particles, as discussed in the following section.

### Cold plasma

The radial variation of electron density along the geomagnetic equator is modeled after *Carpenter and Anderson* [1992] who have used in-situ measurements from the ISEE 1 satellite together with whistler data, to produce an average model covering the range  $2.25 < L < 8$ . The model electron density is shown in Figure 2.5 and is succinctly summarized as follows (for the midnight sector which is our region of interest):

$$L_{\text{ppi}} = 5.6 - 0.46K_{\text{p(max)}} \quad (2.15a)$$

$$\log n_e = (-0.3145L + 3.9043) + \dots$$

$$\left[ 0.15 \left( \cos \frac{2\pi (d+9)}{365} - 0.5 \cos \frac{4\pi (d+9)}{365} \right) + 0.00127\bar{R} - 0.0635 \right] e^{-(L-2)/1.5}$$
(2.15b)

$$n_e = n_e(L_{\text{ppi}}) \times 10^{-(L-L_{\text{ppi}})/0.1}$$
(2.15c)

$$n_e = (5800 + 300t) L^{-4.5} + (1 - e^{-(L-2)/10})$$
(2.15d)

where  $n_e$  is the electron number density,  $L_{\text{ppi}}$  is the plasmapause inner limit,  $K_{\text{p(max)}}$  is the maximum  $K_{\text{p}}$  value in the preceding 24 hours,  $d$  is the day number,  $L$  is the  $L$ -shell parameter,  $t$  is the magnetic local time, and  $\bar{R}$  is the 13-month average sunspot number. For our purposes we set  $d=0$ ,  $t=2$ ,  $K_{\text{p(max)}}=10$ , and  $\bar{R}=90$ . The model consists of three sections described by equations (2.15b), (2.15c) and (2.15d) respectively. Equation (2.15b) describes the saturated plasmasphere segment in the region  $2.25 < L < L_{\text{ppi}}$  where  $L_{\text{ppi}}$  is determined as above. This segment is followed by the plasmapause section described by (2.15c), in the region  $L_{\text{ppi}} < L < L_{\text{ppo}}$  where  $L_{\text{ppo}}$  is the intersection of (2.15c) and (2.15d). The outer segment is known as the plasma trough, and is described by (2.15d) in the region  $L_{\text{ppo}} < L < 8$ . Equations (2.15b) – (2.15d) describe an average plasmaspheric density configuration and are subject to several conditions discussed by *Carpenter and Anderson* [1992].

To determine the variation of electron number density along the field lines, we use the diffusive equilibrium model of *Angerami and Thomas* [1964]. The diffusive equilibrium theory takes into account the effect of the electric field that arises from charge separation of the electrons and multiple ion species, the Earth's gravitational field, as well as the centrifugal force on the plasma due to the Earth's rotation. It is further assumed that the plasma is free to move only along the magnetic lines of force of the Earth. The resulting distribution is given by:

$$n(r) = n_{\text{eq}}(L) \sqrt{\sum_{i=1}^N \alpha_i e^{-G/S_i}}$$

$$G = r_{\text{b}} (1 - r_{\text{b}}/r)$$

$$S_i = 1.506T \left( \frac{r_{\text{b}}}{7370} \right)^2 \frac{1}{4^{i-1}}$$
(2.16)



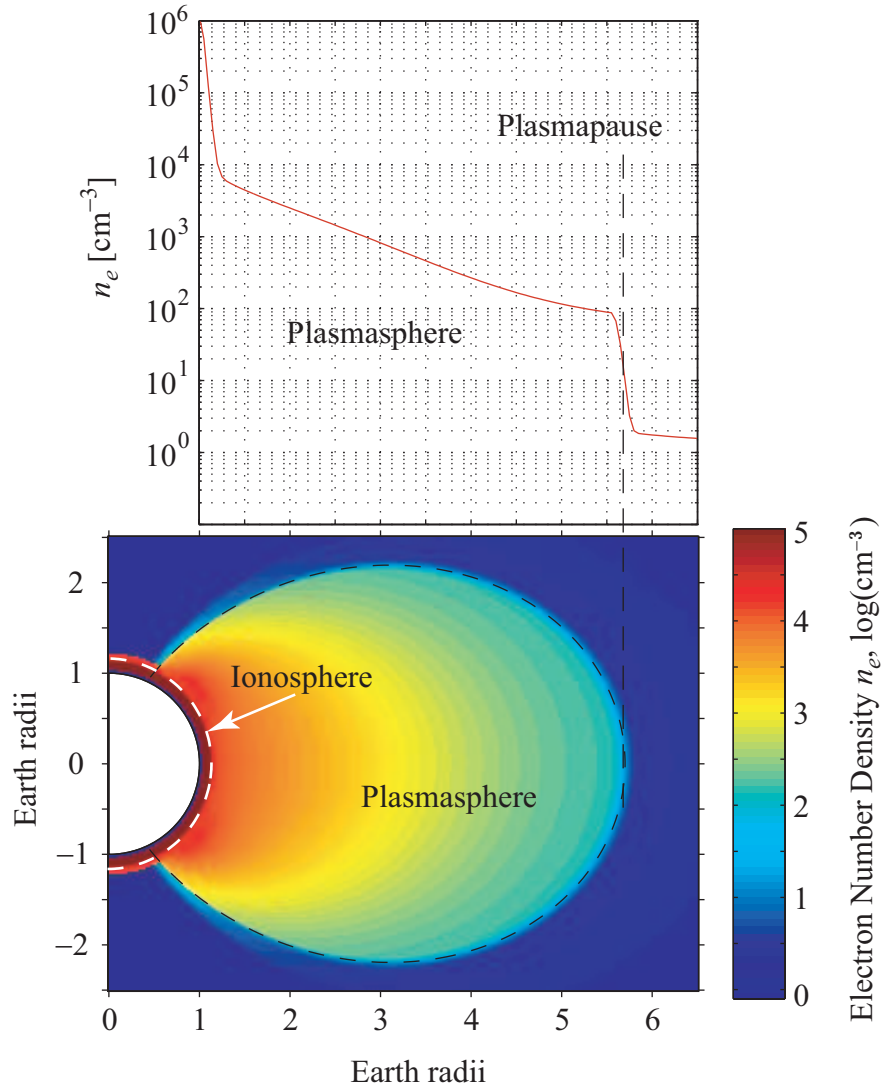


Figure 2.5: Assumed electron density distribution in the plasmasphere, shown on the equatorial plane (top), and on the meridional plane (bottom), indicating the locations of the plasmapause and ionosphere.

where  $r$  is the geocentric distance to the point where the density is evaluated,  $n_{\text{eq}}(L)$  is the equatorial number density at the particular  $L$ -shell in question, and  $r$  is related to  $L$  in a dipole field through the relation  $r = R_E L \cos^2 \lambda$  where  $\lambda$  is the magnetic latitude. The term  $r_b$  is the geocentric distance to the base of the diffusive equilibrium model (set to 7370 km),  $\alpha_i$  is the relative concentration of the  $i^{\text{th}}$  ionic species at  $r_b$ ,  $N$  is the number of ionic species, and  $T$  is the temperature at  $r_b$ .

### 2.3.4 The Stanford VLF ray tracing code

The computation of ray paths was performed using the Stanford VLF ray tracing code [Inan and Bell, 1977] which is the product of more than four decades of usage and improvements by various authors [Yabroff, 1961; Kimura, 1966; Smith and Angerami, 1968; Walter, 1969; Dantas, 1972]. The code performs two dimensional ray tracing by integrating the ray tracing equations (2.3)–(2.4), but neglecting (2.3d) and (2.3f), thereby implicitly assuming that all rays are launched in the meridional plane and that there are no azimuthal gradients (or variations in the spherical coordinate  $\phi$ ). The integration is carried out using the Adams predictor-corrector method, with a Runge-Kutta starting method [Hairer et al., 2000a,b], making estimates of the refractive index, and then refining the estimate by determining  $\mu$  from the magnetoionic theory. The code also includes a provision for automatically doubling or halving the step-size when differences between predictor and corrector values exceed a certain (user-specified) limit, or when the wave normal falls outside the resonance cone.

We show in Figure 2.6 an example output of the VLF ray tracing code for a 3 kHz wave injected at 1000 km altitude,  $30^\circ$  latitude, and with a locally vertical initial wave normal angle. The ray path shown in Figure 2.6a begins to move in a non-vertical direction (since the assumption of a vertical wave normal means that  $\theta \neq 0$  and the ray direction for  $\theta \neq 0$  is not along the wave normal direction) and travels in a curved path, roughly following the geomagnetic field line.

The wave normals, shown as black line segments, indicate that the wave becomes increasingly more oblique (i.e.,  $\theta$  moves further away from zero) throughout its path. The first magnetospheric reflection of the ray is expanded and shown in more detail

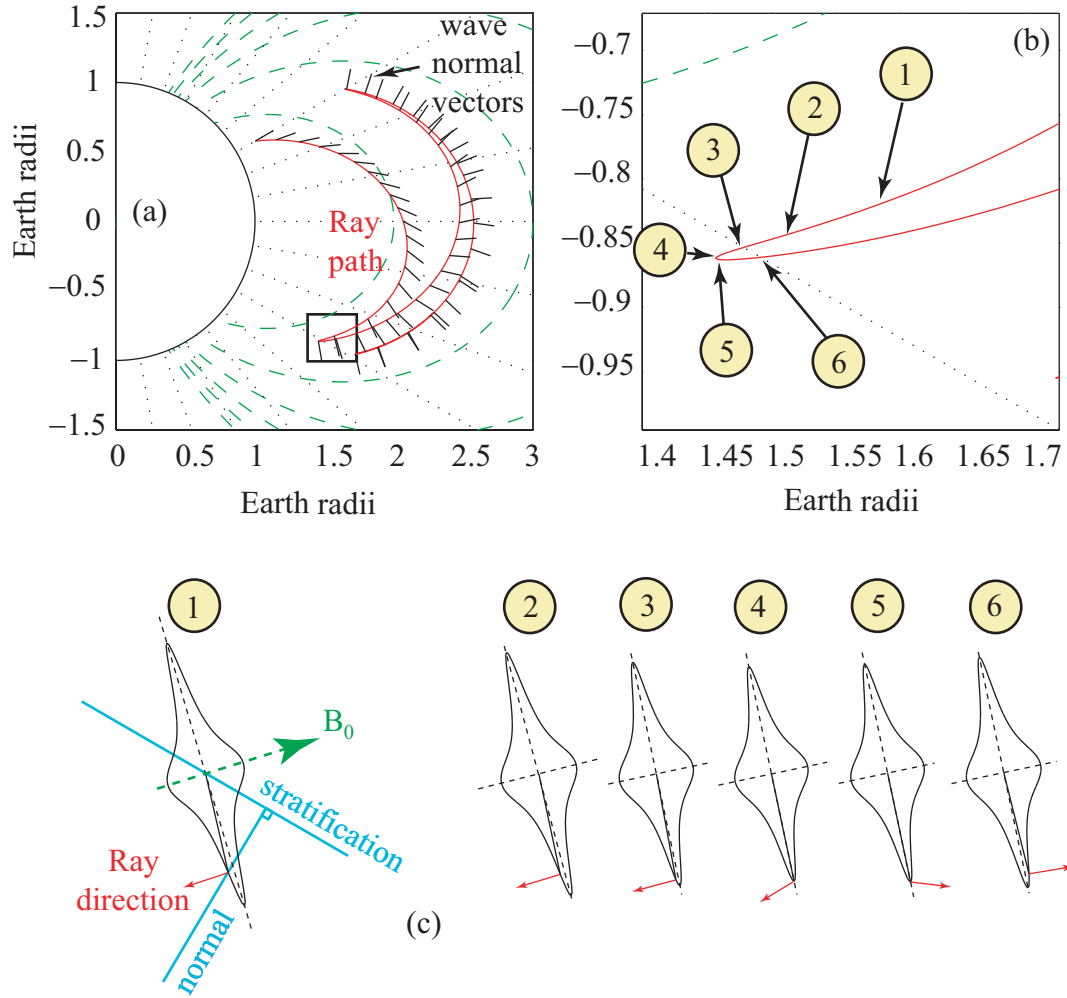


Figure 2.6: VLF ray tracing code example output, (a) 3 kHz ray path injected at 1000 km with selected wave normal vectors shown, (b) an expanded portion of a magnetospheric reflection from ray path shown in (a), and (c) a progression of refractive index surfaces corresponding to the magnetospheric reflection, with (1) showing the magnetic field direction and plane of stratification.

in panel (b), with the progression of indicated refractive index surfaces shown in (c). The ray directions, shown as red arrows, are at  $\sim 180^\circ$  with respect to  $B_0$  in surface 1, but almost completely reverse direction by the time the ray has reached surface 6, in a very small spatial region (compared to other spatial scales of ray propagation), hence the name Magnetospheric Reflection, reminiscent of reflection from a sharp boundary. The process of reflection occurs as follows: from surface 1, the ray propagates into a region where the refractive index becomes progressively smaller. Since the component of the wave vector parallel to the plane of stratification must remain constant (Snell's law), the wave vector is forced to bend towards  $90^\circ$ , where the ray direction shifts from  $\sim 180^\circ$  to lower values (surfaces 3 and 4), until the wave vector rotates past  $90^\circ$  and the ray direction is reversed. From there onwards, the ray moves to a region where once again the refractive index progressively increases and the direction of propagation becomes nearly aligned with the geomagnetic field (surface 6).

In our formulation, we use the VLF ray tracing code to simulate thousands of rays and interpolate between them, in order to more realistically model the whistler wave field in any location in the magnetosphere. The whistler wave field specified as described above is used to determine the perturbing wave forces exerted on the otherwise trapped population of energetic electrons, and the resultant scattering into the bounce loss-cone. A brief theoretical background relevant to the modeling of the wave-particle interaction is provided in the following section.

## 2.4 Oblique wave-particle interaction

The dynamics of a charged particle of species  $s$ , with rest mass  $m_s$  and charge  $q_s$  moving in an electromagnetic field are described by the Lorentz force equation shown in (2.17) below:

$$\frac{d\mathbf{p}}{dt} = q_s \left\{ \mathbf{E}^w + \frac{\mathbf{p}}{m_s \gamma} \times [\mathbf{B}^w + \mathbf{B}_0(\mathbf{r})] \right\} \quad (2.17)$$

where  $\mathbf{p} = m_s \gamma \mathbf{v}$  is the particle momentum vector,  $\gamma = (1 - v^2/c^2)^{-1/2}$  is the relativistic Lorentz factor and  $\mathbf{v} = d\mathbf{r}/dt$  is the particle velocity vector. We have explicitly

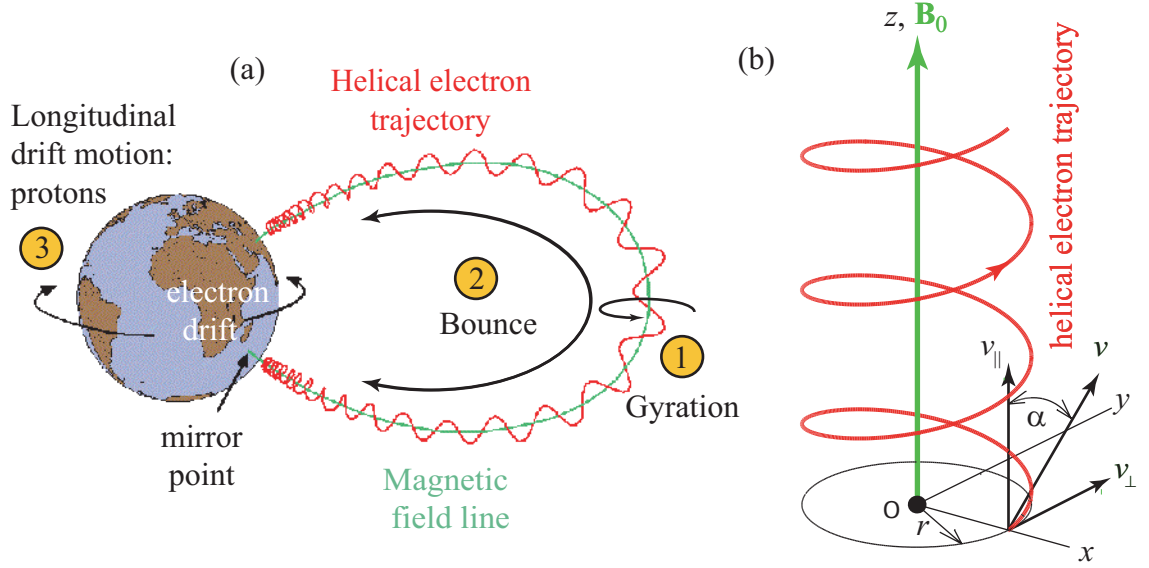


Figure 2.7: Illustration of the three types of periodic motion experienced by electrons in the geomagnetic field: gyration about the field lines, bounce between North and South hemisphere, and longitudinal drift about the Earth.

separated the total field into the wave components  $\mathbf{E}^w, \mathbf{B}^w$ , and static geomagnetic field  $\mathbf{B}_0$  in order to facilitate the discussion of the interaction equations. Before developing the wave-particle interaction equations, it is useful to review the motion of a charged particle in the Earth's static magnetic field in the absence of the wave fields.

### 2.4.1 Adiabatic motion

A charged particle moving in the Earth's magnetic field (in the absence of the wave field) experiences three different types of periodic motion [Walt, 1994, p.36] occurring on three different timescales: rapid gyration about the static magnetic field line ( $\sim 10^{-4}$  sec), bounce motion along the magnetic field line between northern and southern hemispheres ( $\sim 1$  sec), and a longitudinal drift about the Earth ( $\sim 10^3$  sec) as shown in Figure 2.7.

Associated with each of these periodic movements are adiabatic invariants, which play the role of 'constants of motion' and are obtained using the Hamilton-Jacobi

theory [Goldstein *et al.*, 2002, p.430] by integrating the canonical momentum around the orbit path as follows:

$$J_n = \oint [m_s \mathbf{v} + q_s \mathbf{A}] \cdot d\mathbf{l} \quad (2.18)$$

where  $d\mathbf{l}$  is an element of the particle path around the orbit, and  $m_s$ ,  $q_s$ , and  $\mathbf{v}$  are the mass, charge and velocity of a particle of species  $s$  respectively. We focus on the first adiabatic invariant (or rather the violation thereof) since it occurs on the time scales of the wave-particle interaction. Using (2.18) the quantity conserved along the electron's helical trajectory is:

$$J_1 = M = \frac{p_\perp^2}{2m_{s0}B} \propto \frac{\sin^2 \alpha}{B} \quad (2.19)$$

which is referred to as the first adiabatic invariant or magnetic moment (often designated with the symbol  $\mu$  which we avoid so as not to confuse it with the refractive index), where  $p_\perp$  is the perpendicular component of the electron momentum,  $m_{s0}$  is the particle rest mass,  $B_0$  is the magnetic field intensity, and  $\alpha$  is the electron pitch angle shown in Figure 2.7 and defined as  $\alpha = \tan^{-1}(v_\perp/v_z)$ . The velocity components parallel ( $v_z$ ) and perpendicular ( $v_\perp$ ) to the magnetic field can be specified using (2.19) and reference values that are typically specified on the geomagnetic equator (subscript 'eq'), as:

$$v_z(\lambda) = v \cos \alpha(\lambda); \quad v_\perp(\lambda) = v \sin \alpha(\lambda); \quad \sin^2 \alpha(\lambda) = \frac{B(\lambda)}{B_{\text{eq}}} \sin^2 \alpha_{\text{eq}} \quad (2.20)$$

It is clear that at some altitude, the pitch angle reaches  $90^\circ$ , and the particle effectively mirrors and begins to travel in the opposite direction along the field line. This altitude is uniquely related to the equatorial pitch angle, such that decreasing (increasing) the pitch angle corresponds to decreasing (increasing) the mirror height, as discussed below.

We can define a certain minimum altitude  $h_m$  below which electrons are unable to mirror due to the dense upper atmosphere, and above which they can mirror without

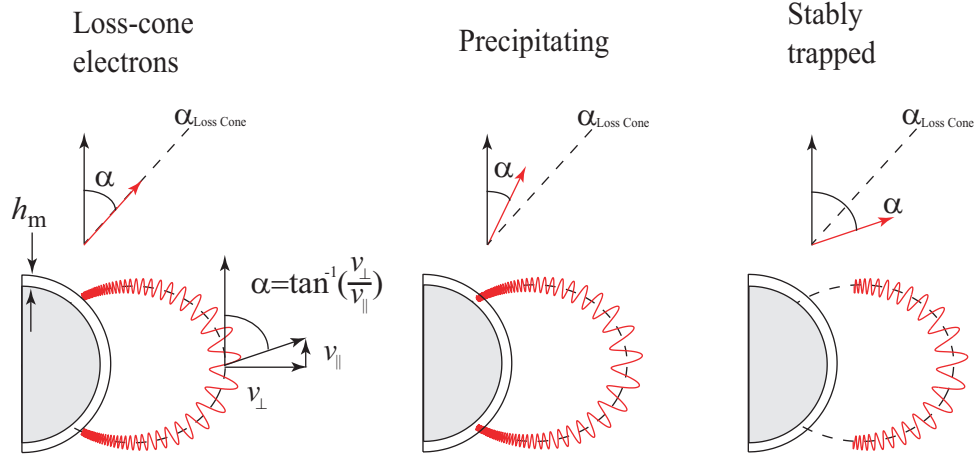


Figure 2.8: The relation of mirror height to equatorial pitch angle, and the concept of a loss-cone angle.

impediment. This can be done because the neutral atmosphere has a relatively small scale height ( $\sim 6$  km at  $\sim 100$  km [Salby, 1996, p.9]) compared with the spatial scales of trapped particle motions, which leads to large changes in atmospheric pressure and thus the density of neutral constituents in relatively small spatial regions. Moreover, the region near  $\sim 100$  km represents a transition in mass stratification and air composition known as the homopause: at altitudes  $< 100$  km bulk transport by turbulent air motions leads to effective mixing and homogenous mixing ratios, whereas at altitudes  $> 100$  km the mean free path becomes large enough ( $\sim 1$  m) to damp turbulent air motions and diffusive transport becomes the dominant mechanism for transporting properties vertically [Salby, 1996, p.11].

This minimum allowable mirroring altitude  $h_m$  is uniquely related to an equatorial pitch angle which we define as the loss cone angle,  $\alpha_{lc}$ . Figure 2.8 is used to illustrate the relationship between the mirror altitude and the equatorial pitch angle, noting that electrons having pitch angles lower than the loss-cone angle, precipitate into the ionosphere and hence are removed from the radiation belts, whereas electrons with pitch angles greater than the loss-cone remain stably trapped. The minimum altitude and loss-cone angle can be related (e.g., using the notation of Lauben *et al.* [2001], which is a slight modification of Schulz and Lanzerotti [1974, p.59]) as follows:

$$\sin \alpha_{lc} = \sqrt{\frac{\zeta_m^3}{\sqrt{1 + 3(1 - \zeta_m)}}}; \quad \zeta_m = (R_E + h_m) / (LR_E) \quad (2.21)$$

where  $R_E = 6370$  km.

Electrons with pitch-angles at the loss-cone are critically trapped, in that if the equatorial pitch angle are slightly lowered, they precipitate. Such a pitch angle change involves a violation of the first adiabatic invariant  $M$ , which occurs when the particle experiences the electromagnetic fields of an oblique whistler wave oscillating (and rotating) at approximately the gyration frequency in the particle frame of reference.

### 2.4.2 Wave-particle interaction

At each point along the field line in Figure 2.7, we can establish a local Cartesian coordinate system as shown in 2.7b, with  $\hat{\mathbf{z}} \parallel \mathbf{B}_0$  and  $\hat{\mathbf{x}}$  pointing towards higher  $L$ -shells, providing a reference frame with which we can formulate the Lorentz force equations describing the interaction of the energetic electron and oblique whistler wave. For this purpose, we need to provide expressions for the various field components in (2.17), and rewrite this equation in a form more suitable for numerical integration. Following the procedure used by *Bell* [1984], we write the oblique whistler wave components as:

$$\mathbf{E}^w = -\hat{\mathbf{x}}E_x^w \sin \Phi + \hat{\mathbf{y}}E_y^w \cos \Phi - \hat{\mathbf{z}}E_z^w \sin \Phi \quad (2.22a)$$

$$\mathbf{B}^w = \hat{\mathbf{x}}B_x^w \cos \Phi + \hat{\mathbf{y}}B_y^w \sin \Phi - \hat{\mathbf{z}}B_z^w \cos \Phi \quad (2.22b)$$

where  $\Phi(\mathbf{r}) = \int \omega dt - \int \mathbf{k} \cdot d\mathbf{r}$  is the wave phase. Since the gyroradius of resonant energetic electrons is typically much smaller than the spatial scales of variation of  $\mathbf{B}_0$  at the  $L$ -shells of interest, we neglect the variation of  $\mathbf{B}_0$  and assume a locally uniform field, i.e.,  $\mathbf{B}_0(x, y, z) = \mathbf{B}_{0z}(0, 0, z) \equiv \mathbf{B}_0(z)$ .

We now insert  $\mathbf{B}_0$  and (2.22) into (2.17) and obtain the detailed equations of motion of an energetic electron in a general obliquely propagating whistler-mode wave field. However, this form would not be particularly useful, since it requires integration on time scales smaller than a gyroperiod. The dynamics of the resonant interaction under typical magnetospheric conditions are such that cumulative changes



in the pitch angle and energy of the particles occur over temporal scales much larger than the gyroperiod, so that it is useful to cast the equations of motion in such a way that the rapid gyration of the particle can be averaged out [*Inan and Tkalcevic*, 1982; *Bell*, 1984]. In addition, the whistler mode wave field is naturally elliptically polarized in the plasma, and so it is convenient to decompose the wave into two circularly polarized components with opposite senses of rotation, i.e.,

$$\mathbf{B}_R^w = \frac{B_x^w + B_y^w}{2} [\hat{\mathbf{x}} \cos \Phi + \hat{\mathbf{y}} \sin \Phi] \quad (2.23a)$$

$$\mathbf{B}_L^w = \frac{B_x^w - B_y^w}{2} [\hat{\mathbf{x}} \cos \Phi - \hat{\mathbf{y}} \sin \Phi] \quad (2.23b)$$

Using the above decomposition together with (2.17) and averaging over a gyroperiod, we obtain the relativistic gyro-averaged equations of motion for a general harmonic resonance  $m$  [*Bell*, 1984; *Jasna*, 1993]:

$$\frac{dp_z}{dt} = \omega_{\tau m}^2 m_e k_z^{-1} \sin \eta - \frac{1}{m_e \gamma} \frac{p_\perp^2}{2\omega_H} \frac{\partial \omega_H}{\partial z} \quad (2.24a)$$

$$\begin{aligned} \frac{dp_\perp}{dt} = & - \left[ \omega_1 \left( \frac{p_z}{\gamma} + m_e R_1 \right) J_{m-1}(\beta) - \dots \right. \\ & \left. \omega_2 \left( \frac{p_z}{\gamma} - m_e R_2 \right) J_{m+1}(\beta) \right] \sin \eta + \dots \\ & \frac{1}{m_e \gamma} \frac{p_z p_\perp}{2\omega_H} \frac{\partial \omega_H}{\partial z} \end{aligned} \quad (2.24b)$$

$$\frac{d\eta}{dt} = \frac{m\omega_H}{\gamma} - \omega - k_z \frac{p_z}{m_e \gamma} \quad (2.24c)$$

where  $\eta$  is defined as the angle between  $B_R^w$  and  $v_\perp$  and is shown in Figure 2.9,  $\omega$  is the whistler wave radial frequency,  $\omega_H = eB/m_e$  is the electron gyrofrequency (where we have used  $-q_e = e = 1.6 \times 10^{-19} \text{C}$  since we are now dealing explicitly with electrons, and have replaced  $\omega_{He}$  with  $\omega_H$ ) in the electron rest frame,  $m_e$  is the electron rest mass and:

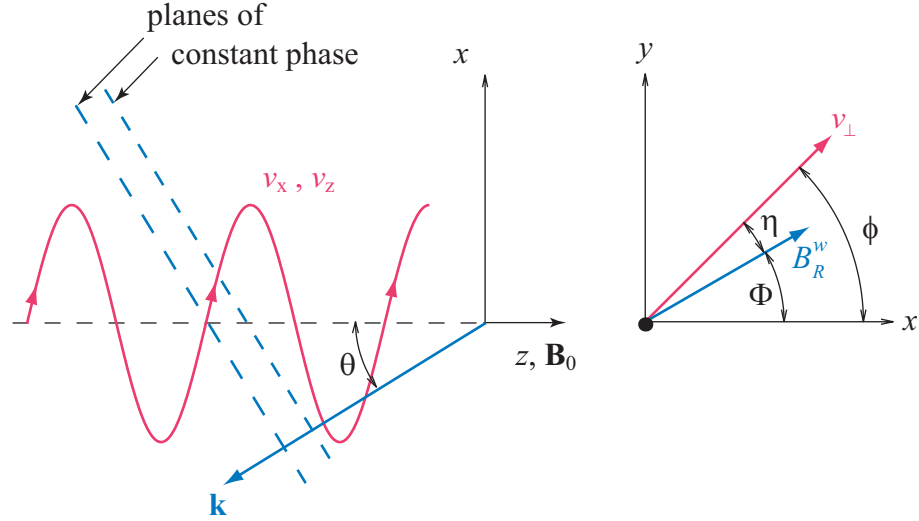


Figure 2.9: Interaction geometry between an energetic electron (red) and an obliquely propagating whistler wave (blue), showing the wave normal angle  $\theta$ , and the angle  $\eta$  between  $v_{\perp}$  and  $B_R^w$  where  $v_{\perp}$  is the velocity component of the electron perpendicular to  $\mathbf{B}_0$  and  $B_R^w$  is the right circularly polarized wave component.

$$\beta = \frac{k_x p_{\perp}}{m_e \gamma \omega_H} \quad (2.25a)$$

$$k_z = k \cos \theta = (\omega \mu / c) \cos \theta; \quad k_x = k \sin \theta \quad (2.25b)$$

$$\omega_{\tau m}^2 = (-1)^{m-1} \omega_{\tau 0}^2 [J_{m-1}(\beta) - \alpha_1 J_{m+1}(\beta) + \gamma \alpha_2 J_m(\beta)] \quad (2.25c)$$

$$\omega_{\tau 0}^2 = \frac{\omega_1 k_z p_{\perp}}{\gamma m_e} \quad (2.25d)$$

$$\omega_1 = \frac{e}{2m_e} (B_x^w + B_y^w); \quad \omega_2 = \frac{e}{2m_e} (B_x^w - B_y^w) \quad (2.25e)$$

$$\alpha_1 = \frac{\omega_2}{\omega_1} \quad (2.25f)$$

$$\alpha_2 = \frac{e E_z^w}{\omega_1 p_{\perp}} \quad (2.25g)$$

$$R_1 = \frac{E_x^w + E_y^w}{B_x^w + B_y^w}; \quad R_2 = \frac{E_x^w - E_y^w}{B_x^w - B_y^w} \quad (2.25h)$$

where  $\mu$  is the refractive index discussed in Section 2.3.2 and  $J_i$  are Bessel functions of the first kind, order  $i$ .

To determine the flux of electrons precipitated into the upper atmosphere as a result of the interaction with the oblique whistler wave, it is useful to explicitly write the variation of the pitch angle of the particle with time by using (2.24a), (2.24b) and  $\alpha = \tan^{-1}(p_{\perp}/p_z)$ :

$$\frac{d\alpha}{dt} = -\frac{m_e \omega_{\tau m}^2}{k_z p_{\perp}} \left( 1 + \frac{\cos^2 \alpha}{mY - 1} \right) \sin \eta + \frac{1}{m_e \gamma} \frac{p_{\perp}}{2\omega_H} \frac{\partial \omega_H}{\partial z} \quad (2.26)$$

where  $Y = \omega_H/\omega$  and all other symbols are as defined above.

Although the behavior described by the set (2.24)–(2.25) is complicated in general, we are primarily concerned with cases where the energetic electron and oblique wave are said to be in resonance, in which case the different components of these equations can be readily understood as follows (we discuss the nonrelativistic case for simplicity). Equations (2.24a) and (2.24b) can be divided into two parts: the rightmost term on the right hand side, which describes only the adiabatic motion of the particle, and the remainder of the terms on the right hand side of both equations, which describe the motion of the particle due only to the forces of the oblique wave. The latter terms are multiplied by a  $\sin \eta$  factor, implying that for any appreciable change to occur in  $v_{\perp}$  and  $v_z$  due to the oblique whistler,  $\eta$  must remain relatively constant over some portion of our integration space, leading directly to the condition required for resonance:

$$\frac{d\eta}{dt} = m\omega_H - \omega - k_z v_z \simeq 0 \quad (2.27)$$

which has the interpretation that resonance occurs when the Doppler-shifted frequency of the wave as experienced by the energetic particle is matched to the particle gyrofrequency (or an integer multiple thereof), so that the gyro-averaged electromagnetic wave fields appear temporarily stationary in the frame of reference of the moving particle.

Equation (2.27) suggests that a given oblique wave field (with a given frequency and wave number along the field) has a preferred electron velocity with which it resonates, expressed as:  $v_z^{\text{res}} = (m\omega_H - \omega)/k_z$  (see [Lauben *et al.*, 2001] or (5.1) for the relativistic version of  $v_z^{\text{res}}$ ). The total energy of the particle can be determined

by choosing to examine only those particles at the edge of the loss-cone, in which case  $v^{\text{res}} = v_z^{\text{res}} \cos^{-1} \alpha_{\text{lc}}$  and the energy follows directly. Further discussion of the derivation and significance of the set (2.24) – (2.25) is beyond the scope of this dissertation but can be found elsewhere [Bell, 1984; Jasna, 1993].

To close our set of equations, we note that the wave electric and magnetic field components in (2.25) are not independent, but are instead related through the physics of the propagation mode, expressed in the set of equations (2.5) – (2.7). Following Bell [1984], Jasna [1993] and Lauben *et al.* [2001], and making use of (2.9), we relate the Poynting flux of the wave  $\mathbf{S}^w = (1/2)\Re\{\mathbf{E}^w \times \mathbf{H}^w\}$ , as well as all other wave components to the single reference component  $B_y^w$  as:

$$|B_y^w|^2 = \frac{2\mu_0\rho_2^2 X^2 \mu \cos \theta |\mathbf{S}^w|}{c\sqrt{(\tan \theta - \rho_1\rho_2 X)^2 + (1 + \rho_2^2 X)^2}} \quad (2.28)$$

$$X = \frac{P}{P - \mu^2 \sin^2 \theta} \quad (2.29a)$$

$$\rho_1 = \frac{E_z^w}{E_y^w} = \frac{(\mu^2 - S) \mu^2 \sin \theta \cos \theta}{D (\mu^2 \sin^2 \theta - P)} \quad (2.29b)$$

$$\rho_2 = \frac{E_x^w}{E_y^w} = \frac{\mu^2 - S}{D} \quad (2.29c)$$

and

$$\begin{aligned} \frac{E_x^w}{B_y^w} &= \frac{c (P - \mu^2 \sin^2 \theta)}{P \mu \cos \theta}, \\ \frac{E_y^w}{B_y^w} &= \frac{Dc (P - \mu^2 \sin^2 \theta)}{P \mu \cos \theta (S - \mu^2)}, \\ \frac{E_z^w}{B_y^w} &= \frac{-c \mu \sin \theta}{P}, \\ \frac{B_x^w}{B_y^w} &= \frac{-D (P - \mu^2 \sin^2 \theta)}{P (S - \mu^2)}, \\ \frac{B_z^w}{B_y^w} &= \frac{D \sin \theta (P - \mu^2 \sin^2 \theta)}{P \cos \theta (S - \mu^2)} \end{aligned} \quad (2.30)$$

where  $c$  is the speed of light,  $\mu_0 = 4\pi \times 10^{-7}$  H/m is the permeability of free space, and all other symbols are as previously defined.

Using the resonance condition (2.27) and typical wave parameters in the inner magnetosphere (see for example Figure 5.14b) to compute the energies of resonantly interacting electrons, we obtain values of  $\sim 100 - 1000$  keV as shown in Figure 5.12. On the other hand, the propagation of the whistler wave in the plasma is largely controlled by the relatively cold particles of the plasmasphere ( $\lesssim 1$  eV) indicating that different energy ranges of the particle population control wave propagation, interact in gyroresonance and experience pitch-angle scattering and precipitation due to the wave ( $\sim 100 - 1000$ ), and as discussed in the following section, cause wave damping ( $\sim 100$  eV to 1 keV).

Before we proceed to the first application of the theory presented above, we examine the manner in which the relatively colder but yet suprathermal magnetospheric plasma attenuates the MR whistler wave, as this damping determines the time duration over which the wave has sufficient power to induce significant changes in the momentum and energy of the resonant energetic particles.

## 2.5 Landau damping

Up to now, we have used a cold plasma analysis (Section 2.3.2) to determine the wave refractive index (which was necessarily assumed to be real) and derived gyro-averaged equations of motion describing the dynamics of a relativistic charged test-particle moving through the whistler wave field in a general harmonic gyroresonance (Section 2.4.2). In this section, we utilize a kinetic approach to determine the small correction of the wave refractive index that comes about due to the presence of suprathermal particles. This correction manifests itself as an imaginary part, leading to the damping of the wave for typical distributions of suprathermal electrons in the inner magnetosphere.

Particles constituting any realistic plasma at a finite temperature are not cold (i.e.,  $\langle v^2 \rangle \neq 0$ ), but in fact have a distribution of velocities that can affect a propagating whistler wave. To account for the effects on the wave of a distribution of particles, we

use the so-called ‘hot-plasma’ theory to re-derive the refractive index  $\mu$  of the wave as a function of frequency, using the more general Vlasov equation together with Maxwell’s equations [Kennel, 1966], rather than the momentum transport equation (2.5) used for the cold plasma analysis.

The solution of the Vlasov-Maxwell equations leads to a refractive index with an infinite number of poles in the complex plane, corresponding to the resonance condition expressed in (2.27). The effect of the poles can be determined using a contour integration method around the poles, yielding a small imaginary component to the refractive index, indicating that near resonance, there exists the possibility of damping or growth of the wave. Writing the total refractive index as  $n = \mu - i\chi$  or  $k = k_r + ik_i$ , the imaginary part can be expressed as [Brinca, 1972]:

$$\begin{aligned}\chi &= -\frac{ck_i}{\omega} \\ &= \frac{A_N}{4\mu(2A\mu^2 - B)} \left\{ \frac{\mu^2 \sin^2 \theta - P}{2(S - \mu^2)} \Gamma_1 \cdot \right. \\ &\quad \left[ (R - \mu^2) J_{m-1} + (L - \mu^2) J_{m+1} \right]^2 G_1 \\ &\quad - 2 \left[ (S - \mu^2 \cos^2 \theta) (S - \mu^2) - D^2 \right] \Lambda_1 J_m G_2 \\ &\quad \left. - 2\mu^2 \sin \theta \cos \theta \Gamma_1 \cdot \left[ (R - \mu^2) J_{m-1} + (L - \mu^2) J_{m+1} \right]^2 G_2 \right\}\end{aligned}\quad (2.31)$$

where the symbols  $A$ ,  $B$ ,  $C$ ,  $D$ ,  $L$ ,  $P$ ,  $R$ , and  $S$  are the Stix parameters introduced in Section 2.3.2,  $A_N$  is the normalization constant defined implicitly by (2.35),  $\delta$  represents the Dirac delta function, the argument of the Bessel functions  $J_i$  is  $\beta$  as given in (2.25a), the real part of the refractive index  $\mu$  is given by (2.12), and the operators  $\Gamma_1$  and  $\Lambda_1$  are defined as:

$$\begin{pmatrix} \Gamma_1 \\ \Lambda_1 \end{pmatrix} = \frac{2\pi^2 \omega_{pe}^2}{\omega k_z} \sum_{m=-\infty}^{\infty} \int_0^{\infty} dv_{\perp} \begin{pmatrix} v_{\perp}^2 \\ v_{\perp} \end{pmatrix} \int_{-\infty}^{\infty} dv_z \begin{pmatrix} 1 \\ v_z \end{pmatrix} \delta(v_z - v_z^{\text{res}}) \quad (2.32)$$

$$G_1 = \left( 1 - \frac{k_z v_z}{\omega} \right) \frac{\partial f}{\partial v_{\perp}} + \frac{k_z v_{\perp}}{\omega} \frac{\partial f}{\partial v_z} \quad (2.33)$$

$$G_2 = J_m \left[ \left( 1 + \frac{m\omega_H}{k_z} \right) \frac{\partial f}{\partial v_z} - m \frac{\omega_H v_z}{\omega v_{\perp}} \frac{\partial f}{\partial v_{\perp}} \right] \quad (2.34)$$

where  $v_z^{\text{res}} = (m\omega_H + \omega)/k_z$  as implied by (2.27), and  $f$  represents the electron distribution function, given as:

$$f(v_\perp, v_z) = \frac{A_N v_\perp^{2p}}{(v_\perp^2 + v_z^2 + v_0^2)^q}; \quad \int_0^{2\pi} d\phi \int_0^\infty v_\perp dv_\perp \int_{-\infty}^\infty f dv_z = 1 \quad (2.35)$$

The normalization defines  $A_N$  and the mean square velocity determines  $v_0$ . In our work we use the suprathermal particle distribution given by  $f(v) = 2 \times 10^5 v^{-4} \text{ cm}^{-6} \text{ s}^3$  [Bell *et al.*, 2002] and the normalization factor  $A_N$  reduces to  $A_N = 2 \times 10^5 / n_e$ , where both numerator and denominator must be expressed in similar units. Further description of this distribution is given in Section 4.2.3.

The set of equations (2.32)–(2.35) is both general and complicated, but fortunately we do not need to deal with the entire set for our application. As shown by past workers [Thorne and Horne, 1994] the dominant contribution to the damping of MR whistlers, even in the presence of significant anisotropy, is the  $m = 0$  resonance, otherwise known as the Landau resonance. Thus, the infinite summation in (2.32) is replaced with only the  $m = 0$  term. In addition, since the last factor of (2.32) is a Dirac delta function, the integral in  $v_z$  amounts to evaluation of the integrand at  $v_z^{\text{res}}$ , and similarly, further simplifications can be made to (2.33) and (2.34) such that the terms  $G_1$  and  $G_2$  depend only on the parallel velocity gradient  $\partial f / \partial v_z$  evaluated at  $v_z^{\text{res}} = \omega / k_z$ .

The form and behavior of (2.32) – (2.35) can be illustrated with the aid of the simplified diagram shown in Figure 2.10. As the MR whistler wave propagates, it has an electric field component ( $E_z$ ) parallel to the static magnetic field due to its oblique nature (as can be inferred from (2.9) or given by (2.31)). This electric field is able to accelerate or decelerate energetic electrons moving with the wave, in the process losing or gaining energy respectively.

To better understand Landau damping, consider the analogy of a water wave resonantly interacting with surfers at the beach. The water wave contains gravitational potential which is analogous to the electrical potential carried by the oblique whistler. As shown in Figure 2.10a, the (somewhat idealized) wave travels to the right with phase velocity  $v_p$ , and there are no particles (surfers) on the wave. In panel (b), we

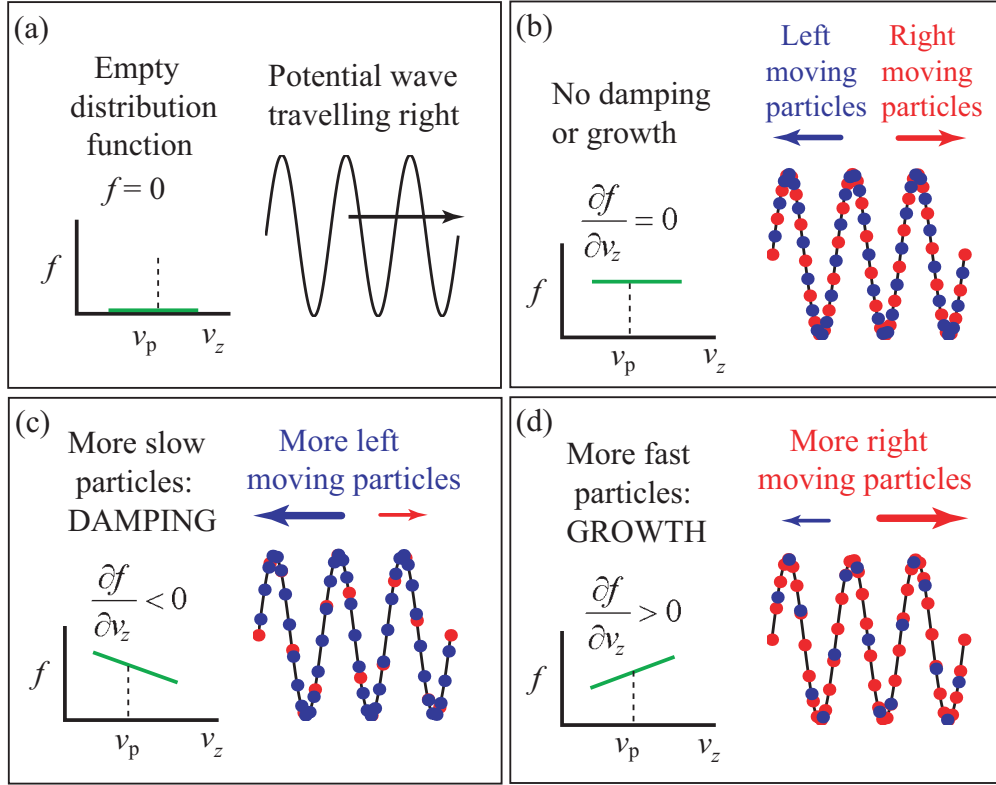


Figure 2.10: Landau resonance interactions; (a) a potential wave travelling right at  $v_p$  with no resonant particles, (b) resonant particles in reference frame of wave with equal number moving left and right, (c) as (b) but more particles moving left (slower) than right, (d) as (b) but with more particles moving right (faster) than left.

introduce a distribution of particles travelling at approximately the phase velocity of the wave, with an equal number of particles travelling both differentially faster, and slower than the wave. Viewed in the reference frame of the wave, the faster (slower) particles slowly drift to the right (left). As the faster particles move up the potential gradient, they are slightly decelerated, and lose energy to the wave. Similarly, as the slower particles move down the potential gradient, they are slightly accelerated and gain energy from the wave. Since there are equal numbers of differentially slower and faster particles, the energy exchange is symmetrical, resulting in no net exchange of energy and hence no damping or growth of the wave. However, if there are more differentially slower particles than faster ones as shown in panel (c), then there are more



particles gaining energy from the wave than those imparting energy to the wave, and the wave is damped. Similarly, if there are more differentially faster moving particles than slower, the wave would exhibit growth as shown in panel (d).

The damping or growth of the MR whistler wave similarly depends on the slope of the distribution function near the particle velocity corresponding to the wave phase velocity. In this work we choose to use the monotonically decreasing distribution function of *Bell et al.* [2002] which was derived on the basis of recent measurements with the HYDRA instrument on the POLAR spacecraft. Examples of path-integrated losses of MR whistlers calculated in this way are shown in Chapter 4, Figure 4.1c,g. Further discussion and examples of our implementation of Landau damping is given in Section 4.2.3. Using the techniques introduced in this chapter, we now proceed to analyze the propagation of MR whistlers in the magnetosphere, including the variation of wave energy along the propagation path, and the resultant precipitation of electrons into the atmosphere.

# Chapter 3

## *L*-Dependence of electron precipitation due to MR whistlers

### 3.1 Introduction

The work presented in this chapter is motivated by recent SAMPEX satellite observations of precipitating high-energy electrons ( $>150$  keV) in the drift loss cone. The drift loss cone is differentiated from the bounce loss cone in that the mirroring particles do not precipitate within one bounce period but rather within one longitudinal drift period around the Earth, as their mirror altitude is lowered in the course of their eastward drift towards the vicinity of the South Atlantic Anomaly [*Blake et al.*, 2001]. The drift loss cone flux enhancements observed on SAMPEX exhibit unique and repeatable  $L$ -dependent signatures consistent with those expected from gyroresonant pitch angle scattering induced by obliquely propagating MR whistlers. An example of SAMPEX observations on July 16<sup>th</sup> 1995 is shown in Figure 3.1 where relatively rare multiple narrow peaks were recorded at lower  $L$ -shells ( $1.4 < L < 1.65$ ), together with a more commonly observed broad precipitation maximum at higher  $L$ -shells ( $L > 1.8$ ).

Association of these drift loss cone flux enhancements with lightning discharges is suggested by coincident UARS satellite observations as in Figure 3.1b [*Blake et al.*, 2001]) which show that the energy spectra of the drift loss cone electrons strongly

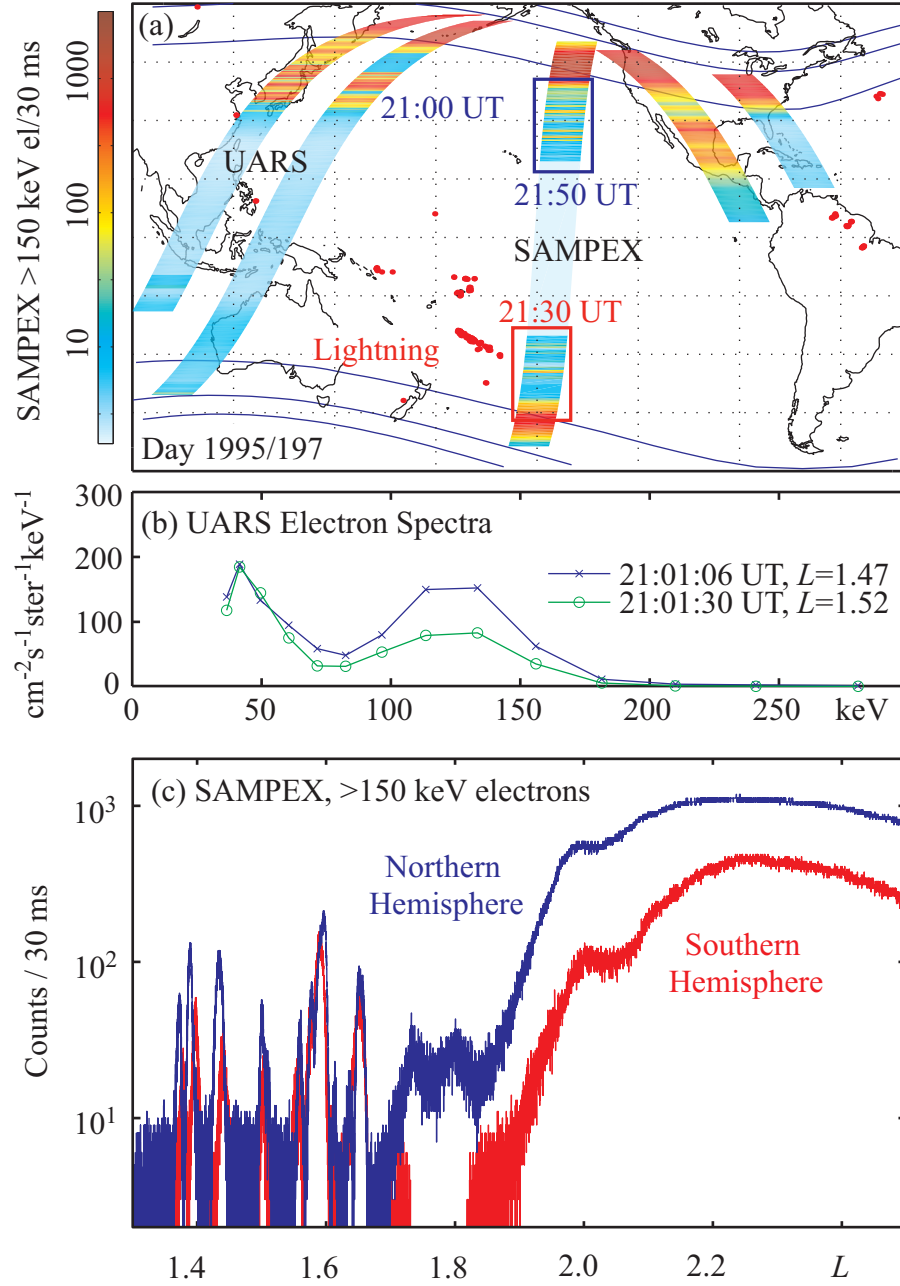


Figure 3.1: (a) SAMPEX and UARS orbit tracks showing in color the amount of precipitation and lightning storm locations as recorded on the OTD instrument; (b) electron energy spectra obtained from the UARS satellite, and (c) electron precipitation shown as a function of  $L$ -shell for the above pass on SAMPEX, where the blue and red curves correspond to the northern and southern hemispheres respectively.

resemble the energy spectra of lightning-induced electron precipitation (LEP) bursts, previously observed in the bounce loss cone on the SEEP spacecraft [Voss *et al.*, 1998]. Further evidence of the causative role of lightning discharges is provided by global lightning flash occurrence data from the Optical Transient Detector (OTD) instrument on the OrbView-1 satellite [Christian *et al.*, 1989] which indicates the presence of several large lightning storm centers located westward of the SAMPEX orbit during the observation. Both UARS and SAMPEX satellite track and data are shown in Figure 3.1a, together with OTD data.

Our goal in this chapter is to develop a numerical model based on ray tracing and a relatively simple treatment of the wave-particle interaction to estimate the  $L$ -dependence of drift loss cone LEP enhancements under various ionospheric conditions and for different source lightning locations. We then apply this model to parameters of the SAMPEX observations, as a means to better understand the physical origin and mechanisms leading to the drift loss cone flux enhancements and their  $L$ -dependent signatures.

We present our model in Section 3.2, and then proceed to analyze in detail the observations of Figure 3.1 in Section 3.3. In Section 3.4 we present model results for a variety of ionospheric conditions and lightning source locations, and summarize the findings of this work in Section 3.5. Much of the work presented in this chapter has already been published [Bortnik *et al.*, 2002a], but is repeated here for completeness, and with some expanded clarifications added as appropriate for a Ph.D. dissertation.

## 3.2 Description of the model

The model used to calculate the  $L$ -dependence of energetic electron precipitation into the drift loss cone driven by MR whistlers consists of two broad parts: the first part involves the construction of a time-dependent wave property distribution, i.e., a specification of the wave properties (e.g., wave power, refractive index, frequency) at appropriately discretized spatial points in the magnetosphere as a function of time. The second part involves the calculation of the energetic electron precipitation flux driven into the drift loss cone at every point in the magnetosphere using the wave

property distribution. This flux is integrated with respect to time, frequency, and the energy range measured by SAMPEX to obtain the total precipitated flux versus *L*-shell which can be compared directly with SAMPEX data.

### 3.2.1 Construction of the wave property distribution

The wave property distribution can be visualized as a three-dimensional block of data, including two spatial dimensions describing a point in the magnetic meridional plane, and time as the third dimension, describing the temporal evolution of a wave as it propagates through the magnetosphere. To determine the wave property distribution we use ray tracing weighted with appropriate initial power densities, and sample each ray at fixed time intervals, adding their properties to the closest three dimensional ‘bin’, as described below.

We analyze the generation of the whistler wave energy using the procedure outlined in Section 2.2. A lightning discharge is taken to occur at a given latitude  $\lambda_s$ , radiating power in all directions. The wave power density at the base of the ionosphere (assumed to be at 100 km altitude) is then calculated using (2.1) in a  $\pm 5^\circ$  region (the illuminated region) about the source and is subsequently multiplied with an appropriate latitude- and frequency-dependent attenuation factor to obtain the wave power density at the top of the ionosphere (assumed to be at 1000 km altitude) in the same  $\pm 5^\circ$  latitudinal region around the source.

Using the Stanford VLF ray tracing code [*Inan and Bell, 1977*] described in Section 2.3.4, we determine the propagation of the wave packet by filling the illuminated region with 200 equally spaced rays for every frequency component, and tracing each ray for a given time duration. The frequency spectrum of the wave packet is discretized into 21 frequency components spaced approximately logarithmically between 500 Hz and 25 kHz (chosen as the 6 dB points of the spectrum relative to its peak). For each frequency component the set of 200 rays is traced for a certain ‘effective lifetime’  $\tau_3(f)$  to approximately account for the effects of Landau damping. The effective lifetime  $\tau_3(f)$  is determined using the Landau damping formulation of *Brinca* [1972] together with recently measured suprathermal fluxes from the POLAR satellite [*Bell*

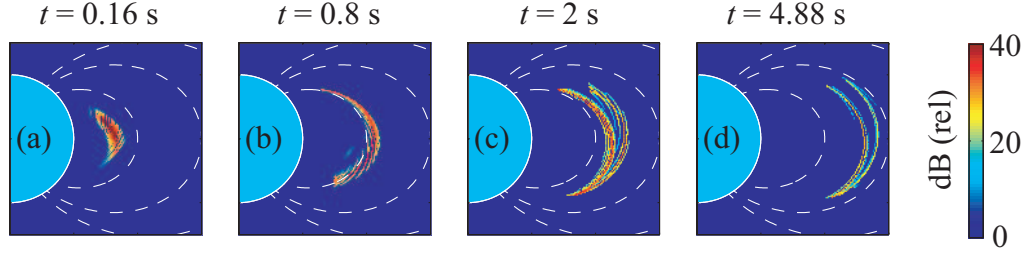


Figure 3.2: Panels (a)–(d) illustrate the progression of a lightning generated whistler wave through the magnetosphere at four different times, including all 21 frequency components.

*et al.*, 2002] for the central ray only (i.e., the one launched at  $\lambda_s$ ) and corresponds to the time at which the power density of the ray diminishes by 3 dB compared to its initial value (e.g., see Figure 4.3 for similarly computed  $\tau_{10}(f)$  values). The power density of each ray is held constant for the duration of its effective lifetime and set to zero thereafter, since the Landau damping of typical magnetospherically reflecting whistler waves is initially slow, but proceeds very quickly after a certain point (assumed at  $\simeq -3$  dB) [Thorne and Horne, 1994]. It should be noted here that we use this relatively crude method of accounting for Landau damping only for the first-order calculations undertaken in this chapter. Later on (Chapters 4–5) when we fully simulate the MR whistler-induced precipitation we continuously vary the wave power density along its propagation path in accordance with the local value of the Landau damping rate.

We illustrate in Figure 3.2 four time slices from our wave property distribution, showing a superposition of all 21 frequency components. The magnetic meridional plane in the magnetospheric space between  $0 \leq X \leq 4R_E$  and  $-2R_E \leq Y \leq 2R_E$  is discretized into  $200 \times 200$  spatial bins (where  $X$  and  $Y$  originate at the center of the Earth, are measured in Earth radii, and are oriented along the geomagnetic equator and axis respectively) with 100 time bins making up the third dimension in the data structure.

As the rays propagate through the magnetospheric grid, their various properties are recorded at every grid point and at each time ‘bin’. In the case where more than one ray traverses a magnetospheric grid point at the same time bin, we assume that

the two rays are sufficiently incoherent that their respective powers would be additive and that the square of the total magnetic field intensity at that point and time would be equal to the sum of the squares of the individual components. The resultant wave vector  $\mathbf{k}$  is taken to be the vector average of the  $\mathbf{k}$ -vectors of the different waves at the particular spatial point and time.

### 3.2.2 Calculation of the wave-induced precipitation

Using the wave property distribution obtained in the previous section (available for only one frequency at a time), the precipitating particle flux at every point and time can, in principle, be computed using a test particle approach similar to that used by *Chang and Inan* [1985*b*] based on the equations of motion described in Section 2.4.2. However, this approach is computationally intensive due to the large volume of space occupied by the waves. In Chapter 5, we utilize a method that involves the use of a combination of test-particle and diffusion analysis to determine the pitch-angle scattering produced at each point along a given field line. In this chapter, however, our goal is to come up with a first order estimate for the precipitated flux using a much simpler interaction model that nevertheless accurately brings out the  $L$ -dependence of the precipitation. As derived in Appendix A, the differential precipitation flux  $\Delta\Phi_E$  at any point is given by the relation:

$$\Delta\Phi_E \propto \frac{B^w v^2}{v_z^{\text{res}} E^3 \gamma^4} \quad (3.1)$$

where

$$v_z^{\text{res}} = \frac{\omega_H / \gamma - \omega}{k_z} \quad (3.2)$$

from the resonance condition (2.27), and  $\Delta\Phi_E$  is the electron energy flux scattered into the loss cone within a particular magnetospheric spatial grid,  $\omega_H$  and  $\omega$  are the local gyrofrequency and wave angular frequency respectively,  $\mathbf{k}$  is the wave vector, and  $B^w$  is the magnetic field intensity of the wave responsible for changing the pitch angle of the highly energetic electrons under consideration,  $\gamma = (1 - v^2/c^2)^{-1/2}$  is the relativistic Lorentz factor,  $v_z^{\text{res}}$  is the component of the resonant velocity of interacting

particles along the static magnetic field, and  $E$  is the energy of the resonant electron.

Equation (3.1) represents a first order approximation designed to bring out the  $L$ -dependence of the whistler-induced precipitation into the drift loss cone. Sample calculations using (3.1) show very similar interaction lengths and locations to those obtained using a test-particle approach performed for the first hop of the wave [Lauben *et al.*, 2001]. The use of (3.1) implicitly assumes that only resonant electrons are pitch-angle scattered enough to be precipitated. We consider electrons with energies  $> 150$  keV, in order to directly compare with SAMPEX data.

After evaluating the incremental flux contributions from every grid point in the wave property distribution, we integrate over all such contributions with respect to time and along each  $L$ -shell. This integration gives the total precipitation flux versus  $L$ -shell for a particular frequency component, and we repeat this process for all 21 frequency components. As a final step, we integrate with respect to frequency by finely interpolating between the different frequency components and summing together the resultant contributions.

### 3.3 Results for $25^\circ$ lightning source latitude

The case of  $\lambda_s = 25^\circ$  is presented separately because it is directly comparable to the event shown in Figure 3.1 where the location of the storm center was at a similar geomagnetic latitude. As discussed in Section 3.2.1 we trace 200 rays per frequency component in the  $10^\circ$  illuminated region centered on  $\lambda_s = 25^\circ$  (i.e., from  $20^\circ$  to  $30^\circ$ ) and initially aim to determine the origin of the sharp precipitation peaks of Figure 3.1 at  $L < 1.65$ .

#### 3.3.1 Focusing of ray ensemble

Noting that wave-induced pitch-angle scattering is maximally efficient near the geomagnetic equator (compared for example to topside ionospheric interactions as considered by Neubert *et al.* [1987]), these sharp precipitation peaks suggest that the rays injected in the illuminated region must have crossed the magnetic equator with a



very narrow spatial extent perpendicular to  $\mathbf{B}_0$ . Such a situation can arise in at least two ways: (1) the wave energy could be trapped in field aligned density enhancements or depletions (ducts), or (2) the rays could be focused by horizontal density gradients in the ionosphere. The first scenario is considered unlikely due to the paucity of ducts at low  $L$ -shells [Cerisier, 1974], and the fact that the presence of ducts would still not prevent the illumination of the intervening magnetospheric region with a continuum of nonducted waves which would also pitch-angle scatter and precipitate electrons [Lauben *et al.*, 2001] and would tend to wash out any peaks due to ducts. The second possibility is considered more likely since horizontal ionospheric density gradients are common at low latitudes [Kelley, 1989, p.192] and this mechanism is explored in detail below.

To investigate the effects of horizontal density gradients, we consider the two outermost rays of the illuminated region (i.e., injected at  $\lambda=20^\circ$  and  $\lambda=30^\circ$ ) noting that all rays injected between these latitudes will be bounded by the outer rays in a smooth magnetosphere (i.e., in the absence of sharp density gradients).

As shown in Figure 3.3, we can adjust the initial wave normal angle of the bounding rays such that both rays (and hence the entire wave packet) will cross the magnetic equatorial plane at a specific  $L$ -shell, thus effectively focusing the whistler wave energy for all the intervening rays.

In fact, as shown in Figure 3.4 the bounding rays are able to focus over a range of  $L$ -shells from  $L \sim 1.2$  to  $\sim 1.6$ , and hence produce sharp precipitation peaks consistent with the observation of Figure 3.1 where the sharp peaks are seen below  $L \simeq 1.65$ . In Figure 3.4 we analyze 11 frequency components, showing on the abscissa the equatorial focusing  $L$ -shell of the bounding rays, and on the ordinate the wave normal angle relative to the local vertical  $\psi$  of the  $\lambda=20^\circ$  ray (solid line), the  $\lambda=30^\circ$  ray (dotted line) and difference in wave normal angles  $\psi(\lambda=30^\circ) - \psi(\lambda=20^\circ)$  (dash-dot line). The gray rectangle in the 5 kHz panel highlights the values illustrated in Figure 3.3, where the equatorial crossing of  $L=1.42$  is achieved when  $\psi(\lambda=30^\circ)=46^\circ$  and  $\psi(\lambda=20^\circ)=24^\circ$ .

This figure suggests that the initial wave normal angles fall within reasonable bounds that are consistent with ionospheric refraction [James, 1972] and that a single

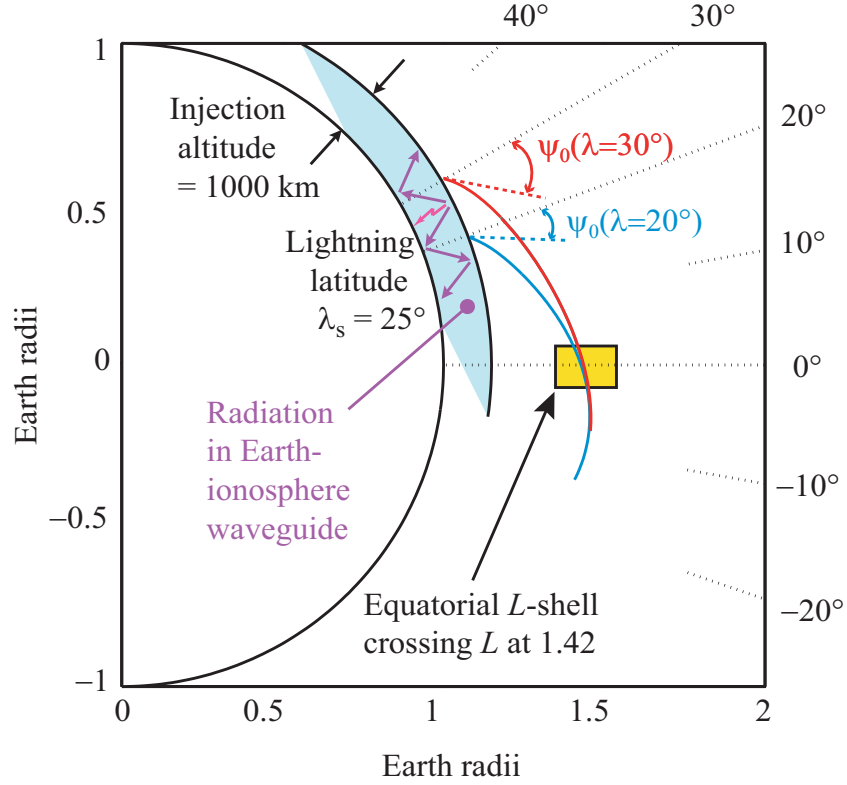


Figure 3.3: The two outermost rays of the illuminated region ray ensemble are shown focusing on the magnetic equatorial plane.

lightning discharge at a particular location could produce a sharp precipitation peak over a range of  $L$ -shells depending on the particular horizontal ionospheric density gradients present at the time.

### 3.3.2 Horizontal density gradients

To test whether typical ionospheric horizontal density gradients could produce the wave normal rotation that is required for focusing (as shown in Figure 3.4), we construct a realistic model of the upper ionosphere using the formulation of *Angerami and Thomas* [1964] with superimposed field aligned density structures [*Bernhardt and Park*, 1977]. We assume that rays enter the bottomside ionosphere at 100 km and

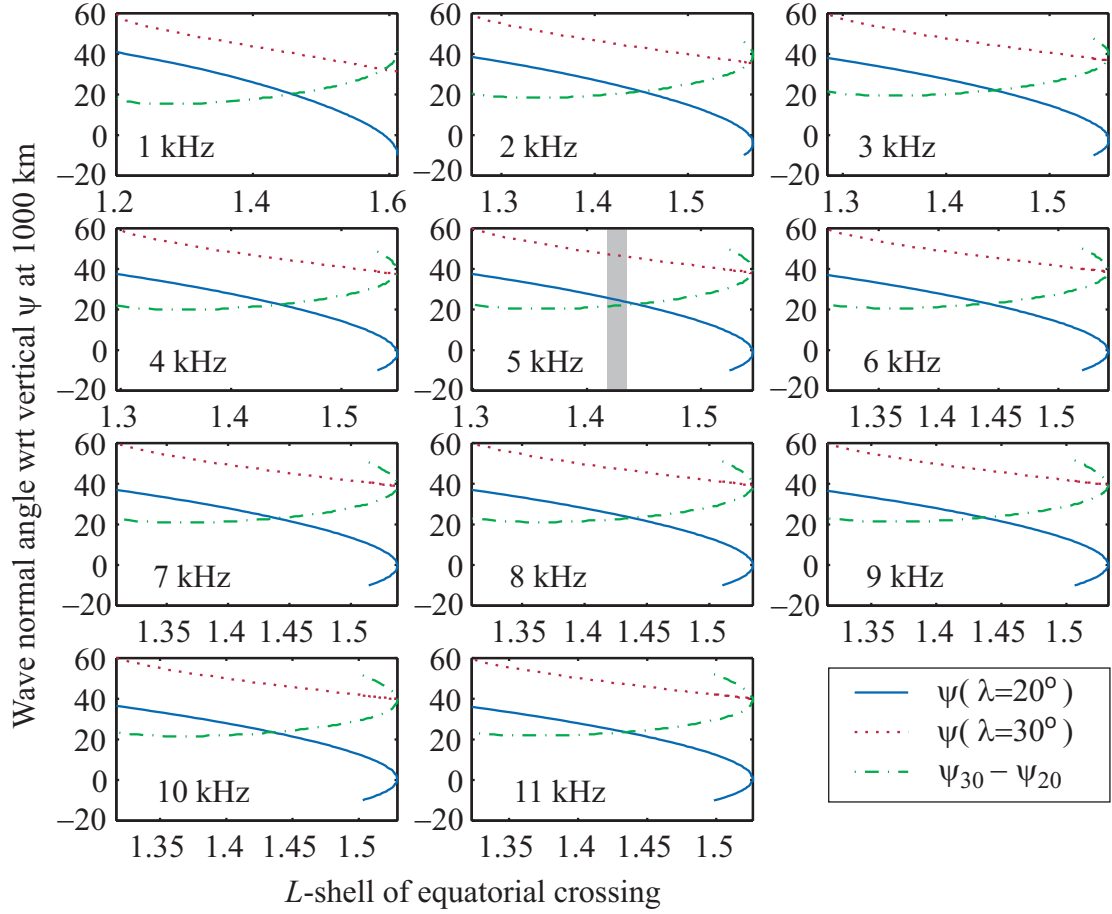


Figure 3.4: Analysis of 11 frequency components showing the equatorial focusing  $L$ -shell of the bounding rays on the abscissa, and the wave normal angle relative to the local vertical of the  $20^\circ$  ray (solid),  $30^\circ$  ray (dotted) and difference (dash-dot). The values used in Figure 3.3 [ $\psi(\lambda=20^\circ)=24^\circ$ ,  $\psi(\lambda=30^\circ)=46^\circ$ ,  $L \simeq 1.42$ ] are highlighted with the grey rectangle.

that due to the large positive vertical density gradient, their wave normal angles become vertical by the time they reach  $\sim 300$  km. We then perform ray tracing between 300 km and 1000 km as shown in Figure 3.5, where we see that the low latitude ray ( $\lambda=20^\circ$ ) and high latitude ray ( $\lambda=30^\circ$ ) attain wave normal angles of  $\sim 24^\circ$  and  $\sim 46^\circ$  respectively at 1000 km, entirely consistent with the values necessary for focusing the ray paths on the magnetic equatorial plane.

We note that the model ionosphere that can produce such refraction is not unique,

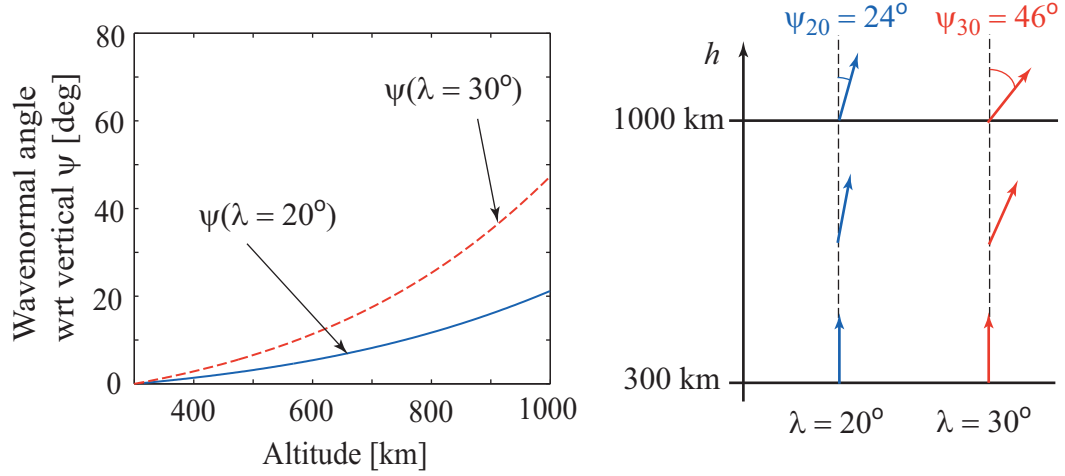


Figure 3.5: Wave normal angle with respect to local vertical of the low and high latitude rays ( $\psi(\lambda = 20^\circ)$  and  $\psi(\lambda = 30^\circ)$  respectively) as they traverse the model ionosphere of Figure 3.6 from 300 km to 1000 km.

since it is the horizontal gradients between  $\lambda = 20^\circ$  and  $\lambda = 30^\circ$  (together with magnetic field parameters) rather than the absolute density that controls the rotation of wave normals away from the vertical direction [James, 1972].

The particular ionospheric model chosen is illustrated in Figure 3.6 showing the electron number density at an altitude of 1000 km, as a function of latitude. Since rays are traced in the magnetic meridional plane, azimuthal density gradients are assumed to be negligible compared to latitudinal gradients, an assumption which is valid particularly in the midnight sector (see Bilitza [2001] and references therein). The model ionosphere shown as a solid line in Figure 3.6, was chosen to be representative of typical ionospheric profiles at the latitudes of interest. A number of density profiles are plotted as dashed lines for comparison, representing different longitudes at 2100 UT, July 16<sup>th</sup> 1995 (the time and date of the observation shown in Figure 3.1), using the International Reference Ionosphere model from the Web pages of NASA's National Space Science Data Center [Bilitza, 2001].

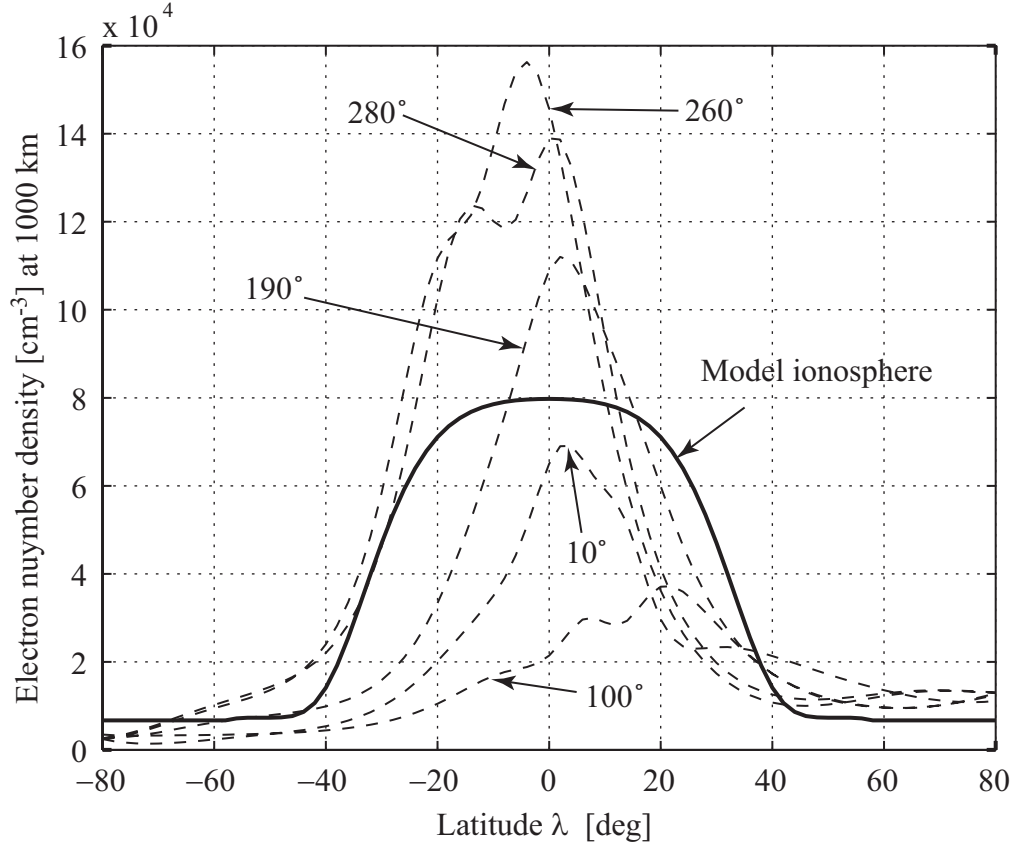


Figure 3.6: Assumed ionospheric electron number density at 1000 km, shown with International Reference Ionosphere (IRI) profiles for 2100 UT, July 16<sup>th</sup>, 1995 (time and date of Figure 3.1 observation) at various longitudes.

### 3.3.3 Pitch angle scattering and interpolation

Using the initial injection wave normal angles at 1000 km  $\psi(\lambda = 20^\circ) = 24^\circ$  and  $\psi(\lambda = 30^\circ) = 46^\circ$ , we perform ray tracing and calculate the wave property distribution as described in Section 3.2.1 for each frequency component, and compute the flux of precipitating particles as described in Section 3.2.2. After a few magnetospheric reflections, different frequency components tend to settle on specific  $L$ -shells [Draganov *et al.*, 1992] as discussed in Section 4.2.2 and shown in Figures 4.1 and 4.2, lower frequencies settling on higher  $L$ -shells and vice versa. Thus, the precipitation occurring on various  $L$ -shells also exhibits distinct energy spectra determined by the

frequencies involved in the resonant interaction. In our calculations, we confine the resonant interaction region to  $\pm 5^\circ$  around the geomagnetic equator, based on the work of *Lauben et al.* [2001] who have used a full test-particle calculation for the first pass of the whistler wave to show that the longest wave-particle interaction was limited to a region of  $\sim 10^\circ$  centered on the geomagnetic equator.

This process is repeated for all 21 frequency components covering the range of 0.5–25 kHz, using interpolation to determine the contribution of intermediate frequency components. Such interpolation is justified since the  $L$ -dependence of the precipitation signature varies slowly with frequency. The final integrated and normalized plot of the  $L$ -dependent precipitation flux produced by a lightning source at  $25^\circ$  latitude, with the inclusion of focusing horizontal gradients is shown in Figure 3.7a.

### 3.3.4 Comparison with SAMPEX data

The similarities between Figures 3.7a and 3.1b are readily apparent. Both exhibit a sharp precipitation peak at  $L < 1.65$ , and a broad precipitation maximum at  $L > 1.9$ . The shape of the broad precipitation maximum exhibits a similar trend with a ‘shoulder’ feature at  $L \simeq 2$  followed by the broad maximum at higher  $L$ -shells. We note that the relative magnitude of the sharp precipitation peak and the broad maximum are slightly different in the two figures, and also that the SAMPEX data in Figure 3.1b contains multiple sharp peaks whereas the calculation only predicts one peak per lightning discharge. These differences can occur due to the presence of other lightning sources nearby, as discussed in Section 3.4.4.

## 3.4 Effect of injection parameters on the precipitation signature

We now extend the methodology used in Section 3.3 to examine the effects of different horizontal ionospheric density profiles on the precipitation signature, with the aim of developing a qualitative guideline for predicting the conditions under which ray path focusing effects occur, and to suggest a possible explanation for the multiple narrow

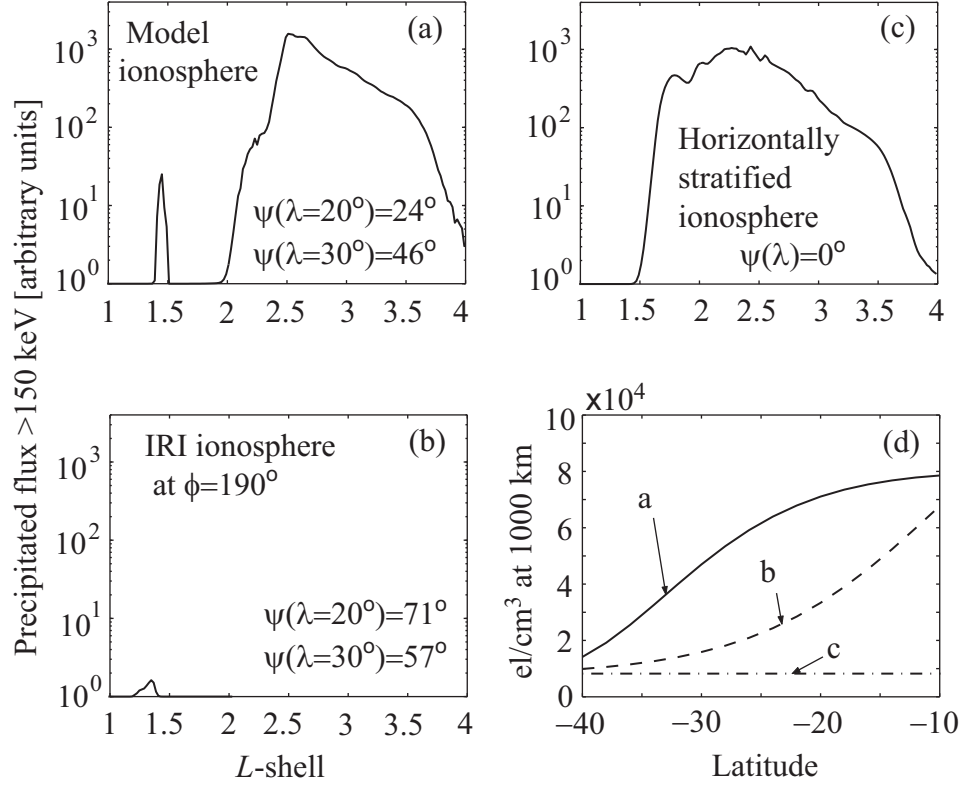


Figure 3.7: Precipitation flux versus  $L$ -shell (normalized) for a lightning source latitude of  $25^\circ$  for (a) model ionosphere with  $\psi(\lambda = 20^\circ) = 24^\circ$  and  $\psi(\lambda = 30^\circ) = 46^\circ$ , (b) IRI model ionosphere at  $190^\circ$  longitude, July 16<sup>th</sup> 1995, with  $\psi(\lambda = 20^\circ) = 71^\circ$  and  $\psi(\lambda = 30^\circ) = 57^\circ$ , (c) horizontally stratified ionosphere with  $\psi(\lambda) = 0$ , and (d) Ionospheric electron density profiles at 1000 km altitude for cases a, b, and c above.

peaks observed in Figure 3.1b.

### 3.4.1 IRI Model at $190^\circ$ longitude

For direct comparison with Figure 3.7a, the IRI ionosphere at a longitude of  $190^\circ$  (i.e., the longitude of the lightning flashes in Figure 3.7a) is modeled as shown in Figure 3.6 and rays traced from 300 km to 1000 km through it, assuming a lightning source latitude of  $25^\circ$  as before. The refraction of the wave normal vectors in this case was more severe, resulting in  $\psi(\lambda = 20^\circ) = 71^\circ$  and  $\psi(\lambda = 30^\circ) = 57^\circ$ . The severe refraction is a result of the higher electron density gradients at the injection

latitudes. Note that the ray injected at  $20^\circ$  refracts further away from the vertical than that injected at  $30^\circ$ , resulting in a “defocusing” of the wave energy. This result is consistent with the observation that the electron density gradient is larger at the lower injection latitude than at the higher. Analysis of the underlying ray paths (not shown) indicates that the rays crossing the magnetic equatorial plane are more diffuse (spread further apart), and re-enter the topside ionosphere after the first hop without any magnetospheric reflections due to their high wave normal angles. The resultant associated integrated precipitation flux signature is shown in Figure 3.7b on the same relative scale as 3.7a and exhibits a relatively weak low  $L$ -shell precipitation peak, without a broad peak at higher  $L$ -shells, due to a lack of magnetospherically reflected components.

### 3.4.2 Injection with vertical wave normals

The case of injection with vertical wave normal vectors at 1000 km is of particular interest because a strictly horizontally stratified ionosphere is assumed in the large body of previous work [*Edgar, 1972; Draganov et al., 1992; Thorne and Horne, 1994; Lauben, 1999; Lauben et al., 2001*] as well as in our later calculations in Chapters 4 and 5, thus eliminating any possibility of ray focusing or defocusing due to horizontal gradients. The resultant precipitation signature for a lightning source latitude of  $25^\circ$  is shown in Figure 3.7c, and clearly demonstrates the effect on the precipitation signature of multiple magnetospherically reflected components. Although the broad high  $L$  maximum robustly maintains its position, the low  $L$ -shell peak is in this case spread out and is effectively blended with the broad higher  $L$  maximum. This result indicates that a horizontally stratified ionosphere does not lead to low  $L$ -shell peaks such as those observed in the SAMPEX data. Our results for this case are also compared (later in Section 5.2.5) with the results obtained with the “full” wave-particle interaction model in Figure 5.23, showing excellent agreement.



### 3.4.3 Lightning source latitudes of $35^\circ$ and $45^\circ$

We now analyze a lightning source at  $\lambda_s = 35^\circ$  by again tracing 200 rays per frequency component over a  $10^\circ$  illumination region centered on the source. As shown in the model profile of Figure 3.6, the horizontal latitudinal gradient at  $40^\circ$  is larger than that at  $30^\circ$  so that the resultant wave normal angles at 1000 km are  $\psi(\lambda = 40^\circ) = 76^\circ$  and  $\psi(\lambda = 30^\circ) = 46^\circ$  respectively for rays injected at these two latitudes. The precipitation signature shown in Figure 3.8a exhibits a diffuse low  $L$ -shell peak, as well as a broad, higher  $L$ -shell maximum. The presence of the low  $L$  peak is caused by horizontal gradient focusing which is not optimal, unlike the  $25^\circ$  case. Much of the whistler radiation at the higher wave normal angle ( $76^\circ$ ) is absorbed by the ionosphere, but a fraction is still able to magnetospherically reflect and escape to higher  $L$ -shells, contributing to the formation of the broad peak visible at  $L > 2$ .

For a source at  $\lambda_s = 45^\circ$ , the model ionosphere of Figure 3.6 shows a large horizontal gradient at  $40^\circ$ , causing the wave normal vector to rotate by  $76^\circ$  off the vertical, and a low horizontal density gradient at  $50^\circ$ , causing a wave normal rotation of  $15^\circ$  away from the vertical. In this case the wave normal vectors refract away from each other, resulting in defocusing. The resultant precipitation flux versus  $L$ -shell signature is shown in Figure 3.8b, exhibiting the distinct absence of a low  $L$ -shell precipitation peak, as well as the robust presence of the high  $L$ -shell, broad precipitation maximum at  $L > 1.5$ . Note also that the precipitation flux resulting from a lightning source at this latitude is more intense than that from lower latitudes, and that the vertical scale in Figure 3.8 is appropriately extended.

### 3.4.4 Formation of multiple narrow peaks

It is evident from Figure 3.1 that multiple narrow peaks at low  $L$ -shells occur at least some of the time, whereas our model calculations predict only one such peak per lightning discharge. Noting that the drift-loss-cone flux enhancements observed by SAMPEX represent the sum of all particles scattered at longitudes due west of the satellite location, multiple peaks can be attributed to the contributions of a number of different source lightning strokes at different longitudes. Each source lightning

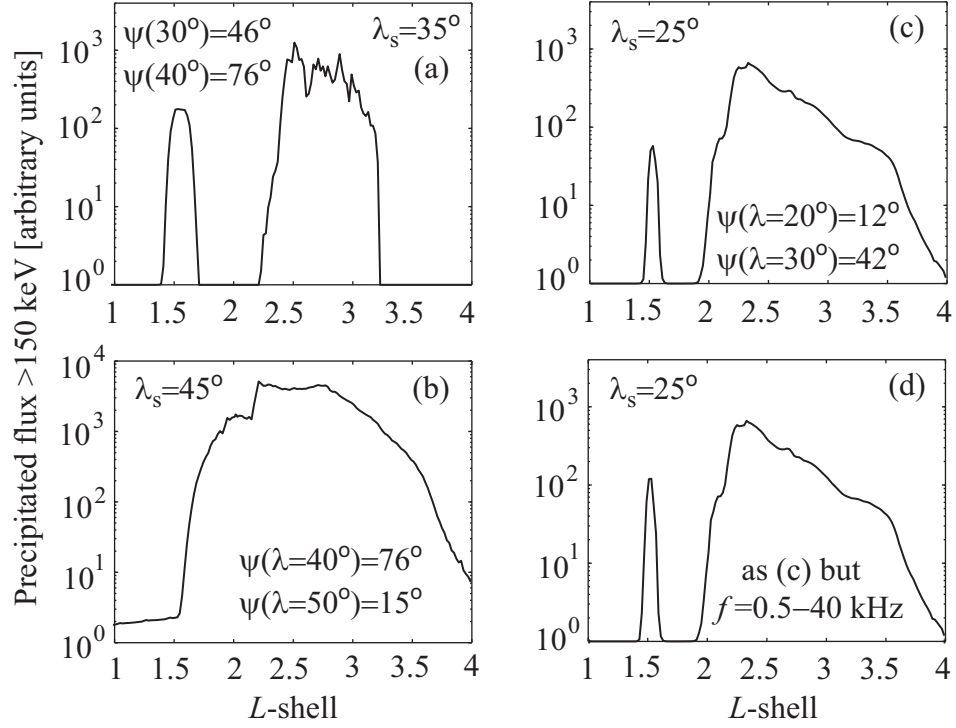


Figure 3.8: Precipitation flux versus  $L$ -shell for model ionosphere shown in Figure 3.6 at (a) lightning source latitude of  $35^\circ$ , (b) lightning source latitude of  $45^\circ$ , note the different vertical scale, (c) lightning source latitude of  $25^\circ$  with slightly modified model ionosphere, and (d) identical conditions to (c) with extended frequency range to 40 kHz.

can account for one low  $L$ -shell precipitation peak, but due to the eastward drift of mirroring electrons in the drift loss cone, electrons precipitated by waves originating at different lightning strokes can superpose to form the multiple narrow peak pattern seen in Figure 3.1. In this connection, we note that the horizontal ionospheric density profiles typically vary with longitude as shown in Figure 3.6, so that the rays originating at different lightning discharges may focus at slightly different  $L$ -shells as they cross the geomagnetic equator.

Consider for example, a longitudinal location slightly west of the location of our model ionosphere in Figure 3.6. Using a slightly modified ionospheric density gradients (as would be the case at a different longitude), a lightning stroke at  $25^\circ$  geomagnetic latitude would produce wave normal angles at 1000 km of  $\psi(\lambda=20^\circ)=12^\circ$  and

$\psi(\lambda = 30^\circ) = 42^\circ$  at injection latitudes of  $20^\circ$  and  $30^\circ$  respectively. The precipitated flux versus  $L$  profile for this case is shown in Figure 3.8c, where the low  $L$ -shell peak has moved to slightly higher  $L$  than in Figure 3.7a, namely to  $L \simeq 1.5$ . We have thus shown that with two slightly different model ionospheres, two distinct peaks can be formed by two different lightning sources. The formation of more peaks is then only a matter of having other lightning strokes occurring at  $L$ -shells near ionospheric focusing regions.

Another important aspect of the comparison of the result of Figure 3.7a with the SAMPEX data in Figure 3.1c is that the intensity of the low  $L$ -shell precipitation peak for the latter is a factor of  $\sim 10$  lower than the maximum intensity of the high  $L$  peak, whereas that for the former is lower by a factor of  $\sim 100$ , and slightly less in Figure 3.8c. This discrepancy results from our restriction of the frequency spectrum to frequencies  $< 25$  kHz. The choice of 25 kHz was rather arbitrary, the wave power radiated by the lightning discharge at 25 kHz being  $\sim 6$  dB lower than the strongest frequency component at 5 kHz, with 500 Hz being chosen to be the lower frequency cutoff for the same reason. Since higher frequency components resonantly interact with lower energy electrons, and the available flux of lower energy electrons is typically much higher than that of higher energy electrons (e.g., Figure 5.9), the contribution to the precipitation flux of the high frequency components does not become negligible at 25 kHz in spite of the substantially reduced wave intensity but instead slowly diminishes with increasing frequency. For instance, for typical parameters at  $L \sim 1.5$  and a wave normal angle  $\theta \sim 45^\circ$ , 25 kHz and 40 kHz wave frequency components resonate with  $\sim 310$  keV and  $\sim 170$  keV electrons respectively. Consideration of wave frequency components above  $\sim 40$  kHz is unnecessary in our example, since resonant energies fall below 150 keV, which is the detection threshold of the SAMPEX satellite particle detectors.

To quantify the effect of the increased bandwidth upon the precipitation signature, we show in Figure 3.8d results for the case when the simulated wave frequency spectrum is extended to 40 kHz. We see that the higher frequency wave components contribute only to the narrow, low  $L$ -shell precipitation maximum since their frequency is too high for them to magnetospherically reflect, and thus contribute to

the high  $L$ -shell peak. As a result, the relative magnitudes of the low  $L$  narrow peak and the high  $L$  peak are now within about a factor of  $\sim 5$ , comfortably reproducing observed precipitation signatures. We note that since higher frequency components contribute only to the low  $L$  peak, the shape of the wave spectrum radiated by lightning essentially controls the relative magnitudes of the low  $L$  and high  $L$  peaks. For example, if the low  $L$  and high  $L$  peaks are very close together in magnitude we might conclude that the source was a relatively rapid lightning discharge producing significantly more power at high frequencies.

It should be mentioned that in the above model, the trapped electron flux at the loss-cone boundary is assumed to be constant with  $L$ -shell. The trapped flux levels for energetic particles can in fact exhibit substantial variations with  $L$  as shown in Figure 5.10, but this variation is highly dependent on geomagnetic conditions [West *et al.*, 1981] and for simplicity is left out of the formulation at this stage. Nevertheless, results for any given variation of trapped flux with  $L$ -shell can be inferred from those presented here since the precipitated flux is linearly proportional to the trapped flux level at the edge of the loss cone (thus, for a particular precipitation versus  $L$ -shell signature e.g., Figure 3.8c, one simply needs to multiply this curve by the particular trapped flux versus  $L$ -shell variation).

### 3.5 Discussion and model limitations

The work presented in this chapter has dealt with the interpretation of a new type of  $L$ -dependent precipitation signature measured in the drift loss cone by the SAMPEX satellite. Using numerical ray tracing and a first order model for the wave-particle interaction, we have shown that the observation is consistent with that of a single lightning stroke that radiates VLF wave energy into the magnetosphere in the form of a nonducted, magnetospherically reflecting whistler mode wave.

The narrow precipitation peak observed at low  $L$ -shells is attributed to the first equatorial crossing of the whistler wave, and underscores the importance of ionospheric horizontal density gradients, which can focus or defocus wave energy. While waves

from a certain lightning location might be focused by the overhead horizontal density gradients, waves from lightning discharges at other locations would be defocused and their contributions would not be significant. Thus the presence and intensity of the low  $L$ -shell peaks depends on the particular distribution of lightning sources and ionospheric density gradients in effect at any given time.

The broad precipitation maximum observed at higher  $L$ -shells seems to be robustly present in both model calculations and in SAMPEX observations, and is formed due to the second and subsequent hops of the MR whistlers. This agreement of theory and observation provides insight into a number of related topics. First, the lifetime of MR whistlers in the magnetosphere is implied to be far longer than originally estimated by *Thorne and Horne* [1994] who used thermal particle data from the OGO 3 satellite, as we show in the following chapter. Recent measurements made with the HYDRA instrument aboard the POLAR satellite [*Bell et al.*, 2002] at the  $L$ -shells of interest have shown consistently lower fluxes of thermal electrons, supporting the notion that Landau damping is indeed less severe and lifetimes of MR whistlers are longer than originally thought. Secondly, due to the demonstrated ability of MR whistlers to scatter energetic electrons and implied longer lifetimes, we believe that the partial contribution of lightning generated MR whistlers to the pitch-angle diffusion rates of radiation belt electrons may have been underestimated in past work [*Abel and Thorne*, 1998*a,b*]. Thus correct inclusion of the effects of these waves could significantly alter the  $L$ -dependent equilibrium distribution functions and lifetimes of energetic electrons.

The model used in the work presented above has inherent limitations that must be taken into account when interpreting the results. First, the equation used to describe the scattered flux due to a wave-particle interaction is only a first order approximation to the far more complicated set of differential equations of motion describing a particle moving through an oblique wave field [*Bell*, 1984], which is used in Chapter 6 for a complete determination of the MR whistler induced precipitation. While the crude method used in this chapter hides some of the microphysics of the interaction, we have found that the  $L$ -dependent precipitation signature varies little with the degree of complexity of (3.1), and is essentially an indicator of whether wave

energy is present or absent near the geomagnetic equator at a given  $L$ -shell.

Equation (3.1) also assumes that precipitation is caused predominantly by first order gyroresonance interactions. The degree of validity of this assumption is demonstrated by quantitatively considering the contributions of higher order resonant interactions in Section 5.2.2. For now, we justify this assumption using two simple arguments. Firstly, higher order gyroresonance interactions involve particles of higher energies as shown in Figures 5.12 and 5.15, which are less abundant (Figure 5.9). For example, a 5 kHz wave at the geomagnetic equator,  $L = 2$ , with a wave normal of  $87.6^\circ$  interacts with particles of energies 196 keV, 604 keV, and 1066 keV in the first three resonance interactions ( $m = 1, 2, 3$ ) respectively. Assuming a phase space distribution  $\propto E^{-3}$  the relative abundances of particles at these energies are 1, 0.03, and 0.006 respectively (normalized to the first gyroresonance abundance). Secondly, higher order gyroresonance interactions are progressively less efficient at scattering electrons in pitch angle [Brinca, 1972],

The final limitation of our model calculations presented in this chapter is that the effects of Landau damping are included in an approximate way, by keeping the power of the ray constant until the -3 dB point (taken as the ‘effective lifetime’ of the ray), and setting the amplitude to zero thereafter. The effective lifetime is determined only for the center ray using the formulation of Brinca [1972] and suprathermal fluxes from Bell *et al.* [2002]. In reality, the wave power density is damped progressively along its trajectory as shown in Figure 4.1; however, since the rate of decay is much more rapid beyond the -3 dB point, our choice of this point as a convenient location to extinguish the ray is an appropriate assumption.

Having examined the effects of a single lightning event in the context of particle precipitation, we now wish to develop a comprehensive wave-particle interaction model. To achieve this, we begin by considering the development of a wave model that includes path-integrated Landau damping and which can be used to reproduce the wave characteristics of an MR whistler at any point in the magnetosphere, due to a lightning discharge located at any given latitude on Earth.

# Chapter 4

## Frequency-time spectra of MR whistlers

### 4.1 Introduction

In the previous chapter we used a first-order model for the wave-particle interaction to estimate the  $L$ -dependence of precipitating electrons driven by lightning generated MR whistler waves. Our aim in the next two chapters is to develop a more exact treatment of the wave-particle interaction so as to more accurately determine the wave-induced pitch-angle scattering resulting from a range of harmonic gyroresonance interactions and to extend the prediction capability of our model to include the detailed frequency-time ( $f-t$ ) signatures of the waves and temporal signatures and energy spectra of the wave-driven precipitation. These more extensive results are also used to validate our earlier estimates.

In this chapter we extend past work [*Edgar*, 1972; 1976] by introducing a numerical method allowing the determination, at any location in the magnetosphere, the observed  $f-t$  spectrogram resulting from a lightning discharge at any given latitude on Earth. Using the two-dimensional Stanford VLF ray tracing code (discussed in Section 2.3.4, and *Inan and Bell* [1977]) we calculate the trajectories of 5330 whistler rays that effectively sample the frequency spectrum of the lightning discharge and latitudinal spread of wave energy about the source, and then use these so-called “sample

rays” to create  $\sim 120$  million interpolated rays. Each interpolated ray is weighted with a measure of wave energy according to its frequency and injection latitude (Section 2.2) resulting from the combined effects of excitation (by lightning currents), propagation (in the Earth-ionosphere waveguide), and attenuation (due to trans-ionospheric propagation). The wave energy is then progressively attenuated along the ray’s trajectory as it propagates in the plasmasphere, in accordance with Landau damping calculated on the basis of realistic suprathermal electron fluxes (Section 2.5). The  $f-t$  spectrogram representative of what would be observed on a satellite located in a given region in the plasmasphere is constructed by defining a detection area and examining the rays that cross this region.

We investigate the role that the lightning source latitude, observation location, and plasmaspheric electron density distributions have on the appearance of the simulated  $f-t$  spectrograms and show that all three parameters lead to distinct and well-defined  $f-t$  features. In particular, we focus on various plasmaspheric electron density structures and explain the connection between these structures and the appearance of specific observed features in the  $f-t$  spectrograms. Using the analysis presented in this Chapter, it may be possible to infer certain features of the source (e.g., latitude) and plasmaspheric density profiles from observed MR whistler spectrograms.

The bulk of the work presented in this chapter has been published [*Bortnik et al.*, 2003b] but is presented here for completeness with clarifications and expansions as appropriate for a Ph.D. dissertation.

## 4.2 Description of the model

To represent the plasmaspheric distribution of VLF waves due to a single lightning discharge, the trajectories of 41 rays injected over a  $\pm 10^\circ$  geomagnetic latitude range about the source are numerically computed for each frequency component using the two-dimensional Stanford VLF raytracing code (discussed in Section 2.3.4 and *Inan and Bell* [1977]). For example, to simulate a lightning source latitude of  $35^\circ$ , rays are injected over the range of  $25^\circ$  to  $45^\circ$  spaced  $0.5^\circ$  apart in latitude, compared with the wave model used in our approximate treatment in Chapter 3 where we only



considered an illumination region  $\pm 5^\circ$  about the source.

Each injected ray is initially assigned a power density (discussed in Section 4.2.1) consistent with the lightning frequency spectrum, the attenuation experienced by the wave during propagation in the Earth-ionosphere waveguide, and the subsequent trans-ionospheric propagation loss. To represent the lightning spectrum in the VLF range of interest, 130 frequency components spaced approximately logarithmically between 200 Hz and 60 kHz are used. The resulting 5330 rays thus form the “sample rays” between which interpolation is performed as described in Section 4.2.5. The Landau damping of each sample ray is calculated continuously along its trajectory as described in Section 4.2.2, and the wave energy represented by the rays that cross a given magnetospheric region is recorded and used in the construction of the  $f-t$  spectrogram at that observation point. The calculation procedure is discussed in greater detail below.

#### 4.2.1 Wave power density at the point of injection of rays

To compute the wave power density at the injection altitude (1000 km) and latitude of the whistler rays, we used the methodology described in Section 2.2 to obtain an array of power density values  $S(f, \lambda, \lambda_s)$ , the entries of which are dependent on the frequency  $f$  and latitude  $\lambda$  and represent the wave power density at 1000 km due to a lightning discharge at a source latitude  $\lambda_s$ .

Since we are considering a transient impulsive signal injected by a lightning discharge, we assume that each ray carries a portion of wave energy in accordance with the frequency spectrum described by (2.1). For this purpose, the initial wave power density represented by each ray at the top of the ionosphere  $S(f, \lambda, \lambda_s)$  is integrated with respect to space, frequency, and time. In performing the spatial integration we multiply the wave power density by the latitudinal extent of the ray converted to units of distance. The latitudinal extent follows from the number of rays injected per degree of latitude, and hence the latitudinal range that each ray is intended to represent. Since we use two-dimensional ray tracing, we cannot integrate the wave power with respect to a longitudinal extent. Instead, we assume azimuthal symmetry

and let the wave energy density (i.e., energy per meter of longitudinal arc-length) vary in inverse proportion to the arc-length of the thin longitudinal slice in which we assume the wave energy to be contained. Similarly, integration with respect to frequency is carried out by multiplying the intensity of each frequency component as calculated by (2.1), with the bandwidth that it is intended to represent. Time integration is performed by assuming that the power of each frequency component was initially constant over a period of 200  $\mu$ s, and zero otherwise, consistent with a typical lightning waveform [Uman, 1987, p.124]. It is important to note that in both frequency and spatial-extent, the above-mentioned integrations are performed after interpolation between sample rays.

#### 4.2.2 Deposition of MR wave energy at frequency-specific $L$ -shells

As mentioned above, lightning generated whistler waves injected into the magnetosphere typically contain a continuum of frequencies in the ELF/VLF bands, assumed to be 200 Hz–60 kHz in our case. If the various frequency components of the whistler were to propagate in the magnetosphere indefinitely without being damped, each wave frequency component would migrate within a few seconds to a “preferred”  $L$ -shell region, and subsequently slowly (tens of seconds) settle on a particular  $L$ -shell within that region in which the wave frequency is approximately equal to the equatorial lower hybrid resonance (LHR) frequency (this type of behavior of the whistler mode ray paths was discussed previously by *Thorne and Horne* [1994], *Ristic'-Djurovic' et al.* [1998], and references therein). In this context, the magnetosphere resembles a resonant cavity to whistler-mode waves, with one difference from a metallic cavity being that at the reflection points it is the transverse (relative to the ambient magnetic field direction) component of the wave magnetic field that vanishes, rather than the electric field.

The ray path behavior described above is illustrated in Figure 4.1 where we contrast rays for two frequency components, 500 Hz (left column) and 5 kHz (right column) injected at 25° geomagnetic latitude. The rows show the ray path in a

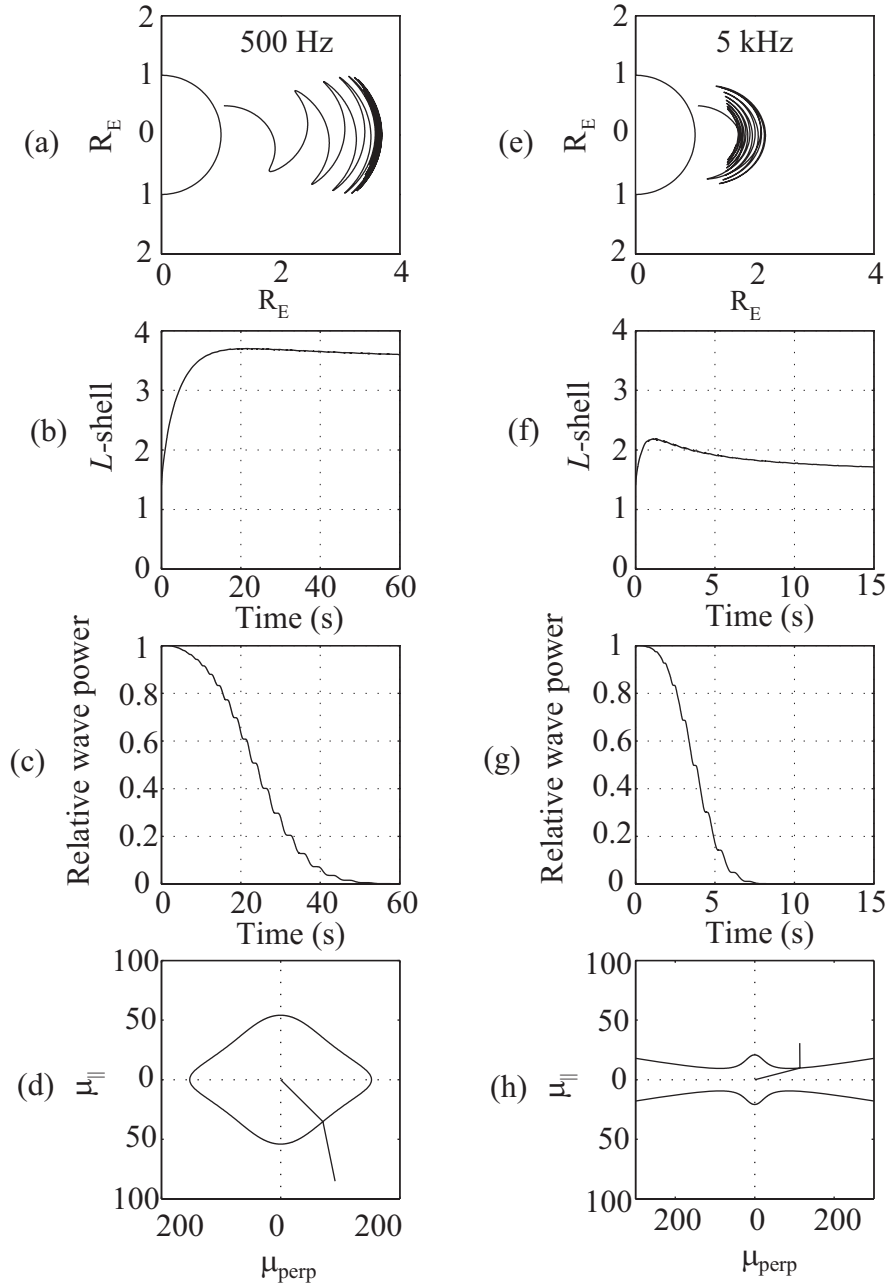


Figure 4.1: MR whistler ray path properties of two frequency components, left column: 0.5 kHz, right column 5 kHz; (a) and (e) ray paths, (b) and (f) ray's local  $L$ -shell as a function of time, (c) and (g) power density decrease due to Landau damping, (d) and (h) typical refractive index surfaces showing a closed surface on the second equatorial crossing (d), and open surface on the sixth equatorial crossing (h).

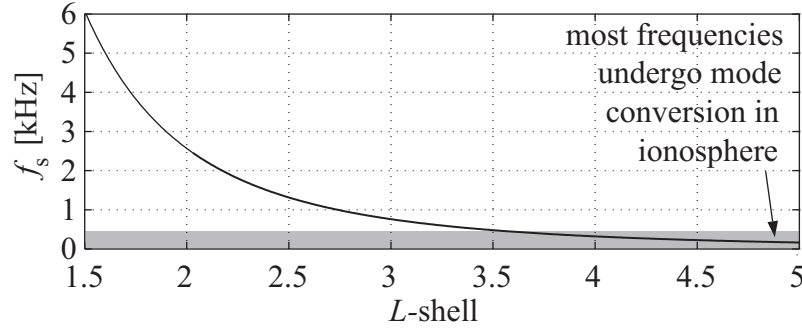


Figure 4.2: Settling frequencies  $f_s$  as a function of  $L$ -shell.

meridional slice (row 1), the  $L$ -shell of the ray as a function of time (row 2), the relative wave power density as a function of time (row 3), and a typical refractive index surface of the ray (row 4). As shown in Figure 4.1b, the 500 Hz ray starts at  $L \simeq 1.4$  ( $\lambda_s = 25^\circ$  at 1000 km altitude), migrates to higher  $L$ -shells, and then slowly converges on its specific settling  $L$ -shell of  $L \simeq 3.45$ . For comparison, Figure 4.1e shows the 5 kHz frequency component initially overshooting its specific settling  $L$ -shell and then slowly moving to lower  $L$ -shells until it settles at  $L \simeq 1.6$ . We note that for injection at mid-latitudes, some frequency components move predominantly from lower to higher  $L$ -shells (e.g., Figure 4.1a,b), whereas others move predominantly from higher to lower  $L$ -shells (e.g., Figure 4.1e,f). Thus, each  $L$ -shell is associated with a particular frequency component  $f_s$  that is most likely to settle there, with  $f_s$  being approximately equal to the equatorial lower hybrid resonance frequency  $f_{\text{LHR}}$  of that  $L$ -shell. A plot of  $f_s$  (or alternatively the equatorial LHR frequency) as a function of  $L$ -shell is shown in Figure 4.2.

### 4.2.3 Lifetime of MR whistler waves

The damping due to Landau resonance interactions between whistler waves and suprathermal electrons (Landau damping) is computed using the formulation of *Brinca* [1972] presented in Section 2.5, with a distribution function of suprathermal electrons given by:

$$f(v) = \frac{2 \times 10^5}{v^4} \quad [\text{cm}^{-6}\text{s}^3] \quad (4.1)$$

where  $v$  is the electron velocity measured in units of  $\text{cm s}^{-1}$ . This distribution represents an approximate numerical fit to recent measurements made with the HYDRA instrument on the POLAR satellite [Bell *et al.*, 2002] of electrons in the range 300 eV–2 keV, which are the particles most heavily involved in the Landau damping of the wave. For reference, the corresponding flux values are  $j(1 \text{ keV}) = 10^5$  and  $j(300 \text{ eV}) = 3 \times 10^5 \text{ cm}^{-2}\text{s}^{-1}\text{sr}^{-1}\text{keV}^{-1}$ . It should be noted that the above flux values are substantially lower than those used by Thorne and Horne [1994] in their study. This discrepancy is discussed by Bell *et al.* [2002] and appears to be due to the fact that the model fluxes for  $L < 4$  used by Thorne and Horne [1994] were based on spacecraft measurements made on a few passes in the outer plasmasphere ( $L > 5.3$ ), whereas the fluxes given by Bell *et al.* [2002] represent an average of many satellite observations in the region  $2.3 < L < 4$  which is most appropriate for MR whistler propagation. As a result of Landau damping, the wave power along the ray path varies as  $P = P_0 \exp(-2 \int k_i ds)$ , where  $P_0$  is the power at the injection point,  $k_i$  is the component of the imaginary part of the wave vector  $\mathbf{k}$  directed along the ray path, and  $ds$  is an element of distance along the ray path. The quantity  $k_i$  is computed at each time step for each ray using the formulation discussed in Section 2.5 [Brinca, 1972]. Subsequent integration of  $k_i$  with respect to the distance traversed by the ray leads to the variation of the wave power density along the ray path. The real part of the refractive index  $\mu$  (used to evaluate  $k_i$ ) is calculated by the VLF ray tracing code [Inan and Bell, 1977] using the cold plasma approximation, which tends to slightly overestimate  $\mu$  when the wave normal is very close (within  $\sim 0.1^\circ$ ) to the resonance cone (where it would otherwise be bounded by thermal effects). Our cold-plasma assumption thus leads to increased damping, and hence the MR whistler lifetime values discussed below should be viewed as a lower bound to actual lifetimes, which can be evaluated with the inclusion of thermal effects.

To examine the effects of Landau damping, we launch rays from four assumed lightning source locations ( $\lambda_s = 25^\circ, 35^\circ, 45^\circ$ , and  $55^\circ$ ) at an altitude of 1000 km with

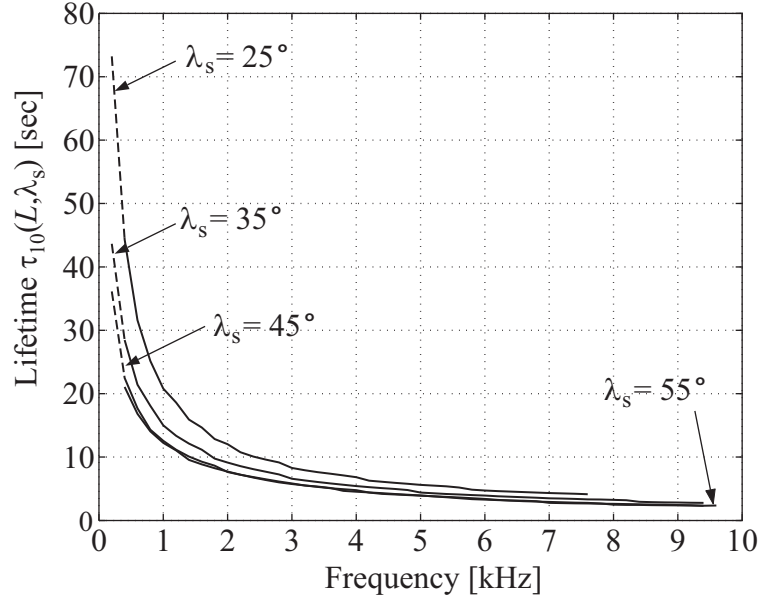


Figure 4.3: MR whistler lifetime (defined as the time when the wave power density along the ray path is diminished by 10 dB) plotted as a function of wave frequency, parameterized in injection latitude (showing  $\lambda_s = 25^\circ$ ,  $35^\circ$ ,  $45^\circ$ , and  $55^\circ$ ).

vertical wave normal angles, and from each location we trace rays in the frequency range 0.2–10 kHz in a smooth magnetosphere modeled after *Carpenter and Anderson* [1992] under geomagnetically quiet conditions ( $K_p \simeq 0$ , resulting in the plasmapause location of  $L \simeq 5.5$ ). We compute the Landau damping along the path of each ray, note the time at which its power density is reduced by a total of 10 dB relative to its initial power density, and designate this value as the lifetime  $\tau_{10}(f, \lambda_s)$  of this particular ray. For example the lifetimes of the 0.5 kHz and 5 kHz rays injected at  $\lambda_s = 25^\circ$  are  $\sim 37$  sec, and  $\sim 6$  sec respectively, as can be inferred from Figure 4.1c and 4.1g. It should be noted that in calculating the lifetimes of individual rays, only wave power dissipation due to Landau damping is considered. Geometrical effects such as spreading or focusing losses (or gains) are accounted for through the behavior of the full set of  $\sim 120$  million rays (Section 4.2.5).

Lifetimes calculated as described above are shown in Figure 4.3. Waves at lower frequencies ( $\leq 1$  kHz) have dramatically longer lifetimes than those at the higher frequencies, with the 200 Hz component launched at  $\lambda_s = 25^\circ$  lasting over 70 seconds.

We note that wave frequency components below  $\sim 400$  Hz are plotted as dashed lines to indicate that in order to propagate up to the radiation belts, they would have to undergo mode conversion from the left-hand polarized ion cyclotron mode into the right-hand polarized whistler mode in the ionosphere. Such mode coupling has been both experimentally observed [Rodriguez and Gurnett, 1971] and theoretically explained in previous work [Arantes and Scarabucci, 1975]. Nevertheless, when considering absolute power levels of such low frequency wave components it is necessary to account for the power loss due to imperfect mode coupling, the determination of which is beyond the scope of this work. The lifetimes of MR whistlers decrease as the injection latitude of the rays is increased, regardless of the wave frequency. For injection latitudes lying in the range  $25^\circ$  to  $45^\circ$ , the lifetime of MR whistlers can be approximately expressed analytically as a function of wave frequency  $f$  (in kHz), and injection latitude  $\lambda_s$  (in degrees) as:

$$\tau_{10}(f, \lambda_s) \simeq \frac{9 + 2^{6.1-0.1\lambda_s}}{f^{0.925-0.005\lambda_s}} \quad (4.2)$$

which is useful in simpler formulations that only require a ray lifetime at which rays can be terminated, as we have done in Chapter 3 using the  $-3$  dB point.

To understand the frequency and injection latitude dependence of MR whistler lifetimes, we refer to Figure 4.2, which shows the equatorial LHR frequency (which is also the frequency  $f_s$  of waves which eventually settle at this  $L$ -shell) as a function of  $L$ -shell. In order to settle at the appropriate  $L$ -shell, a wave component at a given frequency propagates predominantly to either higher or lower  $L$ -shells relative to the  $L$ -shell of injection. In propagating from lower to higher  $L$ -shells, the wave frequency remains almost entirely below the LHR frequency, with the result that the wave refractive index ( $\mu$ ) surface is closed, the magnitude of  $\mu$  is therefore bounded, and stays at relatively low values as shown in Figure 4.1d. If on the other hand, the ray path moves from higher to lower  $L$ -shells, the wave frequency remains above the LHR frequency, with a corresponding refractive index surface that is open (unbounded), resulting in potentially very large values of  $\mu$ . To move to lower  $L$ -shells, the  $\mathbf{k}$ -vector of the ray extends beyond the Gendrin angle [Edgar, 1972] and remains very close

( $< 1^\circ$ ) to the resonance cone, where it is typically large ( $\sim 100 - 1000$ ). The large values of  $\mu$  in turn imply lower phase (and group) velocities, which cause the waves to resonate with lower energy particles of which there are many more (a condition necessary for Landau damping) than higher energy particles, thus resulting in more significant damping.

For rays injected from  $\lambda_s \geq 45^\circ$  latitude and for the 200 Hz to 10 kHz frequency range shown in Figure 4.2, ray paths for all of the frequency components need to move from higher to lower  $L$ -shells, resulting in overall high  $\mu$  values, increased damping rates, and decreased MR whistler lifetimes. Note from Figure 4.3 that the lifetimes of rays injected at  $\lambda_s = 45^\circ$  and  $\lambda_s = 55^\circ$  are very similar. For the lower injection latitude of  $\lambda_s = 35^\circ$ , some of the frequency components need to move to higher  $L$ -shells to reach their settling  $L$ -shells, and since these are primarily the low frequency components, their lifetimes are dramatically longer, whereas the lifetimes of the higher frequency components ( $f \geq 5$  kHz) differ only slightly from the  $\lambda_s \geq 45^\circ$  injection cases. For the lowest injection latitude of  $25^\circ$ , rays for most of the frequency components considered move from lower to higher  $L$ -shells, resulting in significantly larger lifetimes. An additional effect, which accounts for the slight differences between the  $\lambda_s = 45^\circ$  and  $55^\circ$  cases, is that rays launched from higher latitudes damp more rapidly (i.e.,  $k_i$  stays at higher values for a longer portion of the ray path) since they initially follow longer geomagnetic field lines.

#### 4.2.4 Detection of whistler waves at an observation point

Before discussing the interpolation between rays, it is instructive to first consider how the wave properties carried by such rays are to be recorded at a given observation location. For this purpose, we define a small detection area oriented perpendicularly to the magnetic field line (in particular we confine our attentions in this chapter to the magnetic equatorial plane), centered on a given  $L$ -shell, and having a given  $L$ -shell extent (discussed below). After every time-step in the course of our ray tracing calculations, we check whether either of the sample rays or interpolated rays have crossed the detection area. If so, a few key parameters of the ray are recorded into a



file, such as the time of crossing, frequency, injection latitude, fractional wave energy carried by the ray, and wave normal angle.

The key parameter to be chosen in such a formulation is the spatial extent of the detection area. This choice is bounded by the following two constraints: if the detection area is chosen to be too small, a sufficiently large number of rays (typically several thousand in our simulations) do not cross it to subsequently produce a meaningful  $f-t$  spectrogram. If on the other hand, the detection area is chosen to be too large, the derived spectrum no longer represents the wave spectrum as observed at a ‘single’ point in space (e.g., as would be measured on a satellite), and our measured quantity may thus not necessarily remain uniform over the extent of the region chosen. The net result of choosing a detection area that is too large would be a ‘smearing’ of the spectrogram in both frequency and time. This smearing can be understood by considering a wave front at a particular frequency (say  $f_0$ , shown in Figure 4.4, in connection with the interpolation discussion) impinging obliquely upon the detection area oriented along the magnetic equator. The smearing in time depends on the difference in arrival times of the first and last ray to cross the detection area. If the detection area is large, this time difference is large.

In fact, time smearing is unavoidable and occurs for any detection area of finite extent. The criteria which we employ for the choice of this parameter is to ensure that the smearing in time is much smaller than the width of the time-bin used to construct our spectrogram. We briefly note in this connection that the resolution we choose for the  $\Delta f - \Delta t$  bins in our frequency-time spectrograms sets an upper limit on the size of the detection area we employ to detect the rays, and this size, in turn, dictates the number of rays necessary for the simulation (i.e., we need to trace more ray paths if the detection area is small, to ensure that a sufficiently large number of rays cross it), and hence the degree of interpolation. The detection area chosen for the simulation results presented herein is approximately 5 km ( $\sim 0.0008L$ ) in extent ensuring a resolution of  $\Delta t < 7$  ms in the  $f-t$  spectrograms produced.

We note that in launching the rays, the wave energy represented by each ray is determined by integration over its latitudinal extent. As was noted in Section 4.2.1, since we use two-dimensional ray tracing, we account for wave-energy spreading

in the azimuthal direction by assuming that the wave energy is contained within (and uniformly distributed over) a thin longitudinal slice. The energy density (i.e., Joules per meter of longitudinal arc-length) carried by each ray thus varies in inverse proportion to the arc length of the longitudinal slice at any point along the ray path. When the rays cross the detection area, we divide energy density by the extent of the detection area (5 km) to convert to units of J/m<sup>2</sup>. Subsequent division by  $\Delta f$  and  $\Delta t$  during the production of the spectrogram results in the appropriate units for wave power spectral density of W/m<sup>2</sup>/Hz. We note that the precise value of the detection area is not critical so long as it remains within the bounds described above. If it is made larger, many more rays cross it, and are divided by a larger area, thus yielding a similar power density, and vice versa.

#### 4.2.5 Interpolation between sample rays

We now discuss the interpolation scheme that is used to generate a large number of rays (i.e., 100 million) from the 5330 sample rays used in our simulation. As noted in Section 4.2.4, the detection area through which rays must cross in order to be recorded onto the spectrogram is limited in spatial extent, in the present case to 5 km. Although this detection area is large compared to the physical dimensions of satellite-borne VLF electric field antennas (typically a few hundred meters tip-to-tip), it is nevertheless extremely small on magnetospheric scales, representing  $\sim 8 \times 10^{-4} R_E$ , and consequently, the probability of a particular ray crossing any given detection area is extremely small. Further, we have found that in order to produce well defined spectrograms, a total of  $\sim 10,000$  rays must cross the detection area in the course of the simulation run. When this fact is combined with the low probability of a single ray crossing the detection area, it is clear that we are required to simulate a very large number of rays,  $\sim 10-100$  million, in order to have enough rays to construct a meaningful spectrogram.

Computing the trajectories of 100 million individual rays with the inclusion of Landau damping would require a prohibitively long computation time. Fortunately, the general parameters associated with rays vary smoothly with wave frequency and

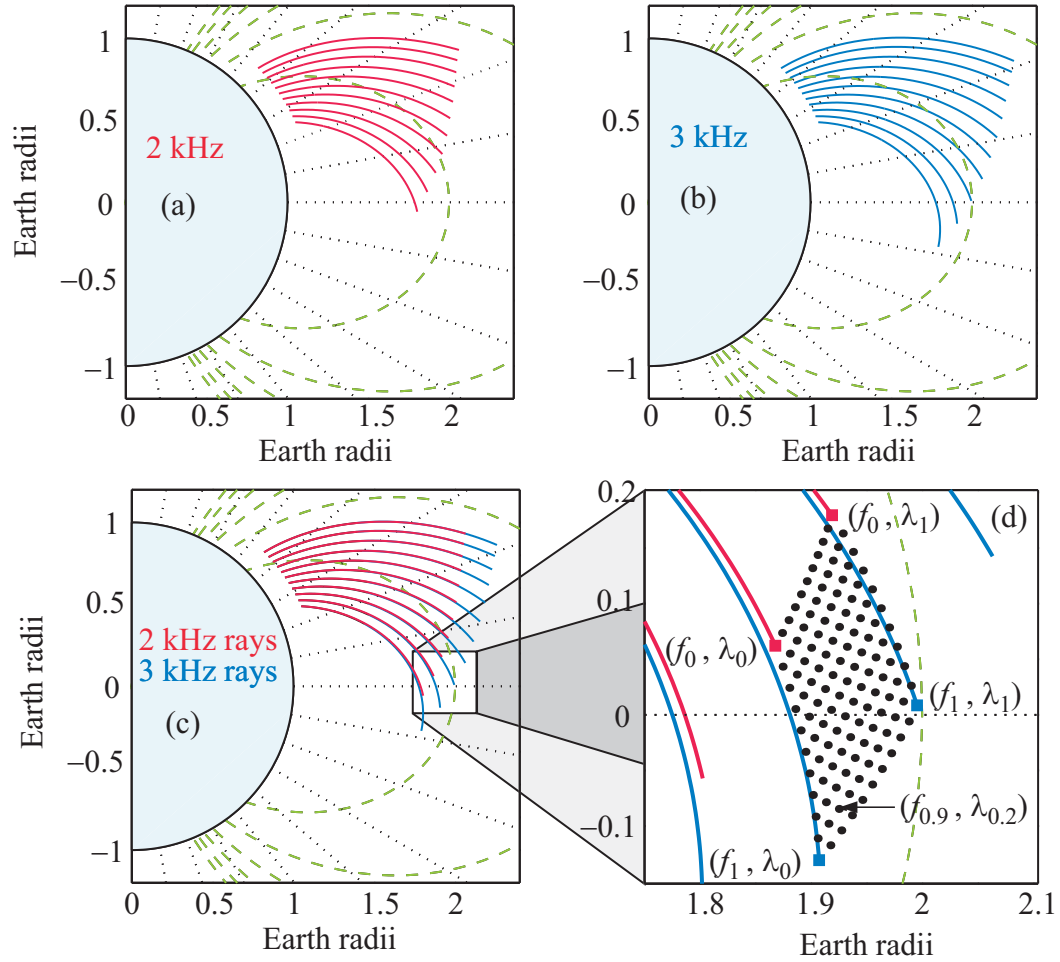


Figure 4.4: Interpolation scheme illustrated. (a) 2 kHz frequency component at 0.3 sec after the lightning discharge, showing 11 rays in a  $\pm 10^\circ$  latitudinal spread about the source at  $\lambda_s = 35^\circ$ , (b) as in (a) but for a 3 kHz frequency component, (c) 2 kHz and 3 kHz frequency components overlaid at 0.3 sec, and (d) a blow-up of 4 adjacent rays, illustrating 100 interpolated rays, and an example of one interpolated ray with the nomenclature used in the text.

injection latitude, thereby allowing us to appropriately sample the spatial extent and frequency spectrum of the source lightning discharge with a smaller number of rays (referred to as “sample rays”), and determine the remainder of the rays via interpolation among the sample rays.

The interpolation scheme we employ is illustrated in Figure 4.4, where we consider a lightning discharge at  $35^\circ$  latitude, and model the spreading in the Earth-ionosphere waveguide in the region  $\pm 10^\circ$  about the source, extending from  $25^\circ$  to  $45^\circ$ , sampled every  $2^\circ$  resulting in 11 rays for every frequency component (this low number of rays is used here for illustration purposes only). Note that wave energy would undoubtedly propagate farther in the waveguide, and would thus be injected at points outside the  $\pm 10^\circ$  range, but with steadily decreasing intensity. In our modeling we choose  $\pm 10^\circ$  because the wave intensity  $B^w$  (which is the parameter that controls the pitch-angle deflection of resonant particles) is diminished by approximately 10 dB at  $\pm 10^\circ$  away from the source latitude. In panel (a) we show the 2 kHz sample rays traced for a time of 300 ms after the lightning discharge, injected at 1000 km with nominally vertical wave normal angles. In panel (b) the 3 kHz wave frequency component is shown in the same manner as in panel (a), illustrating the spatial dispersion (i.e., the separation in space) experienced by individual frequency components. In panel (c) we overlay the 2 kHz and 3 kHz frequency components (each frequency component having 11 sample rays) and in panel (d) we show an expanded plot of the 4 adjacent sample rays together with the interpolated rays all traced up to the time of 300 ms after the discharge.

We label the rays belonging to the lower frequency  $f_0$  and those of the higher frequency  $f_1$ , and similarly the rays launched at the lower latitude and higher latitude as  $\lambda_0$  and  $\lambda_1$  respectively, and thereby obtain the four guiding-ray end-points for our interpolation, namely  $(f_0, \lambda_0)$ ,  $(f_0, \lambda_1)$ ,  $(f_1, \lambda_0)$ ,  $(f_1, \lambda_1)$ . If the frequencies and launch latitudes are chosen sufficiently close together (as outlined below), any interpolated ray of frequency  $f_i$  such that  $f_0 \leq f_i \leq f_1$  injected at a latitude  $\lambda_i$  such that  $\lambda_0 \leq \lambda_i \leq \lambda_1$  is contained within the quadrilateral formed by the guiding points. Further, we let  $n_f$  be a number between 0 and 1 representing the interpolated frequency  $f_i$ , where 0 corresponds to  $f_0$  and 1 corresponds to  $f_1$ , and similarly we let  $n_\lambda$  be a number between

0 and 1 representing the interpolated launch latitude  $\lambda_i$ , 0 and 1 corresponding to  $\lambda_0$  and  $\lambda_1$  respectively. Thus any interpolated quantity  $g_i$  can be obtained by the linear scaling:

$$g_i = a_1 g(f_0, \lambda_0) + a_2 g(f_0, \lambda_1) + a_3 g(f_1, \lambda_0) + a_4 g(f_1, \lambda_1) \quad (4.3)$$

where:  $a_1 = 1 - n_\lambda - n_f - n_\lambda n_f$ ,  $a_2 = n_\lambda - n_\lambda n_f$ ,  $a_3 = n_f - n_\lambda n_f$ , and  $a_4 = n_\lambda n_f$ .

Spatial interpolation is performed using  $\lambda$  and  $L$ -shell parameters since these give by far the most accurate and robust fits. Other interpolated quantities are ray energy and wave normal angle. It is also important to mention that interpolations are performed at fixed times, stepped in intervals of 0.4 ms, representing ‘snapshots’ of the endpoints of the traced rays, with all of the interpolated rays contained between the sample rays at those instants.

The example shown in Figure 4.4 has very coarsely spaced sample rays for purposes of illustration. In our simulations, we have chosen to sample the  $\pm 10^\circ$  region about the source with rays spaced every  $0.5^\circ$  in latitude, resulting in 41 rays per frequency component. The assumed 200 Hz to 60 kHz lightning frequency spectrum was sampled with 130 frequency components differing from each other by no more than 5%. The sampling process results in  $(130 \times 41 =)$  5330 sample rays. To obtain the total number of rays we interpolate the latitude range at every  $0.01^\circ$ , and the frequency spectrum at every 1 Hz, effectively resulting in  $\sim 120$  million rays.

#### 4.2.6 Construction of the frequency-time spectrogram

The frequency-time spectrogram is constructed by defining a two-dimensional array, with time and frequency being the abscissa and ordinate respectively. The variables to choose are total duration,  $t_{\max}$ , and highest frequency  $f_{\max}$ , for which the spectrogram is constructed, as well as the width of frequency and time bins,  $\Delta f$  and  $\Delta t$ . Using  $t_{\max}$  and  $\Delta t$ , as well as  $f_{\max}$  and  $\Delta f$ , we determine the number of bins required for each of the axes, and hence the size of the array. Although  $\Delta f$  and  $\Delta t$  can, in principle, be chosen arbitrarily, they are bounded on the low end by the physical constraint  $\Delta f \Delta t \geq 1$ , and on the high end by a decrease in resolution of the resulting whistler

traces. For our displays we use  $\Delta t = 50$  ms and  $\Delta f = 50$  Hz, resulting in  $\Delta f \Delta t = 2.5$ .

The data obtained using the methodology outlined in Section 4.2.4 is processed so that the wave energy represented by each ray is added into the appropriate  $f-t$  bin, and subsequently each bin is divided by  $\Delta f$  and  $\Delta t$  to give the correct units of  $\text{W/m}^2/\text{Hz}$ . The division by  $\Delta f$  and  $\Delta t$  is necessary to ensure that the correct average power appears at every  $\Delta f$ - $\Delta t$  bin, regardless of the  $\Delta f$  and  $\Delta t$  values chosen for the creation of the particular spectrogram, and is consistent with the a-priori integration of power-density with respect to frequency, space, and time at the injection point of the ray.

#### 4.2.7 Plasmaspheric medium

Since we consider the effects of different cold plasma density structures in this work, special mention must be made of the plasmaspheric medium through which the rays are traced in the context of this chapter. As discussed in Section 2.3.3, the ‘smooth’ plasmaspheric medium is described using a standard dipole model for the magnetic field, appropriate for our  $L$ -shells of interest ( $L \lesssim 4$ ), and a cold plasma electron density model based on typical observed equatorial profiles [*Carpenter and Anderson*, 1992] and the diffusive equilibrium formulation [*Angerami and Thomas*, 1964] shown in Figure 4.10a. In terms of the notation used by *Carpenter and Anderson* [1992] the profile we used is modeled for the conditions,  $d = 0$ ,  $t = 2$ ,  $K_{\text{p(max)}} = 4$ ,  $R = 90$  representing moderate geomagnetic activity, and is given by (2.15a)–(2.15d).

The density features we focus on, shown in Figure 4.10c and 4.10d, are obtained using one or two sided Gaussian ducts as described by *Bernhardt and Park* [1977] and spaced in accordance with occurrence statistics based on data from the ISEE 1 spacecraft [*LeDocq et al.*, 1994]. These non-smooth plasmaspheric density profiles are discussed in greater detail in Section 4.4.

### 4.2.8 Model validation

We have used many of the published MR whistler traces observed on various spacecraft in our model validation process, and have found excellent agreement. The observations made aboard the Magion 4 and 5 satellites [Shklyar and Jiricek, 2000] exhibit the spectral forms predicted by our code for both low and high latitude sources, and Edgar [1972] shows examples of MR whistlers produced by plasmaspheric density structures with a smooth portion below, and a distorted portion above the whistler “nose frequency” as discussed in Section 4.4.2 and shown in Figure 4.9.

As an illustration, we have chosen to simulate arguably the best-known MR whistler spectrogram from Smith and Angerami [1968], shown in Figure 4.5a. We use a standard diffusive equilibrium model, with an ionospheric composition at 1000 km altitude of 50%  $O^+$  and 50%  $H^+$ ,  $T=1380$  K, and the source latitude at  $\lambda_s=25^\circ$ , and have set our observing region to match the location of the satellite at  $L=2.4$ ,  $\lambda=5^\circ$  S. The simulation results are shown in Figure 4.5b, where we have also overlaid a scale outline of the MR whistler of panel (a). As can be seen, model results accurately reproduce frequency-time features evident on the observed spectrogram. Since the recorded wave power levels aboard OGO 1 were controlled by the rapid (typically  $<1$  ms) automatic gain control (AGC) of the receiver, the lower portion of the second component (labeled as  $1_+^{MR}$ ) is suppressed due to the arrival of the more intense “nose” of the third component  $3_-^{MR}$ . In addition, the observed spectrogram overlays the most intense (red) portions of our simulated spectrograms as would be expected. Beyond 3 sec, the observed MR whistler seems to decay faster than what our model predicts, possibly due to somewhat higher suprathermal particle fluxes on this day (leading to more rapid Landau damping) than our assumed average values, or alternatively due to the satellite moving into a more electromagnetically noisy environment where the AGC has suppressed the whistler signal. Since the AGC voltage of the receiver is not available to us, we cannot determine whether such gain variations were indeed in effect.

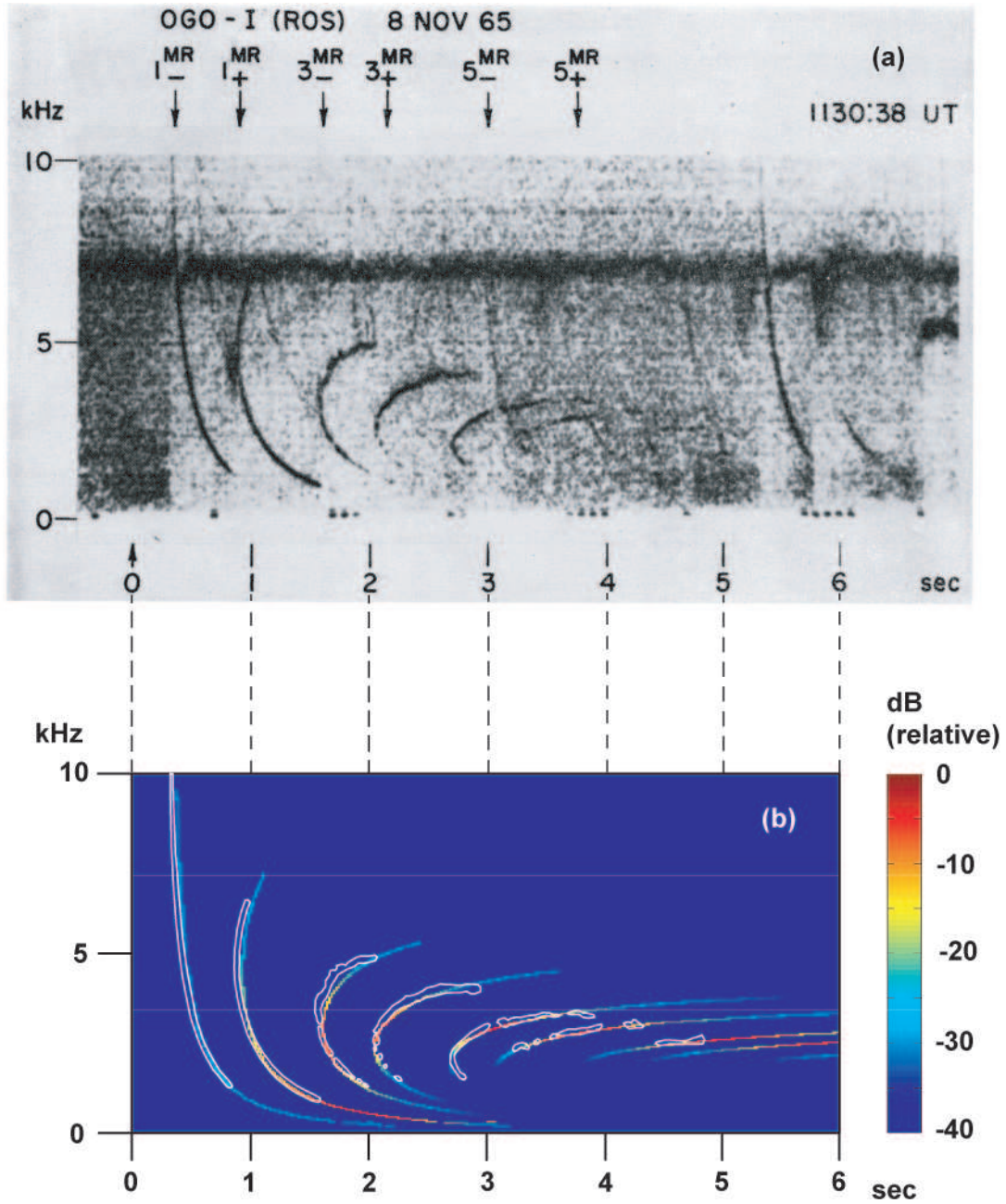


Figure 4.5: (a) Example of an MR whistler echo train observed aboard the OGO 1 satellite at  $L=2.4$  and  $\lambda=5^\circ$  S, and (b) a simulated spectrogram at the same location with a scale overlay of the MR whistler components of panel (a).



### 4.3 Smooth plasmasphere

We present the results for the case of a smooth plasmasphere with a plasmopause at  $L = 3.8$ , in Figure 4.6. The electron density profile is given in Figure 4.10a and is fitted to the model profile of *Carpenter and Anderson* [1992] as discussed above, and in Section 2.3.3.

The columns in Figure 4.6 represent frequency-time spectra arising from a given lightning discharge source latitude – from left to right:  $\lambda_s = 25^\circ, 35^\circ, 45^\circ$ , and  $55^\circ$ , while the rows represent particular observation locations along the magnetic equatorial plane at different  $L$ -shells – from top to bottom,  $L = 2, 2.5, 3, 3.5$ , and 4. In the discussion below we briefly review the general dispersion characteristics observed by previous workers, and then focus on wave damping, spatial dispersion, and other features particular to the case at hand.

#### 4.3.1 General observations

When viewing the power distribution of whistler waves in the plasmasphere as shown in Figure 4.6, certain features are readily apparent: the first is that the radiation is mostly contained within the plasmasphere, and even though some energy leaks out beyond the plasmopause to  $L = 4$ , the wave power levels are generally 30 to 60 dB weaker in this region, compared to the region immediately within the plasmopause at  $L = 3.5$ . The frequency range occupied by the whistlers moves to lower frequencies with increasing  $L$ -shell of the observation location due to the general tendency of ray paths to settle on those  $L$ -shells where the wave frequency is approximately equal to the equatorial lower hybrid resonance (LHR) frequency (as discussed in Section 4.2.2 and previous work [*Draganov et al.*, 1992; *Ristic'-Djurovic' et al.*, 1998; *Shklyar and Jiricek*, 2000]).

Whistlers at low  $L$ -shells tend to have a well-defined lower cutoff frequency due to the combination of the lightning source latitude, the limited injection latitude range [*Edgar*, 1976], and the tendency of the lower frequency components to propagate to higher  $L$ -shells. Such behavior was recently demonstrated with observations aboard the Magion 4 and 5 spacecraft [*Shklyar and Jiricek*, 2000].

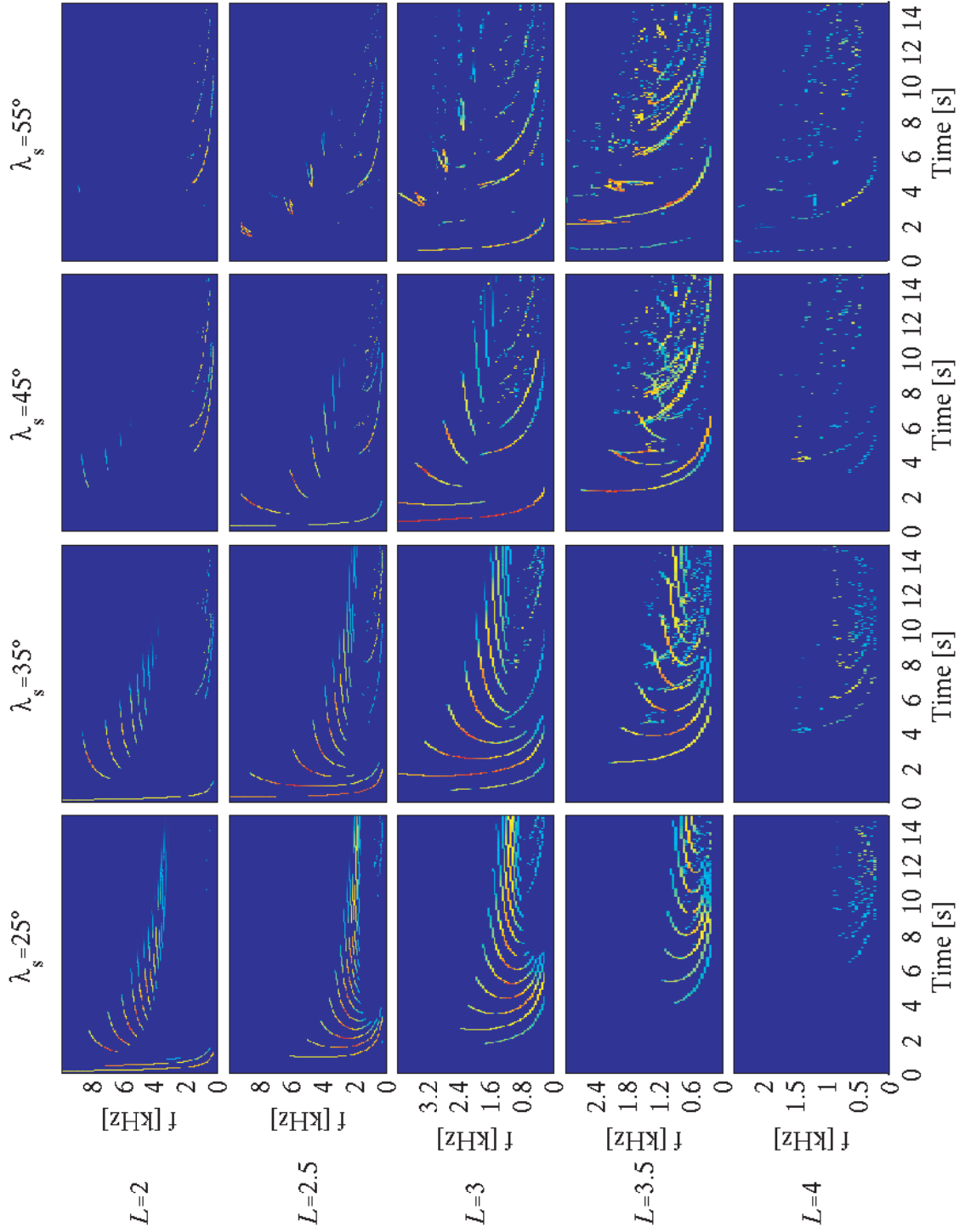


Figure 4.6:  $f-t$  Spectrograms obtained in a smooth plasmasphere (see Figure 4.10a density profile). The common color bar is shown in Figure 4.9.

The frequency band occupied by the whistlers (particularly at the beginning of the spectrogram) increases with increasing lightning source latitude, as does the time between subsequent hops. As discussed by *Shklyar and Jiricek* [2000] and noted by *Smith and Angerami* [1968], the nose frequency (i.e., the frequency of minimum group delay) of the MR whistler tends to decrease with time, and is also lower for lower lightning source latitudes. Somewhat puzzling features of whistler propagation can be seen in the traces for  $\lambda_s = 45^\circ$  and  $\lambda_s = 55^\circ$ , observed at  $L = 3.0$  and  $3.5$ , where we note the presence of additional lower frequency components having seemingly unrelated dispersion characteristics and appearing at irregular times. In addition, the  $\lambda_s = 55^\circ$  case shows high frequency components observed at  $L = 2.5$  and  $L = 3.0$  with peculiar dispersion characteristics. These features are due largely to reflections from the plasmopause boundary and are discussed further in Section 4.3.3.

### 4.3.2 Wave damping and spatial dispersion

In examining the power density and duration of MR whistlers for the case of  $\lambda_s = 25^\circ$  in Figure 4.6, we note that at low  $L$ -shells of observation, the wave power diminishes more rapidly than at higher  $L$ -shells. We show in Figures 4.9a and 4.9b the plots for  $\lambda_s = 25^\circ$ , observed at  $L = 3.0$  and  $L = 3.5$  respectively, similar to the corresponding plots of Figure 4.6, but with a 60 second time scale to emphasize the longevity of the MR whistler waves at these high  $L$ -shells. Note that the frequency band occupied by the whistlers diminishes with time, and the frequency components that tends to settle at a given  $L$ -shell (i.e., the “settling frequency”) is lower at higher  $L$ -shells corresponding to Figure 4.2. As noted above, the wave power persists for a longer time at  $L = 3.5$  than at  $L = 3$ . The intensity of the whistler waves, however, tends to decrease with increasing  $L$ . We note again from Figure 4.6 that in the  $\lambda_s = 25^\circ$ ,  $L = 2.0$  panel, six MR whistler components had intensities in the range 20 to 30 dB (dB is given relative to 1 pW/m<sup>2</sup>/Hz), whereas the  $\lambda_s = 25^\circ$ ,  $L = 3.5$  panel had no whistler waves with intensities in this range.

These observations are consistent with the findings reported by *Bortnik et al.* [2003a], who noted that there is a competition between increased lifetimes of MR

whistlers at higher  $L$ -shells, and higher initial power spectral density for MR components settling at lower  $L$ -shells, resulting in an MR whistler energy deposition maximum in the vicinity of the slot-region between the inner and outer radiation belts. *Bortnik et al.* [2003a] suggested that this maximized deposition of MR whistler wave energy near the slot region may be indicative of an important role played by MR whistler-induced precipitation in the formation of the slot-region.

We note that the tendency for longer lifetimes of MR whistler components at higher  $L$ -shells, and higher wave power intensities at lower  $L$ -shells seems to be independent of the lightning injection latitude as seen from the  $\lambda_s = 35^\circ$ ,  $\lambda_s = 45^\circ$ , and  $\lambda_s = 55^\circ$  columns in Figure 4.6. Figures 4.8 and 4.9 indicate that this trend is also largely independent of ionospheric and plasmaspheric electron density structures and thus appears to be a highly robust feature of MR whistler propagation controlled largely by the disposition of the Earth’s magnetic field.

### 4.3.3 Peculiar frequency-time features

Referring once again to Figure 4.6, we note that in addition to the expected MR components, there are additional features that appear, such as those seen for  $\lambda_s = 35^\circ$  and  $45^\circ$ , at  $L = 3.0$  and  $3.5$ . These features are largely due to reflections from the plasmopause boundary. To demonstrate that such is the case, we ran the  $\lambda_s = 35^\circ$  and  $45^\circ$  cases with the plasmopause moved out to  $L = 5.6$ , simulating the conditions where  $K_{p(\max)} = 0$  (in the previous 24 hours), or very quiet geomagnetic conditions, as shown by the electron density profile in Figure 4.10b. The results displayed in Figure 4.8 columns 1 and 2 show that the MR traces are now “smooth” and follow the same trend as those at lower  $L$ -shells.

To illustrate the reflection process from the plasmopause, we examine the case shown in Figure 4.6, for  $\lambda_s = 45^\circ$ , at  $L = 3.0$ . Looking at a snapshot at  $t = 5$  sec, two seemingly unrelated frequency branches seem to coexist, one at  $2.1 \leq f \leq 2.6$  and another at  $0.2 \leq f \leq 2.0$ . We choose the two frequencies at  $t = 5$  sec and show in Figure 4.7 the origin of the two whistler branches. The ray labeled ‘a’ is the 2.523 kHz component and is injected at  $\lambda = 40.6^\circ$  at  $a_0$ , undergoes magnetospheric reflections

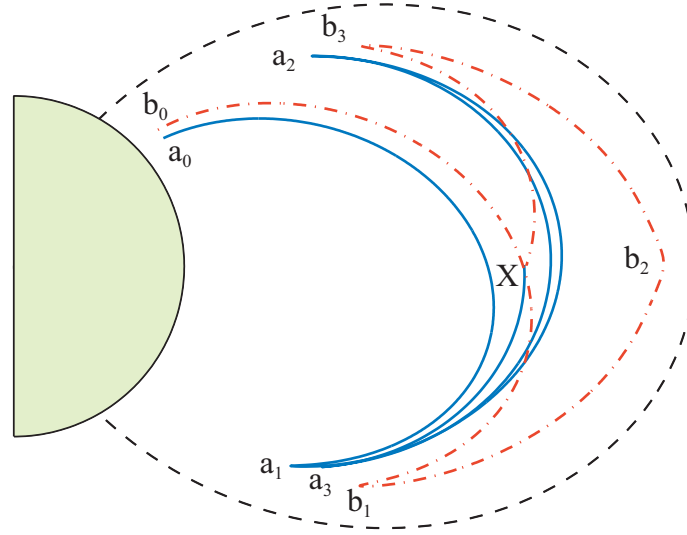


Figure 4.7: Ray paths showing plasmapause reflections, specifically Figure 4.6,  $\lambda_s = 45^\circ$ ,  $L = 3$ , at  $t = 5$  sec. Ray ‘a’ has  $f = 2.523$  kHz,  $\lambda = 40.6^\circ$  and approaches the satellite location X without a plasmapause reflection. Ray ‘b’ has  $f = 1.088$  kHz,  $\lambda = 43.9^\circ$  and reflects off the plasmapause at  $b_2$ . The hook-like features (resembling the letter “h”) shown in Figure 4.6,  $\lambda_s = 55^\circ$ ,  $L = 2.5$  and  $3.0$  develop in the same way, due to plasmapause reflections.

at  $a_1$ ,  $a_2$ , and  $a_3$ , and then crosses the detection region marked X at  $t = 5$  sec. In a similar way, the ray labeled ‘b’ is the 1.088 kHz component and is injected at  $\lambda = 43.9^\circ$  at  $b_0$ . The ray then undergoes a magnetospheric reflection at  $b_1$ , but as it moves to higher  $L$ -shells, encounters the plasmapause at  $L = 3.8$  ( $b_2$ ) and is reflected back into the plasmasphere. It then undergoes another MR at  $b_3$ , and finally crosses the detection region (X) at  $t = 5$  sec. When the plasmapause is moved to higher  $L$ -shells, such plasmapause echoes are eliminated, resulting in traces such as the ones shown in columns 1 and 2 of Figure 4.8.

## 4.4 Non-smooth plasmaspheres

The results presented in the previous section were for a plasmasphere with a smooth density profile, a plasmapause located at either  $L = 3.8$  or  $5.6$ , and rays launched with vertical wave normal angles at an altitude of 1000 km. While the real plasmasphere

(and ionosphere) can on occasion be relatively smooth, it is also known to support field-aligned density structures such as ducts or ledges [Smith and Angerami, 1968; Edgar, 1972; Bernhardt and Park, 1977; Carpenter et al., 2002; 2003]. The ionosphere often has irregularities [Schunk and Nagy, 2000, p.350] or horizontal density gradients [Ibid, p.347] that cause latitude and frequency dependent refraction of the rays as they traverse the ionosphere so that the wave normal angles may not necessarily be vertical at the injection point at 1000 km altitude. In this section, we consider the effect of different types of density irregularities on the  $f$ - $t$  signatures, as would be recorded at various locations in the plasmasphere. We choose three representative cases to study: an irregular ionosphere that produces randomized wave normal angles, a plasmasphere populated with ducts, and a plasmasphere consisting of one-sided ledges. In all cases, we only examine a subset of lightning source latitudes for the purposes of brevity.

#### 4.4.1 Randomizing ionosphere

To study the effects of many small-scale irregularities in the ionosphere, together with larger-scale horizontal density gradients, we perform a simulation similar to that discussed in Section 4.3 with a smooth plasmasphere (Figure 4.10a), but randomize the wave normal angle at the injection point of each ray. In other words, each of the 5330 sample rays (130 frequency components and 41 latitude locations per frequency) are assigned a random number for their initial wave normal angles, uniformly distributed between  $-30^\circ$  and  $30^\circ$  about the local vertical direction. Though such wave normal cones have been shown to exist [James, 1972], it is more common that all wave normal angles at a particular location will be bent somewhat uniformly, generally resulting in a much smaller cone centered on a particular wave normal direction.

Our choice of completely random initial wave normal angles thus represents the extreme situation with dramatic ionospheric wave normal randomization. Also, it is important to note that the spectrograms are constricted with  $\Delta f = 50$  Hz, whereas the rays are interpolated at every 1 Hz, and consecutive sample rays are typically 10 to 100 Hz apart in frequency. Thus, each  $\Delta f - \Delta t$  bin in the spectrograms records a large number of rays with randomized wave normal angles.

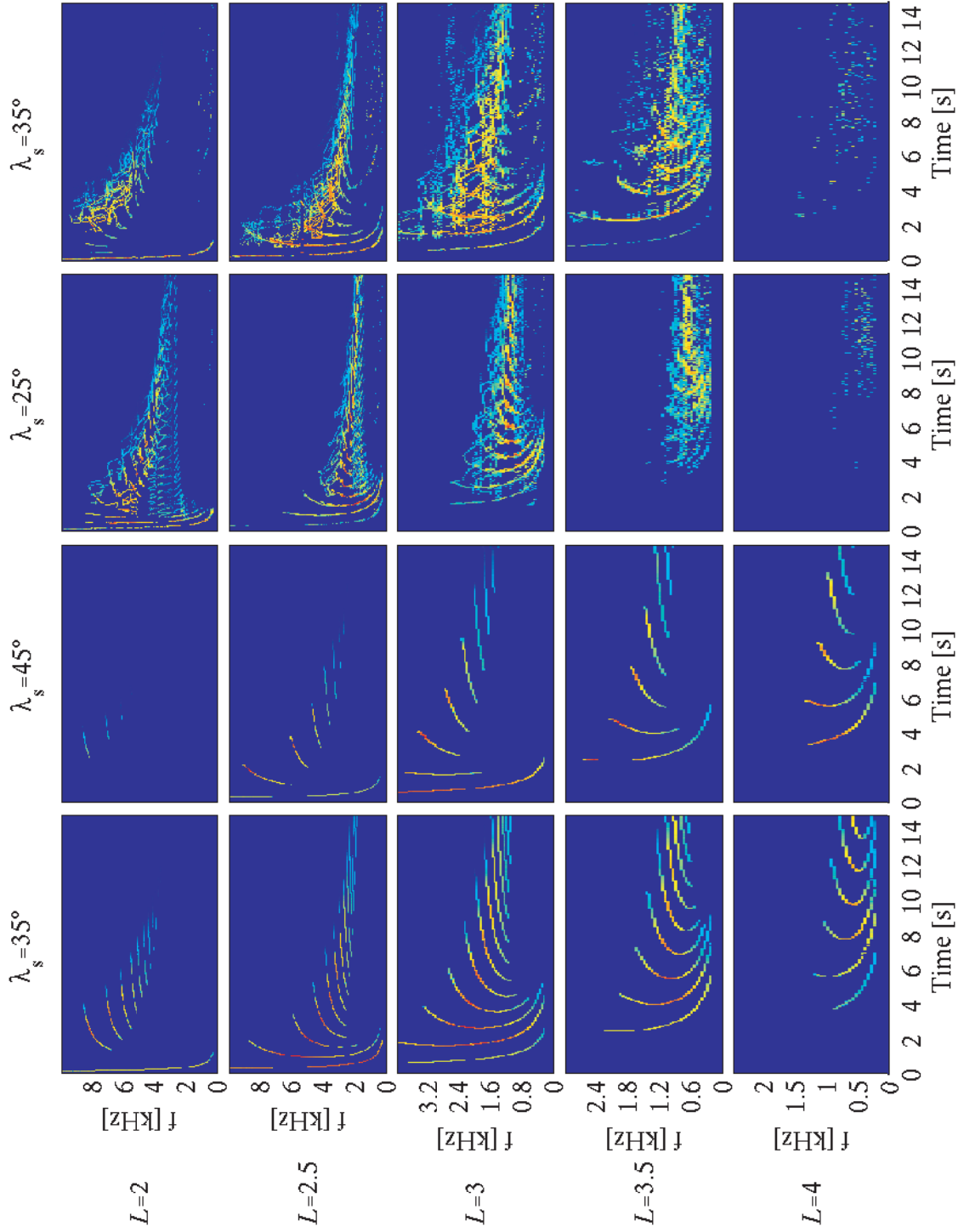


Figure 4.8:  $f-t$  Spectrograms presented in the format of Figure 4.6 for quiet conditions (columns 1 and 2), and randomizing ionosphere (columns 3 and 4).

The results for lightning source latitude of  $\lambda_s = 25^\circ$  and  $\lambda_s = 35^\circ$  are shown in Figure 4.8, columns 3 and 4. We observe that even with such scattered initial wave normals, there are well-defined  $f-t$  features observable in the spectrogram, having all the general features discussed in Section 4.3, such as a nose-frequency,  $L$ -shell dependent damping rates, and frequency separation in accordance with equatorial LHR frequency. The marked difference between the corresponding plots in Figure 4.6 is that the sharply defined MR whistler components evolve into an incoherent noise band far more rapidly. The upper and lower cutoff frequencies of the MR whistler components are similar to the smooth plasmasphere case but are more diffuse. The higher frequency components, particularly in the  $\lambda_s = 35^\circ$ ,  $L = 3.0$  case, quickly become incoherent. An examination of wave damping rates shows the characteristic trends discussed in Section 4.3.2. In this connection, we note that the evolution of the MR whistler into an incoherent noise band that is commonly observed in the plasmasphere (so-called plasmaspheric hiss) has been suggested by previous authors [Sonwalkar and Inan, 1989; Draganov *et al.*, 1992; 1993], and that the results shown in Figure 4.8 columns 3 and 4 clearly demonstrate this evolution. Since Landau damping was not previously included in the ray tracing work of Draganov *et al.* [1992], it was previously unclear whether Landau damping rates would be so fast as to extinguish the MR whistler before it evolved into hiss [Thorne and Horne, 1994]. However, our work which includes the effects of Landau damping shows that this is not the case, and that an incoherent band is likely to be formed as MR whistlers reflect back and forth and settle on their frequency-specific  $L$ -shells.

#### 4.4.2 Plasmasphere permeated by ducts

To simulate an irregular plasmasphere, we inject rays at 1000 km altitude with vertical wave normal angles, but instead of using the smooth plasmasphere of Figure 4.10a, we superpose eight two-sided ducts of 30% enhancement as shown in Figure 4.10c, spaced roughly according to the statistics presented for real whistler duct observations aboard the ISEE spacecraft [LeDocq *et al.*, 1994]. The density enhancement of the duct rises exponentially from 0% at the bottomside ionosphere to its full value of 30%



at an altitude of 1500 km beyond which it remains constant. Using this plasmaspheric profile we examine the observed MR components produced by a lightning discharge at  $\lambda_s = 25^\circ$  and briefly mention the differences due to lightning discharges at higher latitudes (not shown). Figure 4.9 column 1 shows that whistler energy is primarily confined to the plasmasphere, with very little energy leaking out to  $L = 4$  as in the case of the smooth plasmasphere. The frequency bands observed at each  $L$ -shell are also surprisingly consistent with those of nonducted whistlers, indicating that the majority of whistler wave energy is not trapped by the enhancement ducts. The lifetimes at each  $L$ -shell are consistent with those of the smooth plasmasphere.

An interesting feature in Figure 4.9 becomes apparent if we examine the  $f-t$  signature of the MR whistlers above, and below the nose frequency. We see from observations at  $L = 3.0$  and  $L = 3.5$  that for frequency components below the nose frequency, the MR whistler remains coherent, well-defined, and similar in appearance to the case of the smooth plasmasphere in Figure 4.6. However, the portions of the MR whistlers (in Figure 4.9) at frequencies above the nose frequency appear incoherent, randomized, and are not similar to their counterparts in Figure 4.6. To explain this somewhat peculiar behavior, we note that the nose frequency of the MR whistler lies very close to the LHR frequency of that particular  $L$ -shell, and it is the latter frequency that plays a key role in the behavior of the  $f-t$  trace. Following the analysis of *Helliwell* [1965, p.45], for whistler waves below  $f_H/2$ , we see that for ducted propagation (where the duct is an enhancement duct or “crest”) the wave normal angle must remain within a small cone about the static magnetic field direction. Since our waves do not start out in the duct, and have initial wave normal angles well outside the trapping cone, we expect these waves to propagate through the plasmasphere with little influence from the ducts, which is indeed the case for  $f < f_{\text{LHR}}$ . However, when  $f \geq f_{\text{LHR}}$  the refractive index surface becomes “open” and a minimum appears at the Gendrin angles [*Ibid*, Fig 3-17]. For whistlers with wave normal angles near the Gendrin angle, trapping in field-aligned depletions (troughs) is possible, since the ray and wave normal point in opposite sense about the static magnetic field. In our model plasmasphere the outer edges of the crests appear as one sided troughs which are able to partially guide or at least distort the

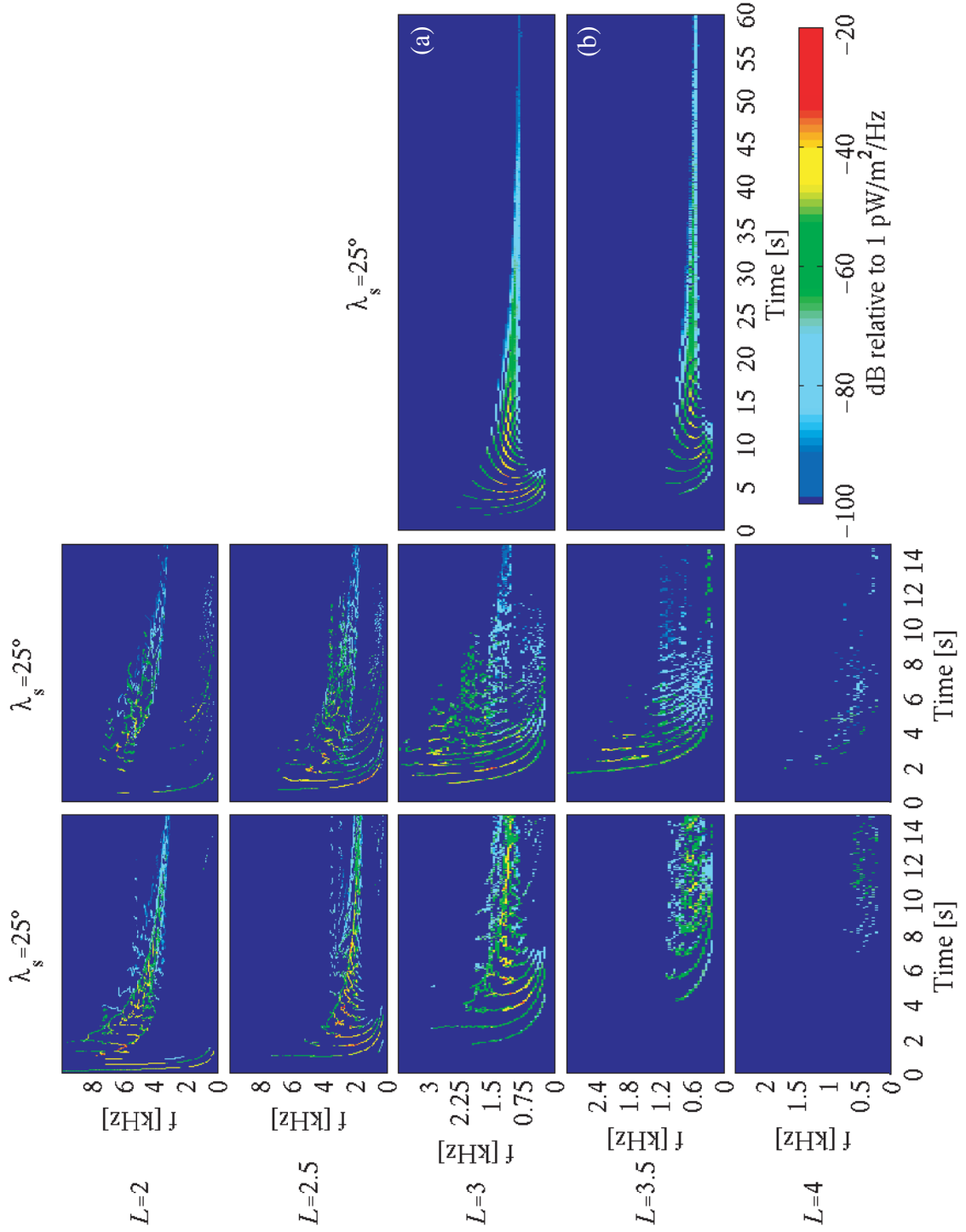


Figure 4.9:  $f$ - $t$  Spectrograms presented in the format of Figure 4.6 for ducted (column 1), ledged (column 2), and smooth (column 3 with extended timescale) plasmaspheres.

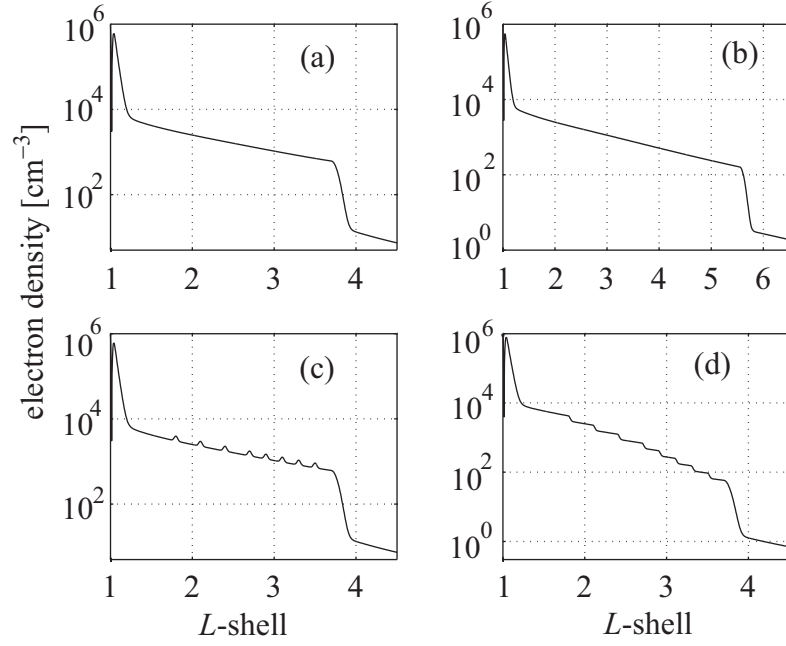


Figure 4.10: Equatorial electron density profiles in  $\text{cm}^{-3}$  as a function of  $L$ -shell, for (a) a smooth plasmasphere under typical conditions,  $K_p = 4$ , plasmopause  $\sim 3.8$ , (b) a smooth plasmasphere under quiet conditions,  $K_p = 0$ , plasmopause  $\sim 5.6$ , (c) plasmasphere with 8, two-sided, 30% enhancement ducts, and (d) as in (c) but with one-sided instead of two-sided ducts.

otherwise smooth trajectories of whistler waves with  $f \geq f_{\text{LHR}}$ , whereas for  $f < f_{\text{LHR}}$ , this possibility does not exist and the ray paths are almost entirely unaffected by the presence of the ducts. This result suggests that MR whistlers observed on satellites with smooth  $f < f_{\text{LHR}}$  and distorted or randomized for  $f \geq f_{\text{LHR}}$  components, can be used as strong indicators of the presence of one or more enhancement ducts.

#### 4.4.3 Plasmasphere permeated by one-sided ledges

We now study the effects of a plasmasphere permeated with one-sided ducts or electron density ledges by converting the two-sided ducts of Figure 4.10c to one-sided ducts (shown in Figure 4.10d), keeping the distribution and locations of the ducts unchanged. Figure 4.9 column 2 shows the observed spectrograms resulting from a lightning discharge latitude of  $\lambda_s = 25^\circ$ . Once again, the wave energy is confined to the

plasmasphere with very weak traces barely visible at  $L = 4.0$ . The frequency bands that are prevalent in Figure 4.6 column 1 are only weakly present in this simulation, and the lifetime of the whistler wave trains is dramatically shortened.

Perhaps the most notable feature in this spectrogram is the absence of a nose frequency, and the much reduced effects of dispersion between subsequent MR whistler components. Both of the above features are attributed to the stronger guiding potential of one-sided ducts, and to the fact that whistler waves in this spectrogram are predominantly confined to lower wave normal angle values. We note in passing that lightning source latitudes of  $\lambda_s \geq 35^\circ$  (not shown) result in only the first and second whistler hops visible on the spectrograms at all  $L$ -shells of observation, since we do not include the ability of rays to specularly reflect from the ionosphere in our ray tracing formulation. Instead we assume that wave energy leaks out into the Earth-ionosphere waveguide, and is eliminated from further plasmaspheric propagation.

## 4.5 Summary and discussion

We have used a numerical method to simulate the population of the plasmasphere by MR whistlers, allowing the determination of the  $f-t$  spectrogram that would be observed at a given location in the plasmasphere resulting from a lightning discharge at any given latitude on Earth. Using a two-dimensional ray tracing code we calculate the trajectories of 5330 whistler rays that effectively sample the frequency spectrum of the wave energy radiated by the lightning discharge and latitudinal spread about the source, and then use these so-called “sample rays” to obtain the properties of  $\sim 120$  million interpolated rays. Each ray is appropriated a measure of energy according to its frequency and injection latitude, and this energy is progressively attenuated along the ray’s trajectory using a Landau damping calculation based on realistic (measured) suprathermal electron fluxes. An equatorial detection region is defined to illustrate what would be observed on a satellite, and the rays that cross it are recorded and subsequently used to construct the final  $f-t$  spectrogram.

Using the technique described above, we studied the effect upon the appearance of the  $f-t$  spectrogram, of variations of the observation location in the plasmasphere

( $L=2, 2.5, 3, 3.5$  and  $4$ ), the location of the lightning discharge ( $\lambda_s = 25^\circ, 35^\circ, 45^\circ$ , and  $55^\circ$ ), and the plasmaspheric and ionospheric density structures.

Our results quantify the effects that all three factors (observation location, source latitude, and plasmaspheric density) have on the appearance of MR whistler waves in the simulated spectrograms. As the observation location is moved further away from the Earth, the frequency band in which MR whistler waves appear moves to lower values, the intensity of the whistler wave components diminishes, and the duration of the entire whistler echo train is increased such that at  $L=3.5$ , wave energy can exist for tens of seconds before being absorbed by the suprathermal plasma.

As the source lightning discharge latitude is increased, we find that the time interval between MR whistler echoes increases, and that the frequency band occupied by the whistlers at every observation point is higher. In addition, we find that at higher lightning discharge latitudes there are whistler components reflecting off the plasmopause and appearing as distinct traces with a unusual dispersion characteristics on the  $f-t$  spectrograms.

Simulations of an ionosphere that strongly randomizes the wave normal angle of the whistler wave during the transionospheric passage, show that MR whistlers appear well defined in the first few hops, but quickly evolve into an incoherent noise band, supporting previous suggestions that MR whistlers may evolve into the so-called plasmaspheric hiss and may thus be an embryonic source for these incoherent emissions [Sonwalkar and Inan, 1989]. The case of a plasmasphere permeated by field-aligned structures again shows distinctive behavior indicative of the nature of the field aligned density structure.

In summary, we show that the MR whistler echo train carries with it a great deal of information about the location of the causative lightning discharge, the exact location in the plasmasphere where it was recorded, and of course, the electron density structure of the intervening plasmaspheric medium. Given the distinct effects that each of these parameters has on the appearance of the  $f-t$  spectrograms, it should be possible to crudely infer the structure of the cold plasma in the plasmasphere, the lightning discharge latitude, and the observation location of the  $f-t$  spectrogram.

Though we have not explicitly investigated the effects of varying fluxes of suprathermal electrons in this work, it is quite possible that information on the suprathermal electron distribution may also be obtained from the lifetimes (or the ratios of intensities of subsequent MR components) of observed MR whistler echo trains.

Having developed a methodology to quantify MR whistler wave parameters at any location in the magnetosphere due to a lightning discharge at any given latitude, we are now in a position to calculate the precipitation of energetic radiation-belt electrons driven by MR whistler waves, a subject which is the topic of the following chapter.

## Chapter 5

# Temporal signatures of electron precipitation induced by lightning generated MR whistler waves

Using the technique developed in Section 4.2 to compute the frequency-time ( $f-t$ ) spectra of MR whistlers at any observation location in the magnetosphere, we now proceed to determine the temporal and spatial signatures of the resulting precipitation of energetic electrons. In this context we note that the critical wave parameters, including the local wave power and  $\mathbf{k}$ -vector are recorded at each point for each frequency and time bin, thus specifying the complete wave structure of the MR whistler along the energetic particle trajectories.

### 5.1 The wave-particle interaction model

The wave-particle interaction model presented in this section consists of two broad parts, namely the specification of the wave characteristics along a particular  $L$ -shell (discussed in Chapter 4 and extended in Section 5.1.1), and the calculation of the precipitated flux driven by the wave (Sections 5.1.2 and 5.1.3). In calculating the pitch-angle scattering of resonant particles, we neglect the feedback effect of the

particles on the wave (i.e., the re-radiated fields), so that our model is not self-consistent in a strict sense. However, this assumption that re-radiated fields are negligible compared to the original MR whistler wave is one that is consistent with past work [*Inan et al.*, 1978; *Inan et al.*, 1982; *Chang and Inan*, 1983a; *Chang and Inan*, 1985a,b; *Inan et al.*, 1985b; *Neubert et al.*, 1987; *Jasna*, 1993; *Lauben*, 1999a; *Lauben et al.*, 2001;] and is considered valid when relatively weak waves are involved ( $B_y^w \lesssim 1$  pT) so that no phase trapping occurs [*Bell*, 1986]. In effect, even if some amplification of the wave is present, as argued by *Inan et al.* [1978] there is no need to perform a self-consistent simulation since we are only concerned with particles at the edge of the loss-cone in this work, and the particle population responsible for wave-growth likely consists of particles with higher pitch-angles. Thus, electrons at the loss-cone experience a wave structure which is seemingly externally-imposed, and are not involved in its growth. To estimate the effects of possible wave-growth, we can simply scale our results to higher values, however, we once again emphasize that satellite observations of MR whistlers typically do not exhibit [*Edgar*, 1972] evidence of wave growth and triggering of VLF emissions, consistent with the fact that the effects of the energetic particles on the wave can be neglected.

### 5.1.1 Wave characteristics along a single field line

We use the methodology described in Section 4.2 [*Bortnik et al.*, 2003b] to calculate the detailed frequency-time ( $f-t$ ) spectra of the MR whistler at  $1^\circ$  latitude intervals along the  $L$ -shell of interest.

This level of discretization was chosen to give the highest sampling rate of the field line possible given our available computational resources, resulting in reasonable computation times (less than 1 week) and ensuring a smooth and slow progression of the recorded wave characteristics with latitude and time. The criterion we use in gauging ‘smoothness’ is that the whistler wave packet should propagate between adjacent latitude bins (i.e., from  $\lambda_{i\pm 1}$  to  $\lambda_i$ ) in approximately one time bin  $\Delta t$ . Since we consider a large distribution of wave frequencies ( $\omega$ ), wave normal angles ( $\theta$ ), plasma ( $\omega_p$ ) and gyro-frequencies ( $\omega_H$ ), each combination of  $(\omega, \theta, \omega_p, \omega_H)$  will result



in a different value of the refractive index through (2.12) and hence different phase and group velocities. However, for typical parameters used in our simulation, refractive index values of  $\mu = 10 - 100$  satisfy our smoothness criterion over the  $L$ -shells of interest.

Another factor in choosing the width of latitude bins is the accuracy of the pitch-angle calculation. Since our assumption (discussed more fully in the following Section) is that the whistler waves at different latitude bins are phase-incoherent from one another, but are coherent within any particular latitude bin, increasing the number of latitude bins along a given field line results in a pitch-angle calculation which is more diffusive in nature than what is actually the case, since the variances of the calculated pitch-angle perturbations within each latitude bin are summed over all latitude bins (see Section 5.1.2). Typical coherent interaction lengths span a few degrees in latitude for monochromatic parallel propagating whistlers [*Helliwell*, 1967; *Inan et al.*, 1983] as shown in Figure 5.6, and less for obliquely propagating, variable frequency waves due to the additional gradients in  $\mathbf{k}$ -vector and frequency. Our choice of  $1^\circ$  latitude bins thus represents a realistic interaction length which is extended by a factor of 2 (effectively a  $2^\circ$  interaction length) in a ‘windowing’ operation as discussed in the following section. The  $1^\circ$  interaction length also allows for effective sampling of the whistler wave characteristics along the field line and reasonable computation run times.

At every  $f-t$  bin of the simulated spectrogram we record the power density of the wave, average wave normal angle (averaged over multiple wave normal angles of many rays), group time, and other parameters necessary for the calculation of wave-induced pitch angle change as a function of time. The resulting set of calculated  $f-t$  spectra effectively provide an approximation of the wave structure experienced by trapped electrons moving between mirror points in the northern and southern hemisphere.

### 5.1.2 Calculation of the change in pitch-angle

Our purpose is to use the wave characteristics computed as described above to calculate the differential number flux of electrons precipitating into the upper ionosphere.

To do this we assume that the different frequency components that constitute the wave packet (i.e., the  $f-t$  spectra) as seen at a given point are phase-incoherent. Clearly, this assumption is not strictly true; however, we show below that the impact of any coherence upon the measurable precipitated flux signatures is minimal. As discussed by *Lauben et al.* [2001], when interacting with a nonducted whistler wave packet at least some portion of the particle population may enter the wave packet in a specific location and with such a velocity and pitch-angle that the interactions with the different frequency components are phase coherent and thus cumulative (i.e., the variations in the medium parameters such as  $\omega_H$ ,  $\omega_p$  are just compensated by the variations in the wave frequency and  $\mathbf{k}$ -vector), resulting in an unusually high pitch-angle perturbation, much higher than can be accounted for on the basis of linear theory alone and/or via a diffusion based analysis. Fortunately, as shown in *Lauben* [1999] and as discussed below, the number of particles that can coherently resonate with the variable frequency wave is quite small (due to the specific particle velocity and pitch-angle that they must have). As a result, the precipitation flux associated with this portion of the particle population is negligible compared with that constituted by the remainder of the particles which essentially undergo a random walk in pitch angle in the wave packet, and the interactions of which can be handled using a linear diffusion analysis. This assumption of phase incoherence between different frequency components at a given point and between interactions which occur at different latitude bins is crucial in our work, because it allows extensive parallelization of the problem, essentially making it solvable within present computational resources.

Figures 5.1 and 5.2 illustrate in graphical and flowchart form the procedure used in calculating the pitch-angle changes of resonant particles as described below. We aim to build a table of equatorial pitch-angle changes acquired by resonantly interacting electrons, displayed as a function of particle energy and time-of-arrival at the ionosphere. To this end, we separately treat the scattering produced by wave energy represented by every  $f-t$  cell in each spectrogram at each latitude, and evaluate the resonant velocity for a particular harmonic resonance mode. This procedure is repeated for each harmonic resonance mode ranging from  $-5$  to  $5$ , for time bins (following the time of the source lightning discharge) ranging from  $0$  to  $20$  sec, for

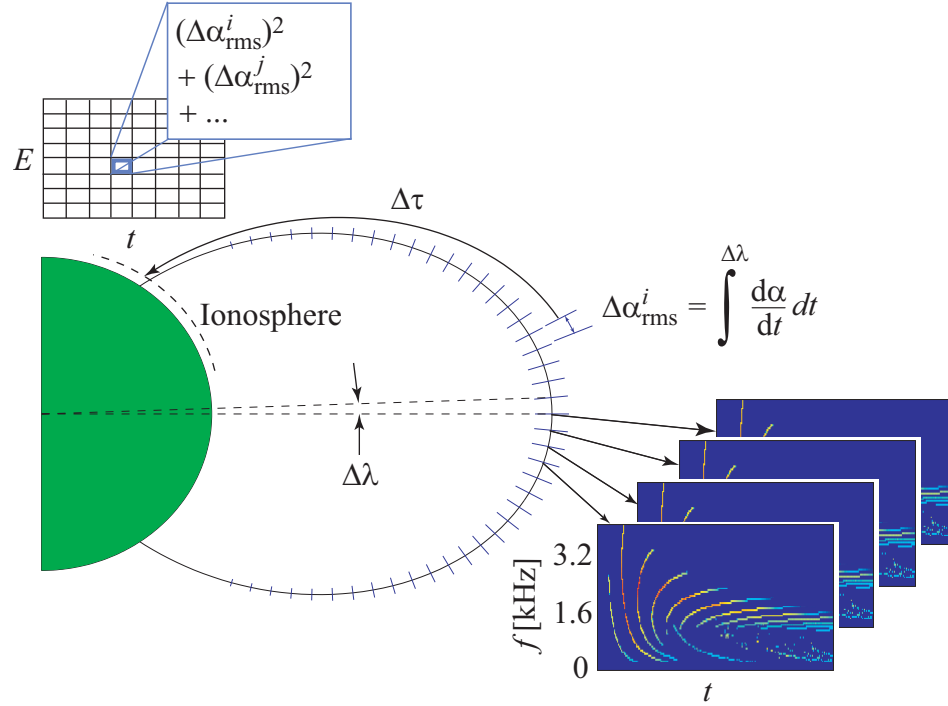


Figure 5.1: Illustration of flux calculation technique: calculate a pitch-angle change  $\Delta\alpha_i$ , and flight time to ionosphere  $\Delta\tau$ , for each  $f-t$  cell in the spectrogram for each resonance mode, over all latitudes; add  $(\Delta\alpha_{\text{rms}}^i)^2$  into the appropriate energy-arrival time bin at the ionosphere.

frequency bins ranging from 200 Hz to 60 kHz, and for geomagnetic latitude bins ranging from  $-40^\circ$  to  $40^\circ$  along the field line.

The resonant electron velocity is calculated by setting (2.27) equal to zero and considering only particles at the edge of the loss-cone [i.e.,  $v_z^{\text{res}} = v_z^{\text{res}} \cos^{-1}(\alpha_{\text{lc}})$ ]. The explicit expression for parallel resonant velocity is then given by:

$$v_z^{\text{res}} = \frac{\pm \sqrt{\omega^2 k_z^2 + [(m\omega_H)^2 - \omega^2] \left[ k_z^2 + \left( \frac{m\omega_H}{c \cos \alpha_{\text{lc}}} \right)^2 \right]} - \omega k_z}{k_z^2 + \left( \frac{m\omega_H}{c \cos \alpha_{\text{lc}}} \right)^2} \quad (5.1)$$

where the  $\pm$  sign on the radical indicates the direction of travel of the particle, the  $+$ ( $-$ ) indicating counter-streaming (co-streaming) particles and must be used with

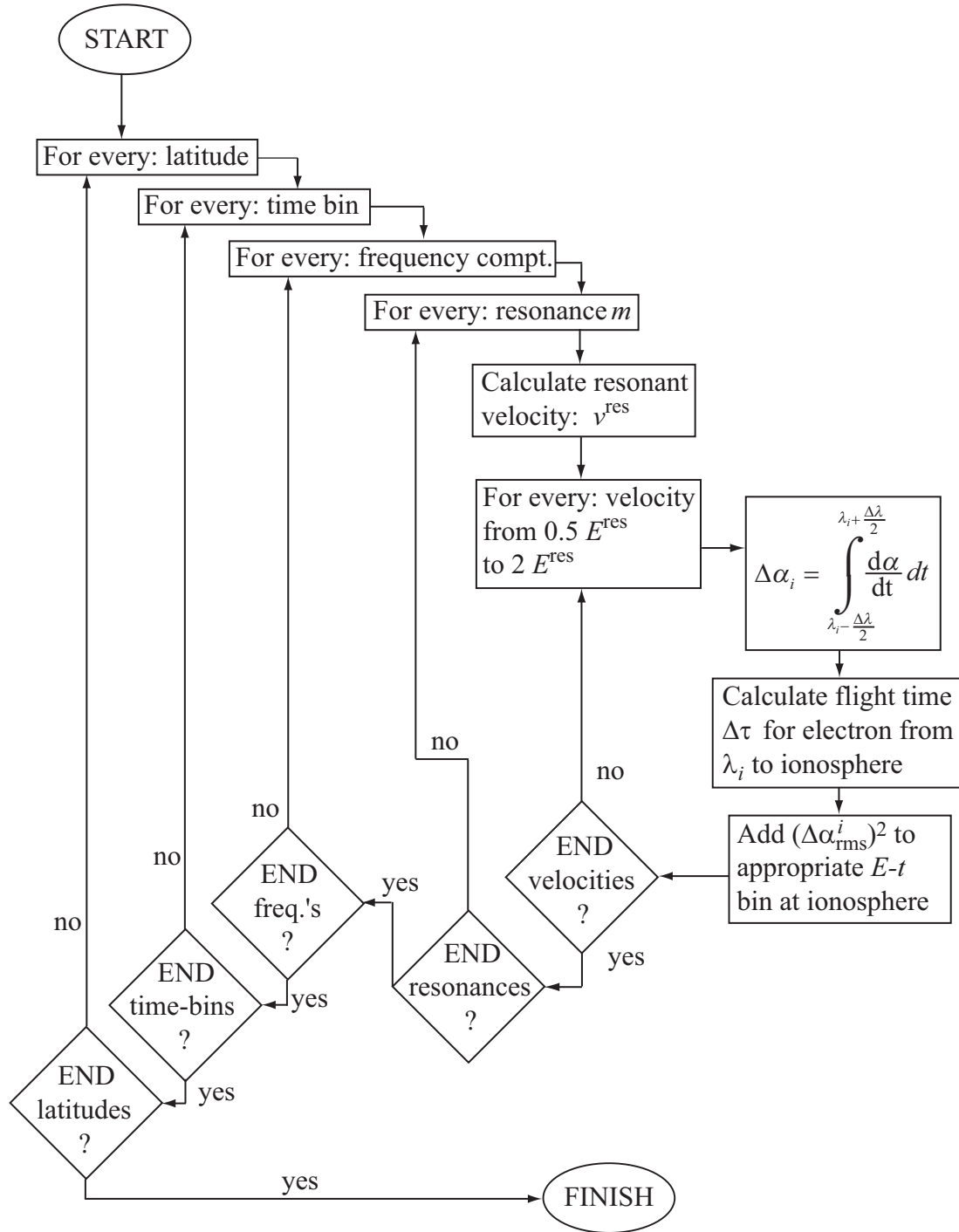


Figure 5.2: Flowchart illustrating the procedure of calculating the pitch angle changes at the ionosphere of resonant particles, as a function of energy and time of arrival.

positive (negative)  $m$ . We define a band of velocities corresponding to a range of parallel energies  $\pm 50\%$  about the resonant parallel energy as given by (5.1), discretize the set and evaluate the pitch angle change for each velocity as described below.

Figure 5.3 shows the equatorial root-mean-square (rms) pitch-angle change of a group of gyrotropic electrons (i.e., a group of monoenergetic electrons having the same pitch-angle, but being uniformly distributed in Larmor phase, or phase in the gyration cycle about  $B_0$ ) propagating through a wave described by a single  $f-t$  cell, at the magnetic equator ( $\lambda_i = 0$ ), with  $f = 3.055$  kHz, and  $t = 0.935$  sec. In this figure, the resonant energy  $E^{res} = 21.6$  keV ( $v^{res} = 8.46 \times 10^7$  m/s) and the band of velocities considered corresponds to the energy range 10.8 keV to 43.2 keV, a wave normal angle  $\theta = 58.32^\circ$ , a refractive index  $\mu = 63$ ,  $B_y^w = 0.37$  pT, and  $L = 3$ . The figure indicates that the change in pitch-angle drops off rapidly as the velocity of the interacting electron moves away from the resonant velocity. Due to this fast dropoff, in past work dealing with coherent wave-particle interactions the pitch-angle change was calculated for only a small band of electron velocities, typically 1%-3% [Inan *et al.*, 1978; Chang and Inan, 1983*a,b*; 1985*a,b*; Jasna, 1993; Lauben *et al.*, 2001] around the resonant velocity. Nevertheless, in this work we chose a broader band of velocities to ensure that “off-resonant” pitch-angle changes are accounted for. Off-resonant interactions can lead to increased precipitation fluxes [Wykes *et al.*, 2001*a,b*] and hence were included in this work – our choice of the bounds for the energy range of  $\pm 50\%$  about the resonant energy was made because at those bounds the pitch-angle deflection is  $\sim 100$  times smaller than at the resonant velocity and hence can be considered negligible. In actual fact, the most significant contribution to precipitated flux comes from those electrons within a few percent of the resonant velocity, so our choice of  $\pm 50\%$  is quite sufficient.

The quasi-periodic nulls in pitch-angle deflection shown in Figure 5.3 are caused by the artificially imposed sharp limit on the wave-particle interaction length, due to our latitude “binning”. While it is more accurate to consider the envelope of pitch-angle deflections (thus avoiding the nulls), a preliminary analysis has shown that after adding the pitch angle contributions from all  $f-t$  bins at all latitudes, the discrepancy is insignificant and the enveloping operation can be omitted for computational

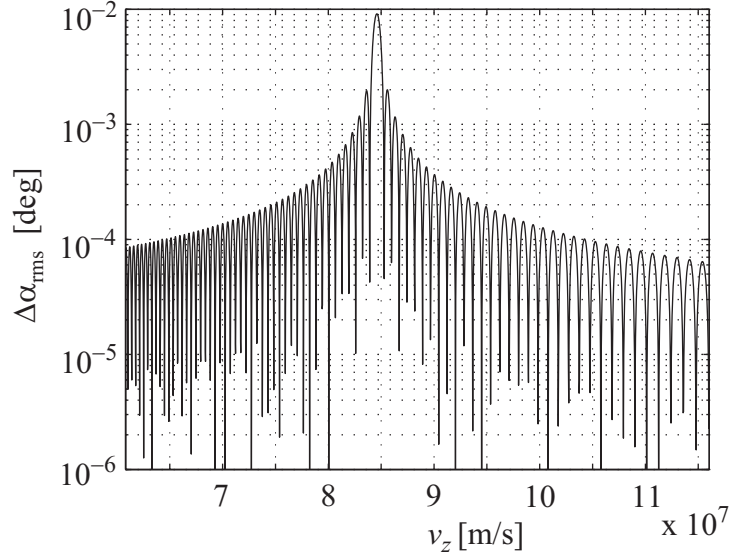


Figure 5.3: Equatorial rms pitch-angle change ( $\Delta\alpha_{\text{rms}}$ ) as a function of electron parallel velocity  $v_z$  for a single  $f-t$  cell at  $\lambda_i=0$ .

simplicity.

The rate of pitch-angle change of a particle moving through an oblique whistler wave-field was described by (2.26) in Section 2.4.2 and is repeated below for convenience:

$$\frac{d\alpha}{dt} = - \underbrace{\frac{m_e \omega_{\tau m}^2}{k_z p_{\perp}} \left( 1 + \frac{\cos^2 \alpha}{mY - 1} \right)}_{T_1} \underbrace{\sin \eta}_{T_2} + \underbrace{\frac{1}{m_e \gamma} \frac{p_{\perp}}{2\omega_H} \frac{\partial \omega_H}{\partial z}}_{T_3} \quad (2.26)$$

Equation (2.26) is integrated about the latitude of interest  $\lambda_i$ , from  $\lambda_i - \Delta\lambda/2$  to  $\lambda_i + \Delta\lambda/2$  where  $\Delta\lambda$  in our case is taken to be  $1^\circ$ . Specifically, to perform the integration we divide (2.26) into three parts labeled  $T_1$ ,  $T_2$ , and  $T_3$ . The term  $T_3$  describes adiabatic motion and is neglected since we account for this separately when we refer the change in pitch angle to its equatorial value. For this purpose, we calculate the pitch-angle change  $\Delta\alpha_i$  in the given latitude bin  $\lambda_i$ , add the local ‘adiabatic’ pitch-angle value  $\alpha_i$  in the center of the latitude bin, refer the sum to the equator through (2.20), and subtract the equatorial pitch-angle value  $\alpha_{\text{lc}}^{\text{eq}}$ .

The factor  $T_1$  generally varies slowly in the interval of interest, so we treat it as a constant evaluated at the center of the integration interval, namely at  $\lambda_i$ . The

factor  $T_2$  is the fastest varying, and typically undergoes many cycles in an integration interval unless the resonance condition (5.1) is approximately satisfied in which case  $\eta$  remains approximately constant (which is why integration of (2.26) only needs to be performed for velocities near resonance as discussed above in connection with Figure 5.3).

To simplify our computation, we approximate the gyrofrequency as a linear function in  $z$  (distance along the field line) at the center of each latitude bin  $\lambda_i$ , i.e.,  $\omega_H \simeq \omega_H^{\lambda_i} + (\partial\omega_H/\partial z)^{\lambda_i}(z - z_0)$  so that  $\eta$  becomes quadratic in  $z$ , and the integrand of  $T_2$  can be evaluated analytically. It is shown in Appendix A that the integration of  $T_2$  involves Fresnel integrals which are readily solved using a fast numerical technique [Mielenz, 2000]. It is important to note that the parallel and perpendicular velocities involved in the integration of (2.26) are also approximated to first order, and are taken to be the adiabatically varying unperturbed velocities, so that nonlinearities due to the wave forces are not included and the equation is analytically integrable (see similar past work such as Das [1971] and Ashour-Abdalla [1972]).

Figure 5.4 shows an example of a comparison of our analytical solution (blue curve) to the full solution (red curve) of (2.26) over two different  $1^\circ$  latitude bins, at  $\lambda_i = 0^\circ$  (left column), and  $\lambda_i = -10^\circ$  (right column). The full solution is obtained by integrating (2.26) together with (2.27) and (2.25) numerically over the entire  $1^\circ$  latitude bin, explicitly calculating the values of all the terms in the integration without resorting to the analytical simplifications described above in connection with the analytical solution. We consider three velocity ranges around the resonant velocity,  $\pm 0.5\%$ ,  $\pm 10\%$ , and  $\pm 20\%$  in rows 1, 2, and 3 respectively, and compute the average error in each band as:

$$\text{Error} = \frac{1}{v_2 - v_1} \sum_{v_1}^{v_2} \frac{|\Delta\alpha_{\text{rms}}^{\text{analyt}} - \Delta\alpha_{\text{rms}}^{\text{full}}|}{\Delta\alpha_{\text{rm}}^{\text{full}}}$$

where  $v_1$  and  $v_2$  are the lower and upper velocity bounds respectively around the resonant velocity.

The figure shows that typical errors between our analytical solution and the full solution are  $< 1\%$  for velocities near the resonant velocity (Figures 5.4a,d), and increase

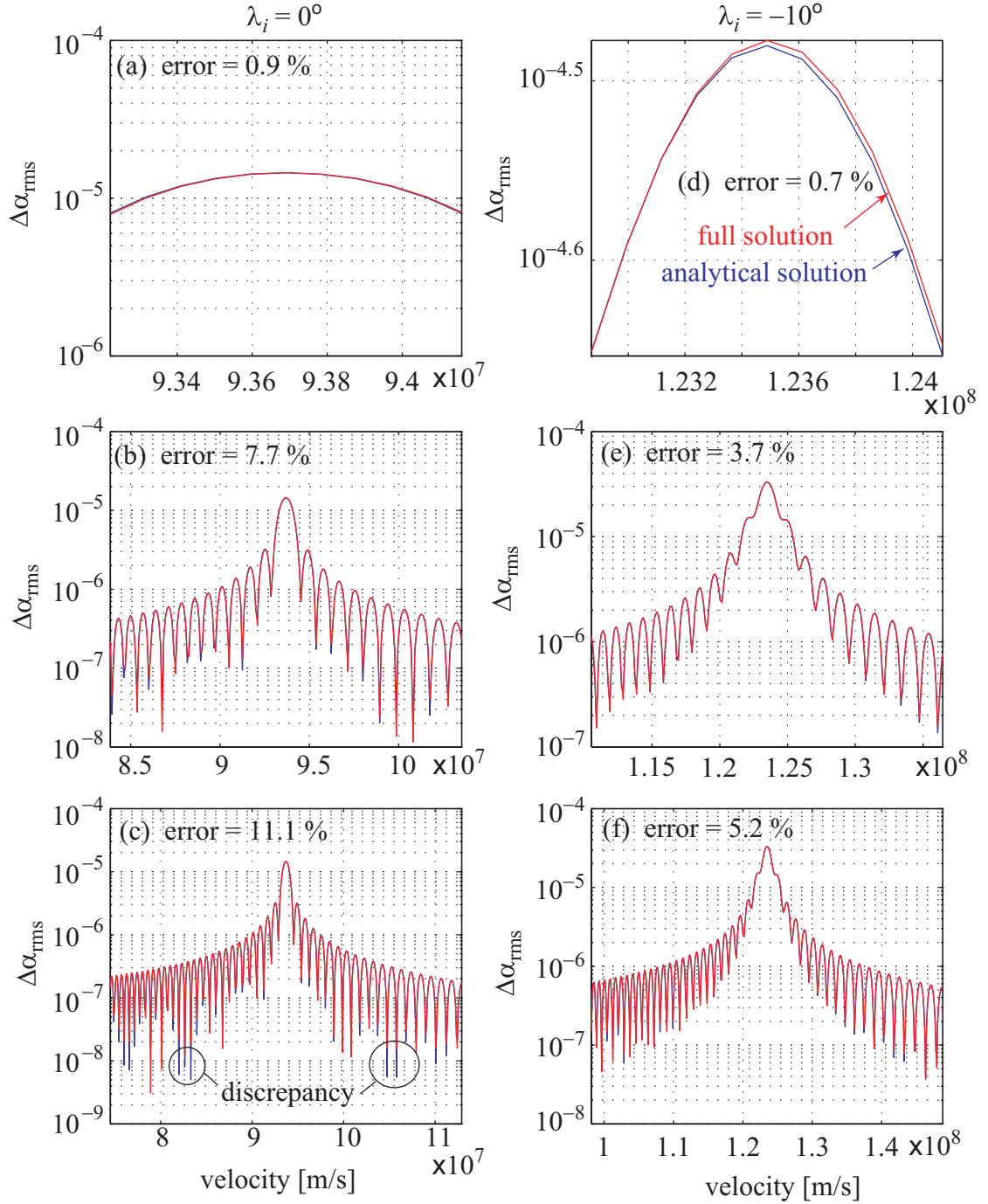


Figure 5.4: Comparison of  $\Delta\alpha_{\text{rms}}$  using analytical (blue) vs. full non-linear solution (red) methods, at two different latitude bins  $\lambda_i = 0$  (left column) and  $\lambda_i = -10$  (right column), using three different velocity bands about the resonant velocity,  $\pm 0.5\%$ ,  $\pm 10\%$ , and  $\pm 20\%$  in rows 1, 2, and 3 respectively.



as the range of velocities around the resonant velocity is increased, as in Figures 5.4b,c and Figures 5.4e,f. This decrease in accuracy occurs primarily due to the formation of nulls as discussed in connection with 5.3, where the deflection in pitch-angle is very sensitive to minor changes in the initial values (labeled as ‘discrepancy’ in our figure). The errors associated with nulls can be as large as 50%, but this does not impact our calculation since the absolute values of  $\Delta\alpha_{\text{rms}}$  are extremely low, regardless of the method used in calculating them.

As  $\lambda_i$  increases, the agreement between the two methods improves, and the error decreases regardless of the velocity band used. This result comes about because the rate of change of  $\mathbf{B}_0$ ,  $v_z$ , and  $v_\perp$  with latitude is dominated by the first derivative which we account for in our analytical solution, compared with the second derivative which we neglect in our calculations, and which is most important at the geomagnetic equator where the first derivative of the above quantities is zero (with respect to latitude).

In integrating (2.27) to obtain  $\eta$  which is used subsequently in (2.26), we are left with the integration constant  $\eta_0$ , which is the initial electron phase angle (known as the Larmor phase) relative to the wave. In past work [*Inan et al.*, 1978; *Chang and Inan*, 1985b; *Inan et al.*, 1985b; *Jasna*, 1993; *Lauben et al.*, 2001], dependence of scattering on  $\eta_0$  was accounted for explicitly by evaluating the equations of motion for 12 or more particles distributed uniformly in Larmor phase, since non-linear effects depend strongly on the relative phasing of the particle and wave. In our case, the interaction is assumed to be linear, in which case the scattering in pitch angle is strictly sinusoidal as a function of  $\eta_0$  [*Inan et al.*, 1978] (with derivation in Appendix A of *Inan* [1977]) as shown in Figure 5.8a. This sinusoidal dependence on  $\eta_0$  provides for a number of analytical conveniences. Firstly, we need only solve (2.26) once, having suitably averaged over initial Larmor phase to find the root-mean-square (rms) scattering, in order to characterize the entire interaction in Larmor phase. Secondly, the pitch-angle of the particles uniformly distributed in Larmor phase can be thought of as a random variable, which (when scattered by the wave) goes through a particular function (or filter) and attains a new distribution in pitch-angle. The probability density function (PDF) of this new distribution is shown in Figure 5.8b.

After calculating the rms pitch angle change of a group of particles of a certain velocity at some given latitude  $\lambda_i$ , the flight time to the ionosphere  $\Delta\tau$  is calculated and the quantity  $\Delta\alpha_{\text{rms}}^i = \sqrt{\langle(\Delta\alpha_i)^2\rangle}$  is added into the appropriate energy-time ( $E-t$ ) bin, where  $E$  is the particular energy of the group of particles under consideration, and  $t$  is the total time taken for the particle to reach the ionosphere from the time of origin of the source lightning discharge (i.e., the time for the whistler wave to propagate from the source to the given  $L$ -shell and latitude  $\lambda_i$ , plus the time taken for the electron to reach the topside ionosphere from this interaction latitude on that  $L$ -shell). The quantity  $\Delta\alpha_{\text{rms}}^i$  is then referred to the equator as described above. The behavior of a resonant particle near the equator is discussed below in connection with Figure 5.6.

There are a number of important assumptions which underlie the methodology outlined above. Firstly, the pitch angle deflections  $\Delta\alpha_{\text{rms}}^i$  that occur at different latitudes along the field-line, at different times, due to various wave frequency components and resonance modes, are grouped on the basis of energy and time. This method of grouping is chosen because the pitch-angle deflections for particles of a certain energy that arrive at the ionosphere at a given time essentially belong to that same particle group, regardless of where (along the field) the pitch-angle changes may have actually occurred. Secondly, we square and add equatorial (rms) pitch angle deflections because the interactions that a certain group of electrons experiences at various latitude bins along the field-line are almost always phase-incoherent. For instance, a 100 keV electron may undergo a first order counter-streaming gyroresonance at  $\lambda = \lambda_0$  with an  $f_0$  kHz wave, then a co-streaming resonance at  $\lambda = \lambda_1$  with an  $f_1$  kHz wave, a higher order counter-streaming resonance at  $\lambda = \lambda_2$  with an  $f_2$  kHz wave, and so on. Each interaction is clearly phase incoherent from the others, and the behavior of the particle population quickly resembles a diffusive process rather than a coherent process [Roth *et al.*, 1999].

It can be shown on probabilistic grounds that in a diffusive ‘random walk’ process, the variance  $\langle(\Delta\alpha_{\text{rms}}^i)^2\rangle$  of the pitch-angle distribution of the particles increases linearly with time. In recognition of this fact, we choose to add together the variances of the interactions that a certain particle group (i.e., a number of particles all having

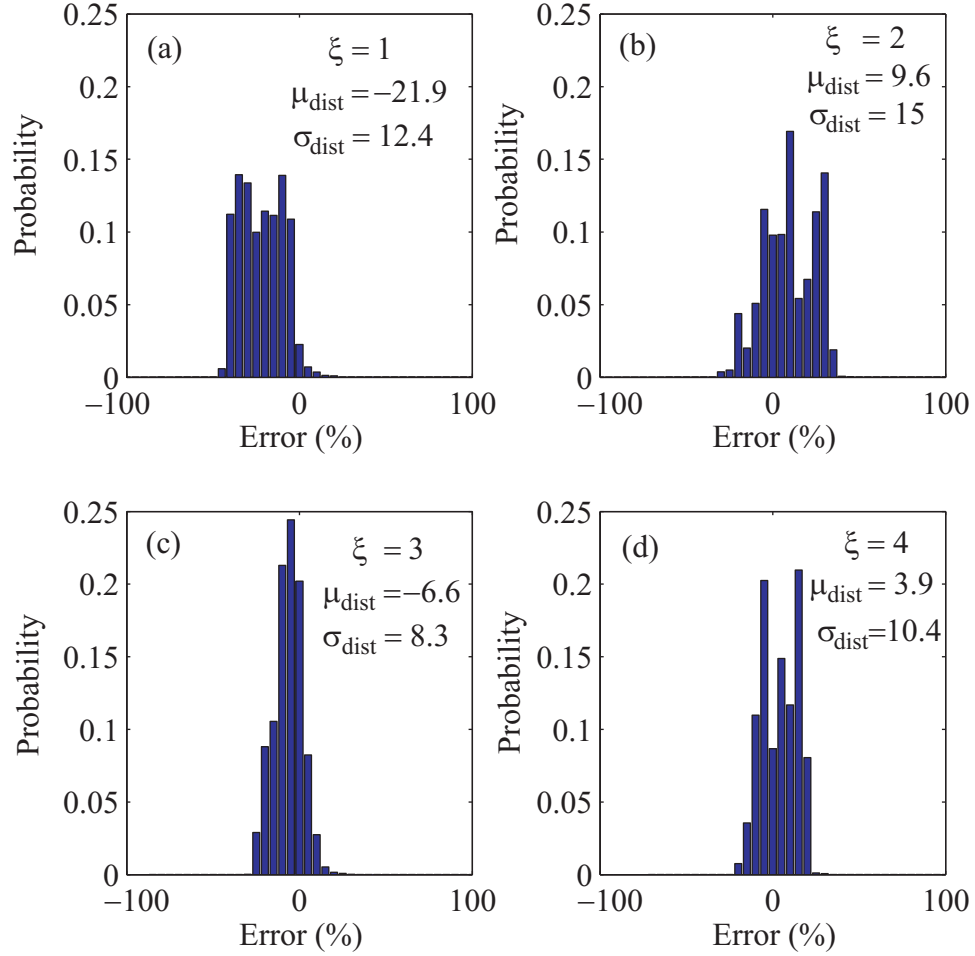


Figure 5.5: Latitude discretization error study for  $L = 2.3$ ,  $f \approx 3$  kHz showing the mean and variance for  $1^\circ - 4^\circ$  latitude windows in panels (a)-(d).

the same energy and pitch-angle, and distributed uniformly in Larmor phase) undergoes along the field-line. This method can lead to errors in the case where the wave-particle interaction is indeed coherent, and the particle group encounters the same wave group coherently over a few adjacent latitude bins.

In order to quantify the errors incurred due to latitude discretization, we compare the pitch-angle changes experienced by a group of particles with and without latitude discretization. For this purpose we chose a typical  $L$ -shell ( $L = 2.3$ ) and frequency band ( $f \simeq 3.2 - 3.3$  kHz) and use  $\sim 26500$  combinations of typical wave parameters

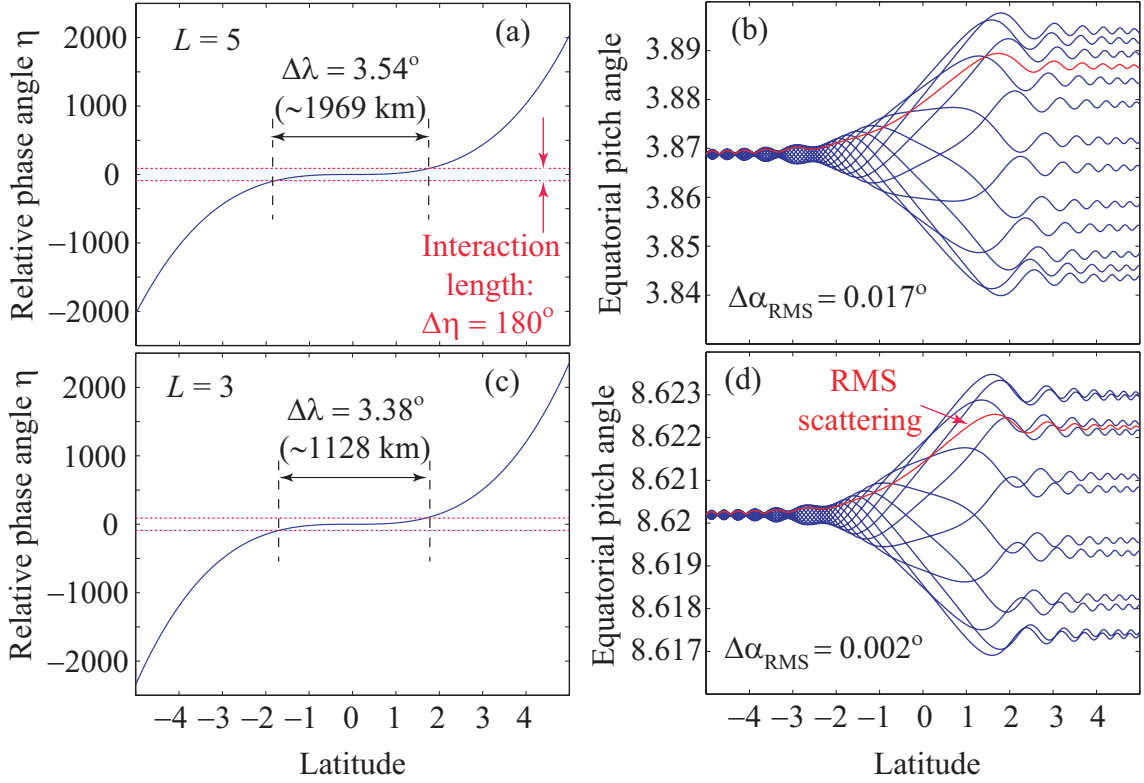


Figure 5.6: The resonant interaction of an energetic particle with an oblique whistler showing the relative phase angle  $\eta$  and equatorial pitch angle change at  $L = 5$  (a),(b) and  $L = 3$  (c),(d).

taken from the  $\lambda_s = 35^\circ$  injection wave simulation. As discussed in Section 5.1.1, the wave parameters were recorded at  $1^\circ$  latitude bins and in this particular case, spanned  $\lambda_i \approx -30^\circ$  to  $40^\circ$ . The wave parameters strictly apply to only the  $1^\circ$  interval, but for the purpose of our error study we extrapolate these parameters over a  $10^\circ$  latitude range, spanning  $\pm 5^\circ$  about  $\lambda_i$ . We then integrate the equations of motion (2.26) for the resonant particles to obtain the pitch angle change  $\Delta\alpha_{i0}$  for the particular  $10^\circ$  latitude span centered at  $\lambda_i$ . To measure how well discretization compares with the nominal pitch angle change  $\Delta\alpha_{i0}$ , we further subdivide the  $10^\circ$  latitude interval into ten  $1^\circ$  intervals, integrate the equation of motion in each interval to obtain the partial pitch angle changes  $(\Delta\alpha_{i1} - \Delta\alpha_{i10})$ , square, add, take the square root, and compare to  $\Delta\alpha_{i0}$ .

To go a step further, we introduced a ‘windowing’ operation, whereby the partial pitch angle changes are evaluated over an interval of  $\xi$  times the latitude bin ( $1^\circ$ ), squared, divided by  $\xi$ , then added into the and square rooted as before. We would expect that as  $\xi \rightarrow 10$ , the error would tend to 0, and this is indeed the case. We have performed this error study for a large range of  $\xi$ -values, and show the results for  $\xi = 1, 2, 3$ , and 4 in Figure 5.5, where the distributions are obtained by adding the value  $\Delta\alpha_{i0}$  into the appropriate error bin and then normalized, and errors span from  $-100\%$  to  $100\%$  divided into  $5\%$  bins. The choice of adding  $\Delta\alpha_{i0}$  into the appropriate error bin as opposed to simply incrementing a counter in that bin was made because not all errors are equally significant. The change in pitch angle spans many orders of magnitude  $\approx 10^{-15} - 10^{-1}$  and often the largest errors occur at the smallest  $\Delta\alpha_{i0}$ ’s (in the nulls shown in Figure 5.4c and discussed above) where the pitch-angle change is well within the numerical noise level.

As shown in Figure 5.5 the discretized results agree reasonably well with the non-discretized results (bearing in mind the huge scale variations of the  $\Delta\alpha_{i0}$ ’s mentioned above). As  $\xi$  increases the mean of the distribution  $\mu_{\text{dist}}$  tends to zero fairly quickly, but the standard deviation  $\sigma_{\text{dist}}$  does not, remaining at  $\sim 10^\circ$  (the distribution does become narrower, but this is only visible for larger values of  $\xi$ ). In the remainder of this chapter we use a ‘window’ of  $2^\circ$  because in general we obtain the largest differential improvement in mean value in changing from  $\xi = 1$  to  $\xi = 2$ , and a marginal increase in  $\sigma_{\text{dist}}$  (we expect that as the sample size increases,  $\sigma_{\text{dist}}$  would actually become slightly smaller in the latter case). Although further improvements may come about with higher values of  $\xi$ , we have chosen not to make the integration window larger because the windowing operation results in a convolution or ‘smearing’ in time. Electrons scattered in an interaction occurring at a certain  $\lambda_i$  arrive at the ionosphere with a time-uncertainty corresponding to the flight time of the particle through the  $\xi^\circ$  latitude interval. For instance, a 10 keV particle at the loss-cone has a time-uncertainty of  $\sim 0.02$  sec at  $L \simeq 5$  and  $\sim 0.01$  sec at  $L \simeq 2.3$ . Since our  $E-t$  plots have a time resolution ( $\Delta t$ ) of 0.02 sec we have chosen not to use higher values of  $\xi$  so as to not make the time-smearing greater than  $\Delta t$ .

For reference, we have shown a typical  $\Delta\alpha_{\text{eq}}$  plot in Figure 5.6 which demonstrates

how a constant frequency pulse at the magnetic equator interacts with a group of particles at the respective resonant energies at  $L = 3$  and  $L = 5$ . In panel (a) we show that for the ‘worst-case’ interaction scenario involving no  $f$ -variation and very slow  $\omega_H$  variation, the interaction length in latitude is still  $\sim 3.54^\circ$ , very similar to the value at  $L = 3$ , though the net pitch-angle change is  $\sim 10$  times greater. In the typical simulations we perform, the interaction length is necessarily shorter because  $\partial f/\partial \lambda$ ,  $\partial k_z/\partial \lambda \neq 0$ .

In the error study discussed above, we have assumed a constant frequency over the entire  $10^\circ$  latitude interval which gives the somewhat pessimistic error estimates near the equator. However, in off-equatorial cases  $\partial f/\partial \lambda = 0$  but  $\partial \omega_H/\partial \lambda \neq 0$  which can also be interpreted as an equatorial interaction (i.e.,  $\partial \omega_H/\partial \lambda = 0$ ) with a varying frequency tone  $\partial f/\partial \lambda \neq 0$ . Since we sample both sides of the equator (i.e.  $\partial \omega_H/\partial \lambda > 0$  and  $\partial \omega_H/\partial \lambda < 0$ ) we effectively capture signals whose frequency both increases and decreases as a function of time.

A final point to note about Figure 5.6 is that we do not need to simulate the entire gyrotropic group of particles as discussed above (twelve particles shown in this case) since we are assuming linear interactions and no phase bunching. Instead, we can compute only the root-mean-square scattering of the entire group as shown in panels (b) and (d) in red and discussed in the following section, Appendix A, and *Inan* [1977].

Figure 5.7 shows a typical equatorial pitch-angle deflection array, calculated as described above, displayed as a function of particle energy  $E$ , and arrival time at the ionosphere  $t$  for both northern (a) and southern (b) hemispheres at the ionospheric endpoints of the  $L \simeq 3$  shell. The most intense pitch-angle scattering is associated with the first ( $m=1$ ) counterstreaming cyclotron resonant interaction between energetic particles and the first few hops of the MR whistler wave. Peak deflections are  $\sim 0.1^\circ$  occurring between  $\sim 100$  keV and  $\sim 1$  MeV. This pitch-angle deflection array corresponds to the precipitated differential number flux shown in Figures 5.11c, and 5.11d, and a more complete discussion of the detailed  $E-t$  features accompanies this figure.

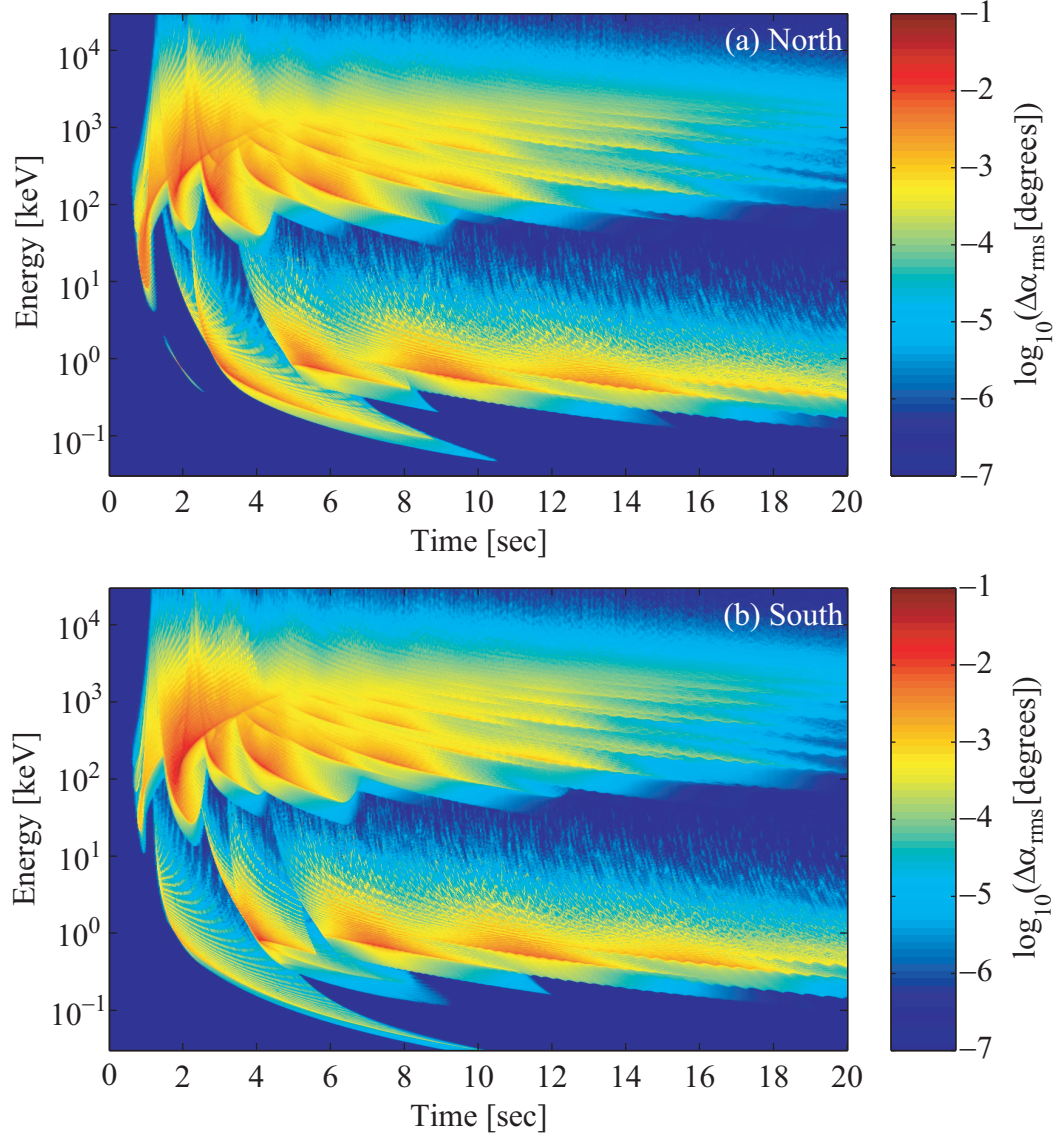


Figure 5.7: The pitch-angle deflection array as a function of particle energy  $E$  and arrival time at the ionosphere  $t$ , for a lightning source latitude of  $\lambda_s = 35^\circ$ , and observed at  $L \simeq 3$ .

### 5.1.3 Determination of the precipitated flux

After carrying out the above procedure as illustrated in Figure 5.2 over every  $f$ – $t$  bin at every latitude location, and for all resonance modes, we are left with two tables (the northern and southern ‘feet’ of the field line) whose entries represent the total equatorial pitch-angle variances  $\langle(\Delta\alpha_{\text{rms}})^2\rangle$  of the perturbed particle distributions as a function of particle energies and ionospheric arrival times, shown in Figure 5.7. In order to obtain results that can be compared with measurement, we need to convert the pitch-angle change table into a corresponding table of precipitated flux. In past work [*Inan et al.*, 1978; *Chang and Inan*, 1985b; *Jasna*, 1993; *Lauben et al.*, 2001], this mapping has been implemented with an algorithm that mapped an unperturbed distribution function in velocity-pitch-angle space, into the perturbed distribution by applying the calculated pitch angle perturbation to each individual test-particle, and then using the distribution function to determine the total flux of particles that has scattered into the loss-cone. Based on the relatively insensitive dependence of scattering on the initial pitch-angles, portions of the distribution function immediately above the loss cone were perturbed with the same set of values as the population at the edge of the loss cone, allowing the determination of all particles that could possibly be scattered.

The procedure outlined above can be summarized with the following steps, and illustrated in Figure 5.8a,b:

1. Calculate a ‘perturbing function’ (e.g., Figure 5.8b that corresponds to the sinusoidal scattering shown in Figure 5.8a) that describes how a group of particles with the same pitch-angle and energy is scattered in pitch-angle as a function of initial phase  $\eta_0$ .
2. Multiply the perturbing function with the value of the distribution function at the loss-cone.
3. Shift perturbing function to slightly higher pitch-angle and multiply with the new value of the distribution function. Continue shifting the perturbing function and multiplying (scaling) by the value of the distribution function.



4. Integrate all the shifted-and-scaled replicas of the perturbing function to obtain the new ‘disturbed’ distribution function, i.e., the distribution function after the wave has scattered a portion of the particles into the loss-cone.

This operation essentially amounts to numerical convolution, and since we have a deterministic scattering function (Figure 5.8a) and deterministic distribution function, the convolution can be performed analytically thereby reducing computation time.

The convolution operation is illustrated in Figures 5.8c, and 5.8d. In Figure 5.8c, we convolve a ‘square’ pitch angle distribution (a uniform distribution in pitch angle, with a sharp cutoff at the loss-cone) of magnitude  $b_0$  with a scattering function characterized by the maximum pitch-angle change  $\Delta\alpha_{\max}$ . The analytical result of the convolution is shown in panel (c). In Figure 5.8d we show a similar result, derived for a ‘ramp’ distribution with the convolution result again shown in the panel. This method can be applied to a distribution function  $p$  of arbitrary shape, by letting  $g(\alpha) = bu(\alpha - \alpha_{lc})p(\alpha - \alpha_{lc})$  (where  $u$  is the step function) and expanding  $p$  into a Taylor series about  $\alpha_{lc}$ . The first two terms are shown in Figures 5.8c and 5.8d respectively, and higher order terms can be readily obtained.

The hatched areas of Figures 5.8c and 5.8d represent the those particles scattered into the loss-cone. Our task now is to obtain the total precipitated flux, and to this end, we convert the perturbed distribution function  $f_p(E, t, \alpha)$  into a perturbed flux function  $\Phi_p(E, t, \alpha)$  using the formula used by *Chang* [1983], given by:

$$\Phi_p(E, t, \alpha) = \frac{f_p(E, t, \alpha)v^2}{m\gamma^3}$$

which is also derived in Appendix A and shown in (A.14). In order to obtain the differential precipitated flux, we consider only those electrons traveling perpendicular to the geomagnetic field line by multiplying with a  $\cos \alpha$  factor, integrating  $\Phi_p$  over the solid angle representing the loss-cone, and finally multiplying the result obtained above by a factor  $g_c = (\sin^2 \alpha_{lc}^{\text{eq}})^{-1}$  representing the contraction of the geomagnetic flux tube as particles travel from the equator to ionospheric altitudes [*Lauben et al.*,

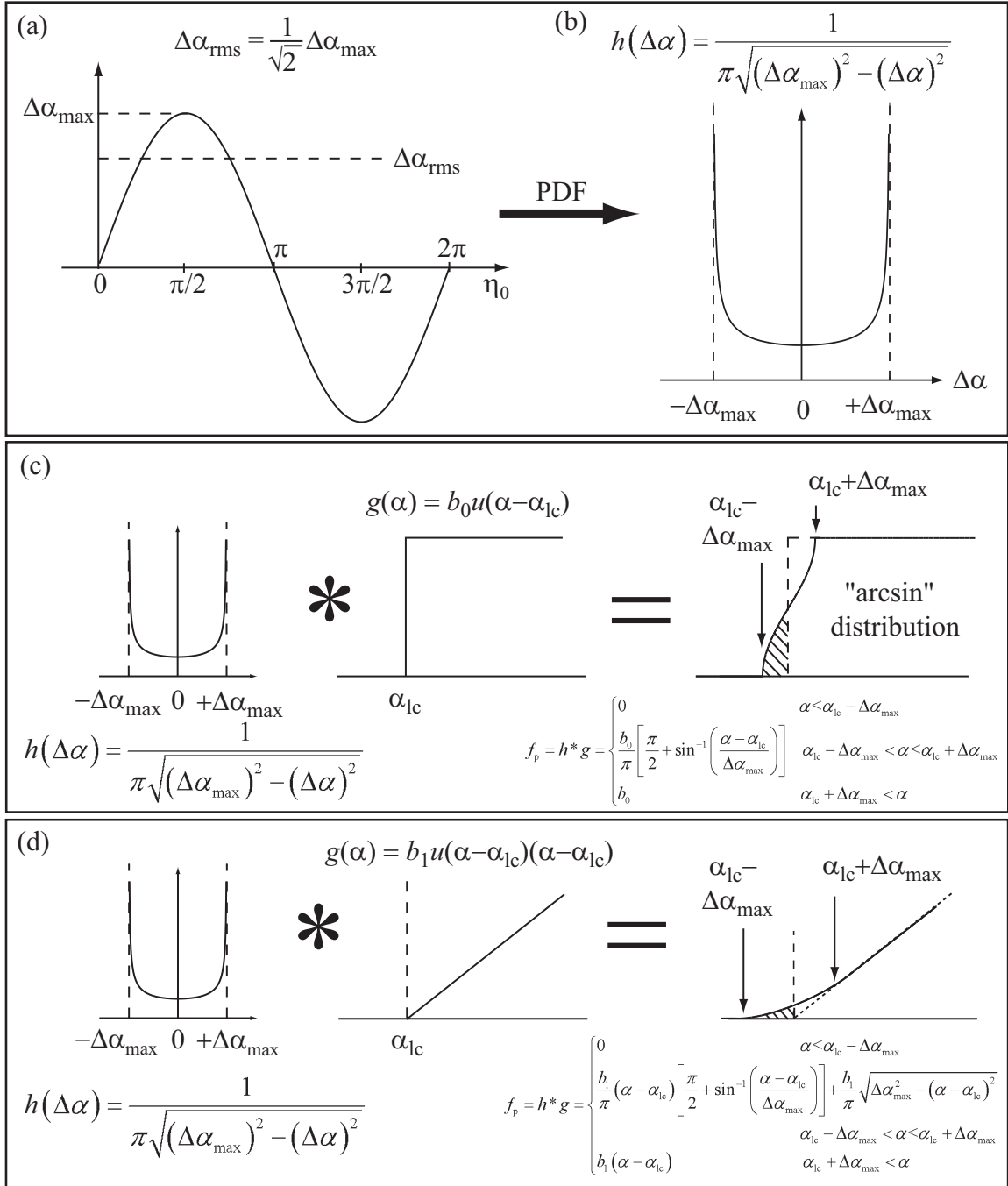


Figure 5.8: Analytic determination of precipitated flux (a) equatorial pitch angle change as a function of initial angle (b) PDF of (a), (c) convolution of ‘sine’ scattering with square distribution, and (d) convolution of ‘sine’ scattering with a ramp function.

2001]. Mathematically this can be written as:

$$\begin{aligned}
 \Phi(E, t) &= \overbrace{\frac{1}{\sin^2 \alpha_{lc}}}^{\text{flux tube contraction}} \int_0^{2\pi} \int_0^{\alpha_{lc}} \Phi_p(E, t, \alpha) \underbrace{\cos \alpha}_{\substack{\text{adjustment} \\ \text{for area } \perp \text{ to } B_0}} \underbrace{\sin \alpha \, d\alpha \, d\phi}_{\text{solid angle } d\Omega} \\
 &= \frac{\pi}{\sin^2 \alpha_{lc}} \int_0^{\alpha_{lc}} \Phi_p(E, t, \alpha) \sin 2\alpha \, d\alpha
 \end{aligned} \tag{5.2}$$

where all values of  $\alpha$  are taken to be equatorial, and  $\phi$  is the azimuthal angle.

Finally, the number of precipitating electrons  $N(t)$  and the associated energy flux  $Q(t)$  which they represent are found by integrating  $\Phi(E, t)$  with respect to energy as:

$$N(t) = \int_{E > E_{th}} \Phi(E, t) dE \tag{5.3a}$$

$$Q(t) = \int_{E > E_{th}} E \Phi(E, t) dE \tag{5.3b}$$

respectively, where we integrate above the lower energy threshold  $E_{th}$  in order to investigate the energy dependence of our results, as well as to facilitate comparison with particle detector measurements made for energies above some sensitivity threshold.

#### 5.1.4 Modeling of the trapped particle distribution

We have used two different models of the available flux of energetic radiation-belt particles: the extrapolated analytic function of *Bell et al.* [2002] with an assumed square loss-cone distribution, and the AE8 radiation belt-model [*Vette*, 1991] with an assumed sinusoidal loss-cone distribution shown in Figure 5.9. These particular distributions were selected in our work for two reasons: (i) in order to compare our work with similar past work, as well as the precipitation signatures of different  $L$ -shells amongst themselves using a simple analytic function, and (ii) to simulate a more realistic  $L$ -dependent particle population with a softer loss-cone distribution. Past workers [*Inan et al.*, 1978; *Chang and Inan*, 1985b; *Jasna*, 1993; *Lauben et al.*, 2001] have relied on the flux measurements taken by OGO 3 [*Schield and Frank*, 1970] for modeling the trapped energetic particle population, and quantitative comparison

with past workers requires that we use the same distribution. On the other hand, the measurements made on OGO 3 were in the region  $4.2 < L < 5.7$ , rely on a very small sample of observations, and are highly atypical in that they represent abnormally intense fluxes (particularly in the suprathermal range) compared to more recent observations made aboard the POLAR satellite [Bell *et al.*, 2002], which were taken in the region  $2.3 < L < 4$ , and rely on the large HYDRA data set. In this connection, it should be noted that we also use the POLAR fluxes in our evaluation of the Landau damping of the whistler-mode rays. In past work the determination of the trapped fluxes for higher energy electrons ( $>10$  keV) were based on crude assumptions of  $E^{-n}$  type of scaling from OGO 3 measurements at  $\sim 1$  keV of  $f(v)$  with  $n$  ranging from 2 to 6. In our work, the distribution of higher ( $>10$  keV) energy electrons is modeled in a manner consistent with HYDRA measurements of lower ( $<10$  keV) energy electrons in that we extrapolate the distribution function of Bell *et al.* [2002] by modifying the particle velocity with the Lorentz factor, giving the expression:

$$f(v) = \frac{a_0}{v_m^4} - \frac{b_0}{v_m^5} + \frac{c_0}{v_m^6} \quad (5.4)$$

where  $f$  is in  $\text{s}^3\text{cm}^{-6}$ ,  $v_m$  is the modified velocity given by  $v_m = v/\sqrt{1 - v^2/c^2}$  where  $v$  is the velocity in  $\text{cm s}^{-1}$ , and  $a_0$ ,  $b_0$ , and  $c_0$  are model constants set to  $4.9 \times 10^5 \text{ cm}^{-2}\text{s}^{-1}$ ,  $8.3 \times 10^{14} \text{ cm}^{-1}\text{s}^{-2}$ , and  $5.4 \times 10^{23} \text{ s}^{-3}$  respectively. This extrapolated distribution is shown in Figure 5.9 and exhibits a rolloff with energy that is similar to typical (solar maximum) AE8 fluxes, but tends to underestimate such fluxes by as much as a factor of a few hundred in the few 100 keV – few MeV range.

The simple analytical distribution function given above can be used to compare our results with past work (as well as the results obtained on various  $L$ -shells among themselves), but lacks certain features necessary when producing ‘global’ views of the MR whistler driven precipitation signatures. Firstly, the actual trapped energetic particle fluxes are clearly  $L$ -dependent, producing the well-known radiation belt zones (inner belt, outer belt, and slot region shown in Figures 5.9 and 5.10). Secondly, the

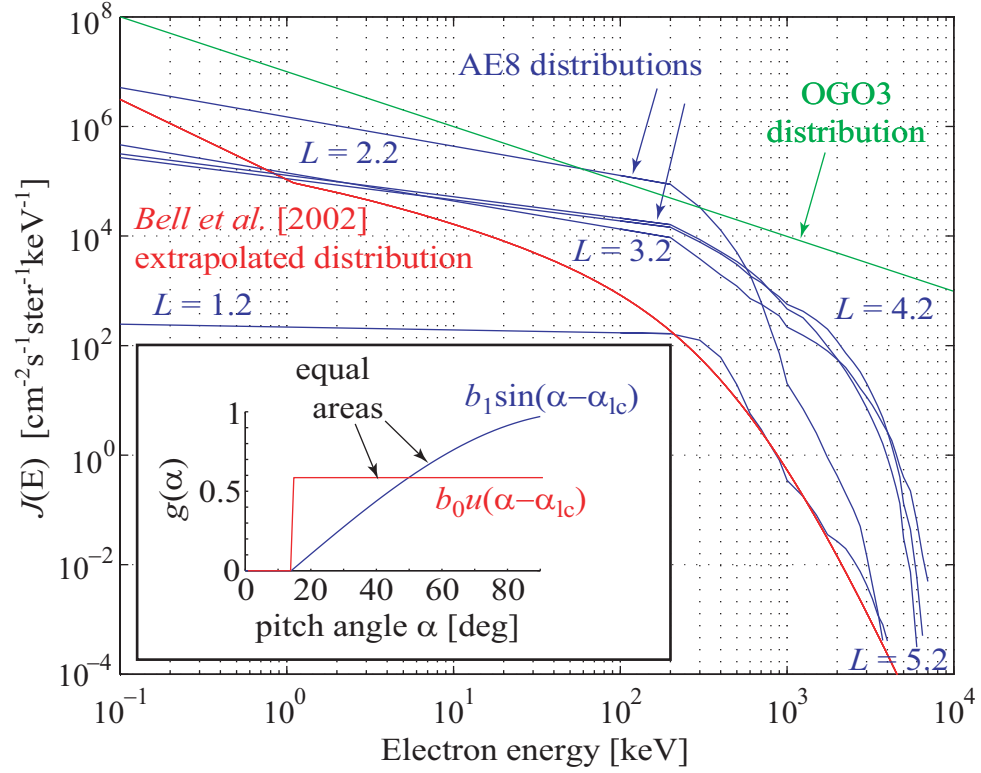


Figure 5.9: Energetic electron fluxes calculated using the AE8 model (blue curves) at  $L = 2.2, 3.2, 4.2$ , and  $5.2$ , and the extrapolated analytical distribution of *Bell et al.* [2002] (red curve). The inset shows the ‘sine’ and ‘square’ pitch-angle distributions associated with the AE8 and analytical distributions respectively.

energy spectrum not only scales with  $L$ -shell, but the energy  $e$ -folding factor is  $L$ -dependent and must be taken into consideration. Finally, a unique feature in the present work that distinguishes it from past work is the increased duration of the precipitation signature, due to the relatively long-lived ( $\sim 10$  sec) MR whistler waves. Previously [*Inan et al.*, 1978; *Chang and Inan*, 1985a; *Jasna*, 1993; *Lauben et al.*, 2001], it was assumed that only the first equatorial crossing was important for wave-induced particle precipitation, and thus only the first equatorial crossing was modeled, so that the resonant electrons would only experience one counter-streaming first-order gyroresonant interaction. It was thus plausible that a fresh particle population would enter the wave-packet with a sharp cutoff at the loss-cone, interact with the

wave resulting in erosion of the near-loss-cone distribution and that the eroded loss-cone distribution would not be encountered again by the wave. In this work, we consider many harmonic resonance interactions and the MR whistlers endure for tens of seconds, providing ample time for the same population of particles to mirror many times between hemispheres. Our solution has been to assume a simple equilibrium loss-cone distribution after *Walt et al.* [2002] (or a simplified form of *Vette* [1991]) of the form  $j_0(E, L) \sin(\alpha - \alpha_{lc})$  where  $j_0$  is found by integrating out the pitch angle dependence and comparing to the predicted model fluxes  $J(E, L)$ . We can then assume that the flux removed by the MR whistler-wave is immediately replenished from higher pitch angles, such that the equilibrium distribution remains constant for the duration of the MR whistler driven precipitation event.

Analytically, this equilibrium pitch angle dependence is treated using a first order Taylor series expansion as shown in Figure 5.8d, which is a good approximation within a few degrees of the loss cone where most of the pitch-angle scattering takes place. Using the AE8 model with the sinusoidal loss-cone distribution is expected to give realistic values of precipitation flux in the inner magnetosphere that are directly comparable to current or future observations.

## 5.2 Simulation results

The results of selected simulation runs are presented in the remainder of this chapter. We begin by contrasting the detailed differential number flux signatures at two representative  $L$ -shells ( $L = 2.3$  and  $L = 3$ ) to highlight some of the typical features, and show the variation of these features with  $L$ -shell. We then compare the corresponding energy flux signatures obtained by integrating the differential number flux plot above various energy thresholds. The above procedure is repeated for a range of  $L$ -shells between 1.3 and 5.5 sampled at  $0.1L$  intervals, obtaining energy flux versus time signatures throughout the inner magnetosphere which we compile into a ‘global’ view of the precipitated energy flux due to a single lightning discharge.

To make the global view information directly comparable to experimental observations, in particular low altitude satellites or ground-based observations, we convert the

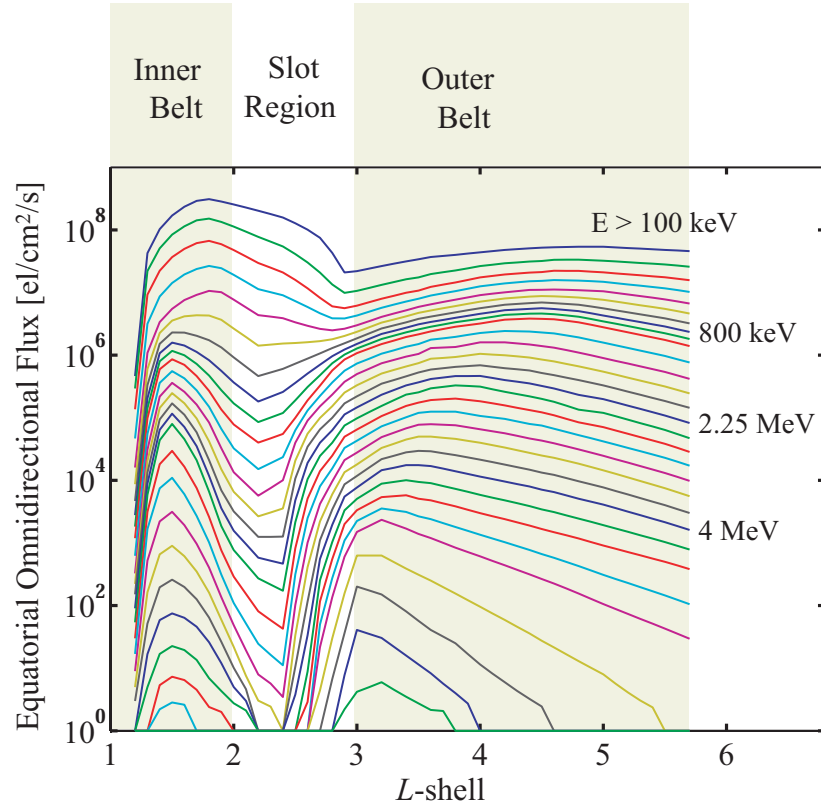


Figure 5.10: Equatorial omnidirectional flux of energetic radiation belt particles used in the computation of precipitated flux, calculated using AE8 model [Bilitza, 2001].

$L$ -shell dependence to latitudinal dependence and extrapolate the precipitation curves in longitude. By transforming from geomagnetic to geographic coordinates, we are left with a time-sequence of geographic patches representing the affected ionospheric region, such as would be observed by means of subionospheric VLF transmitter signal propagations [Inan *et al.*, 1988]. The time sequence of geographic “ionospheric perturbation” patches is integrated with respect to longitude and time to obtain the energy and number of electrons deposited as a function of  $L$ -shell (Figure 5.22).

### 5.2.1 Differential number flux

The precipitating differential number flux signatures at the ionospheric end points (‘feet’) of two different  $L$ -shells are compared in Figure 5.11. The left and right

columns show results for  $L=2.3$  and  $L=3$ , and the top and bottom panels represent the northern and southern hemispheres respectively. The energy is shown in keV on the ordinate, time in seconds on the abscissa, and differential number flux in electrons  $\text{cm}^{-2}\text{sec}^{-1}\text{keV}^{-1}$  on the color scale. The lightning source latitude was located at  $\lambda_s = 35^\circ$  and we have used the extrapolated analytic function of *Bell et al.* [2002] with an assumed square loss-cone distribution for the trapped energetic particle flux.

In examining Figure 5.11, certain common features are readily apparent in all the panels: there is a large band of precipitation between a few hundred eV and  $\sim 10$  keV, peaking at  $\sim 1.5$  keV. This intense flux is due to Landau resonance [also known as the longitudinal resonance, or zero-order cyclotron resonance since it is equivalent to the  $m = 0$  mode in (2.27)] which scatters the lower energy particles into the loss cone. While the Landau resonance itself is less efficient than the ( $m \neq 0$ ) gyroresonance modes resulting in lower average pitch-angle changes, the abundance of lower energy particles compensates for this inefficiency, producing significantly higher number fluxes than other resonance modes.

Near  $\sim 10$  keV the Landau resonance flux becomes weaker with energy and an effective gap in energy is created until a few tens of keV. The fact that Landau interactions occur with particles of such high energies ( $\sim 10$  keV) comes about due to off-equatorial interactions at high wave-normal angles as shown in Figure 5.12. The absence of precipitated flux in the energy band between  $\sim 10$  keV and  $\sim 80$  keV comes about due to the fundamental shift in the physical mechanism coupling particle and wave, from longitudinal resonance to cyclotron resonance with no intermediate stages, and is indicated by the yellow band in Figure 5.12. The precipitated flux above  $\sim 80$  keV is due to cyclotron resonance of energetic particles with the wave. There are multiple ‘swaths’ of precipitation occurring between 0 and  $\sim 6$  sec in Figures 5.11a and 5.11b, and between 0 and  $\sim 14$  sec in 5.11c and 5.11d, resulting from the magnetospheric reflections (and thus multiple equatorial crossings) of the whistler wave packet. Since the wave-particle interaction is generally most efficient near the geomagnetic equator [*Helliwell*, 1967; *Inan et al.*, 1989], these swaths appear discrete, descending in energy with time commensurate with the varying  $f-t$  structure of the underlying wave, and to a lesser degree due the longer flight time to the ionosphere of



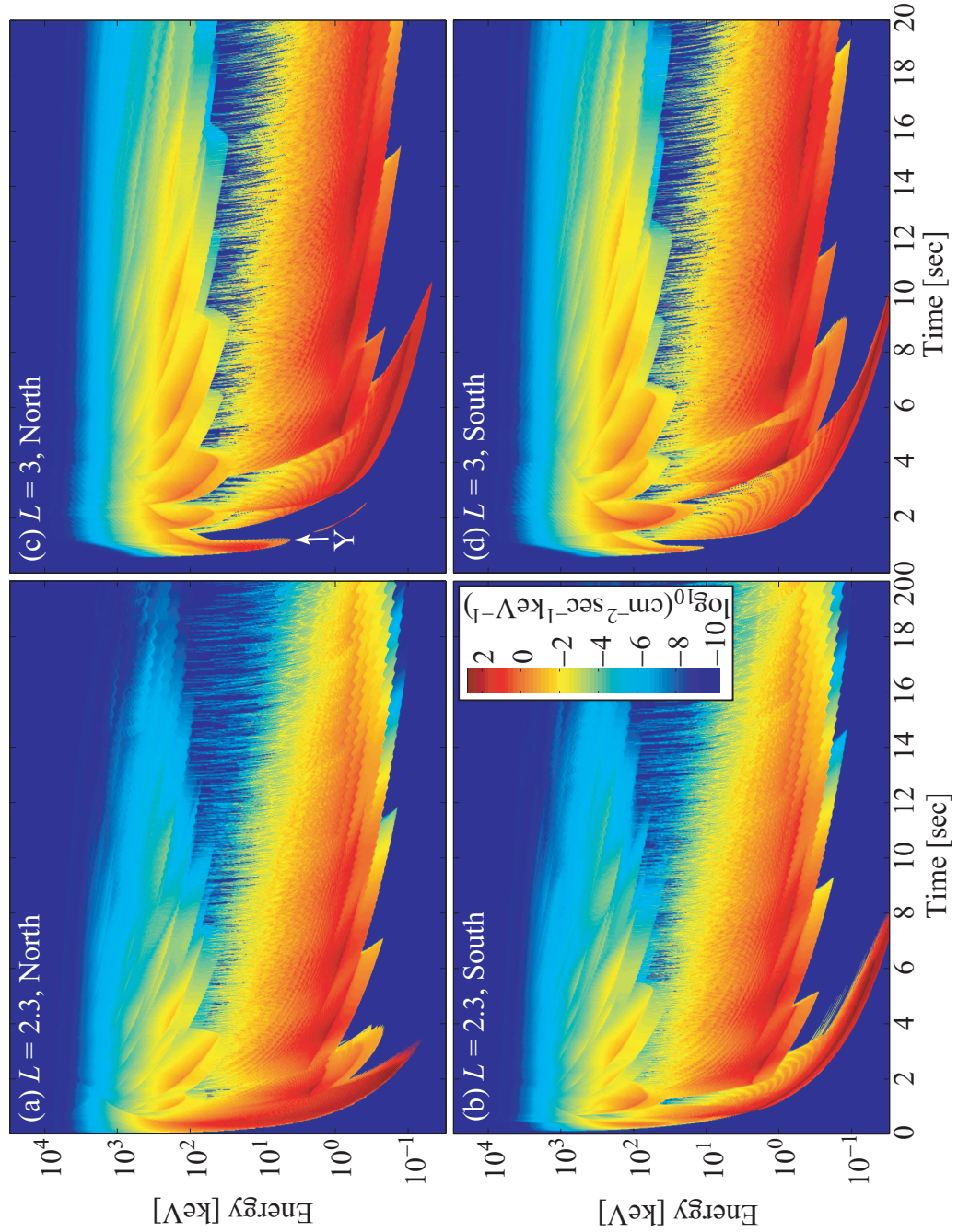


Figure 5.11: Precipitated differential number flux signatures at 100 km altitude, due to a lightning discharge at  $\lambda_s = 35^\circ$  at  $L = 2.3$  and  $L = 3$  in the northern and southern hemispheres, with color-scale as shown.

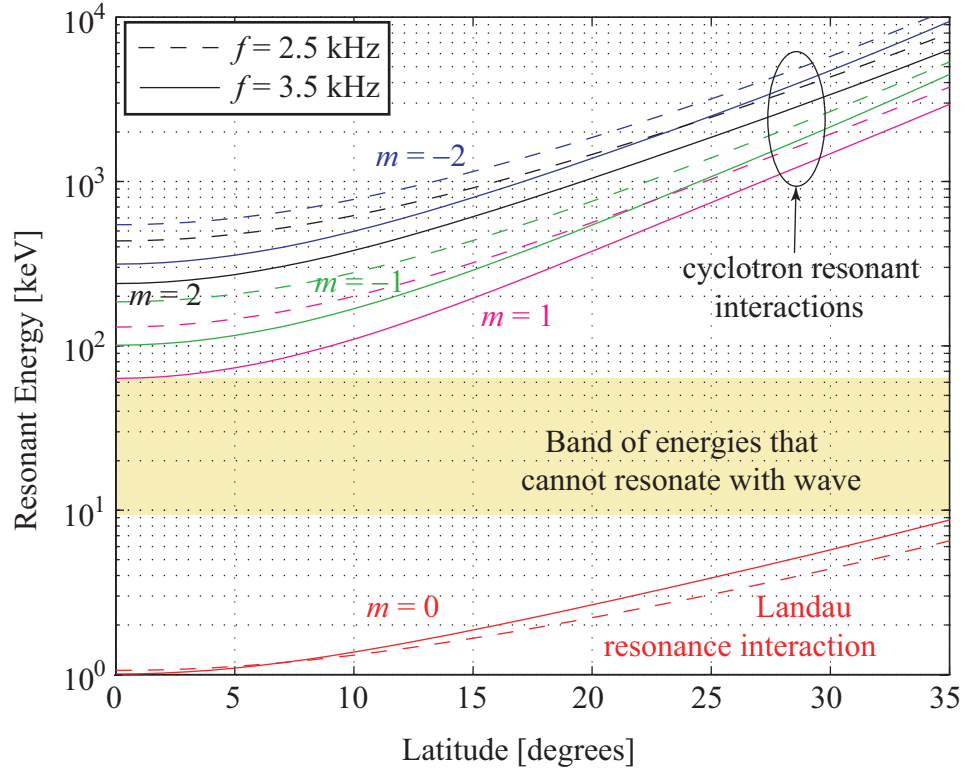


Figure 5.12: Resonant energies of electrons as a function of geomagnetic latitude for wave frequencies  $f = 2.5$  kHz (dashed line) and  $f = 3.5$  kHz (solid line),  $\theta = 80^\circ$  for harmonic resonances  $m = -2$  to 2.

lower energy particles. The first gyroresonance ‘pulse’ in Figure 5.11a,b appears very broad in energy because the first hop of the whistler is wideband, containing frequency components from 200 Hz to 60 kHz, the majority of which ( $\sim 8 - 60$  kHz) do not magnetospherically reflect and are absorbed in the medium after the first equatorial traverse. These higher frequency components resonate with lower energy particles as is implied by (5.1), thus stretching the energy band of precipitated particles to very low levels only in the first pulse. In the context of this discussion, it should be noted that the dependence of resonant energy on wave frequency is not simple, as it also involves the wave normal angle [through (5.1)], determined in the course of the computation of the ray path.

A similar plot of differential number flux is shown in Figure 5.11c,d for  $L = 3$ . The

same broad features are apparent in this plot: an intense band of low energy precipitating particles due to the Landau resonance, absence of precipitation at energies of a few tens of keV, and a higher energy component of multiple swaths of precipitating electrons due to the gyroresonant interactions.

We illustrate the points discussed above by considering a simpler situation, shown in Figure 5.12 where the resonant energies of electrons are plotted as a function of geomagnetic latitude for two different wave frequencies  $f = 2.5$  kHz (dashed line) and  $f = 3.5$  kHz (solid line), a wave normal angle  $\theta = 80^\circ$  and parametrized in harmonic resonance modes  $m = -2$  to  $2$ . We highlight in yellow the band of energies that do not resonate with the chosen wave frequencies over the latitude range shown, noting that they fall in a similar energy range ( $E \simeq 10$  to  $80$  keV) to that in Figure 5.11. The resonant energy of particles increases with latitude for all resonance modes, and is typically higher for the lower frequencies for non-longitudinal wave-particle interactions.

Returning now to Figure 5.11, a number of interesting and telling differences between the precipitation signatures at  $L = 2.3$  and  $L = 3$  are apparent. Firstly, the time of arrival of the first pulse at the ionosphere in both northern and southern hemispheres is significantly greater in Figure 5.11c,d than in Figure 5.11a,b implying a general motion of the precipitation footprint to higher latitudes with time, in agreement with the observations of *Johnson et al.* [1999] and consistent with the theoretical predications of *Lauben et. al* [2001]. The poleward motion of the precipitation footprint with time is due to the longer distance (and hence longer time) that whistlers must travel to illuminate higher  $L$ -shells compared with the lower  $L$ -shells, together with the increasing flight time of energetic electrons from equatorial regions to the ionosphere with  $L$ -shell. Our model results have been verified for the first hop of the oblique whistler and similar conditions, against those of *Lauben [Ibid]* with excellent agreement.

Secondly, the duration of the event at  $L = 3$  is longer than at  $L = 2.3$ , respectively requiring  $\sim 14$  sec versus  $\sim 6$  sec for the precipitation of the main portion of the gyroresonant flux. Lastly, note that the first precipitation pulse is narrower in energy in panels c and d, compared to panels a and b, since the majority of the injected

whistler wave energy remains below  $L = 3$  on its first equatorial traverse, does not magnetospherically reflect, and is absorbed in the medium thereafter.

Other interesting features to note in Figure 5.11c are the “Y” structures (i.e., the apparent bifurcation of the first precipitated flux pulse as it is viewed from lower to higher energies) at  $t \simeq 1$  sec,  $E \simeq 100$  keV, reminiscent of those reported in *Lauben* [1999, p.39]. These structures are caused by different frequency components (of a single wave packet) at different wave normal angles that interact with particles of the same energy but at different latitude locations on the field line, resulting in different arrival times at the ionosphere and the appearance of a ‘gap’ between the two limbs of the “Y-structure”.

At  $t \gtrsim 4$  sec, and  $E \sim 700$  keV, Figures 5.11c and 5.11d show distinct ‘secondary’ swaths of precipitation, appearing fainter and at higher energies than the more intense primary swaths beneath them. These features are a result of second order harmonic gyroresonance interactions, also visible in 5.7. At even higher energies, the higher order gyroresonance scattering merges into the diffuse drizzle of precipitating particles, and loses its discrete appearance. The secondary swaths are also visible in Figure 5.11a and 5.11b though not as clearly.

We note that in Figure 5.11 some diagonal striations are visible in the top portion of the Landau precipitation flux at  $E \sim 10$  keV. These are due to numerical noise related to the latitude discretization and are not a physical feature. As discussed in Section 5.1.1, increasing the latitude sampling resolution (i.e., discretizing latitude in  $< 1^\circ$  bins) reduces the striations, resulting in the appearance of a smoother precipitation signature, but degrades the accuracy of the overall pitch-angle change calculation.

### 5.2.2 Energy flux

Using the information presented in Figure 5.11 we now calculate the precipitated energy fluxes  $Q(t)$  shown in Figure 5.13, by integrating the differential number fluxes  $\Phi(E, t)$  above various energy thresholds using (5.3b).

This calculation is done to facilitate comparison with ground based measurements,

since ionospheric effects (e.g., secondary ionization, optical emissions) are generally interpreted in terms of the precipitated energy flux. As discussed in Section 5.2.1 in connection with Figure 5.11, the timing differences between the two  $L$ -shells are readily apparent, the energy flux at  $L = 3$  arriving later, and enduring longer than that at  $L = 2.3$ .

By comparing the energy fluxes above various thresholds, we can infer the contributions of the different harmonic resonance modes to the total energy flux. Most notably, the energy flux curves  $> 0$  keV and  $> 100$  keV show little difference, implying that the intense Landau precipitation fluxes visible in Figure 5.11 contain little energy and hence do not significantly contribute to ionospheric effects (the two curves differ in some places, but this is due to the lower energy gyroresonant particles). Using the same technique, it is evident that  $\sim 80\%$  to  $90\%$  of the energy flux is composed of electrons in the range 100 keV to 500 keV, and  $> 99\%$  of the energy flux is composed of electrons  $< 1$  MeV. It should be noted, however, that ionospheric effects are also determined by the altitude of penetration, which in turn is dependent on particle energy [Banks *et al.*, 1974]. For example, while  $> 100$  keV electrons deposit their energy at D-region altitudes ( $< 90$  km), any perturbations at E- and F-region altitudes can only be produced by tens of keV electrons.

The curves shown in Figure 5.13 all exhibit a periodic rippled structure which is attributed to the multiply reflecting nature of the whistler wave packet and the fact that interactions are most efficient near the geomagnetic equator. A number of interesting features can be noted by examining the maxima of the various curves. Firstly, as in panel (a), alternate maxima seem to be more intense (e.g.,  $a_1, a_3, a_5$ ), with the intervening maxima ( $a_2, a_4$ ) being less intense. Examining the precipitating energy flux in the conjugate hemisphere, this pattern is again evident but the primary ( $b_2, b_4$ ) and secondary ( $b_1, b_3, b_5$ ) maxima are now reversed relative to those in the northern hemisphere.

The structure of alternating maxima can be understood by analyzing the propagation and characteristics of the whistler wave that drives the precipitation. In Figure 5.14 we plot a representative ray injected at  $35^\circ$  latitude, with a frequency of 2 kHz and examine the first 10 seconds of propagation. As can be seen from panel (a) or (d)

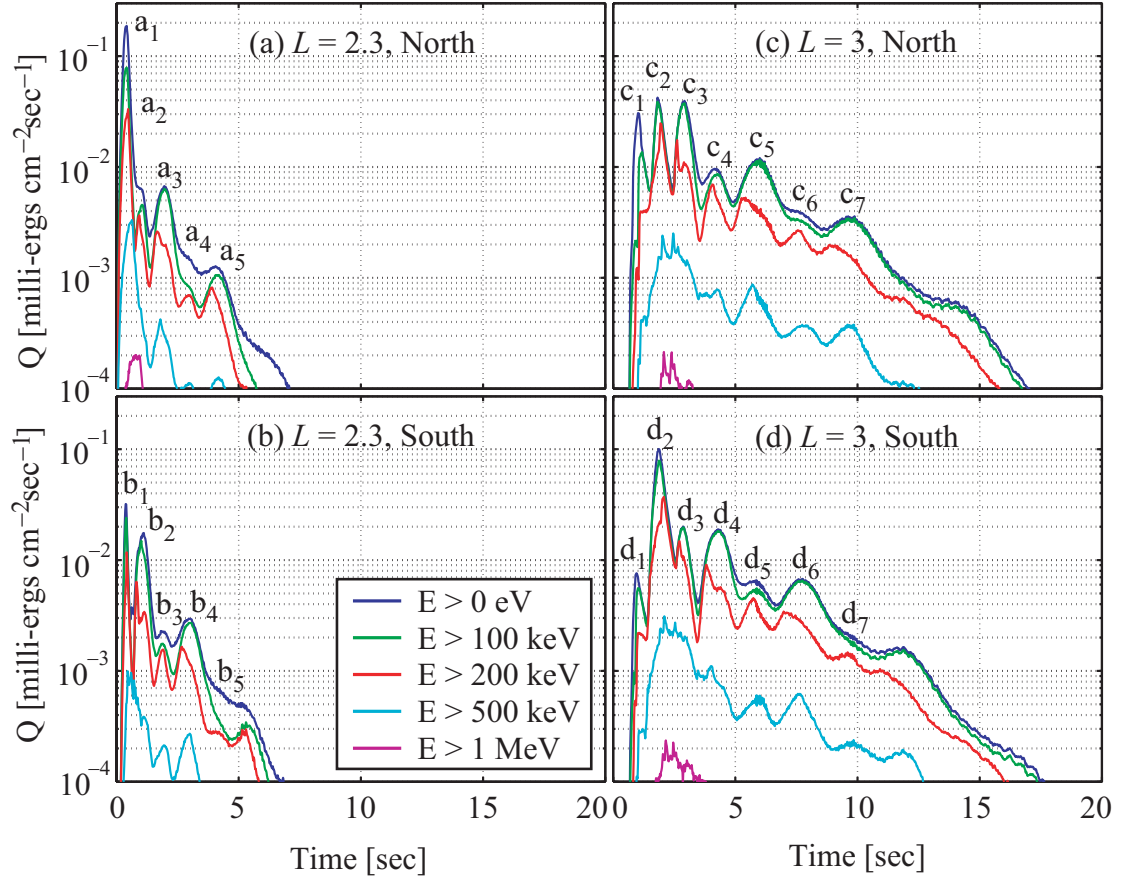


Figure 5.13: The precipitated differential number flux of Figure 5.11 integrated above various energy levels as indicated, giving energy flux. The panels a-d correspond to those in Figure 5.11.

(blue curve) this frequency component illuminates the  $L \simeq 3$  region also indicated by Figure 4.2, so we use it as a crude proxy for the wave packet, and use Figure 5.13c,d to compare wave and particle behavior at  $L=3$ .

We begin by noting that the first pulse in the northern hemisphere ( $c_1$ ) is larger than that in the southern hemisphere ( $d_1$ ), which is similar to that at  $L=2.3$  where  $a_1 > b_1$ . The second pulse also shows the same trend in both  $L$ -shells with  $b_2 > a_2$  and  $d_2 > c_2$ , but note that the magnitude of the precipitated energy flux in  $d_2$  is significantly larger than  $c_1$ , unlike that of  $L=2.3$ . The reason for this can be inferred by examining Figure 5.14a, where the ray injected directly above the lightning

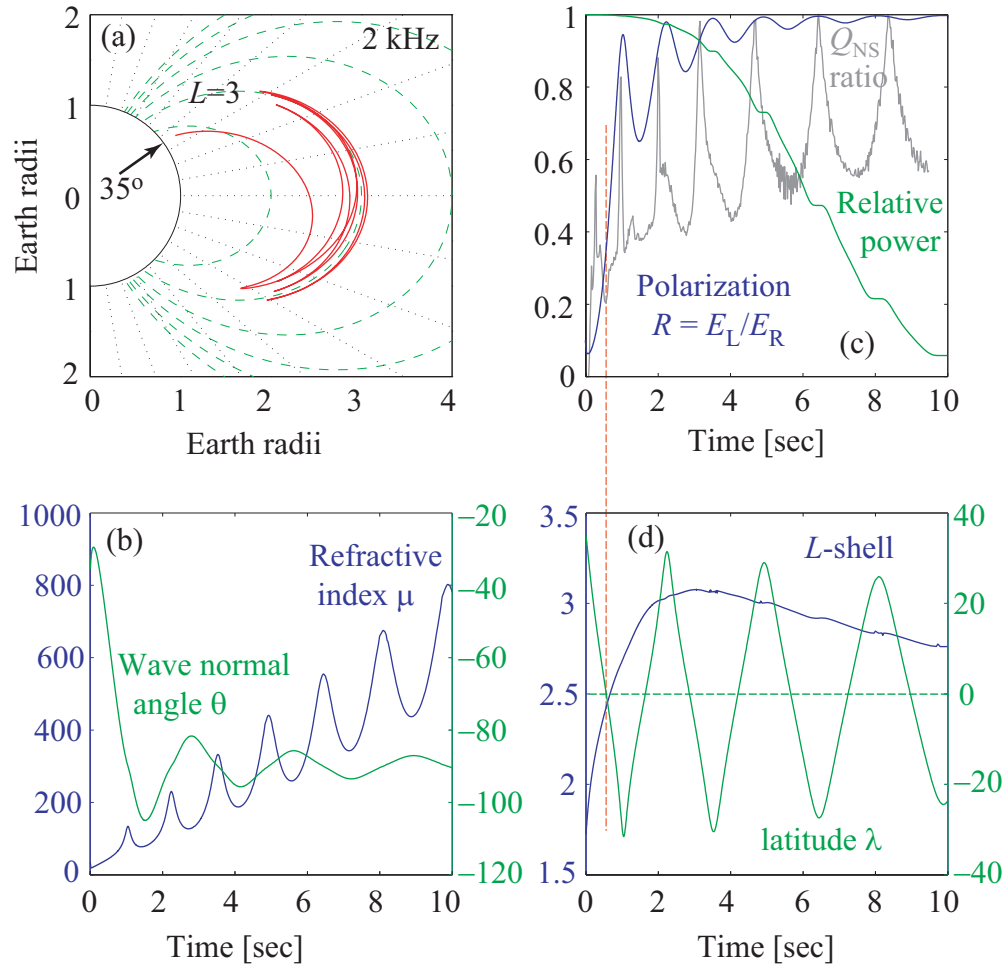


Figure 5.14: A 2 kHz ray showing (a) ray path, (b) refractive index and wave normal angle, (c) polarization ratio, relative power, and ratio of primary to secondary  $Q$  peaks (in Figure 5.13), and (d)  $L$ -shell and dipole latitude, for 10 sec of propagation.

discharge (and hence carrying most of the power) entirely misses  $L = 3$  on its first hop, but illuminates it on its second hop causing the precipitation to be more intense. The first precipitation maxima  $c_1$  and  $d_1$  are caused by the first equatorial traverse of rays injected at higher latitudes ( $\lambda > 35^\circ$ ) than our computed ray and hence carry less wave power, in accordance with (2.1) since they are further from the source.

The alternating primary maxima in energy flux are attributed to the fact that the wave-particle interaction is always more effective in the counterstreaming direction.

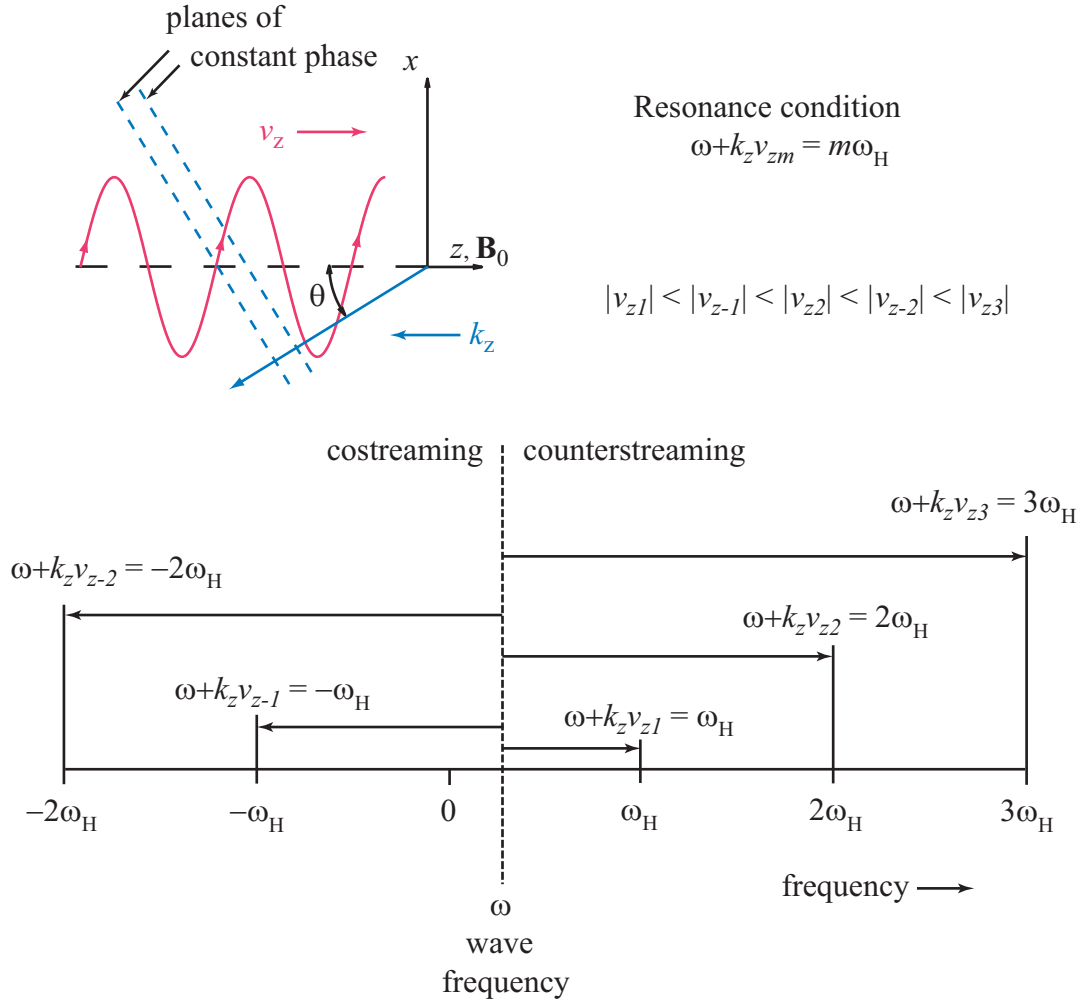


Figure 5.15: Qualitative illustration of the behavior of  $v_z$  for various resonance modes  $m$  for resonant wave-particle interactions.

Hence, on the first hop the wave travels south and the primary precipitation peak ( $c_1$ ) is in the north. After  $\sim 1$  sec, the wave experiences a magnetospheric reflection at  $\lambda \simeq -30^\circ$ ,  $L \simeq 2.6$  according to Figure 5.14d, and begins to travel north, resulting in a primary precipitation peak in the south ( $d_2$ ).

There are a number of reasons why counterstreaming interactions result in higher precipitated fluxes: firstly, according to the resonance condition, (2.27), when the wave and particle move in opposite directions, the Doppler shift resulting from the relative motion naturally raises the apparent wave frequency as shown in Figure



5.15 for  $v_{z1}$ , whereas a particle moving in the same direction as the wave lowers the apparent wave frequency  $v_{z-1}$ . For resonance in the counterstreaming mode, the particle only needs to raise the wave frequency to match a multiple of its gyrofrequency ( $v_{z1}$ ,  $v_{z2}$ , or  $v_{z3}$ ), whereas in the costreaming interaction the particle needs to lower the wave frequency to zero, and then keep lowering it until the apparent frequency is equal to a negative multiple of the particle's gyrofrequency ( $v_{z-1}$ ,  $v_{z-2}$ , or  $v_{z-3}$ ). The particle velocity required for counterstreaming gyroresonance is thus lower than that required for costreaming gyroresonance, for the same absolute value of the resonance harmonic  $|m|$  (because  $\omega$  is positive), and increases with  $m$  such that  $|v_{z1}| < |v_{z-1}| < |v_{z2}| < |v_{z-2}| < |v_{z3}|$  and so on. The lower velocities involved in counterstreaming interactions compared with costreaming interactions also imply that the particle moves slower through the wave packet, experiencing a larger cumulative deflection due to the wave.

Since available particle fluxes fall rapidly with energy (Figures 5.9 and 5.10), even if costreaming and counterstreaming particles did experience the same deflection due to the wave, the energy flux of the counterstreaming particles would still be higher because of the relative abundance of the lower energy particles. For instance, referring to Figure 5.9 again, we see that at  $L \simeq 2.2$ , increasing the energy of resonant electrons from 100 keV to 1000 keV, results in a decrease of the trapped flux by a factor of  $\sim 1000$ , leading to an overall precipitated energy decrease of a factor of  $\sim 100$ .

In addition to the points discussed above, the counterstreaming and costreaming precipitated energy fluxes in the northern and southern hemispheres are asymmetric for yet another reason. In the development of the wave-particle interaction equations, we used (2.23) to decompose the elliptically polarized oblique whistler wave, into left- and right-hand circularly polarized (LHCP and RHCP) components. Since the electrons gyrate about the magnetic field line in a right-hand sense, they can only resonate with electromagnetic waves which are also “apparently” RHCP, and rotating at the same frequency. As we have discussed above, when the wave and electron approach each other (counterstreaming) the RHCP component of the wave is involved, and since  $\omega < \omega_H$  for the whistler mode, its frequency is Doppler shifted to higher values to resonate with the particle. However, in the costreaming mode the particle overtakes the wave, and in fact changes the apparent sense of rotation such that it

is actually the LHCP component of the whistler that interacts with the electron, its left-hand polarization appearing as a right-handed rotation which matches the gyrofrequency of the electron. This realization leads to the question of the degree to which the relative magnitudes of the LHCP and RHCP control the north-south asymmetry of the precipitating energy flux.

We address this question in Figure 5.14c, where we plot the ratio  $R$  of the LHCP electric field magnitude to the RHCP electric field magnitude (blue curve). Initially the ratio  $R$  is very low indicating that the wave is almost entirely RHCP (in fact, according to (2.9) for parallel propagation  $\mathbf{k} \parallel \mathbf{B}_0$ , the whistler is strictly RHCP), and the wave normal angle  $\theta$  in panel (c) is  $\lesssim 60^\circ$  near the geomagnetic equator on the first hop. However,  $R$  increases rapidly and within  $\sim 4$  seconds becomes  $> 0.9$  indicating that the LHCP and RHCP components are almost equal in magnitude. In order to compare the polarization ratio  $R$  with the ratio of costreaming versus counterstreaming precipitated fluxes, we show in Figure 5.14c the “ $Q_{\text{NS}}$ -ratio” (grey), which is obtained by dividing the blue curve ( $E > 0$  keV) of Figure 5.13c by the blue curve of Figure 5.13d, and inverting this ratio when it is  $> 1$ , thus giving the ratio of the secondary flux maxima in one hemisphere to the primary flux maxima in the other hemisphere. The hemispherical energy flux ratio  $Q_{\text{NS}}$  curve was shifted forward by 0.5 sec to roughly compensate for the electron flight time from the equator to the ionosphere.

As shown in Figure 5.14c, at the first equatorial crossing of the wave (panel d, green curve) the hemispherical energy flux ratio  $Q_{\text{NS}}$  and polarization ratio  $R$  are almost identical, but subsequent equatorial crossings indicate that  $Q_{\text{NS}}$  is much lower than  $R$ . We thus observe that the distribution of power among LHCP and RHCP wave components plays a smaller role in controlling the hemispheric precipitation asymmetry compared to the factors described above. The fact that the  $Q_{\text{NS}}$  and  $R$  are approximately equal on the first equatorial traverse is due to the fact that the wave packet contains a significant amount of power in the 8–60 kHz frequency range, and that the ray paths in this band do not experience magnetospheric reflections so that this effect is only evident on the first hop. These higher frequency components also resonate with electrons that are more separated in energy in the costreaming and

counterstreaming modes as implied by (2.27) , and thus result in greater asymmetry in the precipitation and lower  $Q_{\text{NS}}$  due to the higher fluxes at lower energies.

Having examined the details of the precipitated energy flux at two selected  $L$ -shells, we now repeat the calculation of precipitated flux over a range of  $L$ -shells from 1.3 to 5.5 in  $0.1L$  increments, and examine the resulting ‘global’ view of the MR whistler driven precipitation event.

### 5.2.3 Global view of precipitated energy flux

We consider the response of the inner magnetosphere to the MR whistler wave by computing the precipitation flux induced on  $L$ -shells ranging from  $L = 1.3$  to  $L = 5.5$  in  $0.1L$  intervals. In the series of Figures 5.16–5.19 we plot the precipitated energy flux in panels (a) and (d) calculated in the same manner as described in the previous section 5.2.2, the precipitated number flux in panels (b) and (e), and the average precipitated energy  $\langle E \rangle = \Phi(L, t)/N(L, t)$  in panels (c) and (f) calculated by dividing the results of panel (a) by (b) and (d) by (e). The left and right columns correspond respectively to the precipitation flux in the northern and southern hemispheres, and the series of Figures 5.16–5.19 correspond to source lightning discharge latitudes  $\lambda_s = 25^\circ, 35^\circ, 45^\circ$ , and  $55^\circ$  respectively. In each of the panels the trapped energetic electron flux model AE8 is used together with a sinusoidal loss-cone distribution as discussed in Section 5.1.3 and shown in Figures 5.9 and 5.10, to represent the quiet-time equilibrium state of the radiation belts.

Since the earlier results detailed in Figures 5.11–5.14 were for a lightning discharge at  $\lambda_s = 35^\circ$ , we begin by analyzing Figures 5.17a,d. Firstly, we note (as above) the intense precipitation due to the first hop in the north, followed by the primary maximum in the south, then in the north again and so on, driven by the alternate north-south and south-north motion of the MR whistler wave packet. Secondly, evident in this global view is the fact that the average  $L$ -shell location of the precipitating electrons increases slowly with time, which is expected due to the behavior of the whistler-mode ray paths. The various frequency components of the MR whistler tend to settle on different  $L$ -shells, lower frequencies at higher  $L$ -shells and higher frequencies at

lower  $L$ -shells as shown in Figure 4.2 [Bortnik *et al.*, 2003a]. Since it is the lower frequency components that have the longest lifetimes (Figure 4.3) [Bortnik *et al.*, 2003a; Thorne and Horne, 1994] the wave energy appears to advance to higher  $L$ -shells with time as the higher frequency components that have settled at the lower  $L$ -shells are progressively absorbed by the suprathermal plasma.

The broad band of precipitation seen in both hemispheres in Figure 5.17a,d gradually transforms from a collection of discrete swaths, to a more diffuse precipitation signature after a few seconds. This behavior is a result of the disposition of the underlying whistler wave packet which is compact and distinct at the start but progressively undergoes more mixing (due to overlapping ray paths and dispersion), scattering electrons in pitch-angle in a more diffuse fashion. The first of the fine swaths in the beginning of the event was previously modeled (only for the first counter-streaming gyroresonance and only for the first equatorial traverse of the ray path) [Lauben, 1999; Lauben *et al.*, 2001] and experimentally observed by means of the subionospheric VLF method [Johnson *et al.*, 1999]. The tendency of the precipitation to rise in  $L$  as a function of time for the first hop of the whistler is due to a combination of the facts that whistler waves take a longer time to reach the geomagnetic equator of higher  $L$ -shells than at lower  $L$ -shells, and that the travel time of the scattered energetic particle from the near equatorial interaction region to the ionosphere also increases with  $L$ -shell.

The precipitating electron number flux shown in Figure 5.17b and 5.17e exhibits similar features to the energy flux except for the fact that the depression in precipitated fluxes at  $L \simeq 3$  due to the slot-region is more evident. The average energy of precipitating electrons shown in 5.17c,f indicates that typical average energies are in the tens to hundreds of keV.

It is particularly instructive to compare the precipitation signatures of the four lightning source latitudes:  $\lambda_s = 25^\circ$ ,  $35^\circ$ ,  $45^\circ$ , and  $55^\circ$  shown in Figures 5.16–5.19 respectively. Beginning with the first precipitated energy flux pulse, we see that for  $\lambda_s = 25^\circ$  this pulse starts at  $L \simeq 1.5$  and quickly rises in time to  $L \simeq 2.5$ . For  $\lambda_s = 35^\circ$ , the pulse moves from  $L \sim 2 \rightarrow 2.8$ . For  $\lambda_s = 45^\circ$ , the range is  $L \sim 2.6 \rightarrow 3.4$ ,

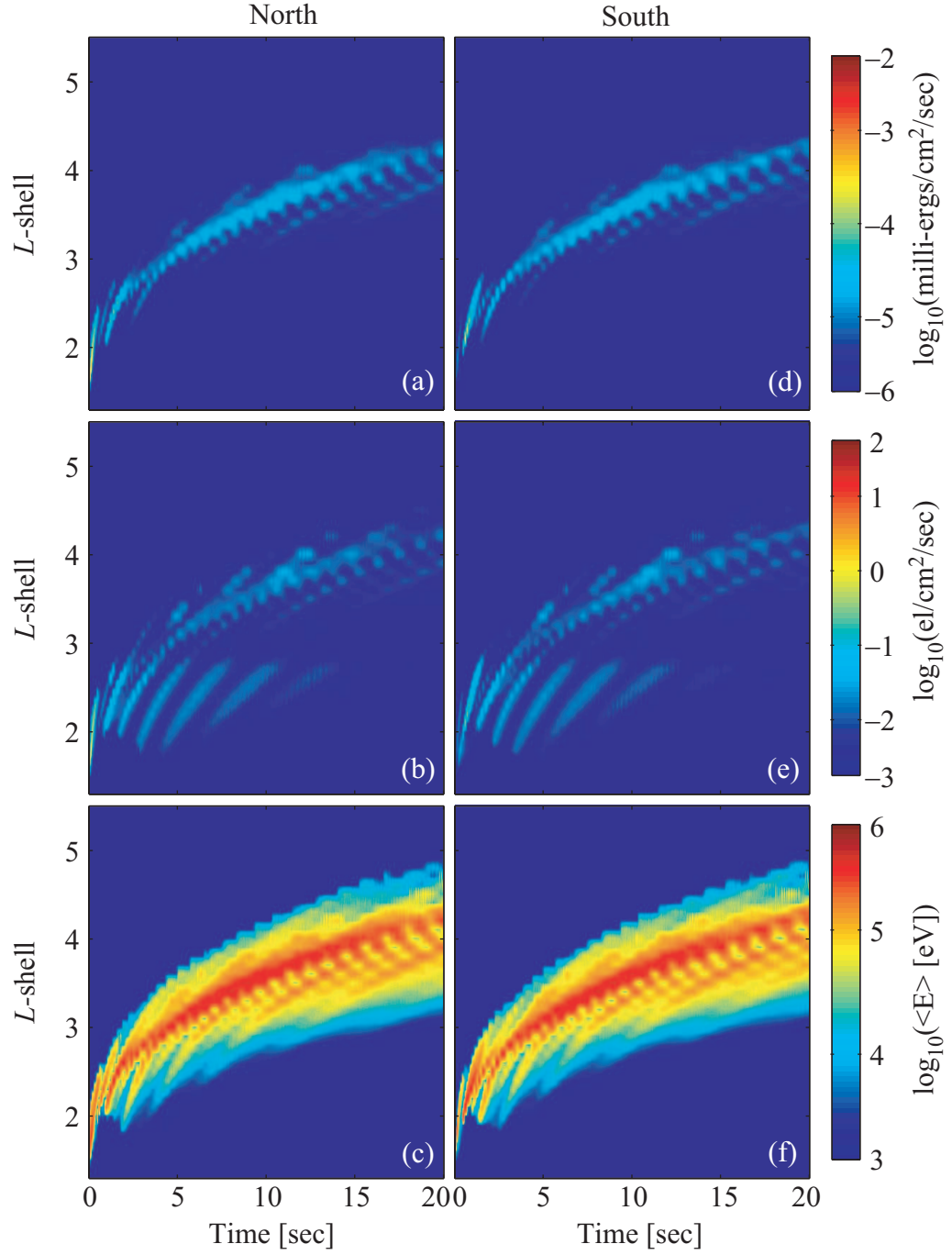


Figure 5.16: A global view of precipitated flux for  $\lambda_s = 25^\circ$ , (a) energy flux  $> 30$  eV, (b) electron number flux, (c) average energy of precipitated electrons, all in northern hemisphere, and (d), (e), (f) as (a) (b) (c) but in southern hemisphere.

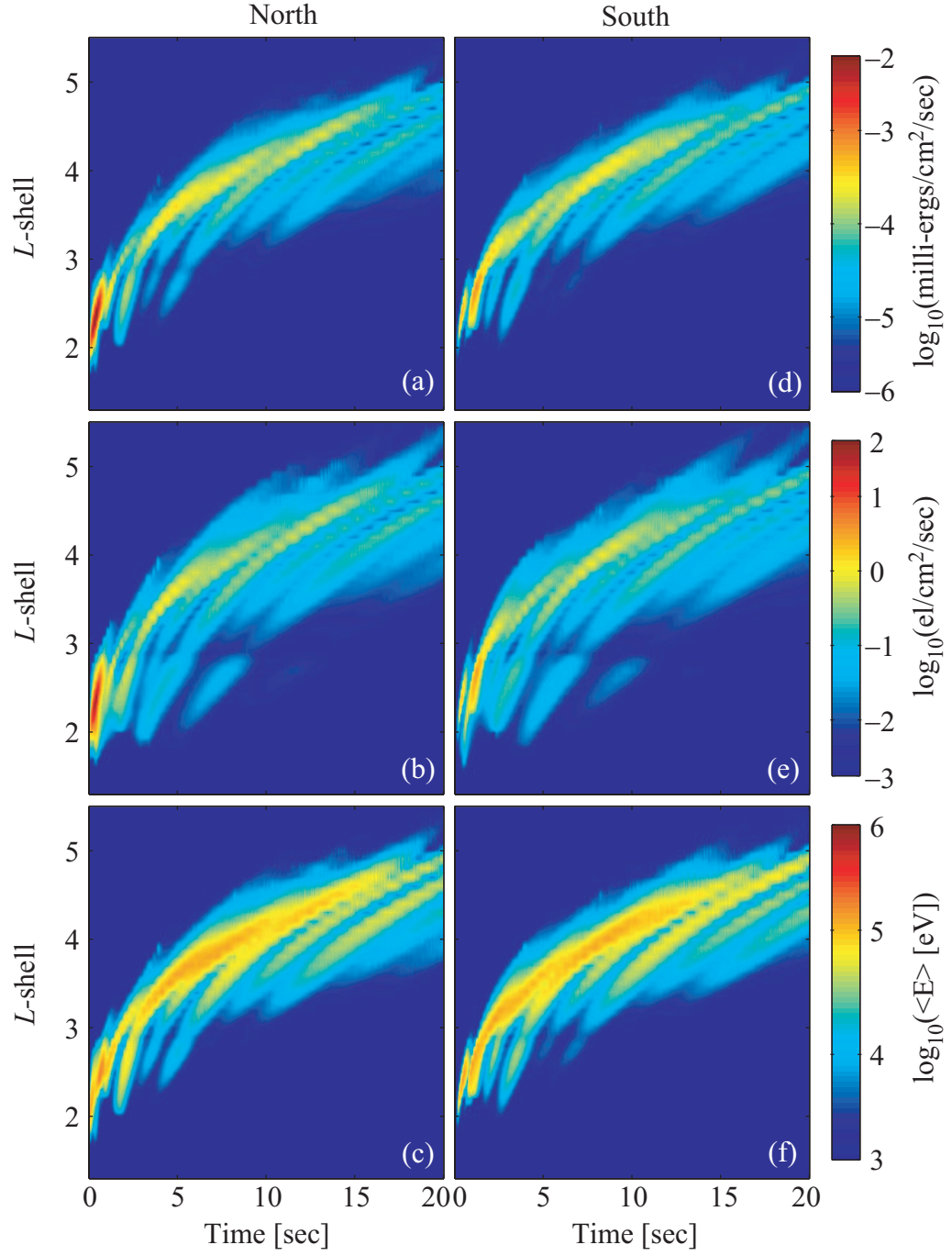


Figure 5.17: A global view of precipitated flux for  $\lambda_s = 35^\circ$ , shown in the same format as Figure 5.16.

and for  $\lambda_s = 55^\circ$ , it is  $L \sim 2.8 \rightarrow 3.5$ . In all cases the  $L$ -shell of the first pulse increases with increasing source latitude, but the latitudinal separation between the lightning discharge and the location of the precipitation pulse becomes narrower because the whistler ray paths do not move out as far in  $L$ -shell for higher latitude lightning strokes, and also due to the decreasing latitudinal separation on the Earth's surface at higher  $L$ -shells [Lauben *et al.*, 2001]. In addition, the period between subsequent pulses increases with increasing source latitude. This feature has already been noted in Section 4.3.1 with regard to Figure 4.6 concerning the wave structure of the causative MR whistler, and can be understood in view of the fact that waves injected at higher latitudes traverse longer field lines and thus take longer to complete consecutive magnetospheric reflections compared to waves injected at lower latitudes.

The behavior of the  $\lambda_s = 25^\circ$  case is interesting in that the peak precipitated energy flux in Figure 5.16a,d is roughly an order of magnitude lower in intensity compared to that of the  $\lambda_s = 35^\circ$  case. Moreover, the average energy of precipitated electrons shown in panels (c) and (f) is almost an order of magnitude higher. These two effects result from the fact that the injection latitude is low, and the injected frequency components remain mostly below the equatorial lower-hybrid-resonance (LHR) frequency, and move up relatively slowly in  $L$ -shell as shown in Figure 4.1a. As shown in Figure 5.14c, the wave normal angle for these waves quickly becomes very oblique and spends the majority of its time near  $\theta \simeq 90^\circ$ . However, in contrast to Figure 5.14c the refractive index value  $\mu$  does not tend to infinity because the refractive index surface is closed for  $f < f_{\text{LHR}}$ , so that while resonant energies become very high due to the low value of  $k_z$  (and subsequent high value of  $v_z$  through (2.27) or (5.1)), the wave itself does not become quasi-electrostatic, in fact, at  $\theta = 90^\circ$  the whistler-mode wave propagates normal to the field line in the so-called X-mode with moderate values of  $\mu$ . The precipitated fluxes due to the Landau resonance that are typically associated with high values of  $\mu$  and  $\theta$  do not dominate the overall number of precipitated electrons with low energy particles as they do for the  $\lambda_s = 35^\circ$  case, keeping the average energies high.

In Figures 5.16b,e a number of additional swaths of precipitation are observed in the range  $2 < L < 3$  for  $t > 5$  sec, which are not seen in the energy flux (5.16a,d)

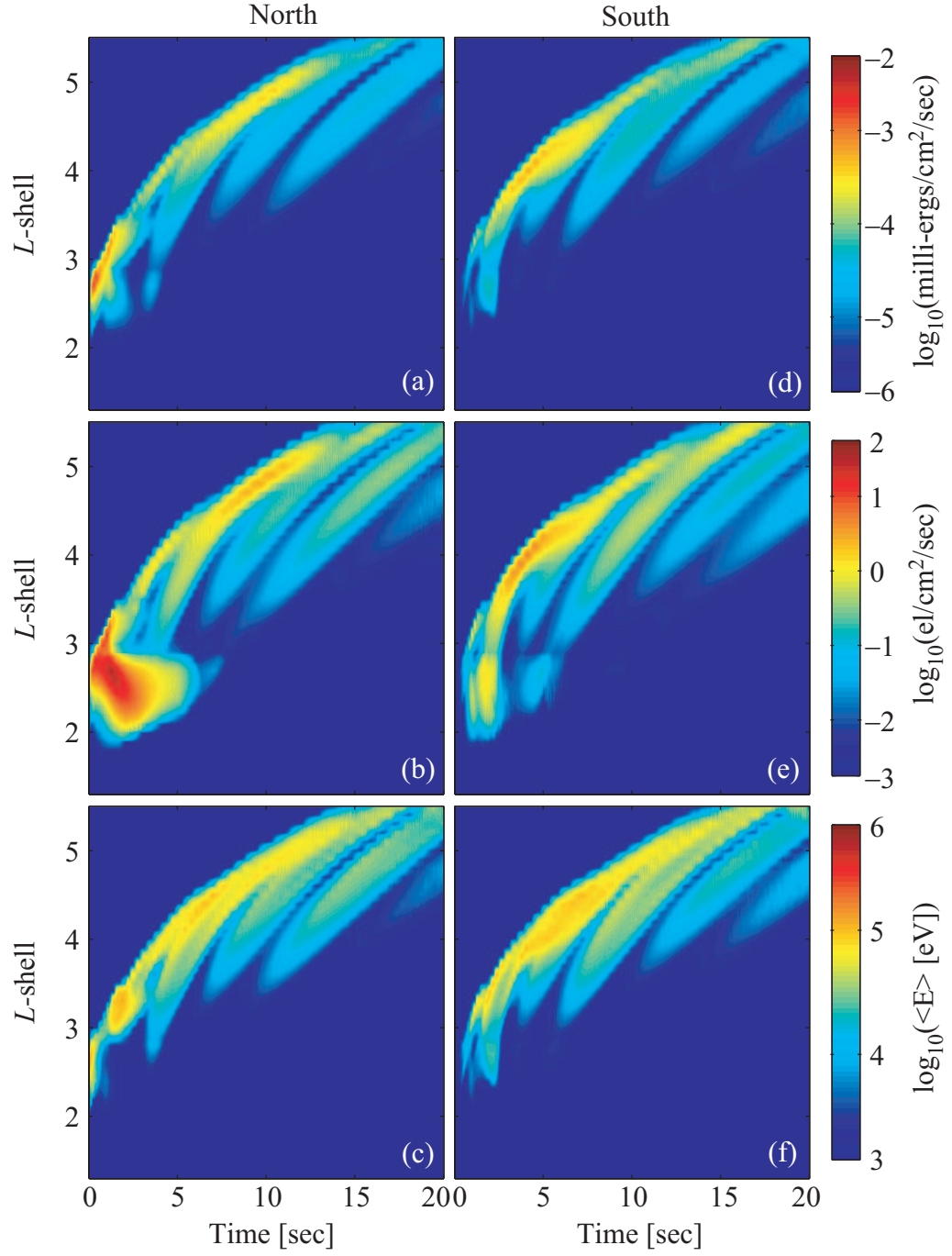


Figure 5.18: A global view of precipitated flux for  $\lambda_s = 45^\circ$ , shown in the same format as Figure 5.16.



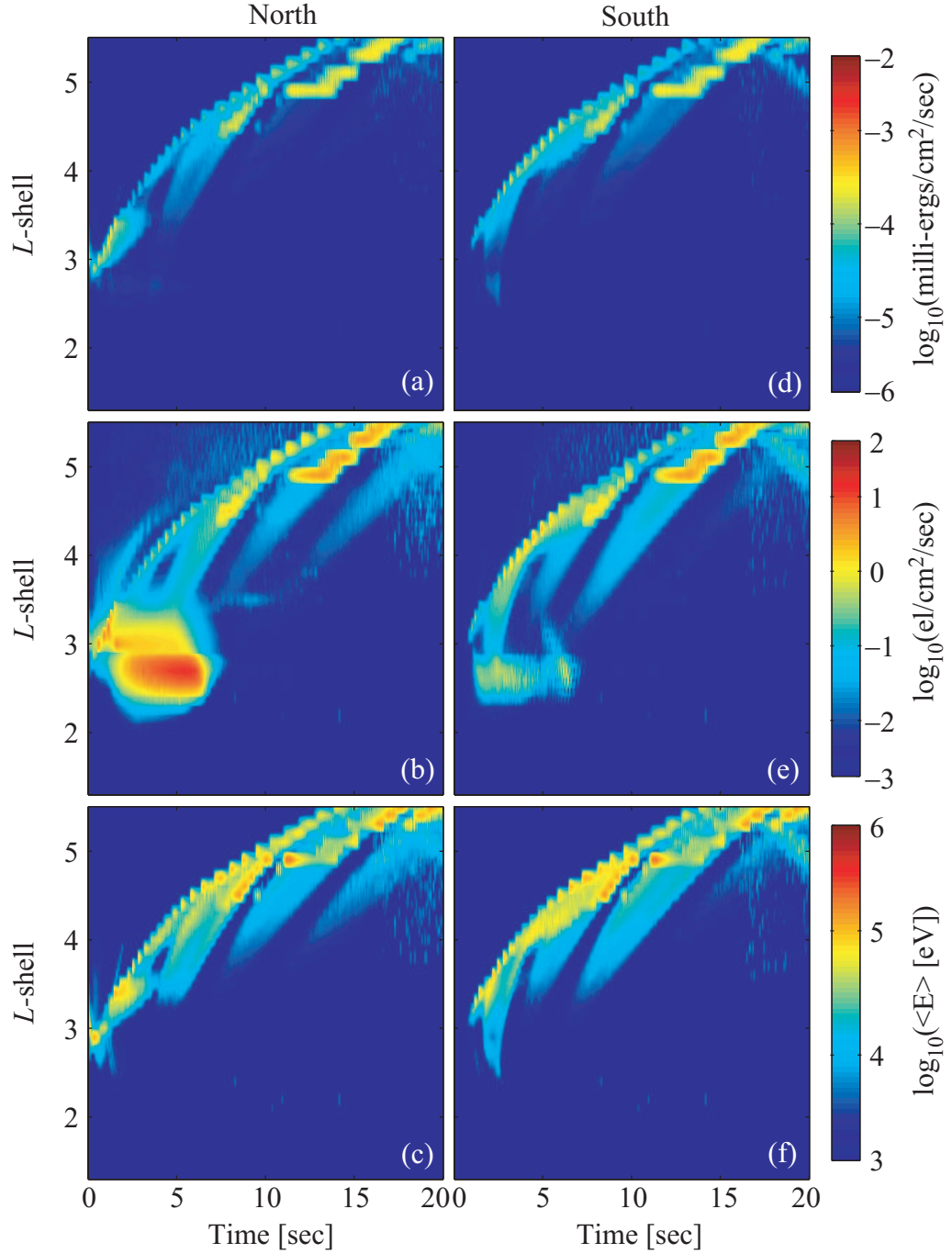


Figure 5.19: A global view of precipitated flux for  $\lambda_s = 55^\circ$ , shown in the same format as Figure 5.16.

or average energy (5.16c,f) because their magnitude drops below the threshold value used in these plots. These additional swaths result from the longitudinal (Landau) resonance driven by frequency components that have moved out sufficiently far in  $L$ -shell that their frequency matches the equatorial  $f_{\text{LHR}}$ , their refractive index surface transitions from a closed shape to an open shape (as illustrated in Figure 2.3 or 2.4) and the  $\mathbf{k}$ -vector tends to infinity causing the wave to become quasi-electrostatic. The swaths are seen initially at the lower  $L$ -shells because the higher wave frequency components tend to settle at lower  $L$ -shells and become electrostatic faster than the lower frequency components, and are observed only in the number flux because the primary interaction which causes their precipitation is the Landau (or longitudinal) resonance, which affects only the lower energy electrons ( $\lesssim 1$  keV). This lower energy population of electrons is relatively more abundant but contains relatively little energy, resulting in low values of precipitated energy flux and average energy that falls below the threshold used in plotting our figures.

While still on the topic of precipitation fluxes driven by the longitudinal resonance, we note the large maximum in number flux in Figures 5.18b and 5.19b occurring in the range  $2 < L < 3$  and over the interval  $2 < t < 4$  sec. This signature is interesting because it only appears in the northern hemisphere panels of both cases, is seemingly connected to the first precipitation pulse, and does not look like the typical rising swaths seen in Figures 5.16b,e and 5.17b,e. In fact, this signature has its origin in the same mechanism discussed in the previous paragraph except that most of the higher frequencies ( $f \gtrsim 4$  kHz) are injected at  $L$ -shells that are higher than their settling  $L$ -shell (cf. Section 4.2.2); as a result the waves become very electrostatic as early as the second hop, and are Landau damped very quickly. As they are Landau damped by the suprathermal population, they also scatter the resonant electrons (of  $\lesssim 1$  keV energies) into the loss cone resulting in large number fluxes in the northern hemisphere coincident with the second hop. The signature seems to be moving to lower  $L$ -shells with time because the higher frequency components move closer to the Earth on their second hop in trying to reach their settling  $L$ -shell. Also visible is a relatively sharp cutoff near  $L = 3$  which is caused by the slot-region.

Finally, we note that the precipitation signature in Figure 5.19 contains even more

unusual features than that in Figure 5.18. Most notably, there is the presence of the large precipitation maximum in panel (b) which we have discussed above, together with only a very thin swath in the energy flux (Figures 5.18a,d) and some ‘non-smooth’ features at  $t \gtrsim 11$  sec,  $L > 4.8$ . These thin rising swaths can be understood by the fact that at this high injection latitude ( $\lambda_s = 55^\circ$ ) there are only a small band of frequency components that remain below the equatorial LHR frequency, that gradually propagate to higher  $L$ -shells and scatter electrons as they propagate. Because of the relatively low power remaining in this band and the obliquity of the wave, the energy fluxes are generally lower than those for the  $\lambda_s = 35^\circ$  and  $\lambda_s = 45^\circ$  events. The remainder of the frequency components move to lower  $L$ -shells and drive the precipitation maximum in panel (b) as discussed above (note the clear depression caused by the slot region at  $L \simeq 3$ ). At  $t \gtrsim 11$  sec we see the emergence of features which are somewhat irregular and which do not follow the typical “rising-swath” pattern seen in the previous figures. These irregular features are caused by plasmopause echoes as discussed in Section 4.3.3 and shown in Figure 4.7. The plasmopause reflections result in smooth  $f-t$  echoes as well as echoes that are not smooth and discrete in  $f-t$  and contain some randomness in them, which have strayed beyond the plasmopause and have come in again due to density gradients, and are consistent with the features apparent in both energy and number flux.

#### 5.2.4 Precipitation hotspot in geographic coordinates

The global view of precipitated energy flux shown in Figures 5.17a and 5.17d provides sufficient information for us to calculate the geographic region of the Earth affected by the MR whistler driven electron precipitation. Such information would be useful in comparing with subionospheric VLF signal perturbations due to D-region disturbances caused by the electron precipitation as was done in previous work [*Carpenter and LaBelle*, 1982; *Carpenter et al.*, 1984; *Inan et al.*, 1985a; *Inan and Carpenter*, 1986; *Lev-Tov et al.*, 1996; *Johnson et al.*, 1999; *Clilverd et al.*, 2002].

At every instant in time the information given in Figures 5.17a and 5.17d provides a one-dimensional plot of energy flux versus  $L$ -shell. We transform the dependence of this plot from  $L$ -shell to geomagnetic latitude  $\lambda_{\text{mag}}$  through the relation  $\cos^2(\lambda_{\text{mag}}) = (R_E + h_{\text{iono}})/LR_E$  where  $R_E$  and  $h_{\text{iono}}$  are the Earth's radius (6370 km) and ionospheric deposition altitude ( $\sim 100$  km) respectively. To obtain a two-dimensional patch we follow the technique used by past workers [Lauben *et al.*, 2001] and extrapolate the energy flux versus latitude curve in geomagnetic longitude. As was shown by [Ibid], the pitch angle change and hence precipitated flux is proportional to the radiated electric field strength of the lightning discharge, and hence we obtain a scaling function by evaluating the square root of the ratio of (2.1) at a range of longitudes with respect to its nominal value at the source lightning longitude, expressed as:

$$s(\phi_{\text{mag}}) = \frac{R_{l0} \sin[\kappa(\phi_{\text{mag}})]}{R_l(\phi_{\text{mag}}) \sin \kappa_0} \quad (5.5)$$

where the subscript '0' denotes longitude of the causative flash,  $\phi_{\text{mag}}$  is the extrapolated longitude, and all other symbols are as defined in connection with (2.1), in geomagnetic coordinates.

The procedure described above is illustrated graphically in Figure 5.20 showing a perspective view of an energy flux versus time curve translated in longitude by applying the scaling function described by (5.5). This curve represents the energy flux deposited in the northern ionosphere at  $L=3$  due to a lightning discharge at a geomagnetic latitude of  $35^\circ$  and is similar to the curve shown in Figure 5.13c (blue curve, i.e.,  $E > 0$  keV).

A few comments are in order regarding the above procedure: firstly, our method differs from that of Lauben [1999] who used the underlying differential energy flux (i.e., Figure 5.11) and scaled every  $E-t$  pixel by the spatial factor (as we have) evaluated at the frequency known to cause the greatest amount of scattering at that  $L$ -shell. In our case this method is not realistic because a single wave frequency component is not dominantly responsible for the scattering at a given  $L$ -shell since we consider a large number of resonance modes, and magnetospheric reflections of

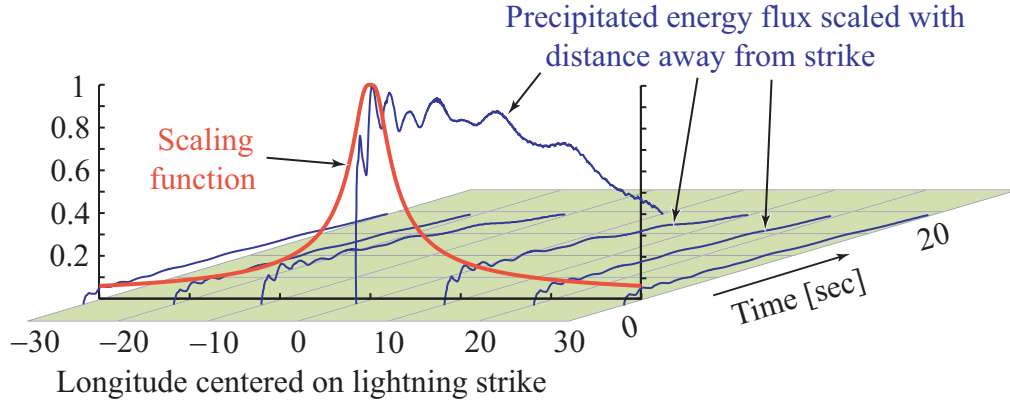


Figure 5.20: Illustration of longitude extrapolation technique showing curves of precipitated energy flux vs. time (blue) at different longitudes away from the lightning source location, multiplied by the scaling function (red).

the injected waves. Instead, we opt to scale the integrated energy flux signature by the spatial factor at the LHR frequency of the particular  $L$ -shell in view of the fact that magnetospherically reflecting wave packets eventually tend to settle at that  $L$ -shell. However, when we take the ratio of (2.1) at some longitude with respect to the longitude of the causative lightning discharge at any constant frequency, the frequency dependent factor simply cancels out, leaving only the spatial dependence.

Secondly, as was noted in Section 2.2, in order to avoid the ideal vertical dipole radiation pattern null we compute the wave power as a function of latitude in a meridian that is displaced by  $0.9^\circ$  from that of the causative lightning. We use the same technique in the above procedure where we evaluate (5.5) for a range of longitudes at a latitude that is similarly displaced by  $0.9^\circ$  from that of the causative flash, resulting in similar power levels as one would have at the precise latitude of the lightning, but once again avoiding the idealized radiation pattern null that would in reality undoubtedly be washed out due to natural ionospheric inhomogeneities.

Finally, horizontal gradients in the ionospheric electron number density are neglected entirely by assuming that the electron density profile varies only as a function of altitude, thereby allowing us to use wave normal vectors which are initially locally vertical and to assume azimuthal symmetry. It is easy to include latitudinally varying horizontal density gradients as we have done in Chapter 3, but this would need

to be performed on a case by case basis and here we have chosen to treat the more basic situation. With respect to azimuthal density gradients, the horizontally stratified assumption is quite reasonable in the night-time sector, but there are significant azimuthal gradients near the day and night terminators that could in general distort the shape of the precipitation region. However, proper inclusion of azimuthal density gradients would involve use of a three-dimensional ray tracing program, which is beyond the scope of the present work. While such programs do exist and have been used [Green *et al.*, 2002; Starks, 2002] their use in our analysis is prohibitive in view of the fact that many thousands of rays need to be run to properly construct the wave property tables.

Having obtained the precipitated energy flux as a function of geomagnetic latitude and longitude (at a given time), we are left with the task of mapping this precipitated flux patch into geographic coordinates. To do this we once again follow the previous work of Lauben [1999] and use a tilted and centered dipole approximation to map every geomagnetic latitude-longitude pair into their corresponding geographic latitude-longitude pair using the standard spherical transform methods described in e.g., Goldstein *et al.* [2002, p.153] and the centered dipole model North pole coordinates ( $79.13^\circ, 288.84^\circ$ ) representing latitude and longitude respectively. These values are typical of DGRF/IGRF parameters [Macmillan *et al.*, 2003] in the period 1990–2000.

The results of the operations described above are displayed in Figure 5.21 where we show the precipitation patch at  $t=0.4$  sec after the time of the causative lightning discharge located at  $35^\circ$  geomagnetic latitude. The geomagnetic longitude was chosen such that the transformed coordinates of the lightning discharge are  $(24.3^\circ, -80.1^\circ)$ , placing the precipitation patch in the north-eastern United States, convenient for observation by the subionospheric VLF measurements regularly conducted by Stanford over these regions (see Johnson *et al.* [1999] and references therein), and off the western coast of the Antarctic peninsula where the precipitation is also regularly measured in the same manner [Burgess and Inan, 1993; Clilverd *et al.*, 2002]. Panel (a) shows the entire globe with topographic data displayed with the ‘topo’ color scale (not shown) for reference, and the precipitation energy flux displayed with the linear

color scale given to the right of the figure.

This view in Figure 5.21 illustrates the large latitudinal separation between the lightning discharge and resultant precipitation patch (as noted previously by *Lauben* [1999]) of  $\sim 15^\circ$  as well as illustrating the disposition of the precipitation patch on a global scale. The distribution of the whistler wave power density in the magnetosphere at  $t = 0.4$  sec is shown in panel (b) (normalized color scale shown below) where the power density of the 5330 sample rays is shown ( $f = 0.2 - 60$  kHz, c.f. Section 4.2), as determined by the initial latitude-dependent power density at the ionosphere and path integrated Landau damping. The wave power is concentrated in the center of the wave packet slightly below  $L = 2.5$ , and the temporal dispersion of the wave packet is also evident. The time of the snapshot is indicated in the semicircle representing the Earth.

The global spatial display of the precipitation flux given in panel (a) is useful in its illustrative capacity but is cumbersome for a detailed examination of the temporal evolution of the precipitation patch. For this purpose we show in panels (c) and (d) the expanded regions of the northern and southern hemisphere precipitation locations with the precipitated energy flux itself displayed on the logarithmic scale shown below the panels. For reference, the footprints of four  $L$ -shells ( $L = 2-5$ ) are superimposed on the maps, and we see that the ‘hotspot’ occurs slightly below  $L = 2.5$ , commensurate with the distribution of the wave structure in the magnetosphere at the time.

Using the format of Figure 5.21 panels (b)–(d), we now present the entire event of Figure 5.17 as a sequence of panels that progress in time from 0.1-20 sec shown in Figure 5.22. We sample the time sequence at 0.1 sec initially and gradually increase the sampling period as the interaction becomes more diffuse. For these results the trapped flux of energetic electrons was derived from the AE8 model [*Vette*, 1991] with an assumed sinusoidal loss-cone distribution.

While many of the characteristics of the precipitated energy flux signature have been discussed in connection with Figure 5.17, there are nevertheless several important features to note concerning Figure 5.22. The first point to note is the fact that the approximate size of the affected ionospheric region is in agreement with past calculations [*Lauben et al.*, 2001], with the lateral extent of the patch being a few

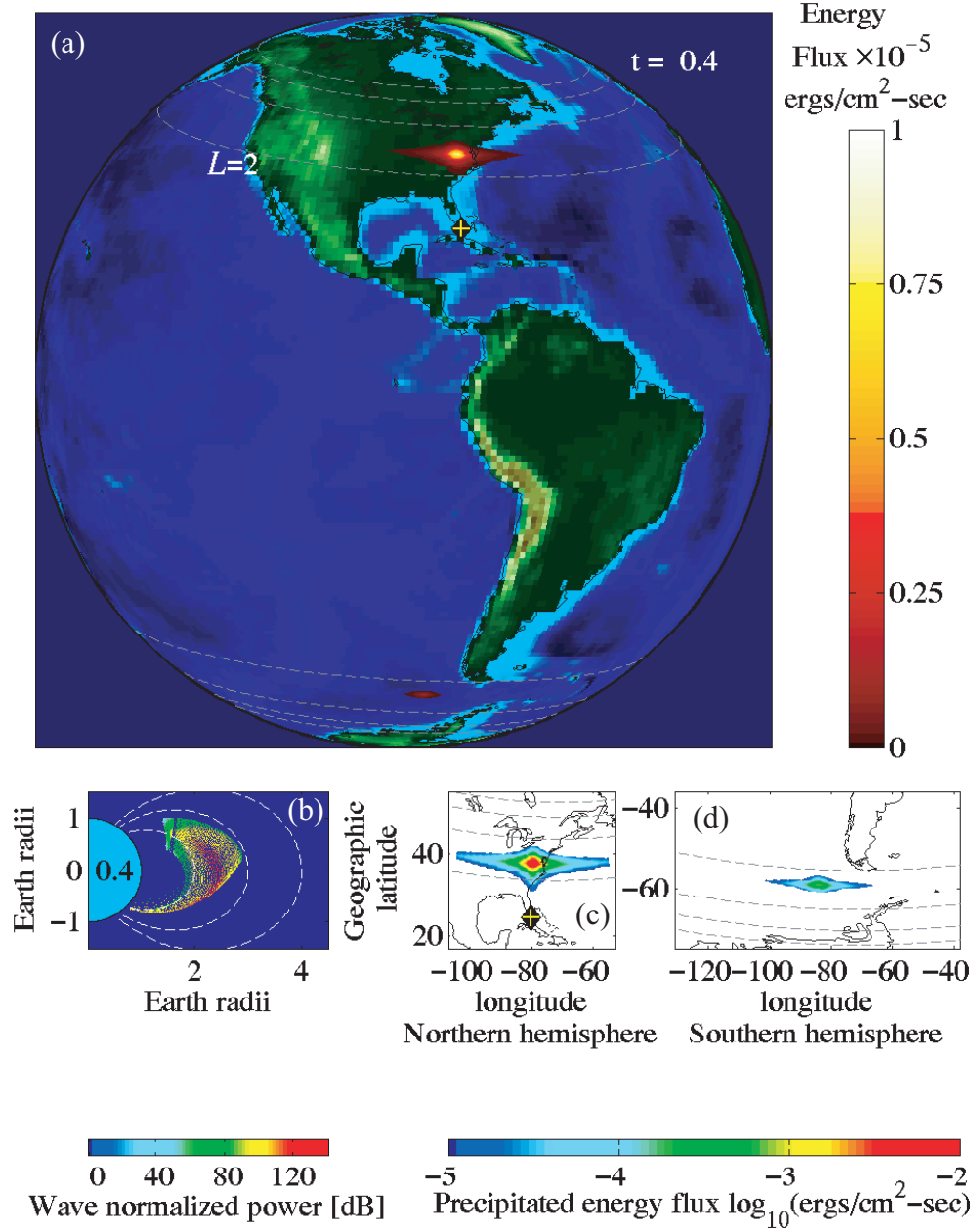


Figure 5.21: Precipitation hotspot at  $t = 0.4$  sec after the lightning discharge at  $\lambda_{\text{mag}} = 35^\circ$ ; (a) Precipitation data plotted on world topography, lightning source shown as yellow cross at  $(24.3^\circ, -80.1^\circ)$ ; (b) whistler wave power distribution at  $t = 0.4$  sec with relative color scale; (c) expanded northern and (d) southern hemisphere maps showing a log color scale and  $L$ -shells 2–5.

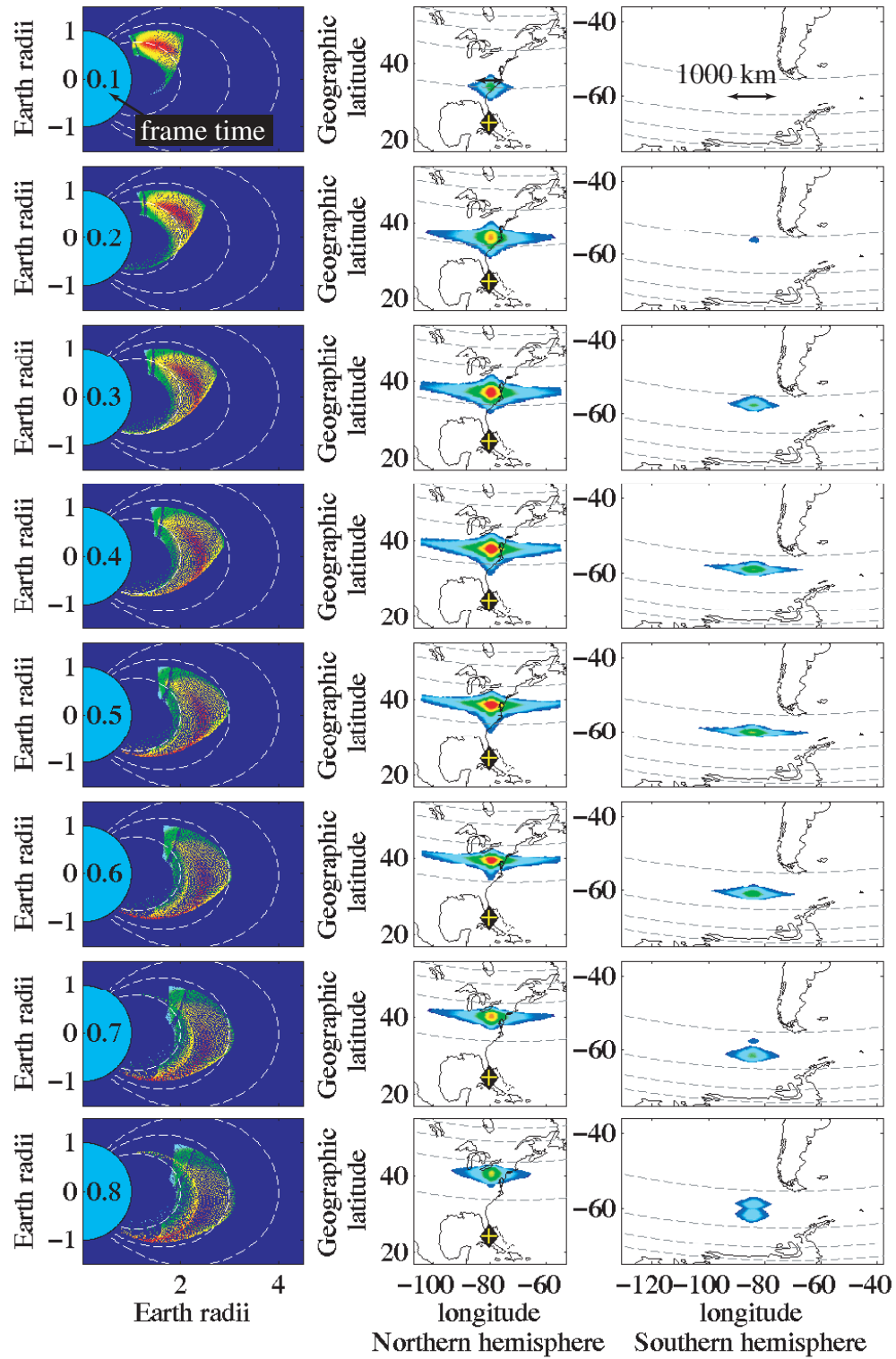


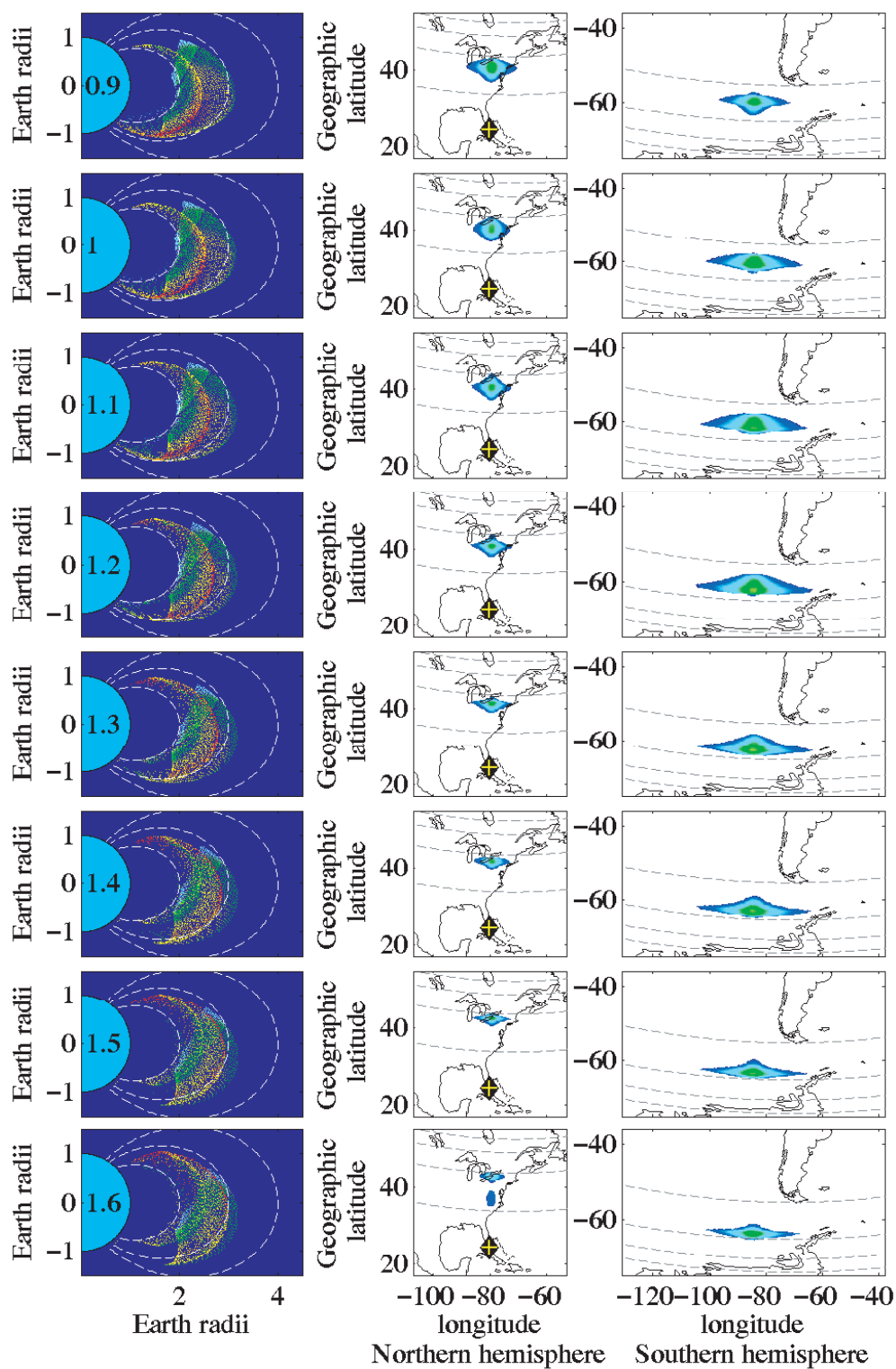
Figure 5.22: [Following 5 pages] Time sequence of MR whistler wave power distribution in the magnetosphere (left column) and resultant precipitated energy flux patch, shown for the first 20 sec of the event. The data is extrapolated from that of Figures 5.17a,d and shows a poleward fluence on both short ( $\sim 0.1$  sec) and long ( $\sim 10$  sec) timescales.

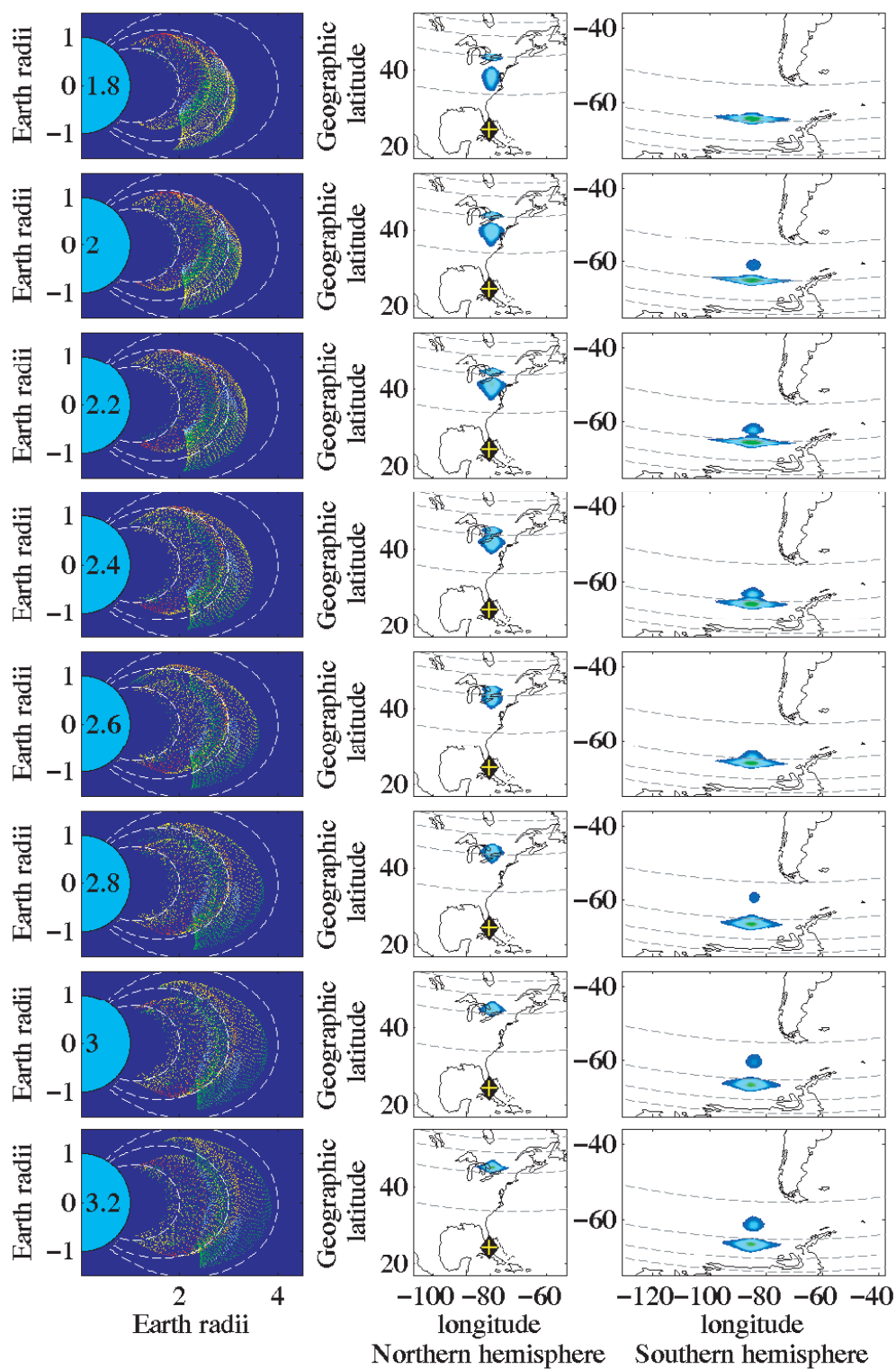
hundred km's for energy fluxes greater than  $\sim 10^{-3}$  ergs cm $^{-2}$ sec $^{-1}$  during the first equatorial traverse of the wave. As observed above (in connection with Figure 5.13), the precipitation in the northern hemisphere is significantly more intense during the first hop than in the southern hemisphere, leading to patch sizes that are larger in size than the southern hemisphere. In keeping with this point, we note that the east-west extent of patch sizes in the southern hemisphere may appear larger in our figure than they actually are due to the cylindrical projection of the map. We have plotted in the  $t = 0.1$  sec panel the lateral extent occupied by 1000 km at latitudes  $35^\circ$  and  $-60^\circ$ , corresponding to longitude ranges of  $11^\circ$  and  $18^\circ$  respectively. The north-south extents remain even since latitudinal lines (parallels) do not converge at the poles.

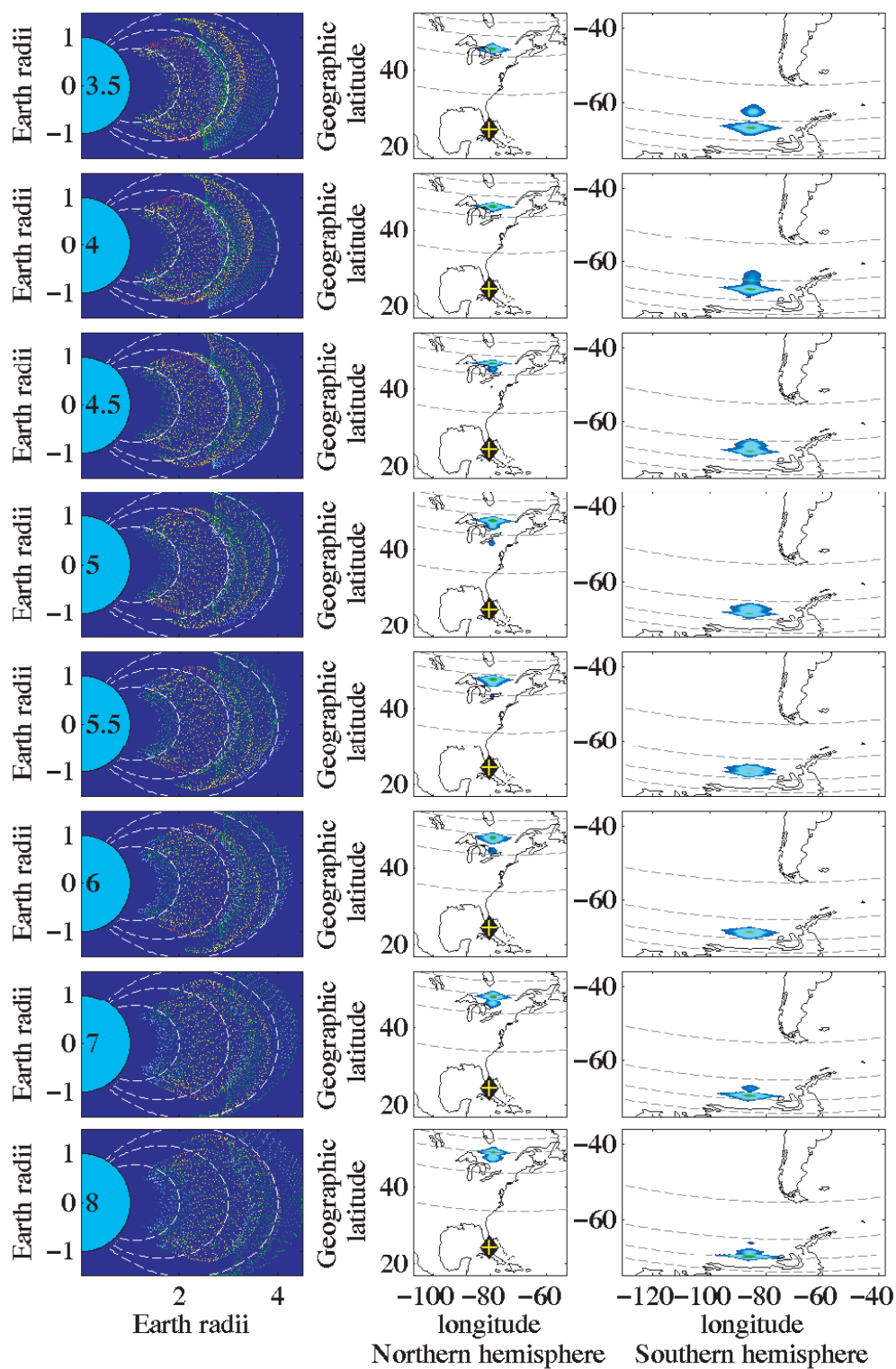
The second point to note is that in panels such as those corresponding to  $2 < t < 3.2$  sec, more than one hotspot appears. There are two contributing factors leading to this phenomenon: the first is a region of depleted energetic electron fluxes available in the radiation belts (the slot region) shown in Figure 5.10, occurring at  $L \simeq 2.8$ , resulting in a spatial minimum of the precipitated energy flux. The second factor is due to the periodic reflections of the whistler wave energy packet, combined with the fact that the most efficient wave-particle interactions occur near the geomagnetic equator. As the wave packet reflects, it gradually moves to higher  $L$ -shells, frequently resulting in a spatial gap in the precipitated flux due to the separation between two simultaneous equatorial traverses.

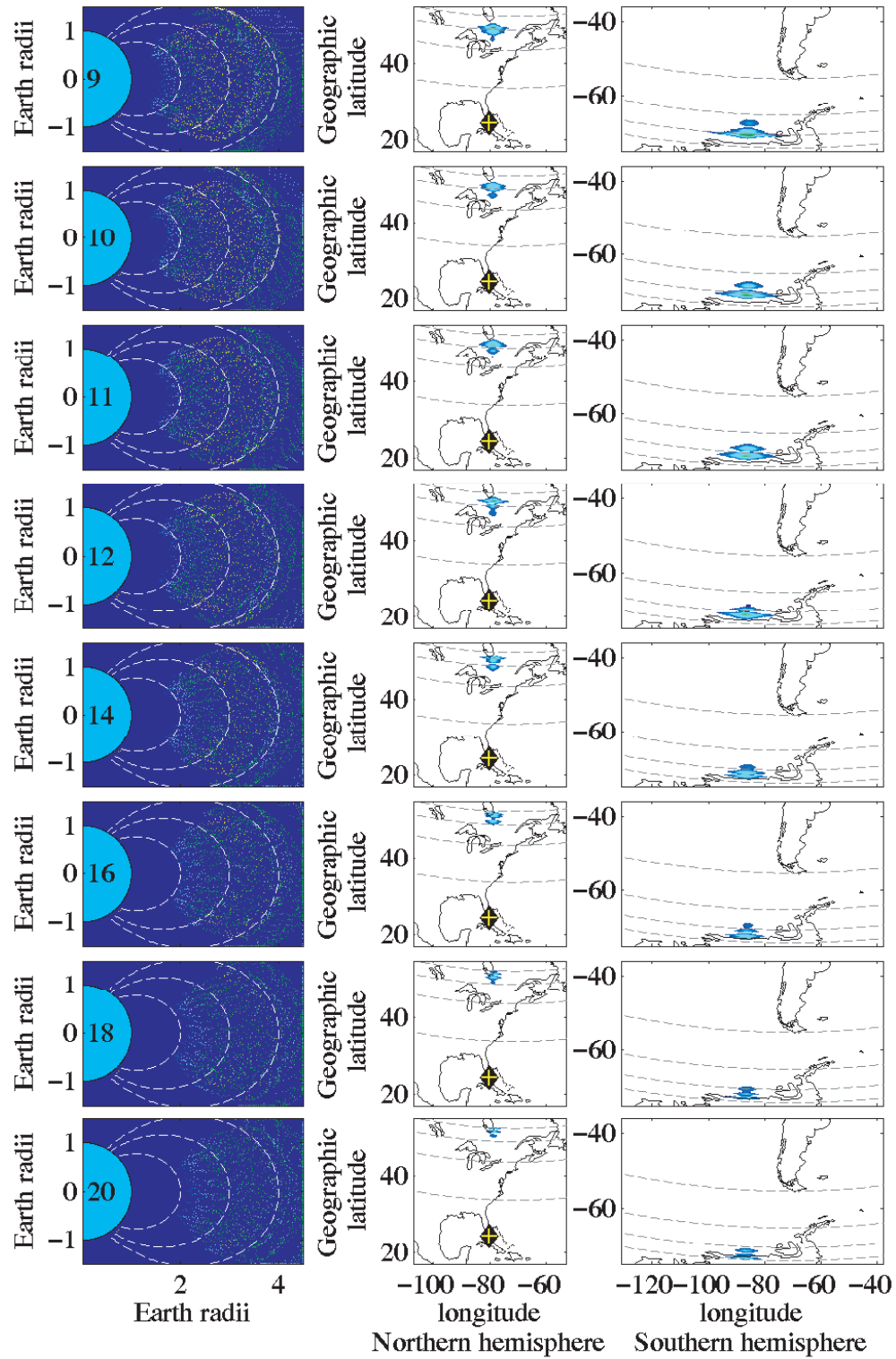
A few final features to mention are the ability of a single lightning discharge to effectively fill the entire plasmasphere with whistler mode energy as seen in the left column of Figure 5.22 at  $t \gtrsim 10$  sec, as well as the poleward motion of the precipitation patch in both hemispheres on both short ( $\sim 0.1$  sec) and long ( $\sim 10$  sec) timescales. In fact, the timescale of the poleward motion of the affected ionospheric region may be the most critical determinant in separating precipitation due to MR whistler waves











(as presented in this work) from other types of oblique wave-drive precipitation which do not necessarily magnetospherically reflect, for instance precipitation driven by the first nonducted hop of the lightning generated whistler wave [Johnson *et al.*, 1999; Lauben *et al.*, 2001] or VLF transmitter signal in the 10–30 kHz range.

### 5.2.5 Longitude integrated fluxes

The total energy or number of electrons precipitated at any given  $L$ -shell in an event such as the one shown in Figure 5.22 is calculated by integrating the corresponding energy and/or number flux with respect to time and longitude. The resulting quantity is shown in Figure 5.23 where we display the total precipitated energy (in Joules/ $L$ ) and number of electrons (in electrons/ $L$ ) as a function of  $L$ -shell in the left and right columns respectively. We plot results corresponding to causative lightning discharges at  $\lambda_s = 25^\circ$ ,  $\lambda_s = 35^\circ$ ,  $\lambda_s = 45^\circ$ , and  $\lambda_s = 55^\circ$  in blue, red, green and magenta respectively, showing both northern (top row) and southern (bottom row) hemisphere precipitation.

Immediately evident is the effect of the slot-region upon the precipitated electron energy and number, as a depression in the fluxes slightly below  $L = 3$ . We thus expect that for a typical radiation belt electron distribution there would be a noticeable decrease in precipitated fluxes near the geographic location of the  $L \simeq 3$  shell, which occurs for our present example in the north-eastern United States slightly south of the great lakes region and in the southern hemisphere near the Antarctic peninsula.

It should be noted that time and longitude-integrated precipitation signatures such as those shown in Figure 5.23 are ideally observed by satellites in the drift-loss-cone as discussed in Section 3.1, and shown in Figure 3.1. In such cases, lightning generated MR whistlers scatter energetic particles into the drift-loss-cone at longitudes east of the South Atlantic anomaly (where geomagnetic field amplitudes as well as energetic particle mirror heights are substantially lowered) where these scattered energetic particles accumulate and remain in the drift-loss-cone (and are thus observable by satellites at locations east of the scattering locations) until they are precipitated at the South Atlantic anomaly.



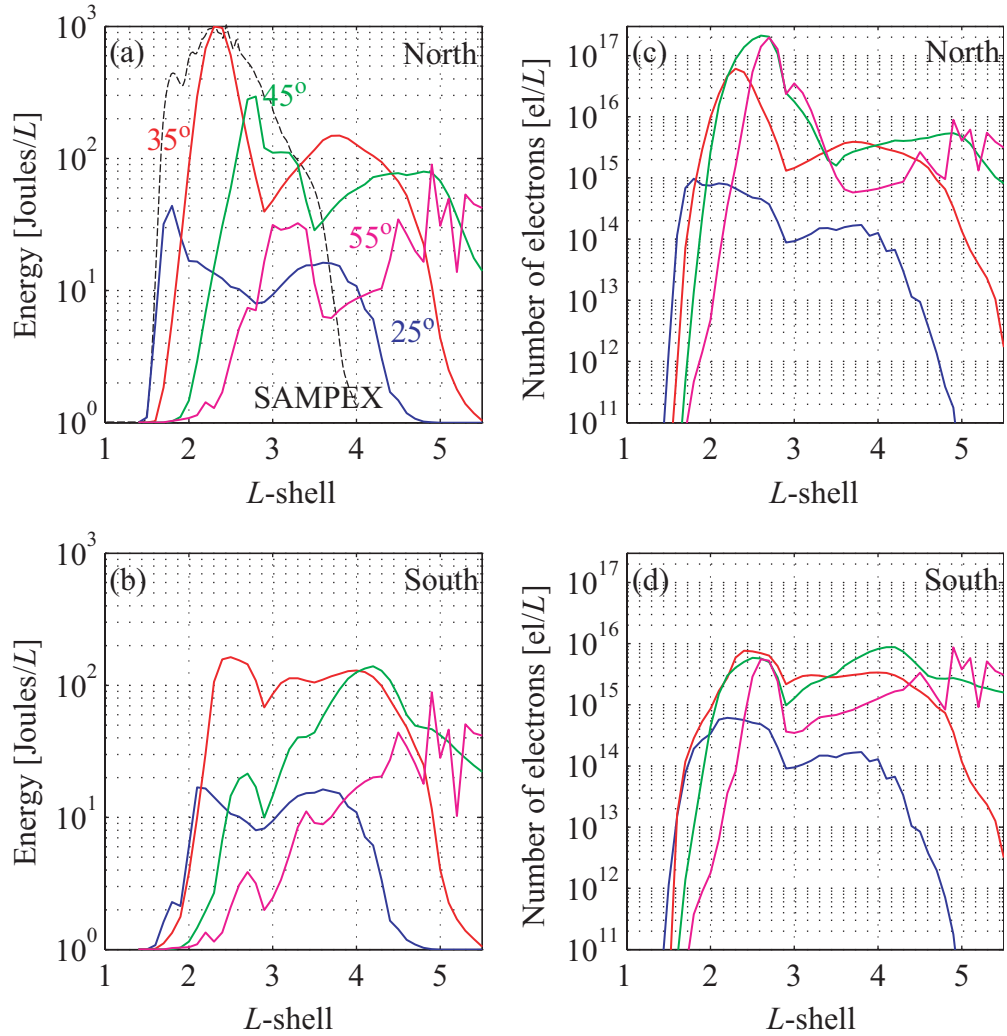


Figure 5.23: Integrated flux of particles shown as a function of  $L$ -shell for the event presented in Figure 5.22, and a similar analysis performed for an event with  $\lambda_s = 35^\circ$ .

The effect of the first hop is evident in the signatures of Figure 5.23 as an asymmetry between the northern and southern hemispheres. It is clear that the precipitation in both energy and number of electrons is always greater in the northern hemisphere than in the southern hemisphere due to the highly efficient  $m = 1$  counterstreaming gyroresonant interaction which has been discussed in connection with Figure 5.13. The dependence on injection latitude is also evident showing that the precipitation



| $\lambda_s$ | Q [Joules] |       | N [electrons]        |                      |
|-------------|------------|-------|----------------------|----------------------|
|             | North      | South | North                | South                |
| 25          | 37         | 26    | $94 \times 10^{13}$  | $66 \times 10^{13}$  |
| 35          | 590        | 280   | $3.0 \times 10^{16}$ | $.97 \times 10^{16}$ |
| 45          | 250        | 170   | $11 \times 10^{16}$  | $1.3 \times 10^{16}$ |
| 55          | 68         | 60    | $6.8 \times 10^{16}$ | $0.7 \times 10^{16}$ |

Table 5.1: Total precipitated energy and electron number due to lightning sources at  $\lambda_s = 25^\circ$ ,  $\lambda_s = 35^\circ$ ,  $\lambda_s = 45^\circ$ , and  $\lambda_s = 55^\circ$ .

signature becomes progressively more asymmetric between the north and south hemispheres as  $\lambda_s$  is increased, because the whistler waves travel over longer field lines, becoming electrostatic and experiencing more severe Landau damping on the first hop, causing second and subsequent hops to precipitate far fewer electrons.

Turning our attention to the electron precipitated energy (Figures 5.23a,b), we see that the average location of the precipitation in  $L$ -shell generally increases with increasing injection latitude, but that the peak flux does not monotonically increase with  $\lambda_s$ . As in our qualitative description of the expected precipitation intensities in connection with Figures 5.16–5.19, we once again observe that the precipitated energies caused by discharges located at midlatitudes ( $\lambda_s = 25^\circ$  and  $35^\circ$ ) are greater than those at either low ( $\lambda_s = 25^\circ$ ) or high ( $\lambda_s = 55^\circ$ ) latitudes.

It is interesting at this stage to compare the results of Figure 5.23a to the rough estimate made previously in Section 3.4.2 and shown in Figure 3.7c. We have plotted the curve of Figure 3.7c as a black dashed line labeled ‘SAMPEX’ in 5.23a for comparison. While the SAMPEX calculation did not account for the reduction of trapped flux near the slot region (being based on a very simple energy dependence for the trapped flux assumed constant with  $L$ ) and was based on a plasmopause located at  $L = 3.8$  instead of  $L = 5.5$  as we do in the current example (consequently ending more abruptly near  $L \simeq 3.8$ ), it nevertheless captures remarkably well the spatial region where the bulk of the precipitation is expected to occur, as well as the relative magnitudes of the precipitated flux. The current analysis thus serves as a valuable confirmation of the results presented in Chapter 3.

We integrate the results shown in Figure 5.23 with respect to  $L$ -shell and present

the results of total precipitated energy and number of electrons in Table 5.1. As mentioned above, we observe the dominance of lightning injection at  $\lambda_s = 35^\circ$  in the precipitation of energy, but surprisingly it is actually the  $\lambda_s = 45^\circ$  case that dominates the precipitated number of electrons, primarily due to the intense precipitation driven by the longitudinal resonance visible in Figure 5.18, at  $2 < L < 3$  and  $2 < t < 4$  sec.

Previous estimates of the total energy and number of electrons precipitated by an oblique whistler on its first hop were made by *Lauben* [1999] giving values of  $\sim 1$  MJ and  $\sim 10^{20}$  electrons respectively for midlatitude lightning source locations. These estimates were calculated using the full nonlinear wave-particle interaction equations (2.24) and (2.25), with similar wave power as our lightning discharges. The fact that both precipitated energy and total number of precipitated electrons are a factor of a few thousand larger than our estimate can be understood as follows: firstly, the trapped flux model used by *Lauben* [1999] was derived from the OGO 3 measurements of *Schield and Frank* [1970], and extrapolated to higher energies using simple assumptions, giving values which are typically higher than those of the AE8 model (e.g., at 100 keV, OGO 3 fluxes are comparable to the maximum fluxes of the AE8 model, at 1 MeV OGO 3 fluxes are a factor of 10 to 100 larger than maximum AE8 fluxes and at 6 MeV the difference is a factor of  $\sim 10^5$ ). Secondly, the *Lauben* [1999] trapped flux model neglects the region of decreased electrons fluxes (slot region) assuming a uniform particle distribution throughout the entire inner magnetosphere which adds a significant amount of particles compared to the AE8 model used in the present work which includes the slot region. Thirdly, *Lauben* [1999] assumes a sharp, step-like pitch-angle distribution (as shown by the red curve in the inset of Figure 5.9), as opposed to a more realistic ‘sinusoidal’ distribution (blue curve of above figure) used in the present work. In view of the strong dependence of precipitation flux [*Inan et al.*, 1982; 1989] to the shape of the pitch-angle distribution near the loss cone, the difference in precipitated flux for a sharp vs. a sinusoidal pitch-angle distribution can be a factor of  $\sim 100$ , even if the total equatorial fluxes are kept constant for the two distributions.

Although resultant total energy flux of electrons precipitated by an oblique whistler was estimated by *Lauben* [1999] to be much higher than our estimates, it is important

to note that these differences are only due to the use of different initial conditions and not to the efficiency of the wave-induced pitch-angle scattering. In fact, when we use the same input parameters in our model as those used by *Lauben* [1999] we find nearly identical precipitation levels.

Aside from the more intense flux distribution, neglect of the slot region, and the assumption of a step-like pitch-angle distribution, *Lauben* [1999] does not take into account the effects of Landau damping upon the wave, which decrease the wave power of the oblique whistler during its first hop (typically a few percent), resulting in lower precipitation as is the case in the present work. Although we consider multiple magnetospheric reflections of the whistler wave, as shown in Figure 5.23 the precipitation driven by this portion of the trajectory of the wave packet is typically dominated by the precipitation driven by the first hop. Consideration of multiple harmonic resonances is also insufficient to produce a significant increase in precipitation flux, since the first counterstreaming gyroresonance interaction is dominant as discussed in 5.2.2.

### 5.3 Summary and discussion

In this chapter we have described a numerical model designed to calculate the differential number flux of precipitating energetic radiation-belt electrons due to an MR whistler wave initiated by a single cloud-ground lightning discharge.

The model first calculates the frequency-time ( $f-t$ ) spectra of the MR whistler along a particular  $L$ -shell at  $1^\circ$  latitude intervals using the ray tracing and interpolation algorithm described in Section 4.2 [*Bortnik et al.*, 2003b]. By making the assumption that the waves at different latitude bins are phase incoherent, we compute the pitch angle changes [*Bell*, 1984] at every latitude bin, due to every  $f-t$  cell in each spectrogram, for multiple harmonic resonance modes (including Landau resonance), and a band of velocities centered on the resonant velocity. We then compile  $E-t$  (Energy-time) tables at both the northern and southern feet of the particular field line, and simply add the variances of the electron scattering into the appropriate bins, based upon the energy of the resonant particles and arrival time at the ionosphere. The tables are then convolved with two different particle distribution functions (a

uniform distribution in  $L$ -shell with sharp pitch-angle dependence [Bell *et al.*, 2002], and an  $L$ -dependent distribution with a softer, sinusoidal pitch angle based on the AE8 model [Vette, 1991]) both to allow for comparison with past work and to provide more realistic predictions of global scattering due to MR whistlers.

A detailed comparison of the precipitated differential number flux at  $L=2.3$  and  $L=3$  has revealed an intense flux of Landau resonant particles at lower energies ( $\lesssim 1$  keV) that contribute little to the precipitated energy flux, together with discrete swaths of higher energy particles resulting from gyroresonance interactions. In both  $L$ -shells, the first order, counterstreaming gyroresonance was found to be the dominant wave-particle interaction mechanism, due to a number of factors namely: the counterstreaming particles interact with lower energy particles (which are more abundant) than costreaming particles, the lower energy particles also move through the wave slower and thus acquire a greater overall pitch-angle change than the higher energy particles, and finally the RHCP wave component always carries greater power than the LHCP component. An unexpected result was that the first precipitation pulse at  $L=3$  contained less energy than the second pulse (i.e., the first energy pulse due to the counterstreaming interaction in the northern hemisphere  $c_1$ , was smaller than the second pulse in the southern hemisphere  $d_2$ ) suggesting that measurements of LEP events with unusually long delays compared to those measured for the first precipitation pulse [Johnson *et al.*, 1999] could potentially be explained using this mechanism.

We have generated and compared the ‘global’ precipitation signatures due to lightning discharges at  $\lambda_s = 25^\circ$ ,  $\lambda_s = 35^\circ$ ,  $\lambda_s = 45^\circ$ , and  $\lambda_s = 55^\circ$ . Our findings show that generally precipitation swaths move from lower to higher  $L$ -shells on both short ( $\sim 0.1$  sec) and long ( $\sim 10$  sec) timescales, the first timescale corresponding to the outward motion (to higher  $L$ -shell) of the whistler-mode ray paths as they propagate upward on the first hop, and the second corresponding to the slow migration of MR whistler wave energy to higher  $L$ -shells. For higher source discharge latitudes ( $\lambda_s = 45^\circ$  and  $55^\circ$ ) a large precipitation maximum appeared in the northern hemisphere in the number flux plots, which was attributed to the strong longitudinal (Landau) resonance between the whistler wave and the suprathermal particle population (in turn, also

leading to strong damping of the wave). For  $\lambda_s = 55^\circ$  there was evidence of plasma-pause scattering and reflections which led to unexpected swaths of precipitation at high  $L$ -shells. Midlatitude lightning discharges were shown to be most effective in precipitating the total amount of particle energy ( $\lambda_s = 35^\circ$ ) and number of electrons ( $\lambda_s = 45^\circ$ ). Turning to a geographic representation of the precipitated energy flux, we saw that the affected ionospheric patch sizes were a few 100 kilometers in lateral extent and at any given time were intense in either the northern or southern hemisphere (depending on the propagation direction of the MR whistler wave at the time) because of the dominant first-order counterstreaming gyroresonance.

The methodology presented in this work is believed to be the first of its kind, allowing for a highly detailed characterization of the temporal, spatial, and spectral signatures of the precipitation of energetic electrons into the loss cone, including the effects of a range of harmonic resonance modes ( $m = -5$  to  $5$ ), multiple magnetospheric reflections, and wave power attenuation due to Landau damping. It has been verified with excellent agreement, against the work of *Lauben et al.* [2001] (i.e., when we use our model with the same initial conditions used by *Lauben* [1999]; not shown here), which has itself been tested experimentally [*Johnson et al.*, 1999]. As such, it constitutes a new and promising tool for the analysis of the impact of lightning and similar radiating structures (e.g., VLF transmitters or satellites-based transmitters) upon the Earth's electron radiation belts.

# Chapter 6

## Summary and conclusions

### 6.1 Summary

This dissertation has dealt with various aspects of lightning generated magnetospherically reflected (MR) whistler waves, and in particular their propagation in the plasmasphere and their pitch-angle scattering and precipitation of energetic radiation-belt electrons via resonant interactions.

Chapter 1 outlined the aim and scope of this work, namely (i) the determination of the  $L$ -shell distribution of MR whistler wave energy and precipitation, (ii) the development of a technique to model the observed  $f-t$  spectra at any location in the magnetosphere, and (iii) the development and application of a method to calculate the detailed temporal and spatial precipitation signature of a complete lightning-induced electron precipitation event, including (for the first time) the contributions of the MR whistler components. The properties of MR whistlers were qualitatively introduced, and then placed into perspective by considering the broad structure of the magnetosphere, plasmasphere, and finally radiation belts. The present work was placed into context by examining several related past studies, and the scientific contributions of the present work were listed.

The common theoretical background of many of the succeeding chapters was presented in Chapter 2. This background included the lightning illumination model, ray tracing methodology, and the quantities associated with ray tracing such as the

refractive index, medium properties (plasmaspheric number density and geomagnetic field models), and the implementation of this theory in the VLF ray tracing code. The interaction of an oblique whistler wave with a mirroring energetic electron was discussed in light of the pertinent equations of motion, before finishing with an intuitive picture of Landau damping.

Chapter 3 dealt with the interpretation of recent SAMPEX observations of energetic electrons precipitating into the drift loss cone. For this purpose, we have used the Stanford VLF ray tracing code (c.f. Section 2.3.4) together with a simple equation estimating the precipitated flux, and have shown that the observed fluxes are consistent with those expected due to MR whistlers. The sharp maximum was attributed to whistler wave focusing by ionospheric horizontal density gradients, and the multiple peaks resulted from different lightning discharge locations displaced slightly in longitude.

We then developed a ray tracing and interpolation algorithm to determine the detailed  $f-t$  signature of the MR whistler as observed at any location in the magnetosphere, caused by a source lightning at any latitude on Earth, which was presented in Chapter 4. The results of this model were verified against an observation made by OGO 1, showing excellent agreement. Our technique involves effectively ray tracing  $\sim 120$  million rays, and predicts absolute power levels incorporating the effects of Landau damping. Different plasmaspheric electron density profiles were examined showing that the MR whistler signature varies in such a way that the underlying density profile structures could be identified by means of *in-situ* observations of MR whistlers.

In Chapter 5 we used the technique developed in Chapter 4 to calculate  $f-t$  spectra of an MR whistler at  $1^\circ$  latitude intervals along a certain  $L$ -shell. Using these spectra as an approximation to the continuous spatial and temporal wave structure, we developed a method of calculating the pitch angle changes of resonant energetic electrons as they traversed the wave packet. By treating the scattering at each of the  $1^\circ$  latitude bins as incoherent from the others, we have estimated the total pitch angle changes of all resonant particles and convolved this with the initial distribution to obtain the differential number flux at the ionosphere. Our simulations involved

the first 20 seconds of the MR whistler wave driven precipitation, with frequency components ranging from  $f = 200$  Hz to 60 kHz, and involving harmonic resonance modes  $-5$  to  $5$ , including the Landau (or longitudinal) resonance. Results reveal that significant and measurable fluxes would be precipitated into the ionosphere, with a periodicity commensurate with that of the underlying whistler magnetospheric reflection period. The first counterstreaming gyroresonance was demonstrated to be dominant in precipitating electrons, resulting in large intensities in the first energy flux pulse in the northern hemisphere. Global views indicate a poleward-directed motion of the perturbed ionospheric region, both on short (0.1 sec) and long (10 sec) time scales, as well as large number fluxes of precipitated electrons of relatively low energies ( $\lesssim 1$  keV) at  $2 < L < 3$  due to longitudinal resonant interactions with the higher frequency components ( $f > 4$  kHz) injected at higher latitudes ( $\lambda_s = 45^\circ$  and  $55^\circ$ ).

## 6.2 Discussion

The results presented in this work greatly improve current understanding of the manner by which lightning-generated whistler waves propagate in and populate the magnetosphere, and the resultant pitch-angle scattering and precipitation of energetic electrons as the waves propagate, become magnetospherically reflecting, and are eventually absorbed by the suprathermal plasma. These results have important implications that are discussed below.

Following the analysis of *Thorne and Horne* [1994] who used suprathermal flux distributions obtained from the OGO 3 satellite [*Schild and Frank*, 1970], MR whistler lifetimes were calculated to be only a few seconds long implying that such waves would be damped too quickly to evolve into (and thereby constitute an embryonic source for) plasmaspheric hiss or to produce any noticeable effect upon radiation-belt precipitation and hence trapped particle lifetimes. However, in our work we use a new and more extensive suprathermal particle distribution data set [*Bell et al.*, 2002] to show that MR whistlers typically persist for several to tens of seconds before being significantly damped, and that they thus are an important potential contributor to



radiation-belt loss processes. Moreover, the work of *Draganov et al.* [1992; 1993] and *Sonwalkar and Inan* [1989] which suggests that MR whistler wave energy accumulates and becomes incoherent after several seconds, constituting an embryonic source for the so-called plasmaspheric ‘hiss’, once again seems viable in light of the long lifetimes of MR whistlers, and deserves a careful reexamination.

In much of the past literature lightning induced electron precipitation (LEP) events were interpreted on the basis of ducted whistler propagation, at times leading to results which were inconclusive. For instance, *Inan et al.* [1989] modeled an LEP event observed on the S81-1/SEEP satellite assuming ducted propagation, and while many of the observed characteristics (e.g., temporal profile, and energy spectra) were reproduced with the model, the whistler wave required an equatorial wave intensity of  $B_{\text{eq}}^w \sim 200$  pT, highly atypical since observed peak wave intensities generally do not exceed  $B_{\text{eq}}^w \sim 100$  pT [*Ibid*]. In addition, even with the large wave intensity, the observed pitch-angle distribution of the precipitation could not be accounted for, and the spatial extent of the region over which the precipitation was observed ( $\sim 500$  km) was far larger than typical duct sizes at the low satellite altitudes. As was discussed in *Inan et al.* [1989], and also *Voss et al.* [1984], it is quite possible that these precipitating electron bursts were scattered by nonducted whistler waves. Due to the wideband nature of oblique whistler wave and distribution of wave normal angles, many interactions are possible with the particle population along the field line, leading to broader pitch-angle distributions, and the larger wave power necessary for the observed particle fluxes can possibly result from a focusing of the wave energy due to ionospheric horizontal density gradients, as shown in Chapter 3.

Similar observations of other LEP bursts [*Voss et al.*, 1998] show precipitation signatures that also fit more comfortably when interpreted as driven by nonducted whistlers, and in fact show a precipitated flux minimum in the energy range  $\sim 10$  to  $\sim 80$  keV, as predicted in our work, e.g., Figure 5.12. Since the precipitation pulse driven by the first hop of the MR whistler is far more intense than subsequent pulses, it can easily be misinterpreted to be driven by a single ducted whistler, particularly since propagation times for ducted and nonducted whistlers in the range  $2 < L < 3$  are quite similar.

There have been instances in the past when certain LEP signatures were observed and did not fit any of the prevailing models of the time, which we now believe may well have been examples of MR whistler driven precipitation. For instance *Goldberg et al.* [1987] reported detailed studies of two LEP events, one of which fitted the model of ducted propagation comfortably, and the other of which they attributed to an ‘unidentified process’. Although the latter event was strongly correlated with lightning, and the peak in precipitation occurred within the energy range 85 to 125 keV similar to other LEP events and to the ducted case, the observed energy range of the precipitated flux was broader than could be explained on the basis of ducted whistler wave-particle interactions, and the duration of the precipitation flux was also longer – lasting for a few seconds, and containing oscillations that could not be accounted for by ionospheric backscatter or any such previously invoked mechanism. In view of our theoretical predictions, this event is quite likely the result of an oblique whistler wave-particle interaction with the longer duration of the burst possibly representing precipitation driven by the MR components. New interpretations of this and other similar results in the same light could produce valuable further insights into the mechanisms and effects of MR whistler-driven precipitation of energetic electrons.

In general, our results support the notion that wave energy originating in lightning discharges could significantly contribute to the loss of trapped radiation-belt electrons, specifically through the mechanism of oblique and MR whistlers as opposed to ducted whistlers. This general idea was assessed by *Abel and Thorne* [1998a,b] who indeed found that oblique whistler-mode waves could dominantly control radiation-belt lifetimes of a few 100 keV particles in the range  $L \sim 2$  to 3, together with contributions from VLF transmitters. In this connection, we have shown in the course of our work (not presented in this dissertation, but discussed in *Bortnik et al.* [2003a]) that the distribution of MR whistler wave energy tends to peak in the vicinity of the slot-region ( $2.5 < L < 3$ ) and is not uniform as assumed by *Abel and Thorne* [1998a,b], also exhibiting frequency and wave normal variations that tend to decouple the precipitated particle energy from any specific  $L$ -shell. We believe that revisiting the *Abel and Thorne* [1998a,b] study in the light of the results presented in this work could reveal a more dominant role of MR whistler waves in controlling radiation-belt lifetimes in

the vicinity of the slot-region.

As discussed in Sections 1.3 and 5.2.5, our work is a direct extension to that of *Lauben* [1999], who modeled the first hop of the MR whistler, considering only the first counterstreaming gyroresonance interaction, retaining only the frequency components below the ‘nose’ frequency, and using a simple trapped flux model with a square pitch-angle distribution. Our results show that indeed the first hop of the MR whistler and first counterstreaming gyroresonance interaction are dominant in the pitch-angle scattering and precipitation of radiation-belt electrons, and confirm the essential predictions of *Lauben* [1999], such as the time of arrival of the first precipitation pulse, and initial rapid poleward motion of the ionospheric region perturbed by the precipitating electrons.

However, the precipitation flux level estimates reported by *Lauben* [1999] are a factor of a few thousand higher than those obtained using our model. However, it should be noted that the difference between our peak fluxes and those reported by *Lauben* [1999] is not in any way due to a significant difference in the efficiency of the wave-induced pitch-angle scattering process. Rather, the differences are simply due to the different trapped flux distributions assumed in our two calculations. In this connection, *Lauben* [1999] used a simple trapped flux model that generally predicts fluxes that are larger than average AE8 fluxes (in the center of the inner belt) which we use in our model. In addition, the simple, uniform trapped-flux model used in *Lauben* [1999] neglects the region of decreased electrons fluxes (slot region), assuming a uniform particle distribution throughout the entire inner magnetosphere, resulting in significantly larger trapped particle fluxes compared to the AE8 model used in the present work which includes the slot region. Since a large portion of MR whistlers tend to propagate and settle in the region  $2 < L < 3$ , and since the precipitated flux is approximately proportional to the trapped flux, the differences between the two flux models in this  $L$ -region leads to large differences in the intensity of the precipitated flux. A third important difference between our model and that used by *Lauben* [1999] is the fact that *Lauben* [1999] assumes a square pitch-angle distribution (as shown by the red curve in the inset of Figure 5.9), as opposed to a more realistic, smoothly-varying ‘sinusoidal’ distribution (blue curve of above figure) used in the present work.

As shown by *Inan et al.* [1982; 1989] the precipitated flux is sensitively dependent on the pitch-angle distribution near the loss-cone and can easily account for a factor of  $\sim 100$  difference between the two model results. An additional factor to consider is the fact that *Lauben* [1999] does not take into account the effects of Landau damping upon the wave. Such damping decreases the wave power of the oblique whistler during its first hop, resulting in lower precipitation fluxes as found in the present work.

Besides providing longitude-integrated,  $L$ -dependent precipitation flux signatures which have been successfully observed on the SAMPEX satellite [*Blake et al.*, 2001] our work shows that there are two distinct timescales of the poleward motion of the ionospheric region perturbed by the precipitating flux.

The first timescale ( $\sim 0.1$  sec) is related to the first hop of the MR whistler and was previously identified and quantified by *Lauben* [1999]. In this case the poleward motion is caused by the differential time delay of the whistler ray paths in illuminating higher  $L$ -shells (which are longer) as well as the differential time delay of electrons traveling from their respective wave-particle interaction regions (typically near the geomagnetic equator) to the ionosphere which increases with  $L$ -shell, again due to the larger distance that the electrons need to travel.

The second timescale involved is much larger ( $\sim 10$  sec), and is associated with the tendency of each of the frequency components of the MR whistler wave to magnetospherically reflect many times and gradually migrate to and settle on frequency-specific  $L$ -shells. Since the frequency components that propagate to the highest  $L$ -shells are also typically the longest enduring, and for typical midlatitude locations of source lightning discharges the resulting region of wave-particle interaction also slowly moves to higher  $L$ -shells with precipitation occurring at higher latitudes in later times.

Experimental evidence for rapid (within  $< 1$  sec) poleward motion of the precipitation region caused by the differential time delay of the whistler-mode ray paths, as well as its poleward displacement (with respect to the source latitude) due to the general tendency of ray paths to move outward have been observed [*Lauben et al.*, 1999; *Johnson et al.*, 1999]. Measurement of the larger scale poleward displacement occurring over slower (many seconds) time scales has been recently realized using the

subionospheric VLF method, where VLF signal perturbations occurring with onset delays (with respect to the causative lightning discharge) and onset durations (representing the continuing precipitation) of many seconds were observed [Inan, 2002; Inan *et al.*, 2004]. These measurements constitute the first observations in the bounce loss-cone of precipitation induced by the magnetospherically reflected components of nonducted whistlers launched by lightning discharges, since the previous observations reported by Johnson *et al.* [1999] were specifically limited to precipitation induced by the very first nonducted ray path during its first equatorial crossing, and before any magnetospheric reflection, along the lines of the predictions of Lauben *et al.* [1999]. Also, while strong experimental evidence for precipitation driven by the MR components is implied in the SAMPEX observations [Blake *et al.*, 2001], these observations are in the drift loss-cone and represent the accumulated sum of precipitation due to many whistlers. The observation of individual events of MR whistler-driven precipitation reported by Inan [2002] and Inan *et al.* [2004] indicate that this relatively weaker component of precipitation induced by whistler wave energy can be measured and may facilitate quantitative studies of magnetospheric particle distributions and more accurate estimates of loss rates for energetic electrons.

### 6.3 Suggestions for future work

In our work we have used initial lightning discharge parameters consistent with those of cloud-to-ground strokes only, which account for approximately one quarter of all observed discharges [Mackerras *et al.*, 1998]. This was done because intracloud flashes generally have much smaller peak current magnitudes associated with their discharges than cloud-to-ground discharges, however they do have a more favorable radiation pattern for effective coupling to the magnetosphere (over a certain frequency range). Modeling of intracloud lightning can be easily incorporated into our code by simply adjusting the initial magnitude and distribution (as a function of latitude) of wave power of the sample rays as they are injected at 1000 km into the plasmasphere. Such a model could determine to what degree the overall lightning-driven loss rate

of radiation-belt electrons is affected by intracloud discharges, whether their precipitation signatures could be detected, and what their typical signature would be as a function of energy and time.

The harmonic resonance modes included in this work were  $-5$  to  $5$  based on previous work done by *Abel and Thorne*, [1998a]. However, as shown by *Albert* [1994], for  $L \gtrsim 3$ , it is necessary to include much higher order resonance modes, i.e.,  $-100$  to  $100$ , in order to avoid underestimating the lifetime values by as much as a factor of  $5$ . Although the partial contribution to the precipitation driven by each successive resonance mode becomes progressively smaller, inclusion of a large number of resonance modes partially compensates for this trend. Future versions of our code should incorporate the broader range of resonance modes in order to examine its effect on the current estimates of total energetic electron precipitation.

To obtain a sense of the global effect of MR whistlers upon the radiation belts it would be interesting to convolve our results of the precipitated energy and number fluxes with latitude dependent lightning occurrence rates (such as the one given by e.g., *Orville and Spencer* [1979]), and a global lightning amplitude distribution. Closely related is the question of the amplitude of MR whistlers injected by lightning on the day side of the Earth. The present study, in keeping with past work [*Lauben et al.*, 2001] has focused on the night side of the Earth motivated by the fact that the transionospheric collisional damping is  $\sim 20$  to  $30$  dB lower in the range  $60$ – $1500$  km (Fig. 3-35 of *Helliwell* [1965]) on the nightside. However, experimental evidence [*Don Carpenter*, personal communication] seems to suggest that more powerful strokes generate clearly observable subionospheric VLF signal perturbations even on the day side, and this effect needs to be assessed in light of the resultant precipitation, and effect on global radiation belt lifetimes.

To extend the study of radiation belt lifetimes even further, we suggest repeating the analysis of the type made by *Abel and Thorne* [1998a,b] using our code over a range of  $L$ -shells covering the inner magnetosphere, and examining the relative importance of MR whistlers versus other wave types such as VLF transmitter signals, plasmaspheric hiss, and power-line harmonic radiation.

Another suggestion for future work involves extending the present code to couple

the various latitude ‘bins’ and include the non-linearity in the evaluation of the equations of motion of the electron in the oblique whistler wave packet. While we do not believe that the resultant precipitation characteristics would be significantly affected, such a code could be used to verify the results shown in the present work and assess the degree to which our results may be affected with the inclusion of the nonlinearity.

A final suggestion for extension of our code deals with assessing the amplitude variation of the rays along their ray paths more accurately. An initial step towards this goal could be inclusion of the effects of linear wave growth calculated parametrically (as was done with Landau damping) using the ‘hot plasma’ approximation, for a range of resonance modes other than the  $m=0$  resonance.

The bulk of the work presented in this thesis has been of a theoretical/modeling nature, and an obvious extension to future efforts would be to experimentally test the many predictions put forth herein. We discuss below several ideas for testing various aspects of our model.

Firstly, the analysis hinges on the correct amplitude values of MR whistlers, which need to be verified. This can be accomplished by correlating observed MR whistler signatures (with amplitude information) aboard a satellite, with lightning discharges whose peak return current is known (such information is commonly available in the United States from the National Lightning Detection Network – NLDN). This experiment will not only test our model but many related issues dealing with transionospheric propagation, role of horizontal ionospheric density gradients, and coupling efficiency.

Secondly, given a number of satellite-based observations of MR whistlers (preferably with amplitude information included) of the type reported by *Shklyar and Jiricek* [2000], future workers could search for evidence of energetic electron precipitation. Such a search could include satellites measurements (ideally) with particle detectors observing within the loss cone, or the observation of associated effects such as ionospheric D-region disturbances of the type observed by *Johnson et al.* [1999] and *Inan et al.* [2004]. The important step is to ensure that the measured precipitation is indeed caused by an observed MR whistler, and hence the electron precipitation signatures would be sought around the times of MR whistler wave observation, and with

temporal signatures consistent with those predicted for MR whistler-induced precipitation. The recent observations reported by *Inan et al.* [2004] of subionospheric VLF signal perturbations with onset delays and durations of many seconds, were indeed identified in this manner and interpreted as being due to the MR components of nonducted whistlers.

We have included many observable precipitation signatures including differential number flux, integrated energy and number fluxes at various  $L$ -shells and perturbed ionospheric patches (together with their poleward motion as a function of time on both short and long timescales) in geographic coordinates. Observation of any one of these signatures (ideally the most detailed differential number flux) would be a defining signature of precipitation induced by the MR components of a nonducted whistler event, and could provide invaluable confirmation of the MR whistler scattering mechanism, as well as information on potential inadequacies of our model, and additional factors which need to be included such as ionospheric or magnetospheric structures, or more self-consistent code.

A final extension of our model which we have not focused on, but is nevertheless equally valid and interesting, is the possibility of using MR whistler wave  $f-t$  signatures to determine the properties of the medium through which the wave propagated. This determination would involve an *in situ* measurement of the plasmaspheric electron density structures (e.g., such as CRRES data) together with the observation of a number of MR whistler waves recorded with sufficient resolution to permit accurate numerical modeling. While this problem has been attempted in the past with some success [Edgar, 1972], the proliferation of cheap computing power makes computation of several thousand potential density profiles both manageable and realistic. For this purpose, wideband measurements of MR whistlers on a high altitude satellite are needed, since these types of whistlers are not otherwise observable.



# Appendix A

## Derivations

### A.1 Calculation of the precipitation flux of Section 3.2.2

We show the derivation of (3.1) describing the differential contribution to precipitation from a given wave component at a given frequency. For convenience, (3.1) is repeated below:

$$\Delta\text{flux} \propto \frac{B^w v^2}{v_z^{\text{res}} E^3 \gamma^4} \quad (\text{A.1})$$

We begin by considering an empirical fit to an electron distribution function in the energy range of interest ( $E > 150$  keV), specified in  $E - \alpha$  space. Distributions of this form have been used previously [*Chang and Inan*, 1983*a*; *Chang and Inan*, 1985*a*], with the assumed energy dependence from *Inan et al.* [1985*a*] and *Lauben et al.* [2001] given by:

$$f(E, \alpha) = A \frac{1}{E^3} g(\alpha) \quad (\text{A.2})$$

where  $A$  is a normalizing constant,  $E$  is the electron energy, and  $g(\alpha)$  is a function of the pitch-angle  $\alpha$  describing the anisotropy of the particle distribution. In the present work we need to know  $g(\alpha)$  only near the loss-cone, the inside of which is taken to

be empty. For this purpose we assume:

$$g(\alpha \geq \alpha_{lc}) = 1 \quad (\text{A.3})$$

$$g(\alpha < \alpha_{lc}) = 0 \quad (\text{A.4})$$

Following an interaction with the wave, the distribution function is perturbed from its initial state. The resonant particles at the edge of the loss-cone scatter into the loss-cone, i.e., those particles whose velocity parallel to the  $\mathbf{B}$ -field ( $v_z$ ) matches the resonance velocity ( $v_z^{\text{res}}$ ), i.e.,  $v = v_z^{\text{res}}$  where

$$v_z^{\text{res}} = \frac{\omega_H/\gamma - \omega}{k_z} \quad (\text{A.5})$$

where  $\omega_H$  and  $\omega$  are the gyrofrequency and the wave frequency respectively,  $k_z$  is the component of the wave-number ( $\mathbf{k}$ ) parallel to the  $\mathbf{B}$ -field, and  $\gamma = (1 - v^2/c^2)^{-1/2}$  is the relativistic Lorentz factor. The configuration of the pitch angles of the resonant particles following the interaction is sinusoidal as a function of initial Larmor phase as shown in *Inan* [1977] and Figure 5.8a, with half of the initially trapped particles scattering into the loss-cone (assuming that the portion of scattered particles precipitated into the loss cone is directly proportional to  $\Delta\alpha_{\text{max}}$ ). The portion of the electron distribution function inside the loss-cone is then given as:

$$f_{lc} \propto A \frac{1}{E^3} \Delta\alpha_{\text{max}} \quad (\text{A.6})$$

evaluated at  $E = E^{\text{res}}$  where  $E^{\text{res}}$  is determined from  $v_z^{\text{res}}$  and  $\alpha_{lc}$ . Expanding the change in pitch angle  $\Delta\alpha$  into a Taylor series and retaining only the first term (under the assumption that  $\Delta\alpha$  is small – as is well known based on past work [*Inan et al.*, 1989]), gives:

$$\Delta\alpha_{\text{max}} \simeq \frac{\partial\alpha}{\partial t} \Delta t \quad (\text{A.7})$$

where  $\Delta t$  is the interaction time, given approximately as:

$$\Delta t \simeq \frac{l_i}{v_z^{\text{res}}} \quad (\text{A.8})$$

and  $l_i$  is the interaction length, i.e., the distance over which the resonant particle stays in resonance with the wave, given by *Inan* [1987] as:

$$l_i \simeq \left[ \frac{16\pi v_z^{\text{res}} L^2 R_E^2}{9\omega_H^{\text{eq}}} \right]^{1/3} \quad (\text{A.9})$$

Typically  $l_i \sim 2000$  km for  $L=2$ , and it can be shown that this term stays constant within a factor of  $\sim 2$  over the range of  $L$ -shells that we are concerned with. We thus treat it as a constant and assert that to first order  $\Delta t \propto 1/v_z^{\text{res}}$ .

Based on the derivation [*Bell*, 1984] of the differential equations (2.24)–(2.25) governing the trajectory of a particle that encounters an obliquely propagating, coherent whistler wave with slowly varying amplitude, frequency and wave-number (assumptions well suited to our present analysis) in the magnetosphere,  $\partial\alpha/\partial t$  can be shown to be proportional to the wave magnetic field amplitude as follows:

$$\frac{\partial\alpha}{\partial t} \propto \frac{B^w}{m\gamma} \quad (\text{A.10})$$

Combining (A.6)–(A.10) we obtain a crude model for the behavior of the distribution function in the loss-cone:

$$f_{\text{lc}} \propto \frac{1}{E^3} \frac{B^w}{m\gamma} \frac{1}{v_z^{\text{res}}} \quad (\text{A.11})$$

Finally, we convert to a flux value using the relativistic formulation described by *Chang* [1983] which is repeated here for convenience. From conservation of particles, the flux  $\Phi$  is related to the distribution function  $f$  using the equation:

$$\Phi dA d\Omega dE dt = f(E, \alpha) v^2 dv d\Omega v dt dA \quad (\text{A.12})$$

We can also relate  $dE$  and  $dv$  as follows:

$$dE = d \left[ mc^2 \left( \frac{1}{\sqrt{1 - v^2/c^2}} - 1 \right) \right] = \frac{mc^2}{(1 - v^2/c^2)^{3/2}} \frac{v dv}{c^2} = mc^2 \gamma^3 \frac{v dv}{c^2} \quad (\text{A.13})$$

Combining (A.12) and (A.13) gives:

$$\Phi = f(E, \alpha) v^2 / m \gamma^3 \quad (\text{A.14})$$

which allows us to write (A.11) in terms of flux as

$$\Delta \text{flux} \propto \frac{B^w v^2}{E^3 v_z^{\text{res}} \gamma^4}$$

giving (3.1) as in the text. Note also that all the constants in the expression (such as rest mass, numeric constants, etc.) have been incorporated into the proportionality sign.

## A.2 Analytical evaluation of (2.26)

As shown in Section 5.1.2, the equation describing the rate of change of the pitch-angle of the resonant particle (2.26) is divided into three parts:  $T_1$ ,  $T_2$ , and  $T_3$ . The term  $T_3$  describes the adiabatic motion of the particle and is neglected in the calculation since it does not change the equatorial pitch angle. The factor  $T_2$  varies slowly in the integration interval and is assumed to be constant, evaluated in the center of the integration interval  $\lambda_i$ . The factor  $T_1$  varies rapidly in the integration interval, thereby controlling the efficiency of the wave-particle interaction. In this section, we discuss the integration of the factor  $T_1$ .

Using (2.27) we write:

$$\begin{aligned} \dot{\eta} &= \frac{m\omega_H}{\gamma} - \omega - k_z v_z \\ &\approx \frac{m}{\gamma} \left[ \omega_{H0} + \frac{\partial \omega_H}{\partial z} \left( z - \frac{\Delta z}{2} \right) \right] - \omega - k_z \left[ v_{z0} + \frac{\partial v_z}{\partial z} \left( z - \frac{\Delta z}{2} \right) \right] \end{aligned} \quad (\text{A.15})$$

where we have expanded  $\omega_H$  and  $v_z$  to first order around the center of the integration interval (i.e., at  $\Delta z/2$ ), the subscript “0” refers to the value of the quantity at  $\Delta z/2$ ,

and the derivatives  $\partial\omega_{\text{H}}/\partial z$ ,  $\partial v_z/\partial z$  are evaluated at  $\Delta z/2$ . The quantity  $k_z$  is obtained from the ray tracing simulation described in 4.2.4, and is taken to be constant in the integration interval since we do not have a simple analytical expression for its variation along  $z$ . In order to perform the integration of  $\dot{\eta}$  we change the variable of integration from time to distance along the field line  $z$ , and expand  $\omega_{\text{H}}$  to first order, giving:

$$\begin{aligned}\eta &= \int_0^z \dot{\eta} \frac{dz}{v_z} \\ &= \int_0^z \left\{ \frac{m}{\gamma} \left[ \omega_{\text{H}0} + \frac{\partial\omega_{\text{H}}}{\partial z} \left( z - \frac{\Delta z}{2} \right) \right] - \omega - k_z v_z \right\} \frac{dz}{v_z} \\ &= \int_0^z \left\{ \frac{m\omega_{\text{H}0}}{\gamma v_z} + \frac{m}{\gamma v_z} \frac{\partial\omega_{\text{H}}}{\partial z} \left( z - \frac{\Delta z}{2} \right) - \frac{\omega}{v_z} - k_z \right\} dz\end{aligned}\tag{A.16}$$

where we initially used the unexpanded value of  $v_z$  so as to cancel with the newly introduced  $v_z$  in the denominator. Expanding  $v_z$  to first order as above, inverting, and applying the binomial approximation gives:

$$\begin{aligned}v_z &= v_{z0} + \frac{\partial v_z}{\partial z} \left( z - \frac{\Delta z}{2} \right) \\ \frac{1}{v_z} &= \frac{1}{v_{z0} + \frac{\partial v_z}{\partial z} \left( z - \frac{\Delta z}{2} \right)} = \frac{1}{v_{z0}^*} \frac{1}{\left( 1 + \frac{1}{v_{z0}^*} \frac{\partial v_z}{\partial z} z \right)} = \frac{1}{v_{z0}^*} \left( 1 - \frac{1}{v_{z0}^*} \frac{\partial v_z}{\partial z} z \right)\end{aligned}\tag{A.17}$$

where

$$v_{z0}^* = v_{z0} - \frac{\partial v_z}{\partial z} \frac{\Delta z}{2}$$

We use (A.17) in (A.16), eliminate second order terms arising from the second term of A.16 and regroup to give:

$$\begin{aligned}
\eta &= \int_0^z \underbrace{\left[ \frac{m\omega_{H0}}{\gamma v_{z0}^*} - \frac{m}{\gamma v_{z0}^*} \frac{\partial \omega_H}{\partial z} \frac{\Delta z}{2} \frac{\omega}{v_{z0}^*} k_z \right]}_{A_0} + \dots \\
&\quad z \underbrace{\left[ -\frac{m\omega_{H0}}{\gamma (v_{z0}^*)^2} \frac{\partial v_z}{\partial z} + \frac{m}{\gamma v_{z0}^*} \frac{\partial \omega_H}{\partial z} \left( 1 + \frac{\Delta z}{2v_{z0}^*} \right) + \frac{\omega}{(v_{z0}^*)^2} \frac{\partial v_z}{\partial z} \right]}_{A_1} dz \quad (A.18) \\
&= \left( A_0 z + \frac{1}{2} A_1 z^2 \right) \Big|_0^z = A_0 z + \frac{1}{2} A_1 z^2
\end{aligned}$$

At the magnetic equator, the first order derivatives  $\partial \omega_H / \partial z = \partial v_z / \partial z = 0$  and we need to treat this case separately as shown in (A.27). Using this expression for  $\eta$  we now return to (2.26) which we write as:

$$\frac{\partial \alpha}{\partial t} = T_1 \sin(\eta + \eta_0) \quad (A.19)$$

where  $\eta_0$  is the integration constant and represents the initial phase angle between the wave and particle. To obtain  $\Delta \alpha$  we integrate (A.19), changing the variable of integration from time to distance (along the field line) as above, giving:

$$\begin{aligned}
\Delta \alpha &= \int_0^{\Delta t} \frac{\partial \alpha}{\partial t} dt \\
&= \int_0^{\Delta z} \frac{\partial \alpha}{\partial t} \frac{dz}{v_{z0}} \\
&= \frac{T_1}{v_{z0}} \int_0^{\Delta z} \sin(\eta + \eta_0) dz \quad (A.20)
\end{aligned}$$

We have used the zeroth order expansion of  $v_z$  because the integrand varies much faster than the first order expansion and does not contribute significantly to the integration.

The final pitch angle change of a particle  $\Delta \alpha$  depends strongly on  $\eta_0$ . However as shown by *Inan* [1977], if the interaction is assumed to be linear, then  $\Delta \alpha$  for a set of gyrotropic particles is a simple sinusoidal function of  $\eta_0$ . This dependence implies that we do not need to calculate the pitch angle change for each  $\eta_0$  explicitly but instead only need to determine a measure of the spreading (amplitude) of the sine function, reducing the number of equations for the gyrotropic distribution to one. For

this purpose we use the root-mean-square (rms) value derived as follows:

$$\begin{aligned}
 (\Delta\alpha)^2 &= \left(\frac{T_1}{v_{z0}}\right)^2 \left[ \int_0^{\Delta z} \sin(\eta + \eta_0) dz \right]^2 \\
 &\quad \left(\frac{T_1}{v_{z0}}\right)^2 \left[ \int_0^{\Delta z} \sin \eta \cos \eta_0 + \cos \eta \sin \eta_0 dz \right]^2 \\
 &\quad \left(\frac{T_1}{v_{z0}}\right)^2 \left[ \cos \eta_0 \int_0^{\Delta z} \sin \eta dz + \sin \eta_0 \int_0^{\Delta z} \cos \eta dz \right]^2 \\
 &\quad \left(\frac{T_1}{v_{z0}}\right)^2 \left[ \cos^2 \eta_0 \left( \int_0^{\Delta z} \sin \eta dz \right)^2 + \sin^2 \eta_0 \left( \int_0^{\Delta z} \cos \eta dz \right)^2 \right. \\
 &\quad \left. + \sin 2\eta_0 \int_0^{\Delta z} \sin \eta dz \int_0^{\Delta z} \cos \eta dz' \right]
 \end{aligned} \tag{A.21}$$

We average over  $\eta_0$  to get:

$$\begin{aligned}
 \Delta\alpha_{\text{rms}} &= \sqrt{\frac{1}{2\pi} \int_0^{2\pi} (\Delta\alpha)^2 d\eta_0} \\
 &= \frac{1}{\sqrt{2}} \left| \frac{T_1}{v_{z0}} \right| \sqrt{\left( \int_0^{\Delta z} \sin \eta dz \right)^2 + \left( \int_0^{\Delta z} \cos \eta dz \right)^2}
 \end{aligned} \tag{A.22}$$

We are thus left with the task of evaluating  $\int_0^{\Delta z} \sin \eta dz$  and  $\int_0^{\Delta z} \cos \eta dz$ . Expanding using (A.18) we get:

$$\begin{aligned}
 \int_0^{\Delta z} \sin \eta dz &= \int_0^{\Delta z} \sin \left( \frac{1}{2} A_1 z^2 + A_0 z \right) dz \\
 &= \sqrt{\frac{\pi}{A_1}} \left[ \cos \left( \frac{A_0^2}{2A_1} \right) F_s \left( \frac{A_0 + A_1 \Delta z}{\sqrt{\pi A_1}} \right) - \sin \left( \frac{A_0^2}{2A_1} \right) F_c \left( \frac{A_0 + A_1 \Delta z}{\sqrt{\pi A_1}} \right) \right]
 \end{aligned} \tag{A.23}$$

where  $F_s$  and  $F_c$  are Fresnel sine and cosine integrals respectively, defined as:

$$\begin{aligned}
 F_s(x) &= \int_0^x \sin \left( \frac{\pi}{2} t^2 \right) dt = \left( \frac{\pi}{2} \right) \frac{x^3}{3 \cdot 1!} - \left( \frac{\pi}{2} \right)^3 \frac{x^7}{7 \cdot 3!} + \left( \frac{\pi}{2} \right)^5 \frac{x^{11}}{11 \cdot 5!} - \dots \\
 F_c(x) &= \int_0^x \cos \left( \frac{\pi}{2} t^2 \right) dt = x - \left( \frac{\pi}{2} \right)^2 \frac{x^5}{5 \cdot 2!} + \left( \frac{\pi}{2} \right)^4 \frac{x^9}{9 \cdot 4!} - \dots
 \end{aligned} \tag{A.24}$$

Similarly:

$$\begin{aligned} \int_0^{\Delta z} \cos \eta \, dz &= \int_0^{\Delta z} \cos\left(\frac{1}{2}A_1 z^2 + A_0 z\right) dz \\ &= \sqrt{\frac{\pi}{A_1}} \left[ \cos\left(\frac{A_0^2}{2A_1}\right) F_c\left(\frac{A_0 + A_1 \Delta z}{\sqrt{\pi A_1}}\right) - \sin\left(\frac{A_0^2}{2A_1}\right) F_s\left(\frac{A_0 + A_1 \Delta z}{\sqrt{\pi A_1}}\right) \right] \end{aligned} \quad (\text{A.25})$$

Inserting (A.23) and (A.25) into (A.22), expanding and simplifying gives the final expression:

$$\Delta\alpha_{\text{rms}} = \sqrt{\frac{\pi}{2A_1}} \left| \frac{T_1}{v_{z0}} \right| \sqrt{F_c^2\left(\frac{A_0 + A_1 \Delta z}{\sqrt{\pi A_1}}\right) - F_s^2\left(\frac{A_0 + A_1 \Delta z}{\sqrt{\pi A_1}}\right)} \quad (\text{A.26})$$

Equation (A.26) is valid everywhere except at the magnetic equator, when the resonance condition is exactly satisfied [i.e., (2.27) is identically zero]. To treat this situation, we return to (A.22) and examine each of the integrals in turn. At the magnetic equator  $\partial\omega_{\text{H}}/\partial z = \partial v_z/\partial z = 0$  and  $\dot{\eta}$  becomes a constant (to first order) given by:

$$\dot{\eta} = \frac{m\omega_{\text{H}0}}{\gamma} - \omega - k_z v_{z0} = \dot{\eta}_1 \quad (\text{A.27})$$

and the integrals in (A.26) can be written:

$$\begin{aligned} \int_0^{\Delta z} \sin \eta \, dz &= \int_0^{\Delta z} \sin(\dot{\eta}_1 z) \, dz = \frac{-1}{\dot{\eta}_1} \cos(\dot{\eta}_1 z) \Big|_0^{\Delta z} \\ &= \frac{-1}{\dot{\eta}_1} \cos(\dot{\eta}_1 \Delta z) - \left( \frac{-1}{\dot{\eta}_1} \right) \\ &= \frac{1}{\dot{\eta}_1} [1 - \cos(\dot{\eta}_1 \Delta z)] \end{aligned} \quad (\text{A.28})$$

and similarly:

$$\begin{aligned} \int_0^{\Delta z} \cos \eta \, dz &= \int_0^{\Delta z} \cos(\dot{\eta}_1 z) \, dz = \frac{1}{\dot{\eta}_1} \sin(\dot{\eta}_1 z) \Big|_0^{\Delta z} \\ &= \frac{1}{\dot{\eta}_1} \sin(\dot{\eta}_1 \Delta z) \end{aligned} \quad (\text{A.29})$$



We now insert (A.28) and (A.29) into (A.22) and simplify, giving:

$$\begin{aligned}\Delta\alpha_{\text{rms}} &= \frac{1}{\sqrt{2}} \left| \frac{T_1}{v_{z0}} \right| \sqrt{\left( \int_0^{\Delta z} \sin \eta \, dz \right)^2 + \left( \int_0^{\Delta z} \cos \eta \, dz \right)^2} \\ &= \frac{1}{\sqrt{2}} \left| \frac{T_1}{v_{z0}} \right| \sqrt{2 \left( \frac{1}{\dot{\eta}_1} \right)^2 [1 - \cos(\dot{\eta}_1 \Delta z)]}\end{aligned}\tag{A.30}$$

We now use the Taylor expansion:

$$\cos(x) \simeq 1 - \frac{x^2}{2} + \frac{x^4}{4!} - \frac{x^6}{6!} \cdots$$

and assume that  $\dot{\eta}_1 \ll 1$  (since we are at, or very near resonance), and retain only up to the second term in the expansion, giving:

$$\begin{aligned}\Delta\alpha_{\text{rms}} &= \frac{1}{\sqrt{2}} \left| \frac{T_1}{v_{z0}} \right| \sqrt{2 \left( \frac{1}{\dot{\eta}_1} \right)^2 [1 - \cos(\dot{\eta}_1 \Delta z)]} \\ &= \frac{1}{\sqrt{2}} \left| \frac{T_1}{v_{z0}} \right| \sqrt{2 \left( \frac{1}{\dot{\eta}_1} \right)^2 \left\{ 1 - \left[ 1 - \frac{(\dot{\eta}_1 \Delta z)^2}{2} \right] \right\}} \\ &= \frac{1}{\sqrt{2}} \left| \frac{T_1}{v_{z0}} \right| \sqrt{2 \left( \frac{1}{\dot{\eta}_1} \right)^2 \left[ \frac{(\dot{\eta}_1)^2 (\Delta z)^2}{2} \right]} \\ &= \frac{\Delta z}{\sqrt{2}} \left| \frac{T_1}{v_{z0}} \right|\end{aligned}\tag{A.31}$$

For small (but non-zero) values of  $\dot{\eta}_1$  at the geomagnetic equator, equations (A.26) and (A.31) give very similar results, which converge as  $\dot{\eta}_1 \rightarrow 0$ . However, since both the numerator and denominator of (A.26) tend to zero as  $\dot{\eta}_1 \rightarrow 0$ , when  $\dot{\eta}_1 = 0$ , (A.26) gives results that are invalid, and only (A.31) must be used.

# Bibliography

- [Appleton, 1927] Appleton, E.V., The influence of the Earth's magnetic field on wireless transmission (summary), *U.R.S.I. Proc. 1927*, Washington Assembly (Brussels 1928)
- [Appleton, 1932] Appleton, E.V., Wireless studies of the ionosphere, *J. Inst. Elec. Engrs.*, 71, 642, 1932
- [Abel and Thorne, 1998a] Abel, B., and R.M. Thorne, Electron scattering loss in Earth's inner magnetosphere - 1. Dominant physical processes, *Journal of Geophysical Research-Space Physics*, 103 (A2), 2385-2396, 1998a
- [Abel and Thorne, 1998b] Abel, B., and R.M. Thorne, Electron scattering loss in Earth's inner magnetosphere - 2. Sensitivity to model parameters, *Journal of Geophysical Research-Space Physics*, 103 (A2), 2397-2407, 1998b.
- [Albert, 1994] Albert, J.M., Quasi-linear pitch angle diffusion coefficients: retaining high harmonics, *Journal of Geophysical Research*, 99 (A12), 23,741-23745, 1994.
- [Angerami and Thomas, 1964] Angerami, J.J., and J.O. Thomas, Studies of Planetary Atmospheres. 1. Distribution of Electrons + Ions in Earths Exosphere, *Journal of Geophysical Research*, 69 (21), 4537, 1964.
- [Arantes and Scarabucci, 1975] Arantes, D.S., and R.R. Scarabucci, Full-wave analysis and coupling effects in a crossover region, *Radio Science*, 10 (8-9), 801-811, 1975.

- [Ashour-Abdalla, 1972] Ashour-Abdalla, M., Amplification of whistler waves in the magnetosphere, *Planetary Space Science*, 20, 639, 1972.
- [Banks *et al.*, 1974] Banks, P.M., C.R. Chappell, and A.F. Nagy, A new model for the interaction of auroral electrons with the atmosphere: spectral degradation, backscatter, optical emissions, and ionization, *Journal of Geophysical Research*, 79 (10), 1459-1470, 1974.
- [Bell, 1984] Bell, T.F., The Nonlinear Gyroresonance Interaction between Energetic Electrons and Coherent VLF Waves Propagating at an Arbitrary Angle with Respect to the Earth's Magnetic-Field, *Journal of Geophysical Research*, 89 (A2), 905-918, 1984.
- [Bell, 1986] Bell, T.F., The wave magnetic field amplitude threshold for nonlinear trapping of energetic gyroresonant and Landau resonant electrons by nonducted VLF waves in the magnetosphere, *Journal of Geophysical Research*, 91 (A4), 4365-4379, 1986.
- [Bell *et al.*, 2002] Bell, T.F., U.S. Inan, J. Bortnik, and J.D. Scudder, The Landau damping of magnetospherically reflected whistlers within the plasmasphere, *Geophysical Research Letters*, 29 (15), art. no.-1733, 2002.
- [Bernhardt and Park, 1977] Bernhardt, P.A., and C.G. Park, Protonospheric-Ionospheric Modeling of VLF Ducts, *Journal of Geophysical Research-Space Physics*, 82 (32), 5222-5230, 1977.
- [Bilitza, 2001] Bilitza, D., International Reference Ionosphere 2000, *Radio Science*, 36 (2), 261-275, 2001.
- [Bittencourt, 1995] Bittencourt, J.A., *Fundamentals of Plasma Physics*, Printed in Brazil, Sao Jose dos Campos, SP, 1995.
- [Blake *et al.*, 2001] Blake, J.B., U.S. Inan, M. Walt, T.F. Bell, J. Bortnik, D.L. Chenette, and H.J. Christian, Lightning-induced energetic electron flux enhancements

- in the drift loss cone, *Journal of Geophysical Research-Space Physics*, 106 (A12), 29733-29744, 2001.
- [Bortnik et al., 2002a] Bortnik, J., U.S. Inan, and T.F. Bell,  $L$  dependence of energetic electron precipitation driven by magnetospherically reflecting whistler waves, *Journal of Geophysical Research-Space Physics*, 107 (A8), 1150, 2002a.
- [Bortnik et al., 2002b] Bortnik, J., U.S. Inan, and T.F. Bell, Temporal signatures of electron precipitation induced by magnetospherically reflecting whistlers, *Eos. Trans. AGU*, 83(47), Fall Meet. Suppl., Abstract SM52A-0558, 2002b.
- [Bortnik et al., 2003a] Bortnik, J., U.S. Inan, and T.F. Bell, Energy distribution and lifetime of magnetospherically reflecting whistlers in the plasmasphere, *Journal of Geophysical Research-Space Physics*, 108 (A5), art. no.-1199, 2003a.
- [Bortnik et al., 2003b] Bortnik, J., U.S. Inan, and T.F. Bell, Frequency-time spectra of magnetospherically reflecting whistlers in the plasmasphere, *Journal of Geophysical Research-Space Physics*, 108 (A1), 1030, 2003b.
- [Brinca, 1972] Brinca, A.L., On the Stability of Obliquely Propagating Whistlers, *Journal of Geophysical Research*, 77 (19), 3495, 1972.
- [Burgess et al., 1993] Burgess, W.C., and U.S. Inan, The Role of Ducted Whistlers in the Precipitation Loss and Equilibrium Flux of Radiation Belt Electrons, *Journal of Geophysical Research-Space Physics*, 98 (A9), 15643-15665, 1993.
- [Carpenter, 1963] Carpenter, D.L., Whistler evidence of a 'knee' in the magnetospheric ionization density profile, *Journal of Geophysical Research*, 68, 1675, 1963.
- [Carpenter and LaBelle, 1982] Carpenter, D.L., and J.W. LaBelle, A study of whistlers correlated with bursts of electron precipitation near  $L = 2$ , *Journal of Geophysical Research*, 87 (A6), 4427-4434, 1982.
- [Carpenter et al., 1984] Carpenter, D.L., U.S. Inan, M.L. Trimpi, R.A. Helliwell, and J.P. Katsufakis, Perturbations of Subionospheric LF and MF Signals Due to

- Whistler-Induced Electron-Precipitation Bursts, *Journal of Geophysical Research-Space Physics*, 89 (A11), 9857-9862, 1984.
- [*Carpenter and Anderson*, 1992] Carpenter, D.L., and R.R. Anderson, An ISEE/Whistler Model of Equatorial Electron-Density in the Magnetosphere, *Journal of Geophysical Research-Space Physics*, 97 (A2), 1097-1108, 1992.
- [*Carpenter et al.*, 2002] Carpenter, D.L., M.A. Spasojevic', T.F. Bell, U.S. Inan, B.W. Reinisch, I.A. Galkin, R.F. Benson, J.L. Green, S.F. Fung, and S.A. Boardson, Small-scale field-aligned plasmaspheric density structures inferred from the Radio Plasma Imager on IMAGE, *Journal of Geophysical Research-Space Physics*, Vol. 107, No. A9, 1258, doi:10.1029/2001JA009199, 2002.
- [*Carpenter et al.*, 2003] Carpenter, D.L., T.F. Bell, U.S. Inan, R.F. Benson, V.S. Sonwalkar, B.W. Reinisch, and D.L. Gallagher, Z-mode sounding within propagation "cavities" and other inner magnetospheric regions by the RPI instrument on the IMAGE satellite, *Journal of Geophysical Research-Space Physics*, Vol. 108, No. A12, 1421, doi:10.1029/2003JA010025, 2003.
- [*Cerisier*, 1974] Cerisier, J.C., Ducted and Partly Ducted Propagation of VLF Waves through the Magnetosphere, *Journal of Atmospheric and Terrestrial Physics*, 36 (9), 1443, 1974.
- [*Chang*, 1983] Chang, H.C., Cyclotron resonant scattering of energetic electrons by electromagnetic waves in the magnetosphere, Technical Report E414-1, Stanford University, Palo Alto, 1983.
- [*Chang and Inan*, 1983a] Chang, H.C., and U.S. Inan, Quasi-Relativistic Electron-Precipitation Due to Interactions with Coherent VLF Waves in the Magnetosphere, *Journal of Geophysical Research-Space Physics*, 88 (A1), 318-328, 1983a.
- [*Chang and Inan*, 1983b] Chang, H.C., and U.S. Inan, A Theoretical-Model Study of Observed Correlations between Whistler Mode Waves and Energetic Electron-Precipitation Events in the Magnetosphere, *Journal of Geophysical Research-Space Physics*, 88 (A12), 53-58, 1983b.

- [Chang *et al.*, 1983] Chang, H.C., U.S. Inan, and T.F. Bell, Energetic Electron-Precipitation Due to Gyroresonant Interactions in the Magnetosphere Involving Coherent-VLF Waves with Slowly Varying Frequency, *Journal of Geophysical Research-Space Physics*, 88 (A9), 7037-7050, 1983.
- [Chang and Inan, 1985a] Chang, H.C., and U.S. Inan, Lightning-Induced Electron-Precipitation from the Magnetosphere, *Journal of Geophysical Research-Space Physics*, 90 (A2), 1531-1541, 1985a.
- [Chang and Inan, 1985b] Chang, H.C., and U.S. Inan, Test Particle Modeling of Wave-Induced Energetic Electron-Precipitation, *Journal of Geophysical Research-Space Physics*, 90 (A7), 6409-6418, 1985b.
- [Christian *et al.*, 1989] Christian, H.J., R.J. Blakeslee, and S.J. Goodman, The detection of lightning from geostationary orbit, *Journal of Geophysical Research*, 94 (D11), 13329-13337, 1989.
- [Clilverd *et al.*, 2002] Clilverd, M.A., D. Nunn, S.J. Lev-Tov, U.S. Inan, R.L. Dowden, C.J. Rodger, and A.J. Smith, Determining the size of lightning-induced electron precipitation patches, *Journal of Geophysical Research-Space Physics*, 107 (A8), 10.1029/2001JA000301, 2002.
- [Crary, 1961] Crary, J.H., The effect of the Earth-ionosphere waveguide on whistlers, Technical Report 9, Stanford University, Palo Alto, 1961.
- [Cummer and Inan, 1997] Cummer, S.A., and U.S. Inan, Measurement of charge transfer in sprite-producing lightning using ELF radio atmospherics, *Geophysical Research Letters*, 24 (14), 1731-1734, 1997.
- [Dantas, 1972] Dantas, N.H., OGO-4 Satellite observations of whistler-mode propagation effects associated with caustics in the magnetosphere, Technical Report 3469-1, Stanford University, Palo Alto, 1972.
- [Das, 1971] Das, A.C., A mechanism for VLF emissions, *Journal of Geophysical Research-Space Physics*, 76, 6915, 1971.

- [*Draganov et al.*, 1992] Draganov, A.B., U.S. Inan, V.S. Sonwalkar, and T.F. Bell, Magnetospherically Reflected Whistlers as a Source of Plasmaspheric Hiss, *Geophysical Research Letters*, 19 (3), 233-236, 1992.
- [*Draganov et al.*, 1993] Draganov, A.B., U.S. Inan, V.S. Sonwalkar, and T.F. Bell, Whistlers and Plasmaspheric Hiss - Wave Directions and 3-Dimensional Propagation, *Journal of Geophysical Research-Space Physics*, 98 (A7), 11401-11410, 1993.
- [*Dungey*, 1961] Dungey, J.W., Interplanetary magnetic field and the auroral zones, *Physical Review Letters*, 6 (47), 1961.
- [*Dungey*, 1963] Dungey, J.W., Loss of Van Allen Electrons Due to Whistlers, *Planetary and Space Science*, 11 (6), 591-595, 1963.
- [*Edgar*, 1972] Edgar, B.C., The structure of the magnetosphere as deduced from magnetospherically reflected whistlers, Technical Report 3438-2, Stanford University, Palo Alto, 1972.
- [*Edgar*, 1976] Edgar, B.C., The upper and lower-frequency cutoffs of magnetospherically reflected whistlers, *Journal of Geophysical Research-Space Physics*, 81 (205), 1640-1646, 1976.
- [*Gendrin*, 1961] Gendrin, R., Le guidage des whistlers par le champ magnetique, *Planet. Space Sci.*, 5, 274-282, 1961
- [*Goldberg et al.*, 1987] Goldberg, R.A., S.A. Curtis, and J.R. Barcus, Detailed spectral structure of magnetospheric electron bursts precipitated by lightning, *Journal of Geophysical Research-Space Physics*, 92 (A3), 2505-2513, 1987.
- [*Goldstein et al.*, 2002] Goldstein, H., C. Poole, and J. Safko, *Classical mechanics - Third Ed.*, Addison-Wesley Publishing Co., 2002.
- [*Green et al.*, 2002] Green, J.L., B.R. Sandel, S.F. Fung, D.L. Gallagher, B.W. Reinisch, and R.A. Helliwell, On the origin of kilometric continuum, *Journal of Geophysical Research-Space Physics*, 107 (A7) pp. SMP 12-1, CiteID 1105, DOI 10.1029/2001JA000193, July 2002.

- [Hairer et al., 2000a] Hairer, E., S.P. Norsett, and G. Wanner, *Solving Ordinary Differential Equations I - Nonstiff Problems*, Springer, 2000
- [Hairer et al., 2000b] Hairer, E., S.P. Norsett, and G. Wanner, *Solving Ordinary Differential Equations II - Stiff and Differential-Algebraic Problems*, Springer, 2000
- [Haselgrove, 1954] Haselgrove, J., Ray theory and a new method for ray tracing, *Report of the Physical Society Conference on Physics of the Ionosphere*, Cambridge, England, 355-364, 1954.
- [Helliwell, 1965] Helliwell, R.A., *Whistlers and related ionospheric phenomena*, Stanford University Press, Stanford, Calif., 1965.
- [Helliwell, 1967] Helliwell, R.A., A Theory of Discrete VLF Emissions from Magnetosphere, *Journal of Geophysical Research*, 72 (19), 4773-4790, 1967.
- [Hill and Dessler, 1991] Hill, T. W., and A. J. Dessler, Plasma motions in planetary magnetospheres, *Science*, 252, 410, 1991.
- [Hines, 1957] Hines, C.O., Heavy-ion effects in audio frequency radio propagation, *J. Atmos. and Terrest. Phys.*, 11 (1), 36-42, 1957.
- [Horne, 2002] Horne, R.B., The contribution of wave particle interactions to electron loss and acceleration in the Earth's radiation belts during geomagnetic storms, *URSI Review of Radio Science 1999-2002*: 801-828.
- [Inan, 1977] Inan, U.S., Non-linear gyroresonant interactions of energetic particles and coherent VLF waves in the magnetosphere, Technical Report 3414-3, Stanford University, Palo Alto, 1977.
- [Inan and Bell, 1977] Inan, U.S., and T.F. Bell, The Plasmopause as a VLF Wave Guide, *Journal of Geophysical Research-Space Physics*, 82 (19), 2819-2827, 1977.
- [Inan et al., 1978] Inan, U.S., T.F. Bell, and R.A. Helliwell, Nonlinear pitch-angle scattering of energetic electrons by coherent VLF waves in the magnetosphere, *Journal of Geophysical Research-Space Physics*, 82 (19), 127-142, 1978.



- [Inan *et al.*, 1982] Inan, U.S., T.F. Bell, and H.C. Chang, Particle-Precipitation Induced by Short-Duration VLF Waves in the Magnetosphere, *Journal of Geophysical Research-Space Physics*, 87 (A8), 6243-6264, 1982.
- [Inan and Tkalcovic, 1982] Inan, U.S., and S. Tkalcovic, Nonlinear equations of motion for Landau response interactions with a whistler mode wave, *Journal of Geophysical Research*, 87, 2363, 1982.
- [Inan *et al.*, 1983] Inan, U.S., R.A. Helliwell, and W.S. Kurth, Terrestrial versus Jovian VLF chorus: a comparative study, *Journal of Geophysical Research-Space Physics*, 88 (A8), 6171-6180, 1983.
- [Inan *et al.*, 1984] Inan, U.S., H.C. Chang, and R.A. Helliwell, Electron-Precipitation Zones around Major Ground-Based VLF Signal Sources, *Journal of Geophysical Research-Space Physics*, 89 (A5), 2891-2906, 1984.
- [Inan *et al.*, 1985a] Inan, U.S., D.L. Carpenter, R.A. Helliwell, and J.P. Katsufakis, Subionospheric VLF/LF Phase Perturbations Produced by Lightning-Whistler Induced Particle-Precipitation, *Journal of Geophysical Research-Space Physics*, 90 (A8), 7457-7469, 1985a.
- [Inan *et al.*, 1985b] Inan, U.S., H.C. Chang, R.A. Helliwell, W.L. Imhof, J.B. Reagan, and M. Walt, Precipitation of Radiation Belt Electrons by Man-Made Waves - a Comparison between Theory and Measurement, *Journal of Geophysical Research-Space Physics*, 90 (A1), 359-369, 1985b.
- [Inan and Carpenter, 1986] Inan, U.S., and D.L. Carpenter, On the correlation of whistlers and associated subionospheric VLF/LF perturbations, *Journal of Geophysical Research*, 91 (A3), 3106-3116, 1986.
- [Inan, 1987] Inan, U.S., Gyroresonant Pitch Angle Scattering by Coherent and Incoherent Whistler Mode Waves in the Magnetosphere, *Journal of Geophysical Research-Space Physics*, 92 (A1), 127-142, 1987.

- [Inan *et al.*, 1988] Inan, U.S., T.G. Wolf, and D.L. Carpenter, Geographic distribution of lightning-induced electron precipitation observed as VLF/LF perturbation events, *Journal of Geophysical Research*, 93 (A9), pp. 9841-9853, Sept. 1, 1988.
- [Inan *et al.*, 1989] Inan, U.S., M. Walt, H.D. Voss, and W.L. Imhof, Energy spectra and pitch angle distributions of lightning-induced electron precipitation: analysis of an event observed on the S81-1 (SEEP) satellite, *Journal of Geophysical Research-Space Physics*, 94 (A2), 1379-1401, 1989.
- [Inan *et al.*, 1990] Inan, U.S., F.A. Knifsend, and J. Oh, Subionospheric VLF “imaging” of lightning-induced electron precipitation from the magnetosphere, *Journal of Geophysical Research*, 95 (A10), pp. 17,217-17,231, Oct. 1, 1990.
- [Inan, 2002] Inan, U.S., Subionospheric VLF imaging of transient ionospheric disturbances: Early/fast events and lightning-induced electron precipitation (LEP) events, *International Union of Radio Science, XXVII<sup>th</sup> General Assembly*, No. 1633, Session HGE1, Maastricht, 2002.
- [Inan *et al.*, 2003] Inan, U.S., T.F. Bell, J. Bortnik, and J.M. Albert, Controlled precipitation of radiation belt electrons, *Journal of Geophysical Research-Space Physics*, 108 (A5), 1186, doi: 10.1029/2002JA009580, 2003.
- [Inan *et al.*, 2004] Inan, U.S., T.G. Wood, R. Moore, and J. Bortnik, Subionospheric VLF evidence of energetic electron precipitation induced by magnetospherically reflected (MR) whistlers, *Journal of Geophysical Research-Space Physics*, [In Preparation]
- [James, 1972] James, H.G., Refraction of whistler-mode waves by large-scale gradients in the middle latitude ionosphere, *Annales Geophysicae*, 28 (2), 301-309, 1972.
- [Jasna *et al.*, 1992] Jasna, D., U.S. Inan, and T.F. Bell, Precipitation of Suprathermal (100 eV) Electrons by Oblique Whistler Waves, *Geophysical Research Letters*, 19 (16), 1639-1642, 1992.

- [Jasna, 1993] Jasna, D., Gyroresonant Scattering of Radiation Belt Electrons by Oblique Whistler Waves, Stanford University Thesis, Palo Alto, 1993.
- [Johnson *et al.*, 1999] Johnson, M.P., U.S. Inan, and D.S. Lauben, Subionospheric VLF signatures of oblique (nonducted) whistler-induced precipitation, *Geophysical Research Letters*, 26 (23), 3569-3572, 1999.
- [Jones, 1970] Jones, D.L., Electromagnetic radiation from multiple return strokes of lightning, *J. Atmos. Terr. Phys.*, 32, 1077, 1970.
- [Kelley, 1989] Kelley, M.C., *The Earth's Ionosphere - Plasma Physics and Electrodynamics*, Academic Press, San Diego, CA, 1989.
- [Kennel, 1966] Kennel, C., Low-Frequency Whistler Mode, *The Physics of Fluids*, 9 (11), 2190-2202, 1966.
- [Kennel and Petschek, 1966] Kennel, C.F., and H.E. Petschek, Limit on stably trapped particle fluxes, *Journal of Geophysical Research*, 71 (1), 1966.
- [Kimura, 1966] Kimura, I., Effects of Ions on Whistler-Mode Ray Tracing, *Radio Science*, 1 (3), 269-283, 1966.
- [Kivelson and Russel, 1995] Kivelson, M.G., and C.T. Russel, *Introduction to space physics*, Cambridge University Press, 1995.
- [Lauben, 1999] Lauben, D.S., Precipitation of Radiation Belt Electrons by Obliquely-Propagating Lightning-Generated Whistler Waves, Stanford University Thesis, Palo Alto, 1999.
- [Lauben *et al.*, 1999] Lauben, D.S., U.S. Inan, and T.F. Bell, Poleward-displaced electron precipitation from lightning-generated oblique whistlers, *Geophysical Research Letters*, 26 (16), 2633-2636, 1999.
- [Lauben *et al.*, 2001] Lauben, D.S., U.S. Inan, and T.F. Bell, Precipitation of radiation belt electrons induced by obliquely propagating lightning-generated whistlers, *Journal of Geophysical Research-Space Physics*, 106 (A12), 29745-29770, 2001.

- [Lauben *et al.*, 2002] Lauben, D.S., U.S. Inan, T.F. Bell, and D.A. Gurnett, Source characteristics of ELF/VLF chorus, *Journal of Geophysical Research-Space Physics*, 107 (A12), 1429, doi: 10.1029/2000JA003019, 2002.
- [LeDocq *et al.*, 1994] LeDocq, M.J., D.A. Gurnett, and R.R. Anderson, Electron number density fluctuations near the plasmapause observed by the CRRES spacecraft, *Journal of Geophysical Research-Space Physics*, 99 (A12), 23,661-23,671, 1994.
- [Lev-Tov *et al.*, 1996] Lev-Tov, S.J., and U.S. Inan, Characteristics of localized ionospheric disturbances inferred from VLF measurements at two closely spaced receivers, *Journal of Geophysical Research*, 101 (A7), 15,737-15,747, 1996.
- [Li *et al.*, 1998] Li, X., D.N. Baker, M. Temerin, T. Cayton, G.D. Reeves, T. Araki, H. Singer, D. Larson, R.P. Lin, and S.G. Kanekal, Energetic electron injections into the inner magnetosphere during the Jan. 10-11, 1997 magnetic storm, *Geophys. Research. Lett.*, Vol. 25, No. 14, pp. 2561-2564, 1998.
- [Lyons *et al.*, 1971] Lyons, L.R., R.M. Thorne, and C.F. Kennel, Electron pitch-angle diffusion driven by oblique whistler-mode turbulence, *Journal of Plasma Physics*, 6 (Part 3), 589-606, 1971.
- [Lyons *et al.*, 1972] Lyons, L.R., R.M. Thorne, and C.F. Kennel, Pitch-angle diffusion of radiation-belt electrons within the plasmasphere, *Journal of Geophysical Research-Space Physics*, 77 (19), 3455-3474, 1972.
- [Lyons and Thorne, 1973] Lyons, L.R., and R.M. Thorne, Equilibrium structure of radiation belt electrons, *Journal of Geophysical Research-Space Physics*, 78 (13), 2142-2149, 1973.
- [Mackerras *et al.*, 1998] Mackerras, D., M. Darveniza, R.E. Orville, E.R. Williams, and S.J. Goodman, Global lightning: Total, cloud and ground flash estimates, *Journal of Geophysical Research-Atmospheres*, 103 (D16), 19791-19809, 1998.

- [Macmillan *et al.*, 2003] Macmillan, S., S. Maus, T. Bondar, A. Chambodut, V. Golovkov, R. Holme, B. Langlais, V. Lesur, F. Lowes, H. Luhr, W. Mai, M. Manda, N. Olsen, M. Rother, T. Sabaka, A. Thomson, I. Wardinski, The 9th-Generation International Geomagnetic Reference Field, *Geophysical Journal International*, Volume 155, Issue 3, pp. 1051-1056, Dec. 2003.
- [Mielenz, 2000] Mielenz, K.D., Computation of Fresnel Integrals II, *Journal of Research of the National Institute of Standards and Technology*, 105 (589), 2000.
- [Neubert *et al.*, 1987] Neubert, T., T.F. Bell, and L.R.O. Storey, Resonance between Coherent Whistler Mode Waves and Electrons in the Topside Ionosphere, *Journal of Geophysical Research-Space Physics*, 92 (A1), 255-265, 1987.
- [Orville and Spencer, 1979] Orville, R.E., and D.W. Spencer, Global lightning flash frequency, *Mon. Wea. Rev.*, 107, 934-943, 1979.
- [Poevlerlein, 1948] Poevlerlein, H., Strahlwege von Radiowellen in der ionosphere, *Sitz. Bayerischen Akad. Wiss.*, 1, 175-201, 1948.
- [Ristic'-Djurovic' *et al.*, 1998] Ristic'-Djurovic', J.L., T.F. Bell, and U.S. Inan, Precipitation of radiation belt electrons by magnetospherically reflecting whistlers, *Journal of Geophysical Research-Space Physics*, 103 (A5), 9249-9260, 1998.
- [Roberts, 1966] Roberts, C.S., Electron loss from the Van Allen zones due to pitch angle scattering by electromagnetic disturbances, in *Radiation Trapped in the Earth's Magnetic Field*, edited by B.M. McCormac, Reidel Pub., Dordrecht, Holland, 1966.
- [Roberts, 1969] Roberts, C.S., Pitch angle diffusion of electrons in the magnetosphere, *Rev. Geophys.*, 7, 305, 1969.
- [Rodriguez and Gurnett, 1971] Rodriguez, P., and D.A. Gurnett, An experimental study of very low-frequency mode coupling and polarization reversal, *Journal of Geophysical Research-Space Physics*, 76 (4), 960, 1971.

- [*Roth et al.*, 1999] Roth, I., M. Temerin, and M.K. Hudson, Resonant enhancement of relativistic electron fluxes during geomagnetically active periods, *Annales Geophysicae-Atmospheres Hydrospheres and Space Sciences*, 17 (5), 631-638, 1999.
- [*Salby*, 1996] Salby, M.L., *Fundamentals of atmospheric physics*, Academic Press Inc., 1996.
- [*Schild and Frank*, 1970] Schild, M.A., and L.A. Frank, Electron Observations between Inner Edge of Plasma Sheet and Plasmasphere, *Journal of Geophysical Research*, 75 (28), 5401, 1970.
- [*Schulz and Lanzerotti*, 1974] Schulz, M., and L.J. Lanzerotti, *Particle diffusion in the radiation belts*, Springer-Verlag, 1974.
- [*Schunk and Nagy*, 2000] Schunk, R.W. and A.F. Nagy, *Ionospheres*, Cambridge University Press, 2000.
- [*Shklyar and Jiricek*, 2000] Shklyar, D.R., and F. Jiricek, Simulation of nonducted whistler spectrograms observed aboard the Magion 4 and 5 satellites, *Journal of Atmospheric and Solar-Terrestrial Physics*, 62, 347, 2000.
- [*Smith and Angerami*, 1968] Smith, R.L., and J.A. Angerami, Magnetospheric properties deduced from OGO-1 observations of ducted and nonducted whistlers, *Journal of Geophysical Research-Space Physics*, 73 (1), 1968.
- [*Sonwalkar and Inan*, 1989] Sonwalkar, V.S., and U. Inan, Lightning as an embryonic source of VLF hiss, *Journal of Geophysical Research-Space Physics*, 94 (A6), 6986-6994, 1989.
- [*Starks*, 2002] Starks, M.J., Effects of HF heater-produced ionospheric depletions on the ducting of VLF transmissions: A ray tracing study, *Journal of Geophysical Research-Space Physics*, 107 (A11), DOI 10.1029/2001JA009197, Nov. 2002.
- [*Stix*, 1992] Stix, T.H., *Waves in Plasmas*, Springer-Verlag New York Inc., 1992.

- [Tascione, 1994] Tascione, T.F., *Introduction to the space environment*, Krieger publishing company, Malabar, Florida, 1994.
- [Thorne and Horne, 1994] Thorne, R.M., and R.B. Horne, Landau Damping of Magnetospherically Reflected Whistlers, *Journal of Geophysical Research-Space Physics*, 99 (A9), 17249-17258, 1994.
- [Uman, 1984] Uman, M.A., *Lightning*, Dover Publications, 1984.
- [Uman, 1987] Uman, M.A., *The lightning discharge*, Academic Press, 1987.
- [Vette, 1991] Vette, J., *The AE-8 trapped electron model environment*, National Space Science Data Center, Report 91-24, Greenbelt, Maryland, 1991.
- [Voss et al., 1984] Voss, H.D., W.L. Imhof, M. Walt, J. Mobilia, E.E. Gaines, J.B. Reagan, U.S. Inan, R.A. Helliwell, D.L. Carpenter, J.P. Katsufakis, and H.C. Chang, Lightning-induced electron precipitation, *Nature*, 312 (5996), 740-742, 1984.
- [Voss et al., 1998] Voss, H.D., M. Walt, W.L. Imhof, J. Mobilia, and U.S. Inan, Satellite observations of lightning-induced electron precipitation, *Journal of Geophysical Research-Space Physics*, 103 (A6), 11725-11744, 1998.
- [Walt, 1994] Walt, M., *Introduction to geomagnetically trapped radiation*, Cambridge University Press, 1994.
- [Walt, 1996] Walt, M., Source and loss processes for radiation belt particles, in *Radiation Belts: Models and Standards*, edited by J.F. Lemaire, D. Heynderickx, and D.N. Baker, AGU Monograph 97, 1996.
- [Walt et al., 2002] Walt, M., H.D. Voss, and J. Pickett, Electron precipitation coincident with ELF/VLF wave bursts, *Journal of Geophysical Research-Space Physics*, 107 (A8), 2002.
- [Walter, 1969] Walter, F., Nonducted VLF propagation in the magnetosphere, Technical report 3418-1, Stanford University, Palo Alto, 1969.

- [*West et al.*, 1981] West, H.I., Jr., R.M. Buck, and G.T. Davidson, The dynamics of energetic electrons in the Earth's outer radiation belt during 1968 as observed by the Lawrence Livermore National Laboratories spectrometer on OGO 5, *Journal of Geophysical Research-Space Physics*, 86 (A4), 2111-2142, 1981.
- [*Wykes et al.*, 2001a] Wykes, W.J., S.C. Chapman, and G. Rowlands, Stochastic pitch angle diffusion due to electron-whistler wave-particle interactions, *Phys. of Plasmas*, Vol. 8, No. 6, June 2001
- [*Wykes et al.*, 2001b] Wykes, W.J., S.C. Chapman, and G. Rowlands, Enhanced phase space diffusion due to chaos in relativistic electron-whistler mode wave particle interactions with applications to Jupiter, *Planetary and Space Science*, Vol. 49, Issues 3-4, pp. 395-404, March 2001
- [*Yabroff*, 1961] Yabroff, I., Computation of whistler ray paths, *J. Res. NBS*, 65 (D), 485, 1961.
- [*Yip et al.*, 1991] Yip, W.Y., U.S. Inan, and R.E. Orville, On the spatial relationship between lightning discharges and propagation paths of perturbed subionospheric VLF/LF signals, *Journal of Geophysical Research*, 96 (A1), 249-258, 1991.